Chapter 7 - Water Chemistry

7.1 Abstract

This chapter explores alternative explanations for the water chemistry variations in perched and pore waters at Yucca Mountain. The chemical databases are integrated with hydrologic databases to evaluate different model conceptualizations of the hydrologic behavior of the mountain at low and high infiltration rates. The premise for this exercise is that chemical data, when combined with hydrologic data, provide the most relevant information for "validating" radionuclide transport models, as the movement of naturally occurring solutes is closely related to the potential migration of radionuclides. Our philosophy for model development and testing is one in which these data are used in the building of conceptual models, rather than as data to "calibrate" these models.

Two end-member hypotheses are evaluated for the origin of perched water at Yucca Mountain: a "fast pathway" fracture flow hypothesis, and a transient-mixing hypothesis. The overall consequence of the "fast pathway" fracture flow hypothesis is that it predicts poor performance for the unsaturated zone, as the Calico Hills transport barrier is essentially bypassed by fracture flow. Since this model is based on non-calibrated fracture properties, we propose an alternative to this model in the transient-mixing hypothesis, based on the integration of all elements of the hydrologic and chemical databases at Yucca Mountain. Its main strength is that it explains simultaneously the inversion in apparent ages between pore waters and perched water in the unsaturated zone, and the low chloride content of perched waters relative to the overlying TSw and underlying CHn pore waters. The apparent dissequilibrium in pore water and perched water contents is consistent with a model of transient flow, and we demonstrate that the stable isotope data and apparent ^{14}C and $^{36}Cl/Cl$ ages can be interpreted as resulting from a mixture of late Pleistocene/early Holocene water with modern waters. The existence of these mixed ancient/ modern perched water bodies therefore implies that an additional retardation mechanism exists

9 8 0 1 2 1 0 0 0 2
- Part 2

above the Calico Hills formation. The ubiquitous young ^{14}C ages in the Calico Hills formation pore waters beneath the perched water bodies and in other areas, also imply that a lateral component of flow occurs in the vitric Calico Hills and that this formation is not bypassed. Finally, this model is consistent with the three-dimensional stochastic mineral distribution model in which zeolitic and vitric tuffs are intricately interbedded beneath the repository horizon (see Chapter 12 for a description of the stochastic model).

The implication of this model for Performance Assessment is an improved performance of the Calico Hills Transport barrier beneath the repository by 1) the additional barrier component which regulates the downward flow of water to the saturated zone, and 2) increased water residence times in the unsaturated zone due to the presence of long term perched water bodies at depth (i.e., no flow), and lateral diversion above the basal vitrophyre and/or the underlying Calico Hills vitric units. This should result in increased sorption of radionuclides at those boundaries, as actinides sorb in clays and vitric tuffs as well as in zeolites. Finally, we expect that the transient mixing model may give rise to different performance predictions than are achieved with the current hydrologic properties.

7.2 Software and Data QA Status

The FEHM code is used to perform all flow and transport calculations in this report. The code is qualified in accordance with Los Alamos quality assurance requirements and is documented in (Zyvoloski et al, 1992, 1995a, 1995b). The QA status of the data used in this report is shown in Table 7-1 below.

Table 7-1. QA Status of Data used in this Chapter

REFERENCE	Q Status	DTN	COMMENT
Bodvarsson et al., 1997 "The Site-Scale Unsaturated Zone model of Yucca Mountain, Nevada, For the Viability Assessment, LBL Technical Report LBNL-40378.	Q	LB970601233129.001	No DTN assigned. Hydrologic property sets computed in this report are used throughout the present study.
Broxton, D. E., S. J. Chipera, F. M. Byers, and C. A. Rautman, 1993 Geologic Evaluation of Six Nonwelded Tuff Sites in the Vicinity of Yucca Mountain, Nevada for a Surface-Based Test Facility for the Yucca Mountain Project, Los Alamos National Laboratory Report LA-12542-MS, Los Alamos, New Mexico.	non-Q		Accession No. NNA.930826.0064
Fabryka-Martin et al., 1996b "Summary Report of Chlorine-36 Studies: Sampling, Analysis and Simulation for Chlorine-36 in the Exploratory Studies Facility, YMP Milestone Report 3783 M"			Accession Nos.
	Q	LAJF831222AQ95.005	MOL.19961015.0100
	Q	LAJF831222AQ95.007	MOL.19961015.0103
	Q	LAJF831222AQ96.013 *	* DTN supersedes DTN: LAJF831222AQ95.013
	Q		
	Q	LAJF831222AQ96.002	
	Q	LAJF831222AQ96.003	
	Q	LAJF831222AQ96.004	
	Q	LAJF831222AQ96.014	
	Q	LAJF831222AQ96.015	
	Q	LAJF831222AQ96.016	USGS DTN
	Q	GS950708315131.001	USGS DTN
	Q	GS960308315131.001	USGS DTN
	Q	GS950508314224.003	USGS DTN
	Q	GS960408314224.001	USGS DTN
	Q	GS960408314224.003	USGS DTN
	Q	GS960408314224.004	USGS DTN
	Q	GS060708314224.009	USGS DTN

Fabryka-Martin et al., 1996c "Summary Report of Chlorine-36 Studies, YMP Milestone Report 3782M"	non-Q Q Q Q Q Q Q Q Q Q Q Q Q Q Q Q Q non-Q	LAJF831222AN96.001 LAJF831222AQ96.002 LAJF831222AQ96.003 LAJF831222AQ96.004 LAJF831222AQ96.005 LAJF831222AQ96.006 LAJF831222AQ96.007 LAJF831222AQ96.008 LAJF831222AN96.009 LAJF831222AQ96.010 LAJF831222AQ96.011 LAJF831222AQ96.012 LAJF831222AQ96.013 LAJF831222AQ96.014 LAJF831222AQ96.015 LAJF831222AQ96.016 LAJF831222AQ95.003 LAJF831222AN95.004	Accession Nos. MOL.19961015.0094 MOL.19961015.0097
Flint et al., 1996 Conceptual and numerical model of infiltration for the Yucca Mountain Area, Nevada",USGS WRIR MOL 19970409.0087	Q	GS960908312211.003/ MOL.19970409.0087	USGS DTN 3GUI623M
Kwicklis, E.M. and J.P. Rousseau, 1996 Implications for waste isolation, *Hydrogeology of the unsaturated zone, North Ramp area of the Exploratory Studies Facility, Yucca Mountain, Nevada*, J.P. Rousseau, E.M. Kwicklis and D.C. Gillies (Eds.), U.S. Geological Survey Water Resources Investigations Report, (*in review*).	non-Q	Indeterminate	
Levy et al., 1997 "Investigations of Structural Controls and Mineralogic Associations of Chlorine-36 fast pathways in the ESF,. Yucca Mountain Project milestone report SP2301M4	Q	LASL831222AQ97.001	LANL DTN
Phillips, F.M., 1994 Environmental tracers for water movement in desert soils of the American southwest, Soil Sci.Soc. Am. J., 58, 15-24.	non-Q		

Rousseau, J.P. et al., 1996 Hydrogeology of the unsaturated zone, north ramp area of the exploratory studies facility, Yucca Mountain, Nevada, U.S. Geological Survey Water Resources Investigation Report 96-####, (in review).	non-Q	GS960308312232.001	USGS DTN
Yang et al., 1996, Interpretations of Chemical and Isotopic Data From Boreholes in the Unsaturated Zone at Yucca Mountain, Nevada, USGS Water-Resources Investigations Report WRIR 96-4058.	Q	GS951108312271.006	USGS DTN
Yang et al., 1997, Hydrochemical Investigations and Geochemical Modeling in Characterizing the Unsaturated Zone at Yucca Mountain, Nevada, (In Preparation).	non-Q		

7.3 Introduction

In other chapters, we have used geochemical databases to constrain and evaluate the validity of our flow and transport models in order to provide a strong scientific basis for the abstractions of these products used by Performance Assessment. In this chapter, we will focus on the water chemistry databases for pore waters and perched waters, in order to identify and discuss alternate models for flow and transport in Yucca Mountain.

7.4 Hydrochemical setting

Our present conceptual model for the hydrochemical system at Yucca Mountain has evolved from the earlier hydrologic models of Winograd (1981) and Montazer and Wilson (1984) and more recent hydrochemical databases (Fabryka-Martin et al., 1996b-c; Flint et al., 1996; Bodvarsson et al., 1997; Levy et al., 1997; Yang et al., 1996, 1997), and is the product of the integration of hydrologic, mineralogic, structural, hydrochemical and geochemical field and laboratory databases collected over the past 14 or so years (see Table 15-1). This model is

represented briefly by the following components involving two end member behaviors as a function of low and high infiltration rates, representing modern and ancient climates respectively.

7.4.1 TCw: Surface Infiltration

Under all climatic conditions the downward migration of meteoric waters through the Tiva Canyon welded tuffs (i.e., TCw) occurs via fracture flow. The water chemistry will reflect spatial and temporal changes in evapotranspiration and is not expected to undergo any modifications during the *rapid downward migration* of surface waters through the TCw, to the top of the Paintbrush non-welded Tuffs (i.e., PTn).

7.4.2 PTn: Transition from fracture dominated flow to matrix dominated flow

Under low infiltration rates and with the exception of discrete fracture flow paths, associated with large scale faults at the surface (Levy et al., 1997), matrix flow is the dominant mechanism sustained throughout the PTn. For higher infiltration rates, fracture flow is more predominant but only represents approximately 20% of the total water flux (see Chapter 6, this report). This is because these discrete "fast paths" are not ubiquitous, are not associated with large catchment areas at the surface, and therefore do not involve large volumes of water. Under present climate conditions, fractures do not contribute substantially to the total water flux through the PTn even though they may represent "fast pathways". The water chemistry in the PTn matrix pore waters is believed to represent a mixture of modern meteoric waters derived directly from the surface, and having undergone different degrees of evapotranspiration.

7.4.3 TSw: Transition from matrix dominated flow to fracture dominated flow

Under all infiltration rates, the flow of water in the non-lithophysal welded Topopah Spring hydrologic unit (i.e., TSw) is predominantly via fracture flow. As in the case of the TCw, ground water travel times from the base of the PTn to the top of the basal TSw vitrophyre are very short. In terms of water chemistry, different degrees of chemical maturation may occur as a function of infiltration rate, as indicated by the solution- precipitation textures from Yucca Mountain fracture fillings (Vaniman and Chipera, 1996).

At high infiltration rates, lateral diversion, down-dip along the top of the basal TSw vitrophyre is possible in most areas in the vicinity of the repository area, leading to the formation of perched water bodies on the down dropped side (i.e., west) of large normal faults (e.g., Figure 7-1; boreholes USW UZ-14/UZ-1, USW SD-9, USW SD-12). Exceptions include areas where the vitrophyre is missing (e.g., borehole USW G-2), areas possibly associated with complex tectonic disruptions in the vicinity of intersecting fault zones (e.g., boreholes NRG 7/7a, Drill Hole Wash/ Ghost Dance fault intersections; USW SD-7, south-west splay of Ghost Dance fault/ Dune Wash / Abandoned Wash fault intersections; c.f., Figure 7-1). This lateral flow combines with a vertical flow component to produce a mixed perched water chemistry with low chloride concentrations at the top of the vitrophyre. Relatively slow seepage from perched water bodies and/or during lateral flow is expected through fractures in the basal TSw vitrophyre. These seepage waters possibly mix with underlying waters into the underlying non-welded tuffs of the Calico Hills formation (i.e., CHn).

At low infiltrations or in the case where the vitrophyre does not appear to be a barrier to vertical flow locally, water flux is unimpeded and reaches the top of the Calico Hills formation.

7.4.4 CHn: composite vertical flow and lateral diversion

The Calico Hills non-welded tuffs are comprised of interlayered zeolitized and non-zeolitized units underlying the repository horizon. The flow in the CHn is probably complex due to the intricate spatial distribution of vitric and zeolitic rocks (c.f., Chapters 6 and 12). Slow percolation through matrix and fractures through intermingled pathways in vitric and zeolitic rocks, is expected to retard and divert vertical flow through the mountain. In all cases, the flow in the CHn is complex due to the complex spatial distribution of vitric and zeolitic rocks (c.f., Chapters 6 and 12). The perched water chemistries should reflect mixing as in the case of the basal TSw vitrophyre.

In the case where the basal vitrophyre is non-existent or bypassed by fracture flow, a permeability barrier may occur, due to the low permeability of the underlying zeolitic Calico Hills

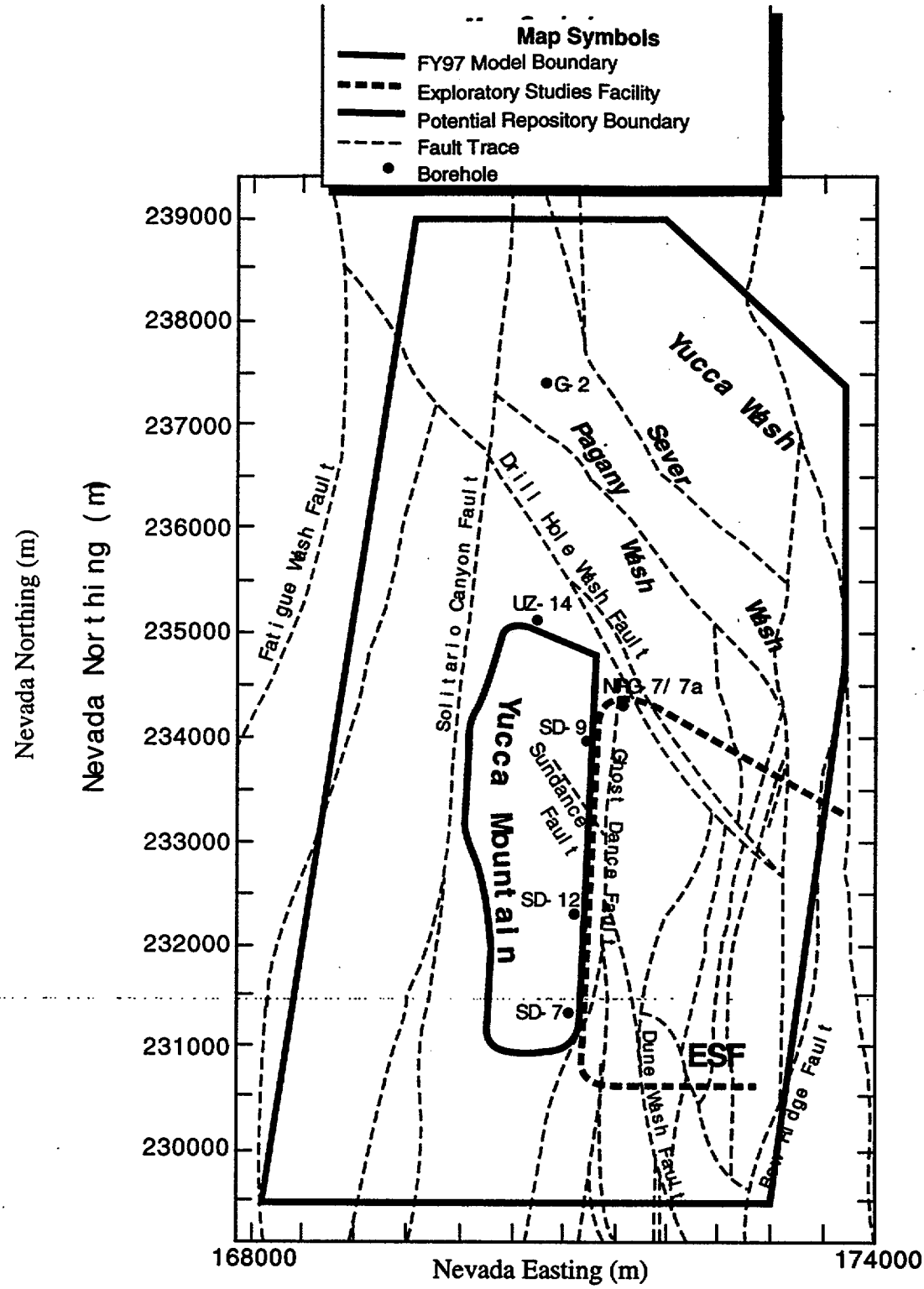

Figure 7-1. Map of Yucca Mountain site area with boreholes (i.e., G-2, UZ-14, NRG-7/7a, SD-9, SD-12, and SD-7)where perched water has been observed. Green line: site-scale model boundary. Blue: ESF. Red line: outline of potential repository.

formation, when present. This mechanism is possible for any infiltration rate and can result in the formation of perched water and lateral flow within the vitric Calico Hills. The pore water chemistry is expected to be strongly influenced by both the lateral flow component in the matrix (i.e., high chloride concentrations) and the vertical flow beneath the perched water bodies (i.e., low chloride concentrations).

7.4.5 Water Table: Seepage via fractures and matrix flow from the base of the CHn into the saturated zone

This conceptual model allows for some fast pathways through tectonic disruptions of the original stratigraphic sequence, but under present climatic conditions, these pathways are not associated with the bulk of the water flux through the mountain. Both the PTn and the TSw Basal vitrophyre/CHn horizons play an important role in retarding the flow of meteoric waters to the water table.

7.5 Perched Water Chemistry

7.5.1 The Origin and Significance of Perched Water

In complex geologic settings, where the intrinsic hydrologic properties of rocks can be heterogeneous, the state of saturation above the static water table can vary so that saturated zones may be nested in vadose zones. These saturated conditions can be discontinuous in time as well as space, and form when contrasting hydrologic properties between juxtaposed formations give rise to a barrier to flow (Freeze and Cherry, 1979). The formation of perched water bodies also described as inverted water tables, typically involves a discrete boundary with a large permeability contrast and/or the transition from predominantly fracture flow to predominantly matrix flow and vis-versa. Heavy rainfall or climatic changes can lead to the formation of a temporary perched water body via transient effects in ground water flow systems. These are the result of time-dependent changes in the inflows and outflows at the ground surface (e.g., precipitation, evapotranspiration and infiltration). Therefore transient perched water bodies can exist at different time scales; from hours to months, associated with heavy rainfalls and snow melt infiltration, to

hundreds or several thousands of years, associated with climatic changes, and depending on the nature of the flow barrier, its depth from the surface, and the source and sink terms controlling the flux of water into and out of the perched system.

Several lines of evidence point to the existence of perched water bodies at depth in the vicinity of the potential repository site at Yucca Mountain. Their existence can be explained in part by the heterogeneous hydrologic properties exhibited by the various volcanic layers, enhanced locally by the juxtaposition and alteration of rocks along major fault systems identified in the mountain. Our knowledge of the existence of perched water bodies, their geometry and the processes that lead to their formation, is key to understanding the response behavior of Yucca Mountain to changes in local precipitation and global climate.

Unfortunately, the hydrologic characterization of these bodies when detected is scarce, the geochemistry complex and the hydrologic and chemical databases are often incomplete and/or unreliable. These factors allow for the existence of a wide range of conceptual models for the formation of perched water at Yucca Mountain, with the potential for drastically differing consequences for the performance of the unsaturated zone barrier and its ability to retard the migration of radionuclides from the repository to the water table and the accessible environment.

With some variations, most conceptual models advanced thus far, to explain the presence of perched water, involve a hydrologic system dominated by fracture flow (Bodvarsson et al., 1996, 1997), in which the movement of surface waters through fast vertical pathways in the mountain, rapidly reach the water table or saturated zone. In these models, perched waters represent local perturbations to that system due to the presence of anomalous properties associated with faults and some localized hydrologic heterogeneities in the tuffs of Yucca Mountain (i.e., Paintbrush Group, Topopah Spring and Calico Hills formations). These models imply that strong lateral and vertical heterogeneities exist in the Yucca Mountain hydrologic system. For example the basal vitrophyre must be relatively impermeable to vertical flow in areas where perched water exists (i.e., negligible fracture and matrix permeabilities), but be highly permeable elsewhere (i.e.,

high fracture permeability) so as to allow water to reach the saturated zone via fracture flow. Such a system also implies lateral flow is minimal to non-existent, and that perched waters represent modern meteoric waters. Furthermore these models imply that the fault systems that act as fast path channels for surface waters into the perched water zones also serve as lateral barriers to flow, in those same zones.

In this section, we will attempt to demonstrate that a "piston model" or "fast pathway" fracture flow model as presented above for the unsaturated zone at Yucca Mountain is not consistent with all observations. The alternative model involves a complex heterogeneous system of fracture/matrix interactions and takes into account the past climatic history of the Yucca Mountain area. The consequences for the performance of the unsaturated zone barrier at Yucca Mountain are diametrically opposite to those of the previous conceptual models. We will demonstrate that in the vicinity of the repository environment, the hydrologic and hydrochemical databases can be best explained by a basal vitrophyre of mostly homogeneous intrinsic hydrologic characteristics, which impede vertical flow during high infiltration conditions, and accommodates vertical flow during low infiltration conditions. This model allows for a lateral component of flow at high infiltration conditions, essential to the formation of perched water bodies. Perched water bodies in the repository footprint (i.e., boreholes USW UZ14/UZ1, USW SD-9 and USW SD12) are all composed of waters ranging from late Pleistocene to early Holocene in age implying that an inverted water table may exist at depth that retards the vertical movement of surface waters for up to 10,000 years prior to release through seepage into the underlying Calico Hills formation. They also exhibit lower chloride concentrations than from areas directly above or below them. These two conditions require that a lateral component of flow be present in the formation of perched water. The existence of these mixed/ancient perched water bodies therefore imply that an additional retardation mechanism exists above the Calico Hills formation.

7.5.2 Hydrologic evidence for perched waters

Perched water occurrences in the unsaturated zone at Yucca Mountain have been summarized by Striffler et al., 1996, and their detailed hydrologic and chemical signatures

described elsewhere (e.g., Kwicklis et al., 1996; Yang et al., 1996; Bovardsson et al., 1997). Typically peroxide waters at Yucca Mountain have been reported in the vicinity of a zone of fractured rock overlying a layer of lower fracture permeability (e.g., boreholes USW UZ-14/1, NRG-7/7a, USW SD-7, USW SD-9, USW SD-12, and G-2). However the data on most perched water bodies is incomplete as only USW UZ-14 and USW SD-7 produced sufficient perched water for pumping tests. Consequently, the hydrologic and geochemical evidence available for understanding the origin of perched-waters at Yucca Mountain does not allow for definitive answers.

The following represent the conditions necessary for perched waters to exist at Yucca Mountain.

Based on the observation of free water in some boreholes, it implies that:

- In perched water bodies where free water is observed, the water saturation within must have been high enough to initiate fracture flow. The water pressure within that body of water must have also exceeded static atmospheric gas pressures that would be expected for that elevation.
- A large contrast in hydraulic conductivity between adjacent geologic formations must be present.
- A permeable layer or pathway system must overly a relatively impermeable layer and/or a well-connected fractured formation must overly a locally unfractured or poorly connected fractured formation.
- Perched water in a dipping horizontal plane suggests a lateral barrier to down dip flow, such as a fault, may be present.
- The flow pathway is unlikely to pass vertically through the unsaturated zone to the water table, without being retarded by the perched water body, as water must be diverted laterally to a higher permeability channel to reach the water table.

Perched water at depth was located, from North to South, in boreholes G-2, USW UZ-14/ UZ-1, NRG-7/7a, USW SD-9, USW SD-12, USW SD-7 (Figure 7-1).

G-2: Located at the northern end of Yucca Mountain, near the site model boundary (Figure 7-1), a composite water level (c.f., Czarnecki et al., 1994), was detected at an elevation of 1,032m in 1981. Since then, the water level has declined by approximately 12m to an elevation of 1,020m (Czarnecki, 1997, personal comm.). The water level was originally thought to represent the saturated zone potentiometric surface, implying a large hydraulic gradient to the north of Yucca Mountain. The persistent decline since in water level since 1981, and the observation of water flow in fractures above the apparent water table point to the possibility that in fact this is a perched water body. Several pump tests were conducted recently (O'Brien, 1996), and perched water chemistry can be found in Yang et al. (1996).

USW UZ-14/UZ-1: As can be seen in Figure 7-1, both are situated in Drill Hole Wash. The USW UZ-14 hole is located N-NW of the potential repository site at Yucca Mountain, and 26.2 m from USW UZ-1. A perched water zone was detected initially as wet core samples just above the top of the Topopah Spring basal vitrophyre, at a depth of 383m. Several pumping tests were conducted and complete drawdown recovery occurred after 5.6 days indicating a large body of perched water (Czarnecki, 1997, personal comm.). USW UZ-14 comprises the most complete hydrologic and geochemical database of any of the perched water bodies at Yucca Mountain. Drilling of the hole was started on April 15, 1993, cored to a depth of 672.6m by April 29, 1994, and completed to a total depth of 677.8m on May 1994. Predominant rock types are similar to those of USW UZ-1 reported by Whitfield et al. (1990). Methods of sample collection and analysis are given in Yang et al.(1996).

NRG-7/7a: As for USW UZ-14/UZ-1, this borehole is also located in Drill Hole Wash (Figure 7-1). Drilled to a depth of 461 m, through the basal TSw vitrophyre and into the top of the Calico Hills non-welded tuffs, perched water was present between 458m and 461 m depth, near the contact of a series of highly fractured welded tuffs overlying relatively unfractured, nonwelded tuffs.

No pump tests were conducted for this borehole. Perched water chemistry was collected by Yang et al. (1996).

USW SD-9: This borehole is located to the south of Drill Hole Wash and west of the Ghost Dance fault. Perched water was detected at 413 m depth, above the basal vitrophyre of the TSw, and 157 m above the water table. Insufficient free water yield prevented the use of hydraulic pump tests. Perched water chemistry was collected by Yang et al. (1996).

USW SD-12: This borehole is located in Antler wash, west of the Ghost Dance fault (Rautman and Engstrom, 1996). Perched water was detected by the attenuation of the surface barometric signal within and below the crystal poor vitric zone of the TSw. No pump tests or water chemistry data are available to confirm the existence of a perched water body at this location.

USW SD-7: This hole is located near the southwest corner of the ESF, west of the Ghost Dance fault and east of the Abandoned Wash fault trace. Perched water in this hole was located at the bottom of the Calico Hills zeolitic unit, 150m above the water table. Although pump test were conducted, a small volume of water is indicated as the water level did not recover to the pre-pumping levels after testing (Bodvarsson et al., 1997). Perched water chemistry was collected by Yang et al. (1996).

7.5.3 Chemical Composition of Perched Waters

Perched waters are generally dilute sodium bicarbonate waters, chemically distinct from pore waters in the unsaturated zone, and somewhat compositionally similar to saturated zone waters. Below are some of the key characteristics of perched waters from Yucca Mountain.

- Lower chloride concentrations with respect to unsaturated zone pore waters situated above and below. Pore waters have chloride concentrations that range from 10-250 mg/l whereas perched waters have concentrations of 4-8 mg/l.
- Cl/Br ratios in perched waters have a range of 25-120 with an average of approximately 100. This distinguishs them from saturated zone waters which range from 120-150 with an average of approximately 130. Unsaturated zone pore waters ratios range from 162-428, whereas the

ratio in precipitation at Yucca Mountain averages about 74.

- Older apparent ages, with respect to pore water ages from the PTn and the CHn, located above and below respectively (Yang et al., 1997). Apparent ages range from 3,000 to 12,000 years using ^{14}C radioisotope techniques (Yang et al., 1996, 1997). At USW UZ-14 the ^{14}C apparent ages range from 8,000 to 12,000 years (Fabryka-Martin et al., 1996). Although younger ages have been suggested based on age correction schemes (Yang et al., 1996; Kwicklis et al., 1996) ^{14}C and ^{36}Cl isotope data indicate that Yucca Mountain perched waters (i.e., USW UZ-14, USW SD-7 and NRG 7/7a) fall along a characteristic "meteoric water curve" suggesting that the perched water primarily consists of meteoric water, unaffected by any geochemical processes affecting carbon or chloride isotopic compositions (Fabryka-Martin et al., 1996a-c).
- Stable isotope values measured in perched waters at Yucca Mountain fall in the range of -12.1 to -13.8 per mil $\delta^{18}O$, and -87.4 to -100 per mil δD (Yang et al., 1997). These values are generally between modern and ancient water compositions. Pore waters show a greater range and slightly higher average values compared to perched waters (Yang et al., 1996). However, perched waters $\delta^{18}O$ and δD values are slightly higher than those measured in most of the saturated zone waters analyzed to date except UE 29a#2 and J-13, dated at 10,000 years B.P. (Benson and McKinley, 1985).

7.6 Conceptual Models for Perched Water

7.6.1 Fast-Pathway Fracture Flow Hypothesis

Geochemical Models: The US Geological Survey has used hydrological and hydrochemical data to develop a model for the origin of perched water found in USW UZ-14 and several other drill holes (Rousseau et al., 1996). This model builds on an earlier USGS model (Montazer and Wilson, 1984), and attributes the perched zones primarily to vertically percolating fracture waters that were intercepted and accumulated at the boundary of a low permeability barrier (i.e., the top of the To-

popah Springs vitrophyre, or the top of the Calico Hills non-welded tuff). This model is essentially a "steady-state" model in that the volume of water in the perched zones represents a balance of in-flow from fracture flow and outflow by leakage to the underlying units.

Several types of data have been cited in support of the "steady-sate" model. One is the finding of "bomb-pulse" tritium (^{3}H), and ^{36}Cl in the Calico Hills tuff and in the ESF. This finding is taken to mean that there are preferential "fast pathways" (i.e., <50 years B.P.) for the percolation of water in Yucca Mountain. These pathways are assumed to be intercepted by the low permeability layers below the Topopah Springs welded unit to create the perched layers.

Another set of data used to support the "steady-state" model involves ^{14}C ages. Data presented by Yang et al (1996), suggests that pore waters in the Calico Hills tuff are younger than pore waters higher in the system. According to Rousseau et al. (1996), such an arrangement of ages cannot be explained by vertical percolation through the matrix of the units overlying the Calico Hills tuff.

The observation that chloride concentrations in pore waters in the Calico Hills tuff exceed chloride concentrations in perched waters by factors of 3-4 when combined with the ^{14}C "age inversion" was interpreted by Rousseau et al. (1996) to indicate that the Calico Hills pore waters did not originate by slow seepage of perched water through the low permeability layers. The observed chloride concentrations in pore waters from the nonwelded unit at the base of the Topopah Springs tuff are significantly higher than those found in perched water or Calico Hills pore water. This is also taken as evidence that vertical percolation of pore water from the lower Topopah Springs welded unit into the upper non-welded Calico Hills tuff is not consistent with the data.

Hydrologic Models: The formation of perched water was recently investigated by Bodvarsson et al. (1996, 1997), using a 3-D steady-state hydrologic model. The simulations involved the use of hydrologic data from up to 6 boreholes with perched water bodies (i.e., USW UZ-14/UZ-1, G-2, USW SD-7, USW SD-9, USW SD-12 and NRG-7/7a), and combined with the surface infiltration

map of Flint et al. (1996). Steady-state simulations were compared to measured water saturation and water potential profiles. Perched water ages were also used to compare with the simulated groundwater travel times.

In the latest conceptual model, it is assumed that perched water occurs where the percolation flux exceeds the capacity of the geologic media in the unsaturated zone to transmit flux. Based on an interpretation of the geochemical data base of Yang et al. (1996), they conclude that perched waters at Yucca Mountain are unlikely to represent past climate conditions. This is based on the interpretation that:

- Corrected ^{14}C perched water ages are relatively modern.
- Perched water chloride concentrations are low relative to the overlying PTn values.
- Perched water and pore water chemistries at depth, are in apparent dissequilibrium.
- ^{3}H and ^{36}Cl bomb pulse signals in the ESF and the Calico Hills respectively (Yang et al., 1996; Fabryka-Martin et al., 1996a-c; Levy et al., 1997), require fast pathways at depth.

The "fast-pathway" fracture flow model hypothesis therefore requires circumventing the PTn matrix and the Calico Hills zeolitic tuffs, and is characterized by the following:

- With the exception of local occurrences of perched water, water fluxes travel predominantly through fractures from the surface to the water table with little interaction with matrix pore waters in the unsaturated zone.
- Surface waters undergo very little evaporation prior to infiltration.
- Rapid transport through the PTn, circumventing matrix flow, represents the largest flux component of water.
- With the exception of zones of local perching, a large volume water fraction circumvents the Calico Hills through fracture flow in the zeolites.
- Travel times to the water table vary generally from 50 to 3,000 years.

7.6.2 Transient Mixing Hypothesis

Hydro-geochemical Models: Beginning with the observation that there are zones of perched water present at depth today, it follows that under earlier, higher infiltration conditions (i.e., 10,000-20,000 years ago), larger perched waters bodies must have formed in the same locations and possibly other locations as well. If the rate of seepage from these perched water bodies is sufficiently slow, one would expect that with some modifications, remnants of the Late Pleistocene/Early Holocene perched water bodies still exist today.

7.6.2.1 Climatic Evidence

Over the past 10,000 years, the global climate has changed from a glacial cycle to a post- or interglacial cycle (Imbrie and Imbrie, 1980; Imbrie, 1985). In the southwestern United States, the glacial periods are typically associated with wet climates, whereas the interglacials are dry (Gauthier and Wilson, 1994). Studies of Yucca Mountain demonstrate that the present climate belongs to a dry, interglacial period and that the recent past climate (i.e., 10,000 years ago.) was pluvial (Spaulding, 1985; Benson and Klieforth, 1989; Paces et al., 1993; Marshall et al., 1993; Forester, 1994; Forester and Smith, 1994). Although glacial cycles recur every 100,000 years or so, higher frequency global climate perturbations are also indicated (Imbrie et al., 1984; GRIP, 1993; Gauthier and Wilson, 1994). Although there is no direct evidence for smaller recurrence interval climate fluctuations (i.e., 1,000 to 2,000 year intervals) in the Yucca Mountain area (Winograd et al., 1992), there is evidence for an important climate change over the past 10,000 years, which is expected to have had a significant influence on net infiltration at Yucca Mountain (Gauthier and Wilson, 1994).

The evaluation of past and present climates at Yucca Mountain has recently been used to relate changes in near-surface processes (e.g., infiltration) to climate, and understand the hydrologic response above and below the potential repository site at Yucca Mountain (Flint et al., 1996). Using global ocean $\delta^{18}O$ time data from Imbrie et al. (1984), Flint et al. (1996) have simulated hydrologic conditions at Yucca Mountain over the past 600,000 years. Based on this

analysis, they predict a mean recharge rate of almost 5mm/yr, consistent with average infiltration estimates from environmental isotope studies (Fabryka-Martin et al., 1996a-c), and with a maximum of 10mm/yr 18,0000 years ago and a minimum of 1mm/yr at present. They also predict that over the past 10,000 years the average precipitation at Yucca Mountain has decreased from approximately 260mm/yr to a present day average precipitation rate of 170mm/yr (Hevesi et al., 1991). Based on model predictions, Flint et al. (1996) estimate that this results in a decrease in infiltration rate of approximately a factor of 5 (Flint et al., 1996).

Given that climate changes of the same order of magnitude are possible over the next 10,000 years (Gauthier and Wilson, 1994; Flint et al., 1996), understanding the effects of this recent past climate on the hydrologic system at Yucca mountain is a key to understanding the behavior of the system in the future. In order to accomplish this, it is necessary to comprehend the coupled hydrochemical system at Yucca Mountain. In this model, the measured environmental isotope abundances, radioactive and stable isotopic compositions and water chemistry of perched- and pore waters, are believed to capture both the recent and ancient hydrologic histories of the mountain, integrated temporally and spatially. Kinetically driven equilibrium and dissequilibrium hydrochemical processes, coupled with an understanding of the complex dynamics of the hydrochemical system at Yucca Mountain, can provide an insight into the behavior of the system over time. This concept represents the foundation for the conceptual model presented in this work. By integrating hydrologic and geochemical databases into model simulations, we will attempt to demonstrate that the pluvial pleistocene period and its transition to a dry interglacial present climate are both captured by the hydrochemical signature of Yucca Mountain at depth.

7.6.2.2 Structural and Mineralogical Setting

As discussed previously, the formation of perched water bodies typically requires that a flow barrier exist. The most commonly invoked flow barriers involve a discrete boundary with a large permeability contrast (Bodvarsson et al., 1997) and/or the transition from predominantly fracture flow to predominantly matrix flow and visa-versa (Robinson et al., 1996, present study; Fabryka-Martin et al., 1996a-c).

In the case of Yucca Mountain several such hydrologic settings might exist, the simplest and most obvious ones being the boundary between the base of the PTn and the upper TSw vitrophyre, and the boundary between the top of the basal Tsw vitrophyre and the overlying devitrified tuffs of the Topopah Spring formation. The first of these boundaries, the PTn, represents a matrix permeability contrast of approximately 2 orders of magnitude (i.e., 0.2×10^{-12} to 0.67×10^{-14} m^2; Bodvarsson et al., 1997), and results in a transition from matrix flow to fracture flow with increasing depth, at low to intermediate infiltration rates (Fabryka-Martin et al., 1996a-c; Robinson et al., 1996, present study). Conversely, the permeability contrast between the top of the basal TSw vitrophyre and the overlying devitrified TSw tuffs is only a factor of 2 (Bodvarsson et al., 1997). The absolute matrix permeabilities however, are much lower (i.e., 0.13×10^{-15} to 0.65×10^{-16} m^2), so that both lithologies exhibit dominantly fracture flow properties.

Vitrophyre Mineralogy: With the exception of data from boreholes USW SD-7 and NRG 7/7a, most perched water bodies in the vicinity of the potential repository footprint, are located just above the vitrophyre (e.g., USW UZ-14, USW SD-9, and USW SD-12). As both the basal vitrophyre and the overlying TSw devitrified tuffs have low matrix permeabilities and are predominantly characterized by fracture flow, perching at the vitrophyre is consistent with a model of lower fracture permeabilities than in the overlying devitrified TSw. Field investigations support this contention as fractures in the basal TSw vitrophyre can be classified into three categories:

- Perlitic cracks which tend to be concentric, non-penetrative curviplanar features of very small aperture and with no secondary alteration (Vaniman et al., 1993). The absence of clays or alteration products suggest that these do not contribute to the bulk fracture permeability of the vitrophyre.
- Penetrative fractures filled with devitrification alteration products (e.g., clays, clinoptilolite, opal CT). Although these features penetrate into the top of the vitrophyre they are not throughgoing (Levy and O'Neil, 1989). They have not been observed at the base of the vitrophyre and are interpreted as representing an alteration front associated with the

devitrification of the unit.

- Discrete fracture systems, commonly throughgoing and which may be associated with lower order fault systems. Generally poorly documented, these are believed to be tectonic in origin and are commonly associated with alteration minerals (e.g., clinoptilolite and smectite; Broxton et al., 1993).

Therefore, whereas fractures are commonly observed throughout the basal TSw vitrophyre in outcrop, most of them though penetrative, are not throughgoing. Though of variable aperture (i.e., 1-10mm), the throughgoing discrete fractures identified in the vitrophyre, are commonly coated or filled with secondary mineral alteration products (Vaniman, 1997, personal comm.). Based on these observations, fracture permeabilities of the basal vitrophyre are expected to be substantially lower than those of the overlying devitrified tuffs of the Topopah Springs formation. The basal vitrophyre is therefore likely to produce a barrier to flow under moderate to high infiltration rates, consistent with the occurrence of perched water above the basal vitrophyre (e.g., USW UZ-14, USW SD-9, USW SD-12).

Fault Mineralogy and Hydrologic Consequences: Given the nearly continuous eastward dip of the depositional bedding planes at Yucca Mountain (up to 10 degrees eastward dip), and the apparent ability of the basal vitrophyre in the vicinity of the potential repository area to impede vertical flow, it is likely that lateral diversion also occurs. As we will see in other sections perched water chemistries and isotopic compositions support a lateral flow hypothesis. However, in addition to a vertical barrier to flow, in this scenario a lateral barrier is also required for perched water to exist at Yucca Mountain. Based on these and other observations, several authors have suggested that faults may be responsible for impeding lateral flow at Yucca Mountain (Winograd, 1981; Montazer and Wilson, 1984; Bodvarsson et al., 1997).

Whereas fractures associated with larger scale fault structures have been shown to result in preferential pathways through the PTn (Fabryka-Martin et al., 1996a-c; Paces et al., 1996; Robinson et al., 1996, present study), it has been suggested that faults may also act as barriers to

flow at depth (Winograd, 1981; Montazer and Wilson, 1984). Because the Calico Hills nonwelded unit is more ductile than the overlying Topopah Spring welded unit, and because it is prone to gouge formation along shear zones and faults, Montazer and Wilson, (1984) suggest that fracture/ fault conductivities may be smaller in the vicinity of faults. Further, wesuspect that this is most likely at depth. Under most geologic settings and in the presence of humidity, gouge material typically increases mineral surface areas and consequently enhances reaction rates, leading to recrystallization along fault planes. This idea is supported by the extensive alteration observed in the vicinity of major fault zones affecting the Calico Hills formation (e.g., Fran Ridge, Busted Butte and Paintbrush faults; Broxton et al., 1993). At Busted Butte where such an exposure exists, the nonwelded tuffs of the Calico Hills formation which are largely unaltered, exhibit a localized zone of intense zeolitization next to a major normal fault that displaces the vitrophyre by several tens of meters vertically. Next to the fault, the non-welded base of the Topopah Spring member is thoroughly altered to clinoptilolite (i.e., 98wt.% zeolite). Though not as extensive, this zeolitization extends down the fault plane to the underlying vitric tuffs of the Calico Hills, and extends laterally several tens of meters on either side of the fault. Such a system is expected to act as a lateral barrier to flow because of the decreased fracture and matrix permeabilities associated with alteration, or in the absence of alteration, because of matrix/fracture permeability contrasts on either side of the fault. Even in the absence of alteration, the juxtaposition of low permeability devitrified Tsw tuffs on the downthrown side of the fault against high permeability vitric Calico Hills tuffs may form a capillary barrier. The effectiveness of the barrier will depend on the flux of water, and in a dual permeability system, the relative fracture and matrix permeabilities. A fault may act as a barrier at high infiltration rates if the fracture permeability contrast is high enough so as to impede flow. The same system however, may drain at lower infiltration rates. Conversely a fault may act as a barrier at low infiltration rates if the matrix permeability contrast and effective permeability are high enough so as to impede fracture flow. Again, this same configuration may drain via fracture flow at higher infiltration rates. At Yucca Mountain, in the probable case where geologic structures such as faults cause hydraulic discontinuities, water may either become

perched or drain depending on both extrinsic (e.g., infiltration rates and water flux) and intrinsic variables (e.g., effective fracture/matrix hydrologic properties). For perched water to be present either at the upper contact of the basal TSw vitrophyre (e.g., USW UZ-14, USW SD-12, USW-SD9) or the upper contact of the Calico Hills nonwelded unit (e.g., USW SD-7, NRG7/7a, USW G-2), such favorable conditions to flow barrier formation must exist. The proximity of USW UZ-14 to the down dropped side of the Drill Hole Wash fault (SW side) and of USW SD-12, USW SD-9, NRG7/7a, and USW SD-7 to the down dropped side of the Ghost Dance fault may be evidence that this perching mechanism is viable for Yucca Mountain in the area of the potential repository horizon.

From the evidence presented above, lateral flow along barriers to vertical flow is likely at Yucca Mountain. The existence of perched water bodies today, in the vicinity of known fault systems suggests that faults may impede continued horizontal water movement at depth by acting as barriers to lateral flow. Because the emplacement and tectonic histories responsible for the formation of the major geologic structures at Yucca Mountain (i.e., layering and fault systems), are believed to be over 5 million years old, and because associated fractures and mineral alterations in the basal vitrophyre and along faults are equally ancient (Levy and O'Neil, 1989), it follows that given the correct intrinsic hydrologic properties, the lithologic and structural boundaries that perform as barriers to flow today (i.e., low to moderate infiltration conditions), should have performed as such during the last ice age 10,000 to 20,000 years (i.e., moderate to high infiltration conditions).

7.6.2.3 Hydro-geochemical Model

A model which includes the existence of modified Late Pleistocene/Early Holocene perched water bodies at depth in Yucca Mountain would be distinguishable from a model that does not, using the following simple and testable geochemical and hydrologic criteria:

Hydrologic Criteria:There is a paucity of hydrologic criteria that can help distinguish between the various conceptual models. Calibrations to saturation data are non-unique and can therefore not be

used reliably to distinguish between the required hydrologic properties required for the models (Robinson et al., 1995, 1996, present study; Bodvarsson et al., 1996). The important difference between the proposed transient mixed water model, and fast pathway fracture models for the existence of perched water at Yucca Mountain, is that of a transient versus a steady-state model respectively. If one is to recognize the importance of the drastic change in climatic conditions over the past 10,000 years to the development of the present day hydrochemistry of the Yucca Mountain system, then only a transient model is appropriate. But, because this involves a past history, present day hydrologic measurements cannot hope to explain any differences between these models. Finally the alternative steady-state models, calibrated to matrix properties, invoke transient fracture flow as a dominant mechanism to provide a bypass mechanism of the PTn matrix (c.f., Bodvarsson et al., 1997), even though fracture properties are not well constrained by this approach.

Geochemical Criteria: Pleistocene perched water would be mixed with modern (i.e., post-pleistocene) waters so that the perched water bodies today would be identified as having a range of ages (assuming linear mixing) less than or equal to approximately 10,000 years old and always greater than present age. A model that does not allow for the presence of Pleistocene water implies all modern ages for the perched water body as travel times to the vitrophyre via fracture flow (Ptn bypass) are between several tens of years (e.g., ^{3}H; Yang et al., 1996) to less than 1,000 years (present study).

At Yucca Mountain, the apparent ages for perched waters range from 3,000 to 12,000 years using ^{14}C radioisotope techniques (Yang et al., 1996, 1997). However, Yang et al. (1996, 1997) has suggested that these apparent ^{14}C ages be corrected for caliche contamination and soil-zone carbon. When this correction is applied, residence times of perched waters drop to values between 2,000 to 8,000 years.

However, samples of perched water from USW UZ-14 measured for $^{36}Cl/Cl$ range from 392×10^{-15} to 675×10^{-15}, are consistent with late Pleistocene to Holocene ages (Fabryka-Martin et

al., 1996a-c), and are in agreement with the apparent ^{14}C age determinations above. Fabryka-Martin et al. (1996a-c) have shown that the independent behavior through time between ^{14}C and ^{36}C isotope decay rates (Figure 7-2, allows us to predict that "ancient water" will fall along a

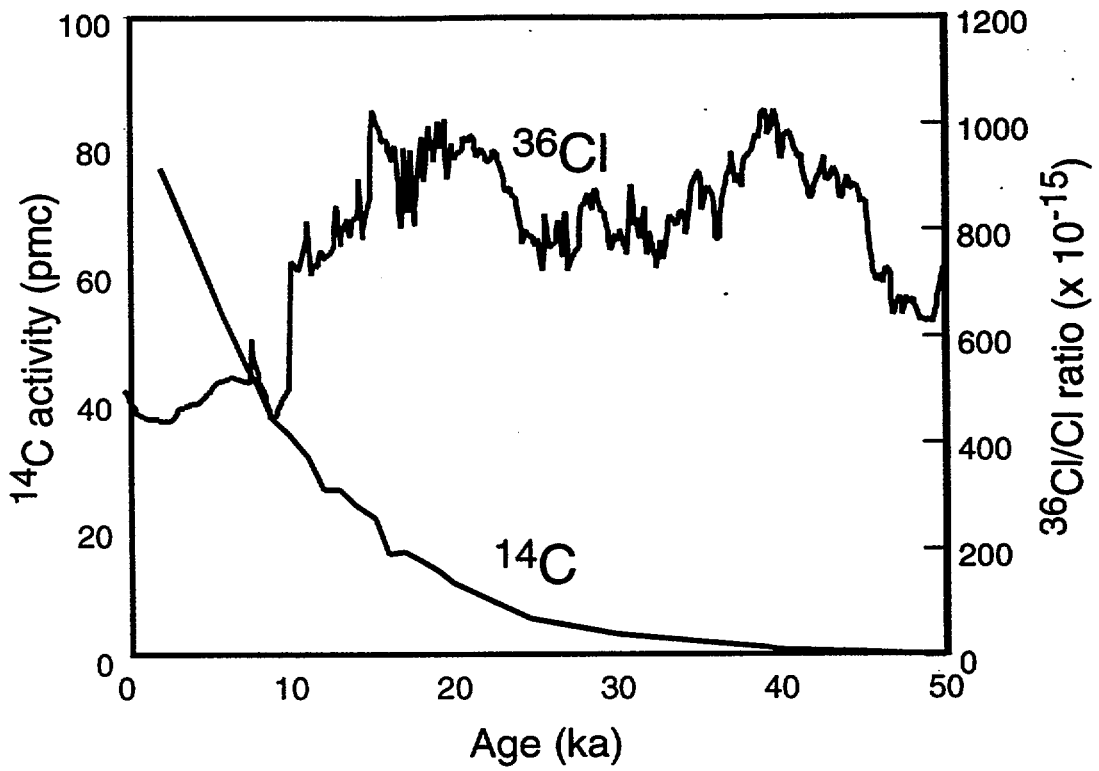

Figure 7-2. Reconstructed ^{14}C and ^{36}Cl activities for the last 50 ka. From Fabryka-Martin et al. (1996c).

characteristic "meteoric water curve" when plotted on a graph of ^{14}C versus $^{36}Cl/Cl$ (Figure 7-3). When perched water data are plotted together for various boreholes (i.e., USW UZ-14, USW SD-7 and NRG 7/7a), the data is shown to fall along "the meteoric water curve." This result strongly suggests that the ^{14}C and ^{36}Cl reconstructions are reasonable, and also that the perched water primarily consists of meteoric water, unaffected by geochemical processes such as caliche contamination, affecting carbon or chloride isotopic compositions. At a minimum, this would indicate that the apparent ^{14}C age determinations for perched water are more reliable than their

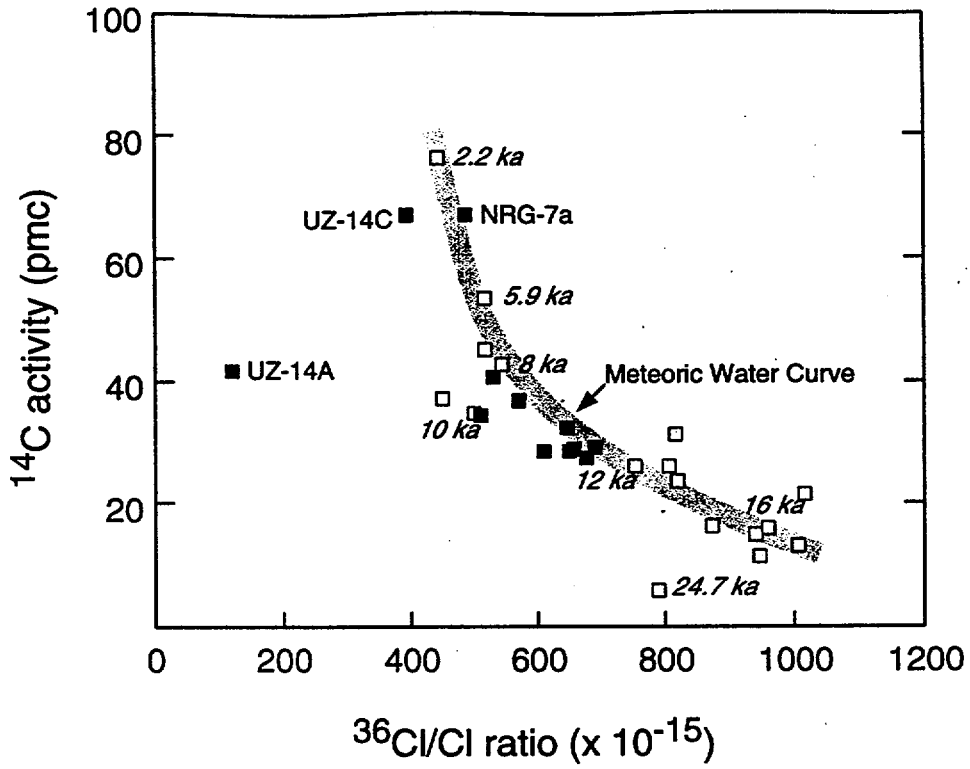

Figure 7-3. Reconstructed ^{14}C and ^{36}Cl activities in the atmosphere for the last 20 ka, from Fabryka-Martin et al. (1996c). USW UZ-14A and UZ-14C were shown to be contaminated with modern water. Perched water data from UZ-14, SD-7 and NRG-7/7a.

ages corrected for caliche contamination (e.g., Yang et al., 1996, 1997), and that the perched water at USW UZ-14 for example, is between 8,000 and 12,000 years B.P. corresponding to 25 to 40 pmc and consistent with the very low ^{3}H analyses from USW UZ-14 (Yang et al., 1996). This data also implies that a simple piston-flow (i.e., no mixing) model is not correct for the origin of perched water (Fabryka-Martin et al., 1996a-c).

In a Pleistocene perched water model, the isotopic compositions of perched waters measured today (i.e., $\delta^{18}O$ and δD) should fall between values from the last ice age (e.g., -15 to -20 per mil $\delta^{18}O$; -105 to -120 per mil δD; Yang et al., 1996) and modern compositions. Modern stable isotopic compositions vary a great deal both spatially and temporally but reported values

from 1984 rain storms at Yucca Mountain fall in the range -10.0 to -15.0 per mil for $\delta^{18}O$ and -70 to -90 per mil for δD (Yang et al., 1997).

In a mixed Pleistocene to modern perched water model, stable isotopic compositions are therefore expected to range between -13 and -15 per mil for $\delta^{18}O$, and -90 and -105 per mil for δD. In alternate models not involving a mixture with Pleistocene waters, the stable isotope values for perched waters should be modern.

The range of stable isotope values measured in perched waters today at Yucca Mountain fall in the range of -12.1 to -13.8 per mil $\delta^{18}O$, and -87.4 to -100 per mil δD (Yang et al., 1997), consistent with a mixing trend between modern and pleistocene waters, consistent with infiltration under cooler late-Pleistocene/early-Holocene climatic conditions, thus supporting the proposed model for perched water formation.

In order to be consistent with a Pleistocene perched water model, the chloride concentration (i.e., $[Cl]_{pw}$= 4 to 8 mg/l) of present day perched waters $[Cl]_{pw}$, should be consistent with higher infiltration rates (i.e., pluvial conditions) relative to the overlying unsaturated zone which should reflect the influence of a more recent, drier interglacial climate. Models that do not invoke Pleistocene water are required to bypass the PTn matrix, as the chloride concentration is high (i.e., [Cl]= 45 to 100mg/l, USW-14; Yang et al., 1996). Two bypass scenarios have been proposed:

- water travels via fracture flow through the PTn thereby bypassing the Ptn matrix and retaining low chloride concentrations (Bodvarsson et al., 1997; Kwicklis et al., 1996).
- water travels via fast matrix/fracture flow through the PTn in areas of high infiltration (i.e., lower chloride concentration), and then moves laterally underneath the low infiltration areas until a lateral barrier is encountered.

The chloride concentrations measured in the perched water bodies today are lower than those measured in PTn pore waters (e.g., 4 to 8 mg/l vs. 45 to 100mg/l, USW UZ-14; Yang et al., 1996). Simulations using calibrated hydrologic properties of Yucca Mountain rocks demonstrate

that this condition can be met *without bypassing the PTn matrix*, using a transient integrated flow model consistent with the past 10,000 year climatic history where a transition from pluvial (i.e., high infiltration) conditions to drier interglacial conditions existed.

Conversely, the other models postulate minimal matrix flow through the PTn and require fracture-dominated flow above the perched water bodies. This scenario is inconsistent with $^{36}Cl/Cl$ data from the ESF which indicate that a dominant proportion of the flow involves matrix flow through the PTn (Fabryka-Martin et al., 1996a-c; see also Chapter 6, present study). Whereas fast flow paths have been identified in the PTn using environmental isotope data (Fabryka-Martin et al., 1996a-c), these pathways have been shown to be discrete features, strongly correlated to large structural discontinuities (i.e., major fault zones; Levy et al., 1997) and are therefore not capable fo handling large volumes fractions of water under present climatic conditions. Fast water velocities are therefore not synonymous with large water volumes or fluxes, and present day measured matrix saturations are well calibrated for conditions of matrix dominated flow in the PTn (see Chapter 6, present study). Without completely bypassing the PTn matrix, these conceptual models fail to produce low enough chloride concentrations in perched water bodies under present day infiltration conditions.

7.6.3 Evaluation of Alternate Conceptual Models

The alternate conceptual models for the origin of perched water bodies in the unsaturated zone at Yucca Mountain can be grouped into "fast pathway"fracture flow models and transient mixing models. The first are "steady-state, piston flow models that predict that perched waters primarily reflect current climatic conditions. The latter are transient flow models that put a greater emphasis on paleoclimatic conditions in addition to present-day conditions. Hydrochemical data can be used to evaluate these various models. The intent in this section is to review the available hydrochemical data and to discuss the extent to which the data are consistent with or contradict the existing models.

7.6.3.1 The Radioactive Isotopes of Hydrogen, Chlorine and Carbon

Hydrogen and Chlorine: Radioactive isotopes of hydrogen (^{3}H) and chlorine (^{36}Cl) have been particularly useful in investigations of potential flowpaths of waters infiltrating Yucca Mountain under current conditions. This results from the fact that substantial quantities of these isotopes were added to the atmosphere during nuclear weapons testing between 1952 and 1958 and the early 1960's (Fabryka-Martin et al., 1996a-c). Elevated concentrations of ^{3}H and ^{36}Cl (i.e., bomb-pulse) have been detected in pore waters in the PTn, and occasionally in the Calico Hills tuffs (Yang et al., 1996; Fabryka-Martin, 1996a-c). Elevated concentrations of ^{36}Cl have also been found at several locations in the Exploratory Science Facility (ESF). These observations are difficult to explain with any model that does not include fast flow paths within the unsaturated zone at Yucca Mountain at least to the depth of the ESF.

What the available data do not constrain very well are the amounts of water that moved through the fast-pathways to transport the observed ^{3}H and ^{36}Cl. Tritium in particular, travels readily in the gas phase which obscures its interpretation with respect to water pathways and travel times. The current thinking is that these fast flow paths are associated primarily with highly fractured or faulted portions of Yucca Mountain in discrete zones and that they involve relatively small water fluxes due to small catchment areas associated with their surface expressions.

Carbon: The radioactive isotope of carbon (^{14}C) can be used to trace pre-bomb waters in the unsaturated zone at Yucca Mountain. Analyses of ^{14}C activities in pore waters from samples representing the PTn, the Topopah Springs tuffs and the Calico Hills tuffs have been reported by Yang et al. (1996; 1997). Analyses of perched waters were also reported. Surprisingly, the measured range of activities of ^{14}C in the Calico Hills pore waters are similar to the range of activities measured in the PTn pore waters. Both are relatively young (i.e., 300-5,000 years B.P.). The activities measured in perched waters are generally less than those measured in the pore waters and imply

that the perched waters are older than the pore waters, eventhough the pore waters are found above and below the perched waters.

According to the USGS model, the inverted age distribution below perched water bodies precludes explanations that require vertical percolation of water from the TSw matrix above the perched water, to the CHn matrix below the perched water bodies. This not necessarily the case, however, because the pore waters in the Calico Hills tuffs could represent mixtures of perched water and pore water from above the perched water bodies via lateral flow mechanisms identified in the simulations. The proportions of perched water and pore water required cannot reasonably be quantified because the chemical parameters involved are rather poorly constrained. Importantly, the young "ages" derived for Calico Hills *pore waters* have significant implications for transport that are discussed further below.

The apparent ^{14}C "ages" calculated for perched waters are in the range of 3,500-11,000 years B.P. (Yang et al., 1996). As noted above this implies the perched waters are older than pore waters above and below them. It could be argued that the apparent "ages" for perched waters must be corrected for dead carbon dissolved along the path these waters took to their current location (Yang et al., 1997). However, this correction is controversial in that there is not agreement on how much dead carbon the perched waters may have dissolved. The assumption by Yang et al. (1997) that the concentrations of the major chemical constituents in perched and pore waters are entirely the result of water rock interaction, and not the result of evapotranspiration of precipitation incident on Yucca Mountain is difficult to defend as discussed further below. In any case, a dead carbon correction would also need to be applied to the pore waters. In the end, perched waters would still be older than the pore waters.

7.6.3.2 The Conservative Environmental Tracers Chloride and Cl/Br

Chloride: Pore waters are chemically distinct from perched waters in the unsaturated zone. This is clearly evident in a comparison of chloride concentrations. Pore waters have chloride concentra-

tions that range from 10-250 mg/l whereas perched waters have concentrations of 5-8 mg/l. Pore waters in the PTn tend to have higher chloride concentrations than pore waters in the Calico Hills Tuff. Further, pore waters in the PTn tend to be calcium and magnesium chloride/sulfate waters while pore waters in the Calico Hills tuffs tend to be sodium bicarbonate/carbonate types. Perched waters tend to be similar to saturated zone waters in composition in most constituents and are generally dilute sodium bicarbonate waters.

The concentration of chloride in pore waters obtained from the three samples of the Topopah Springs tuff that overlap the perched zone in UZ-14 have chloride concentrations that are a factor of 10 higher than the chloride concentrations in perched waters (Yang et al., 1996). The implication is that perched waters have not chemically equilibrated with pore waters in this horizon over time frames of thousands of years. The reasons for this apparent disequilibrium are unclear, but likely involve processes unique to the devitrified-vitrophyre transition at the base of the Tpt. The fractures in this zone are highly mineralized (Levy, 1984), and various unusual mineral species have found in this zone. For example, a ferrous chloride phase (Lawrencite) was identified in at least one sample from this zone (Vaniman, 1997, personal comm.). Further, the amounts of pore water recovered from samples in this zone was small compared to samples from the PTn and the Calico Hills Tuff (Yang et al., 1997). The pore waters recovered from this zone have unusually high chloride to sulfate ratios compared to pore waters from the PTn (Meijer, 1996). These observations taken together suggest that the pore waters from the lower Topopah Springs Tuff are unusual and that the chemical data for them must be interpreted with caution.

Yang et al. (1997) have suggested that the concentrations of chloride in pore waters and perched waters reflects primarily chemical reaction of dilute infiltrating waters with the host rock. This suggestion ignores the fact that the chloride mass balance method for calculating infiltration rates produces values that are in the range of values calculated on the basis of physical measurements (Flint et al., 1996). To the contrary, a detailed analysis of pore water chemistry data (Meijer, 1996), has lead to the opposite conclusion that pore waters in the unsaturated zone at Yucca Mountain show very little evidence of reaction with the host rock.

Cl/Br: One other aspect of water chemistry that is of interest in this discussion is the ratio of chloride to bromide in waters within the Yucca Mountain flow system. Because both of these constituents show conservative behavior in ground water systems, their ratio can be used to differentiate waters of different origins. This ratio has been measured in many different waters by Fabryka-Martin et al. (1996, and personal comm.) and Yang et al. (1996). The available data suggest Cl/Br ratios in saturated zone waters at Yucca Mountain are in the range of 120 to 150 with an average of approximately 130. Perched waters have a range of 25 to 120 with an average of approximately 100. Pore water ratios range from 162 to 428. The ratio in precipitation at Yucca Mountain averages about 74. At low infiltration rates, the concentrations are assumed to differ from the chloride values by a factor similar to that in the PTn pore water samples (200:1, chloride:bromide). In high infiltration zones, the fluids are assumed to enter the mountain at ratios typical of precipitation, namely 100:1, chloride:bromide.

These data suggest that Cl/Br ratios could be quite useful as a tracer in the Yucca Mountain flow system. For example, the Cl/Br ratio is one of the few chemical parameters that distinguishes perched waters from saturated zone waters.

7.6.3.3 The Stable Isotopes

In terms of stable isotopes $\delta^{18}O$ and δD, pore waters show a greater range and generally higher average values compared to perched waters (Yang et al., 1996). However, perched waters $\delta^{18}O$ and δD values are slightly higher than those measured in most of the saturated zone waters analyzed to date except J-13 and UE 29a#2. This is consistent with the fact that J-13 and UE 29a#2 waters and perched waters have similar apparent ages (i.e., 9-10 ka) and were therefore infiltrated under similar climatic conditions. The somewhat higher average $\delta^{18}O$ and δD values in perched waters are also consistent with the younger apparent ^{14}C ages for these waters (Yang et al., 1996) and a post-glacial climate.

Values for $\delta^{13}C$ have been measured in many water samples by Yang et al. (1996). This parameter is of importance to the interpretation of ^{14}C data because it provides an approximate means of assessing the amount of dead carbon that may have been incorporated into a given water sample. Yang et al. (1996) have used this parameter to "correct" apparent ^{14}C ages for inherited dead carbon. Unfortunately, the values obtained for this parameter in pore waters show rather large variability. Further, the pore water $\delta^{13}C$ values are commonly out of equilibrium with the $\delta^{13}C$ measured in the gas phase (Yang et al., 1996), which is problematic. Finally, there could be effects from drilling and the pore water extraction techniques that further complicate the analysis. The conclusion reached here is that "correction" of $\delta^{14}C$ "ages" using the $\delta^{13}C$ data is fraught with difficulties and the results should be interpreted with caution.

7.7 Simulation Results

In this section we present results of simulations of major ions present in unsaturated zone fluids, including chloride, sulfate, and bromide. To recap the conceptual model used to simulate these species, each are assumed to be conservative ions once they transport into the bedrock below the soil zone. The distinction between chloride, sulfate, and bromide is in the source term for fluid entering the bedrock. Chloride is assumed to be conservative even in the soil zone, whereas sulfate and bromide undergo reactions within the soil zone that lower their concentrations. For sulfate and bromide, these reactions could be biological in origin, whereas sulfate concentrations could also be affected by precipitation under conditions of evapotranspiration (Freeze and Cherry, 1979).

The concentration of dissolved species such as chloride are presumed in this modeling to be inversely proportional to the deep percolation rate, that is, the flow escaping evapotranspiration and entering the bedrock. This model assumes that the deposition rate of chloride is constant and not spatially variable, and that the controlling factor for concentration in the percolating fluid is evapotranspiration. Therefore, fluid entering at high infiltration rate has low chloride

concentration, and low infiltration correlates to high concentration. The concentration values themselves are based on the midpoint of the range of estimated values of chloride deposition rate of 75 to 150 $mg/m^2/y$ reported by Phillips (1994).

For reasons discussed above, the ratios of sulfate and bromide to chloride appear to be lower than in precipitation for many pore water samples in the unsaturated zone. An exception is in the perched waters, which appear to have ratios more reflective of precipitation. To simulate this behavior, we postulate that in regions of high enough infiltration, evapotranspirative effects and reactivity of bromide and sulfate are minimal due to short residence times in the soil zone. This results not only in lower concentrations of major ions, but also a shift to ratios closer to that of precipitation in fluids that enter at high infiltration. Therefore, the concentrations in the infiltrating fluids are assumed to fall into two categories. At low infiltration rates, the concentrations are assumed to differ from the chloride values by a factor similar to that in the PTn pore water samples (1:1 for chloride:sulfate, and 200:1 chloride:bromide). In high infiltration zones, the fluids are assumed to enter the mountain at ratios typical of precipitation, namely 1:3 sulfate:chloride and 100:1 chloride:bromide. The cut-off infiltration rate is assumed to be 10 mm/y, above which the latter ratios apply. In essence, the ion ratios are used as an additional natural tracer in the simulations.

When this chloride concentration model is input at the top of the three-dimensional site model, the concentration entering the mountain is a strong function of the spatially varying chloride map as controlled by infiltration rate. Figure 7-4 shows the concentration along the top surface of the model (top figure) and in a horizontal slice at an elevation of 900 m (bottom figure). The concentration entering the system is a direct result of the correlation to infiltration rate described earlier. At depth, the concentration patterns are somewhat more uniform due to mixing of fluids with different concentrations. The values, in general, appear lower because the fluid that supplies the subsurface is heavily weighted toward the high infiltration (low concentration) values.

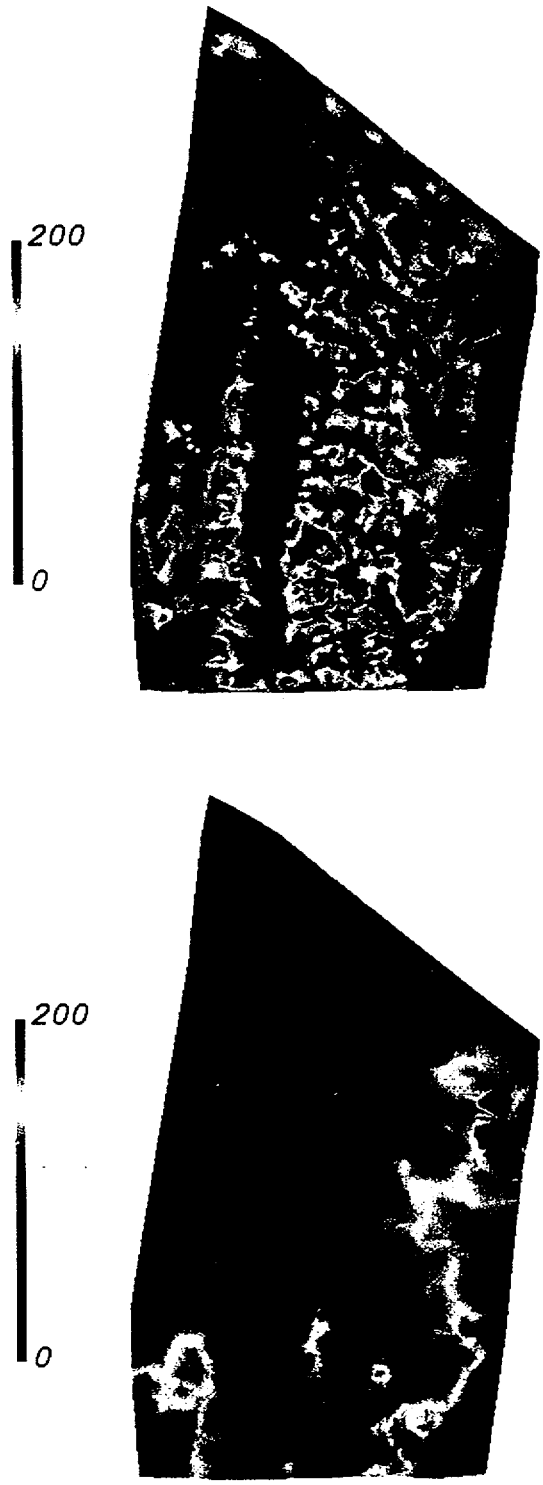

Figure 7-4. Chloride concentration predicted in the three-dimensional model. Top figure: map of chloride concentrations at the surface. Bottom figure: concentrations at and elevation of 900 m. Top of page is North.

In the surface chloride map, only a small fraction of the fluid actually entering the mountain has high concentrations.

Figure 7-5 shows the predicted chloride concentrations for a steady state dual permeability

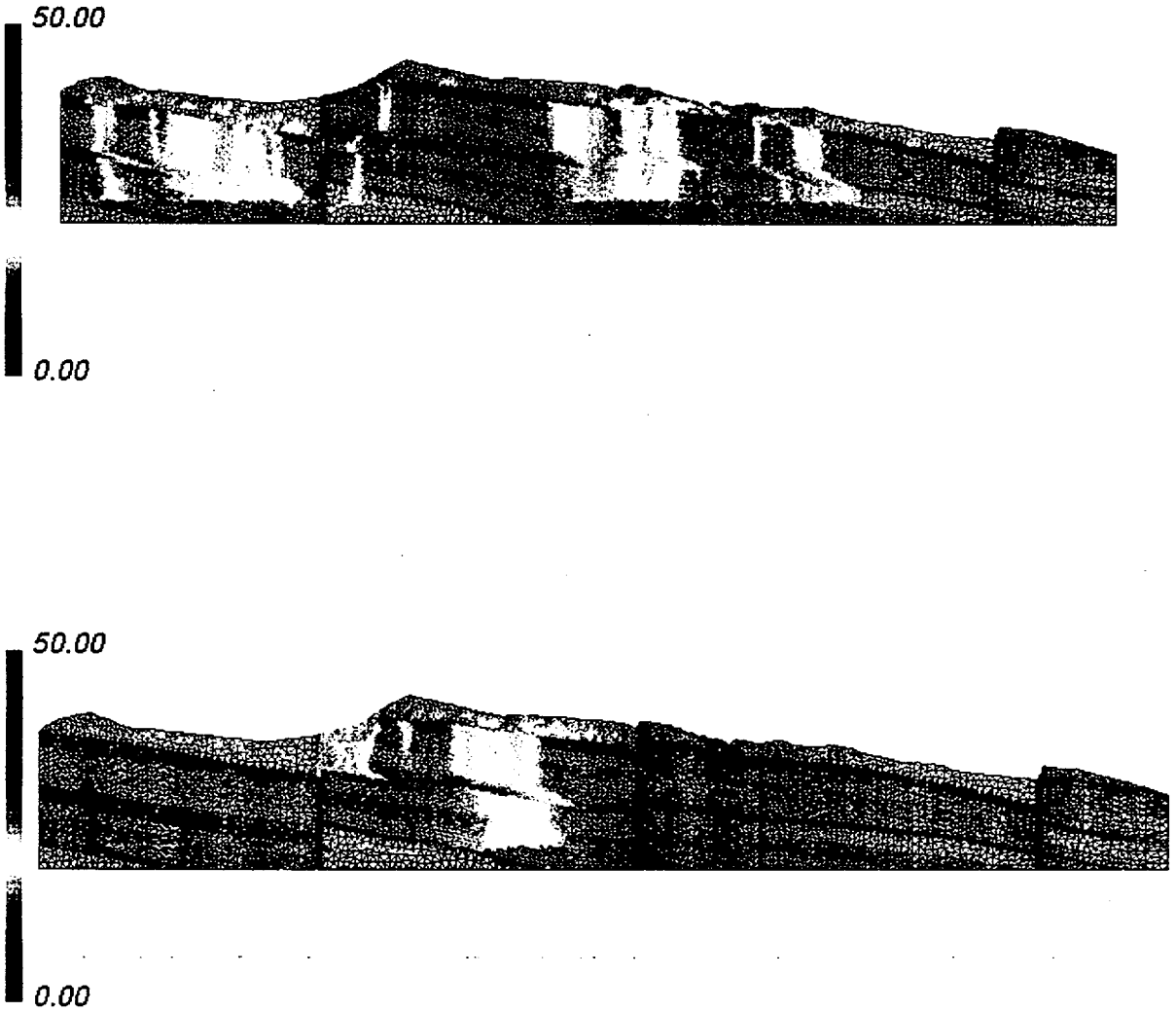

Figure 7-5. EW cross-section of transport site-scale model looking North. Chloride concentrations for the base infiltration map (upper figure) and the I/3 infiltration scenario (bottom figure).

model for the base case infiltration map of Flint et al. (1996), and a scaled map where all values are reduced by a factor of three. Within a given simulation, the concentration values in the subsurface are a reflection of the concentration entering at the surface, which in turn is inversely

proportional to infiltration rate. The pore water compositions measured in the PTn fluids are therefore strongly controlled by the infiltration rate at the surface.

An infiltration rate equal to one third (i.e., I/3) of the Flint et al. (1996) values, distributed over the entire site surface, was used to investigate the effects of infiltration rate on the behavior of the hydrologic system. The I/3 values were used as they provided the best fit to the $^{36}Cl/Cl$ values from the ESF (Chapter 6, present study). The values themselves are higher at all locations for the I/3 case, since the chloride deposition rate is held constant throughout this simulation exercise. At greater depths, there is some tendency for lateral diversion to result in lower concentrations beneath higher concentrations (see close-up in Figure), but in general, for the property values used in this calculation, the flow and transport is predominantly vertical.7-6)

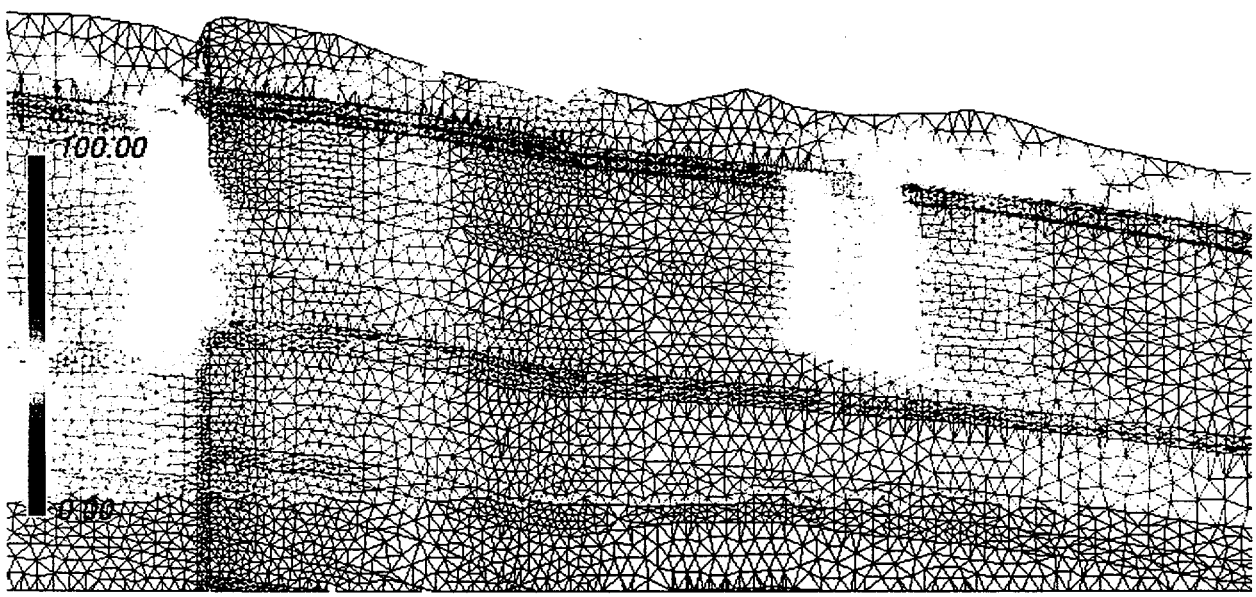

Figure 7-6. Detail of EW cross-section of transport site-scale model in area of relatively low infiltration. Close-up of chloride concentrations to the East of the Ghost Dance fault for the I/3 scenario.

The simulations for bromide and sulfate are closely related to those for chloride, except for the presumed difference in ion ratio for fluids of infiltration rate greater than 10 mm/y. Figure 7-7

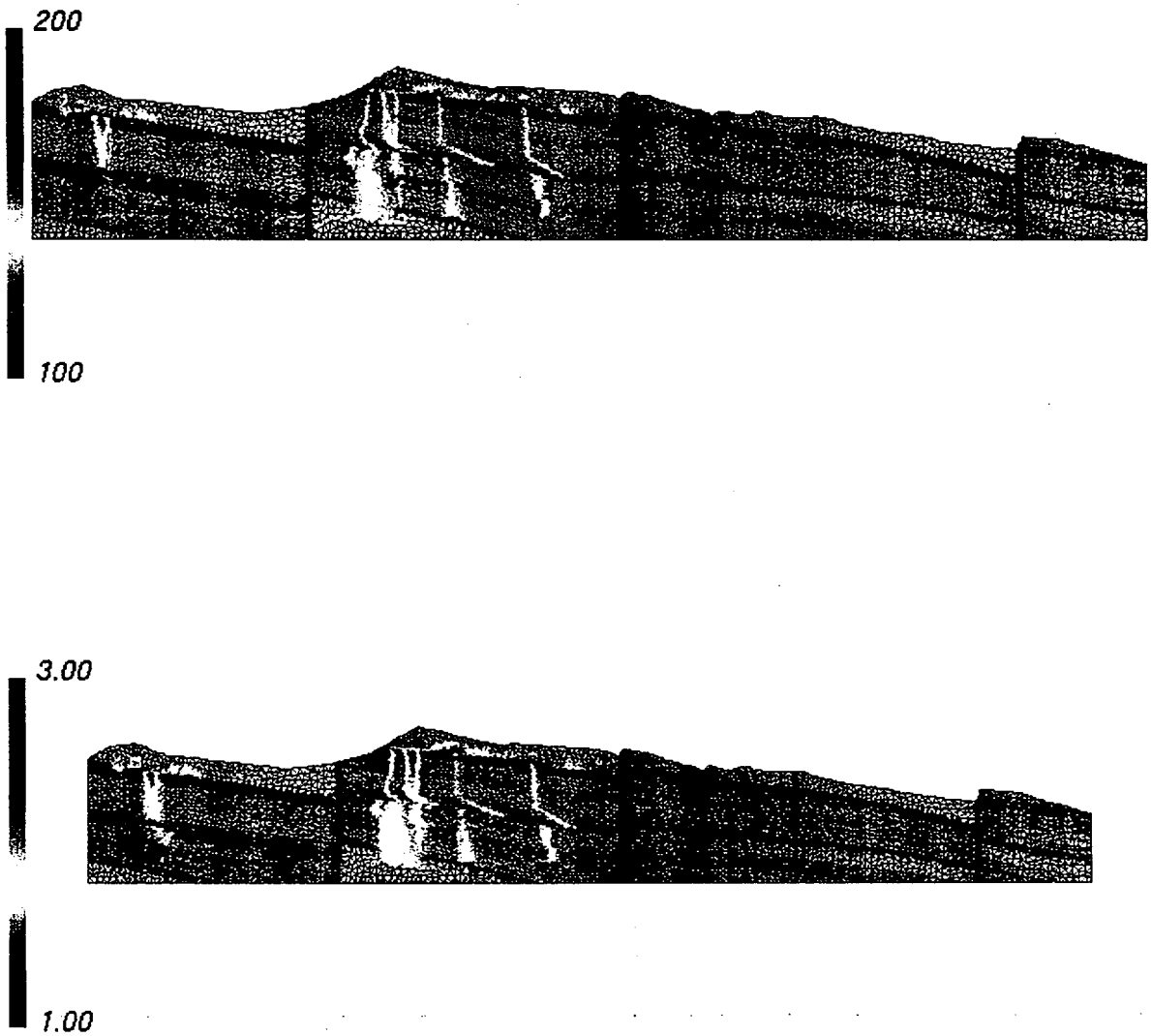

Figure 7-7. EW cross-section of full site scale transport model, lookin North through Yucca Crest. Chloride to bromide ratio (top figure) and sulfate to chloride ratio (bottom figure) simulated using the base case property set and infiltration map.

plots the chloride to bromide ratio (top figure) and sulfate to chloride ratio (bottom figure) predicted by the model for the base infiltration case. Beneath high infiltration zones the ratio is that of precipitation, whereas elsewhere in the model the ratios reflect the presumed values in lower infiltration areas. Although there is a hint of lateral diversion at the TSw basal vitrophyre leading

to water with "precipitation ratios" underlying fluid with the low infiltration ratio, the effect is minor.

Although they explain some of the features observed in the data, the calculations presented so far, predict predominantly vertical downward flow, consistent with model parameters of the unsaturated zone flow model (Bodvarsson et al., 1997). However, such model results are seemingly at odds with data suggesting lateral diversion, including the perched water data (see Section 7.6). We now develop a model that includes perching due to lateral diversion at the TSw basal vitrophyre. We accomplish this by uniformly reducing the fracture permeability in this unit to 4×10^{-17} m^2 while leaving the matrix permeability unchanged from the base-case value. This permeability is too low to support flow issuing from high infiltration regions, so that lateral diversion downdip from the source region occurs. To obtain perched water, we also reduce the permeability of the fault zones to values sufficiently low that they cannot drain the perched water. Figure 7-8 shows the steady state saturation profiles in the fracture domain for the base infiltration and the scaled I/3 scenario. The perched water bodies can exist under steady state conditions for these hydrologic parameters. Higher infiltration rates lead to a more extensive perched water body adjacent to the Ghost Dance fault.

Chemical transport predictions for this type of perched water scenario are now presented. Figure 7-9 shows the simulated chloride concentration (top figure), sulfate concentration (middle figure), and sulfate to chloride ratio (bottom figure) in the fracture domain for the base infiltration case. Dilute fluids enter the mountain in high infiltration regions, travel laterally at the basal vitrophyre, and result in a perched water body that is low in concentration of sulfate and chloride (about 11 ppm chloride), and higher in sulfate to chloride ratio than fluids entering at lower infiltration regions. Thus, several aspects of the perched and pore water chemical composition data are explained well with this lateral diversion model.

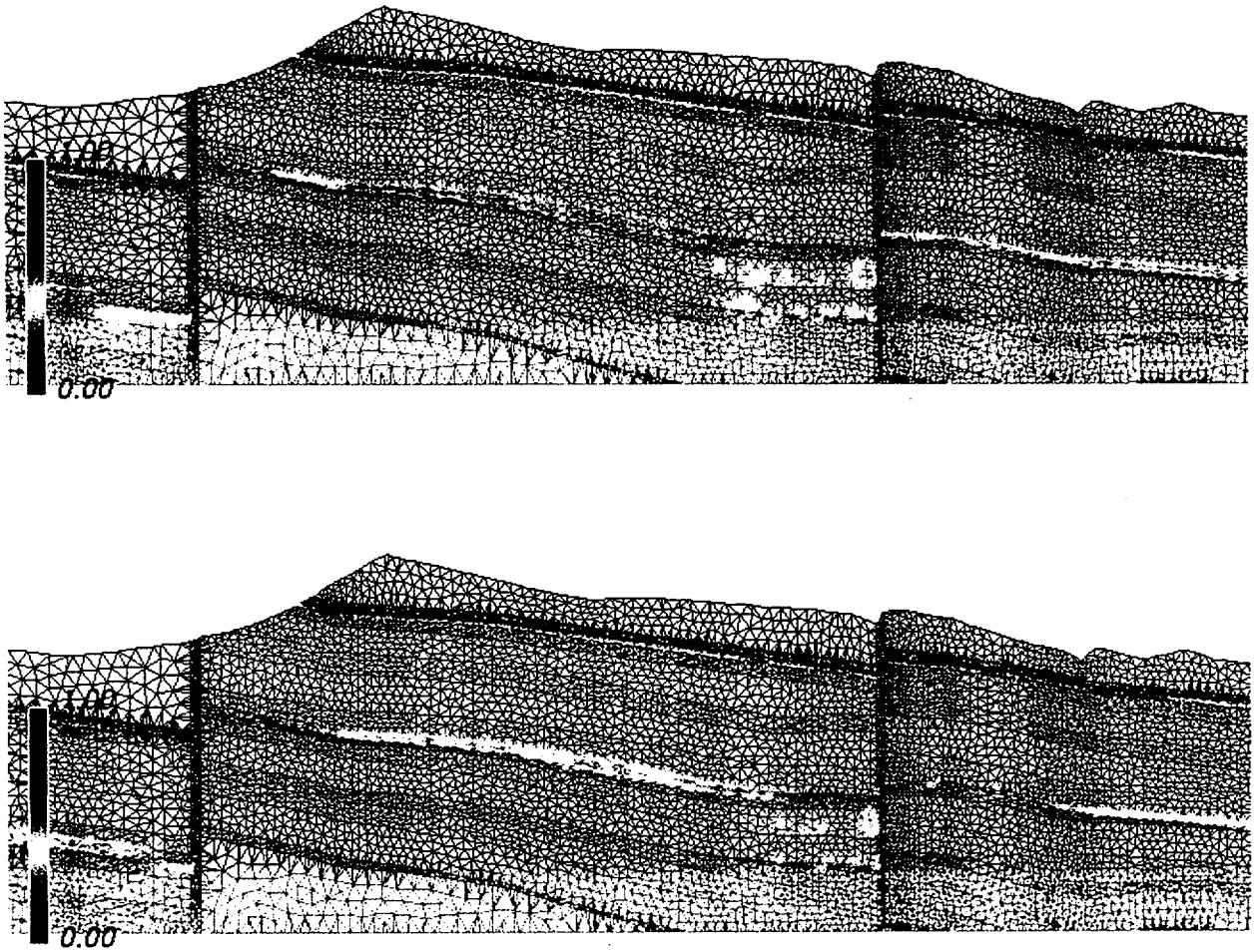

Figure 7-8. Detail of EW cross-sections from the site scale transport model through Yucca Crest, looking North. Fracture saturations predicted using the basal vitrophyre lateral diversion model. Top figure: base infiltration map; bottom figure: I/3 scaled map. Blue areas represent zones of perching with lateral flow along the top of the basal TSw vitrophyre. Principal source of water is from Yucca Crest in both cases.

7.8 Summary and Discussion

The LBNL and USGS models for flow in the unsaturated zone at Yucca Mountain emphasize fracture flow in which chemical constituents in the fracture waters have minimal interaction with the rock matrix (Rousseau et al., 1996; Bodvarsson et al., 1997). In addition,

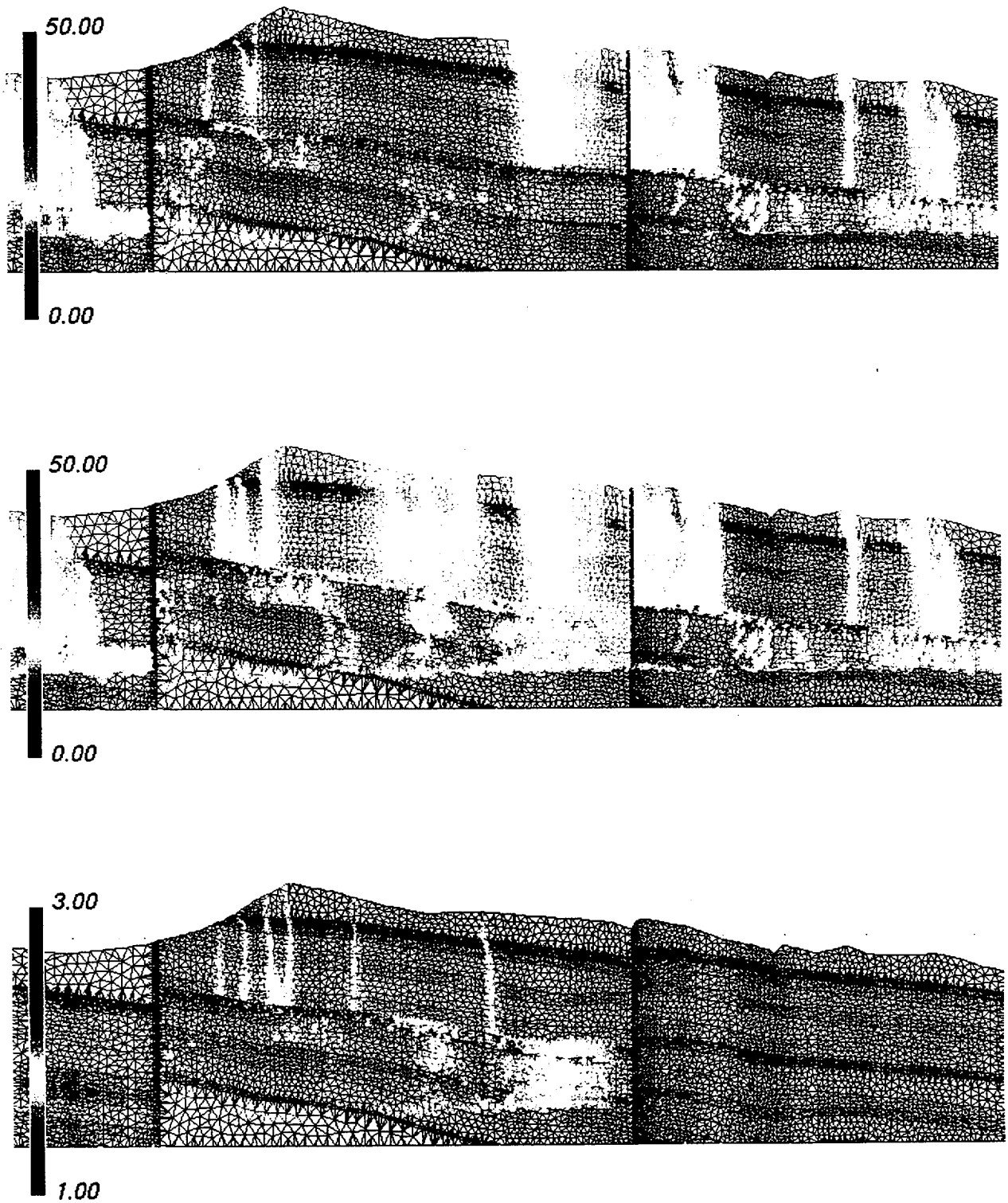

Figure 7-9. Detail of EW cross-section (looking North) of transport site-scale model through Yucca Crest.Chloride concentration (top), sulfate concentration (middle), and sulfate to chloride ratio (bottom) for the basal vitrophyre lateral diversion hydrologic scenario.

Bodvarsson et al. (1997) believe that the matrix of the Calico Hills tuff will also be bypassed as downward percolating waters follow fracture pathways to the saturated zone. This has significant implications for transport modeling because the Calico Hills tuff has been thought of as, potentially, a significant barrier to radionuclide transport. The previous evaluations of retardation in the Calico Hills tuff are not consistent with available hydrologic and hydrochemical data. This section discusses an alternative position on the hydrologic behavior of the unsaturated zone at Yucca Mountain.

7.8.1 The Hydrologic Data

Whereas a substantial amount of hydrologic data exists for the Yucca Mountain area, the integrated flow and transport models that rely on these data cannot be calibrated on hydrologic data alone (Robinson et al., 1995, 1996, present study). Indeed, water saturation data can be fit to a wide range of parameter values. This is particularly true when advancing dissequilibrium fracture flow as a dominant mechanism for water infiltration as the water saturation data is based on matrix saturations. Water potentials could be more useful but the data range greatly and are difficult to match (Bodvarsson et al., 1996, 1997). Hence, models calibrated only to hydrologic data are non-unique, and need additional constraints from hydrochemical data.

7.8.2 The Hydrochemical Data

As noted above, relatively high ^{14}C activities have been measured in pore waters extracted from samples of the Calico Hills tuff (Yang et al., 1996; 1997). These activities imply apparent ages of 300-3,000 years. Many of these pore waters were extracted from samples that were strongly zeolitized (e.g., USW UZ-14). These observations imply that relatively young waters are percolating into and presumably through zeolitic zones in the Calico Hills Tuff everywhere that measurements have been made. This observation points to the fact that the Calico Hills matrix is not bypassed by water migrating to the water table, in contradiction with some conceptual models. It also points to the fact that the pathways, volumes of water and their residence times can only be

constrained using environmental chemical tracers; synthesis and integration of hydrochemical data provides more robust conceptual models.

Chloride concentrations and environmental isotope, stable isotope and radioisotope measurements in other regions of high infiltration at Yucca Mountain are required to evaluate the conceptual models presented to date for Yucca Mountain. At present, no such measurements exist and our ability to distinguish further between the various conceptual models for flow is impaired by this lack of data.

7.8.3 The Model Results

Several aspects of the perched and pore water chemical composition data are explained well with the numerical model presented above. Despite this encouraging start, several aspects of the model need improvement. First, the anion compositions in the pore water above the perched water body adjacent to the Ghost Dance fault are lower in the model than in wellbores such as USW UZ-14. However, since this cross section is to the south of USW UZ-14, the model is really a tool for exploring various conceptualizations of the processes giving rise to the chemical measurements, rather than a calibrated model capturing the data at any location. More importantly, this simulation predicts fluids with low concentrations beneath the perched water zones, whereas the data at USW UZ-14 suggests higher concentrations, and, perhaps more problematic, younger ages than the perched water. Since the fluid underlying the perched water in these simulations clearly results from slow percolation through the basal vitrophyre (a leaking perched water body), its age will be similar to that of the perched water itself, and thus inconsistent with the data. Finally, the age of the perched water in this steady state simulation is roughly 1,000 years, much younger than the measured values.

Several corrections to the hydrologic properties would be required to improve the model. First, a transient model is clearly in order, since the chemical signature in the pore and perched waters is suggestive of a residual imprint from the Pleistocene Epoch. A transient model would also explain the generally higher chloride compositions in PTn pore water, which, based on water

ages, clearly reflect infiltration from the past 1000 years or so. This model would require a significantly lower infiltration rate under present day conditions to prevent relatively modern water from completely flushing the system in the past 10 ka. Finally, younger waters beneath the perched water zones may indicate additional lateral diversion of fluid in the vitric Calico Hills matrix on top of zones of extensive zeolitic alteration. This relatively modern water could be passing laterally under the perched water zones, thereby resulting in waters of distinctly different origin than the perched water. In fact, the current three-dimensional site scale transport model predicts such lateral diversion, as shown for a particle pathway calculation in Figure 7-10. This lateral diversion

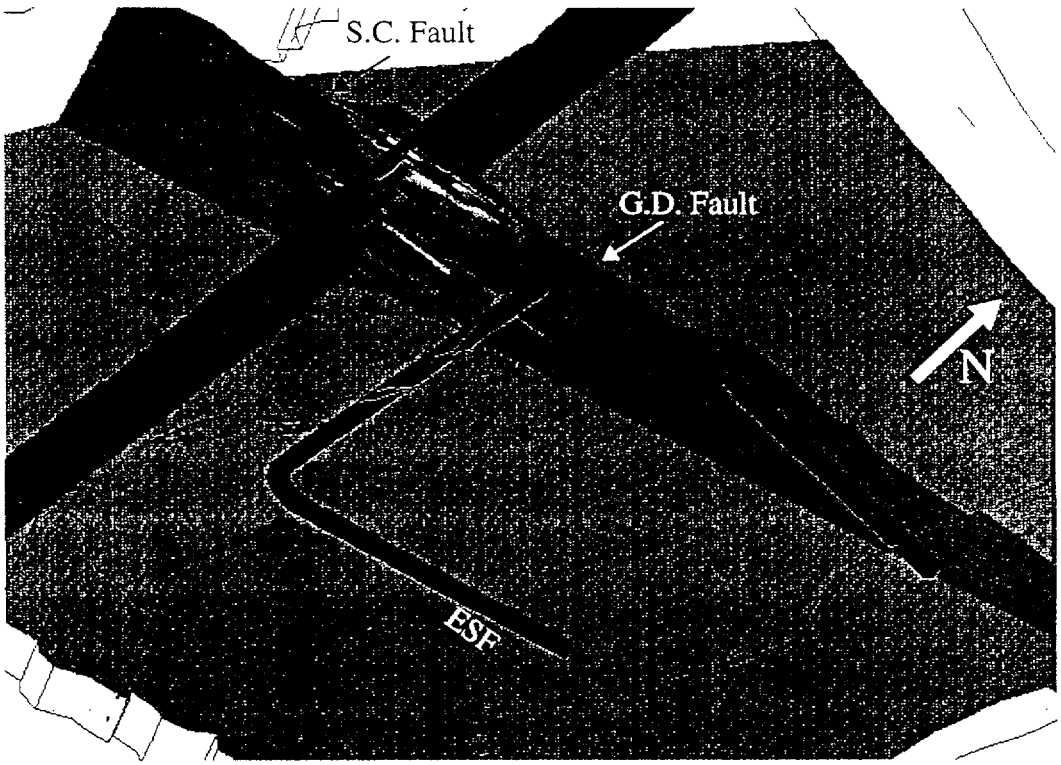

Figure 7-10. Three-dimensional simulation of transport for particles injected at the surface above the potential repository. Image represents a cut-away fence diagram from the three-dimensional grid. Represented are the Solitario (S.C.) and Ghost Dance (G.D.) faults and the ESF. Particles undergoing matrix flow are represented with the red colors corresponding to a high particle concentration. Significant lateral diversion is predicted in the vitric Calico Hills matrix (beneath the TSw basal vitrophyre) and to the Ghost Dance fault.

predicted in the vitric Calico Hills, beneath the TSw basal vitrophyre, is consistent with the observation that chloride concentrations and younger pore waters are observed from core samples taken beneath perched water bodies (Yang et al., 1996). This scenario is also consistent with the tendency for perching to occur to the west of the Ghost Dance fault. Therefore, an adjustment to the current model that will be explored is a combined model with the following features:

- partial lateral diversion at the TSw basal vitrophyre at higher infiltration;
- minimal lateral diversion at lower infiltration, such as present-day conditions;
- partial lateral diversion of fluid within the vitric Calico Hills.

A model with these features will be consistent with the transient mixing model for the hydro-geochemical system in the unsaturated zone.

7.9 Conclusions

In terms of extrapolation for Performance Assessment, the relevance of a conceptual model may be overlooked if the predictions overlap with other models. We have attempted in this chapter, to tie the different conceptual models to the fundamental physically-based differences among them so that extrapolations of the results can be better assessed. However, it is important to note that the weakest link in the analysis and evaluation of the different conceptual models, resides in the paucity of data for zones of high infiltration at Yucca Mountain (e.g., Yucca Ridge), and in some cases the reliability of both the hydrologic and geochemical databases on which the models are based.

The exploration of these alternative explanations for the perched and pore water chemical data are important in that different model conceptualizations may give rise to different performance predictions. We believe that when combined with the hydrologic database, the chemical data provide the most relevant information for "validating" radionuclide transport models, because the movement of naturally occurring solutes is closely related to the potential

migration of radionuclides. Our philosophy for model development and testing is one in which these data are used in the building of conceptual models, rather than as data to calibrate models against. The sparseness of the data sets and the ambiguities regarding the processes giving rise to the chemical composition preclude a more formal calibration exercise at this time. Therefore, we will examine these and other conceptual models for explaining the chemical data in future studies, attempting to pin down the conceptual model for flow and transport that is most consistent with all observations.

The overall consequence of the "fast pathway" fracture flow hypothesis is that it predicts poor performance for the unsaturated zone, as the Calico Hills transport barrier is essentially bypassed by fracture flow. It is important to note however, that the flow model which encompasses this hypothesis (Bodvarsson et al., 1997), and the transport simulations using the hydrologic parameters derived from that model (present study), are not uniquely calibrated as fracture and fault properties are still unknowns. Indeed the flow model calibrations were accomplished using measured matrix properties and fracture and fault properties derived from air permeability measurements. Bounding fracture and fault properties therefore relies on additional sources of data, and in particular the use of hydrochemistry. This is because the modern and ancient flow pathways have left behind a chemical imprint in the mountain, that if deciphered will help bound the effective properties and behavior of the unsaturated zone at Yucca Mountain. The transient-mixing hypothesis was designed to capture all elements of the hydrologic and chemical databases at Yucca Mountain. Its main strength is that it explains simultaneously the inversion in apparent ages between pore waters and perched water in the unsaturated zone, and the low chloride content of perched waters relative to the overlying TSw and underlying CHn pore waters. The apparent dissequilibrium in pore water and perched water contents is consistent with a model of transient flow, and it has been demonstrated that the stable isotope data and apparent ^{14}C and $^{36}Cl/Cl$ age determinations can be interpreted as being caused by a mixture of late Pleistocene/early Holocene to modern perched waters. The existence of these mixed ancient/modern perched water bodies therefore implies that an additional retardation mechanism exists above the Calico Hills formation.

The ubiquitous young ^{14}C ages in the Calico Hills formation pore waters beneath the perched water bodies and in other areas, also imply that a lateral component of flow occurs in the vitric Calico Hills and that this formation is not bypassed. Finally, this model is consistent with the 3-D stochastic mineral distribution model (Robinson et al., 1996; Chipera et al., 1997a; see also Chapter 12, present study) in which zeolitic and vitric tuffs are intricately interbedded beneath the repository horizon.

The implication of this model for performance assessment is improved performance of the Calico Hills transport barrier beneath the repository by 1) the addition of an additional barrier component which regulates the downward flow of water to the saturated zone, and 2) increased water residence times in the unsaturated zone due to the presence of long term perched water bodies at depth (i.e., no flow), and lateral diversion above the basal vitrophyre and/or the underlying Calico Hills vitric units. This should result in increased sorption of radionuclides at those boundaries as actinides sorb in clays and vitric tuffs as well as in zeolites (Triay et al., 1996a).

In conclusion, it appears that although the fracture and fault properties of Yucca Mountain tuffs require further refinement, the hydrochemical database is consistent with a model in which the flow system can be represented by an interlayered sequence of units characterized by matrix or fracture dominated flow, depending on infiltration rate. The current integration of the databases at Yucca Mountain continue to support a conceptual model for waste isolation, based on the concept of multiple and redundant engineered and natural barriers to radionuclide migration. It is suggested that the unsaturated zone remains one of the principal natural barriers to radionuclide migration to the accessible environment and that the Calico Hills formation and the overlying basal vitrophyre of the Topopah Springs unit play an important role in that process.

Chapter 8 - Two-Dimensional Radionuclide Transport Simulations

8.1 Abstract

Multiple parameter sets from the LBNL site-scale flow model and variations on the USGS infiltration map are used in the simulation of radionuclides from the potential repository to the water table. For most of these parameter sets, radionuclides tend to bypass the zeolites of the Calico Hills via fracture transport when base-case infiltration conditions are simulated. When the infiltration rate is scaled by 1/3, significant fracture flow in the zeolites is still simulated with most parameter sets. A modification increasing CHn zeolite matrix permeabilities by a factor of 5 leads to substantially greater matrix flow and, hence, retardation of sorbing radionuclides. This process leads to dramatic improvement in the performance of the unsaturated zone. These studies demonstrate the overriding importance of proper characterization of the zeolitic units for performance assessment. Colloid-facilitated transport of otherwise immobile radionuclides like Plutonium is also addressed in this chapter. In the absence of sorption onto the mobile colloids, Plutonium migration is limited due to large sorption coefficients. When partitioning onto colloids approaches 99% or more, Plutonium mobility becomes potentially important to performance. Long-time transients capturing climate change related phenomena are also simulated in this chapter. The results show that the flux of radionuclide at the water table under transient conditions is closely approximated by a quasi-steady state model. Finally, for wetter future climates, the combined effect of a shorter travel distance to the water table and high fluxes under a wetter climate scenario yield prediction of poorer unsaturated zone performance than for the present climate conditions.

8.2 Software and Data QA Status

The FEHM code is used to perform all flow and transport calculations in this report. The code is qualified in accordance with Los Alamos quality assurance requirements and is documented in (Zyvoloski et al., 1992, 1995a, 1995b). The QA status of the data used in this report is shown in Table 8-1.

Table 8-1. QA Status of Data used in this Chapter

REFERENCE	Q Status	DTN	COMMENT
Bodvarsson et. al., 1997 "The Site-Scale Unsaturated Zone model of Yucca Mountain, Nevada, For the Viability Assessment, LBL Technical Report LBNL-40378	Q	LB970601233129.001	No DTN assigned. Hydrologic property sets computed in this report are used throughout the present study.
Chipera et. al., 1997b "Mineralogic Variation in Drill Holes USW NRG-6, NRG-7-7a, SD-7, SD-9, SD-12, and UZ#14: New Data from 1996-1997 Analysis Los alamos National Laboratory YMP Deliverable SP321BM4"	Q	LADV831321AQ97.001	
Triay et. al., 1996a, "Summary and Synthesis Report on Radionuclide Retardation for the Yucca Mountain Site Characterization Project, Los Alamos National Laboratory YMP Milestone Report 3784	Q	LAIT831341AQ96.001	
Triay et. al, 1996b, "Radionuclide Sorption in Yucca Mountain Tuffs with J-13 Well Water,: neptunium, Uranium, and Plutonium, Los alamos National Laboratory Yucca Mountain Site Characterization Project" Milestone 3338, Technical Report LA-12956-MS	Q	LAIT831341AQ96.001 *	* DTN supersedes DTN LA000000000104.001
Triay et. al., 1996c, "Batch Sorption Results for neptunium transport through Yucca Mountain tuffs, Los alamos National Laboratory Yucca Mountain Site Characterization Project Milestone 3349, Technical Report LA-12961-MS	Q	LAIT831341AQ96.001 *	*DTN supersedes DTN LA000000000090.001

Triay et. al., 1996d, "Comparison of Neptunium Sorption Results using batch and column techniques, Los Alamos National laboratory Yucca Mountain Site Characterization Project Milestone 3041, Technical Report LA-12958-MS	Q	LA000000000106.001	DTN Accession No. MOL.19950630.0300

8.3 Introduction

In this chapter we use the two-dimensional, East-West cross section model to examine the predicted behavior of radionuclides migrating through the unsaturated zone from the potential repository to the water table. In this report we use a combination of one-, two-, and three-dimensional simulations to evaluate the sensitivity of transport to many uncertain aspects of the unsaturated zone. One-dimensional simulations were used mainly for mechanistic and screening studies, where the number of parameters or the time scale of the process being studied precludes performing the simulations in two or three dimensions. The two-dimensional simulations presented in this chapter examine behavior that does not necessarily require full three-dimensional simulations, including the following uncertainties and processes:

- hydrostratigraphy and its effect on radionuclide transport;
- percolation flux;
- different hydrologic parameter sets;
- transport parameters;
- long-term transients due to climate change;
- heterogeneities and the distribution of zeolites;
- repository heat effects; and
- near-field environment (NFE) radionuclide release rate.

8.4 Methodology for Radionuclide Migration Calculations

In the present study the particle tracking module in FEHM is used to simulate radionuclide migration from the potential repository to the water table. The reasons for using this module for transport relate to the extensive use of the dual-permeability model formulation in the present study. In Chapter 4, we discuss in detail the computational advantage of the cell-based particle tracking technique for unsaturated zone dual-permeability transport modeling is discussed.

Green's Function Analysis Method

The primary type of simulation presented in this chapter is a steady state flow field simulation, followed by particle tracking on this flow field. Some individual analyses are performed to test the steady state flow assumption by examining the possibility of climate-induced, long-term transients (Section 8.11), heat-induced transients (Chapter 11), and episodic transients in Chapter 6. However, for steady state flow, the flow and radionuclide transport system can be decoupled from the NFE (near-field environment) source term through the use of convolution. Instead of determining the transport of a radionuclide for each NFE release scenario, we compute the response of the system to an instantaneous release of a unit mass of radionuclide at time 0. Generally, the response is the resulting radionuclide mass flux at the water table resulting from the instantaneous injection of particles at the potential repository. This response curve, $f_{uz}(t)$, is a Green's function (e.g. Wylie, 1975), which can be used as the kernel of a convolution calculation in which the time-varying source term mass flux, m_{NFE}, is applied to the following equation:

$$m_{UZ}(\tau) = \int_0^{\tau} m_{NFE}(t) f_{UZ}(\tau - t)\,dt \qquad \text{(Eq. 8-1)}$$

In words, Equation 8-1 states that the radionuclide mass flux at the water table is the sum of the contributions of all paths of different residence times of radionuclides that entered the system that long ago. The primary assumptions underlying the convolution approach are steady state flow and a release rate that is independent of position in the repository. The more complex cases are consid-

ered separately and do not use this convolution approach.

The instantaneous injection breakthrough curve f_{UZ} will be presented first for a number of hydrologic cases, infiltration rates, and transport parameters, but in the presentation of the two-dimensional base case, we also show the nature of the convolution results for an actual release scenario. In this way, an example is provided that will allow the reader to interpret the instantaneous injection breakthrough curve results more readily. The integral of the f_{UZ} curve, is also presented which is a cumulative residence time distribution function. This curve demonstrates the extent to which radionuclides take rapid pathways to the water table, compared to slower pathways.

8.5 The Base Case

The Ten Percent Zeolite Map

Because zeolites are formed through secondary alteration, the distribution of zeolites in the Calico Hills do not follow the primary geologic stratigraphy (Chipera et al., 1997b). Therefore, we map the zeolite distribution of Chipera et al. (1997b) on top of the geologic model as described in detail in Chapter 2. In Chapter 12 we investigate the relationship between percent alteration, permeability changes due to alteration, and the effect on radionuclide transport. In this chapter, we choose a threshold percent alteration and assign zeolitic parameters according to the unit in which the alteration occurs. For example, the first geologic layer in the CHn below the basal vitrophyre contains both altered and unaltered minerals. If a location in this unit is identified as having zeolitic alteration greater than the threshold value, 10% in this case, then cells in the grid are assigned CHn1z (zeolitic) properties while all other cells in that layer are assigned CHn1v (vitric rather than zeolitic hydrologic properties). Thus, each cell in each geologic unit in the CHn can be either zeolitic and non-zeolitic depending on where it falls. This approach is a major improvement to the previous approach of representing entire layers in the CHn as either zeolitic or nonzeolitic.

Property Sets

In this chapter, the hydrologic property set 6541 is regarded as the base case for the purposes of comparison and the execution of variations from the base-case conditions. Recall that this property set was derived by LBNL (Bodvarsson et al., 1997) using a calibration to matrix fluid saturations assuming the base-case infiltration map of Flint et al. (1996), with upstream saturation weighting for the reduction factor for fracture/matrix flux in nonwelded units, and upstream relative permeability weighting for the reduction factor for fracture/matrix flux in the welded units. This parameter set is used for this base-case analysis because both PA and site characterization scientists identified it as most appropriate. This set, and all other sets from LBNL, contain hydrologic properties for both zeolitic and non-zeolitic material in each CHn geologic unit. Therefore, with the threshold approach described above, the properties of each cell in each layer are obtained from the LBNL property set being used for the particular simulation. All property sets referred to in this chapter are described in Table 5-2.

Simulations

The steady-state fluid flow field is generated after mapping the spatially varying infiltration values (see Figure 6-6, this report) onto the two-dimensional domain. The steady-state matrix and fracture saturations for this case are shown in Figure 8-1 along with the infiltration maps. Estimated infiltration rates above the potential repository are highest at, and just east of, the crest of Yucca Mountain (Flint et al., 1996). These higher infiltration rates have ramifications for radionuclide migration, as shown below. The basic pattern of fluid saturations in the matrix is typical of the models presented in Bodvarsson et al. (1997), and, in general, follow the results from the one-dimensional results in Chapter 5. Fracture saturations are controlled by the matrix permeabilities (what cannot pass through the matrix must percolate through the fracture domain), the local percolation rate, and the fracture properties. In addition, the fracture/matrix interaction term controls the ability of fluid to transfer from fracture to matrix and back at the interface

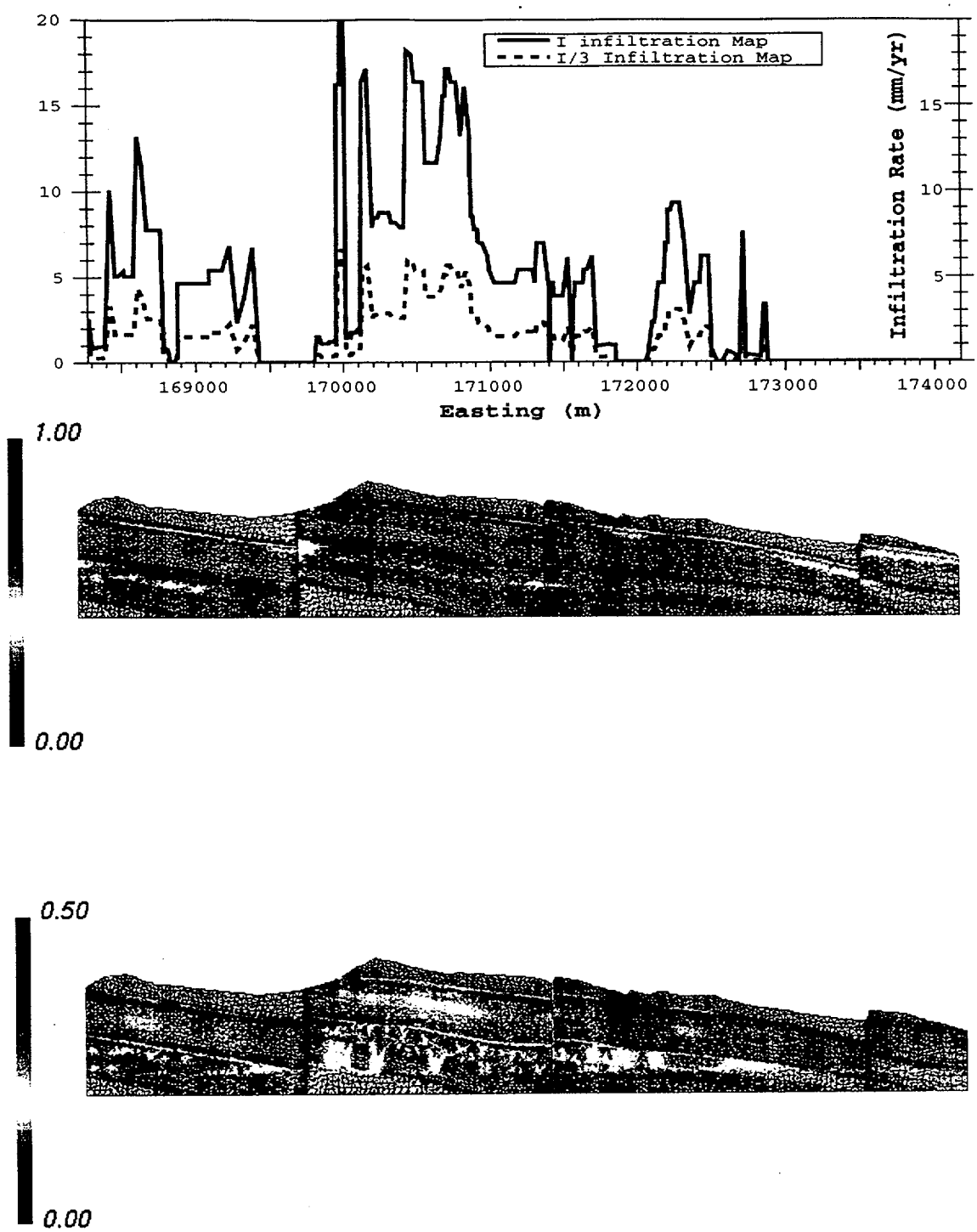

Figure 8-1. Matrix (top) and fracture (bottom) saturations for the two-dimensional base-case simulation. Parameter set 6541, base infiltration map (I). Also shown are the I and I/3 infiltration map values across the model domain.

between units of contrasting properties. The implications of this effect for flow and transport in nonwelded tuff were addressed in Chapters 5 and 6 of this report.

Radionuclide transport from the repository to the accessible environment is simulated using the steady-state flow field. The repository is identified as a series of point sources located 22 m apart at the repository horizon. An equal number of particles is released at each node at time 0. The simulation is carried out to one-million years, and the exit time of each particle is written to an FEHM output file where the particle times are sorted and binned to produce the residence time distributions (the Green's function). Figure 8-2 shows the results for the base case for different

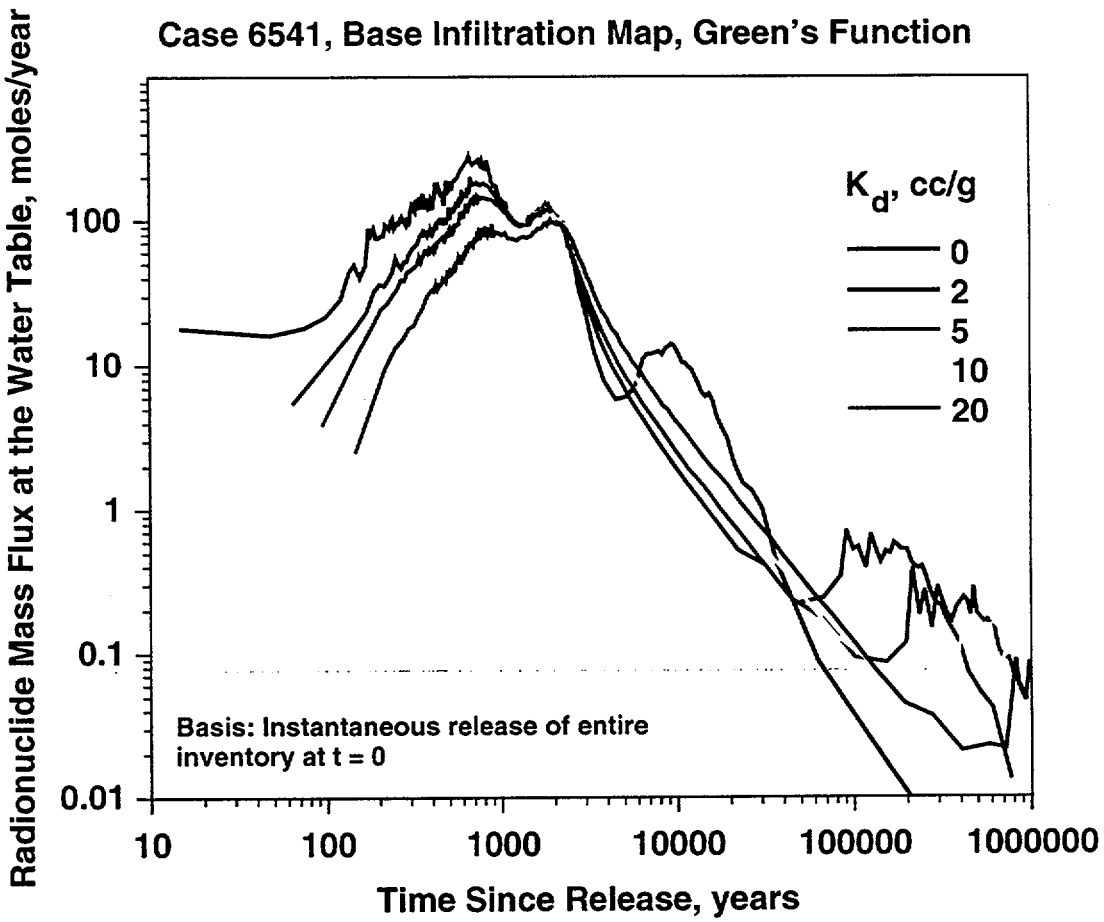

Figure 8-2. Green's function residence time distributions for transport of radionuclides in the two-dimensional site scale model. Property set 6541, base infiltration map.

assumed sorption coefficients in the zeolitic tuff (no sorption occurs in the other units for this case). The assumption of sorption only in the zeolites is appropriate for ^{237}Np and uranium (Triay et al., 1996a), with values of 2 cc/g typical of ^{237}Np, and values ranging from 5 to 20 cc/g for uranium. The no-sorption case is indicative of the migration of non-reactive radionuclides such as ^{99}Tc, ^{127}I, and perhaps ^{14}C. Sorption occurs in the matrix only, either as a retardation of the portion of the radionuclide travelling through the matrix by advective transport, or via sorption in the matrix diffusion model of fracture transport. For the matrix diffusion model, the matrix diffusion coefficient and fracture aperture are required: for this case they are 10^{-11} m^2/s and 0.1 mm, respectively. Recall from the one-dimensional screening analysis in Chapter 5 that for the property sets supplied by LBNL, the curves exhibited a distinct bimodal character, with rapid transport through fractures and long-time pathways through the matrix. This behavior is also exhibited in the two-dimensional simulations. With no sorption (the $K_d = 0$ curve), a small fraction of the inventory travels quite rapidly to the water table (less than 100 years), but the main portion of the first peak takes roughly 1000 years to reach the water table. This is roughly the travel time of the radionuclide through the matrix of the vitric nonwelded tuffs. Sorption onto the zeolites has little impact on this peak, since the early-arriving radionuclide travels through fractures, where it has only limited contact with the zeolitic tuffs in the matrix diffusion model.

The second peak is associated with matrix flow and transport. Without sorption, this peak arrives at roughly 10 ky, and for sorption onto zeolitic tuffs, the peak is pushed out to much larger residence times. The relative proportions of radionuclides arriving at the water table in each peak is more easily seen in Figure 8-3, the cumulative breakthrough curve. The first plateau in each curve represents the fraction of the radionuclide inventory that travels rapidly through to the water table. For the base-case parameters and infiltration rate, roughly 70% of the mass travels through these paths. Sorption onto zeolites affects this value very little, since there is not much contact of radionuclides with the zeolitic matrix for these flow paths.

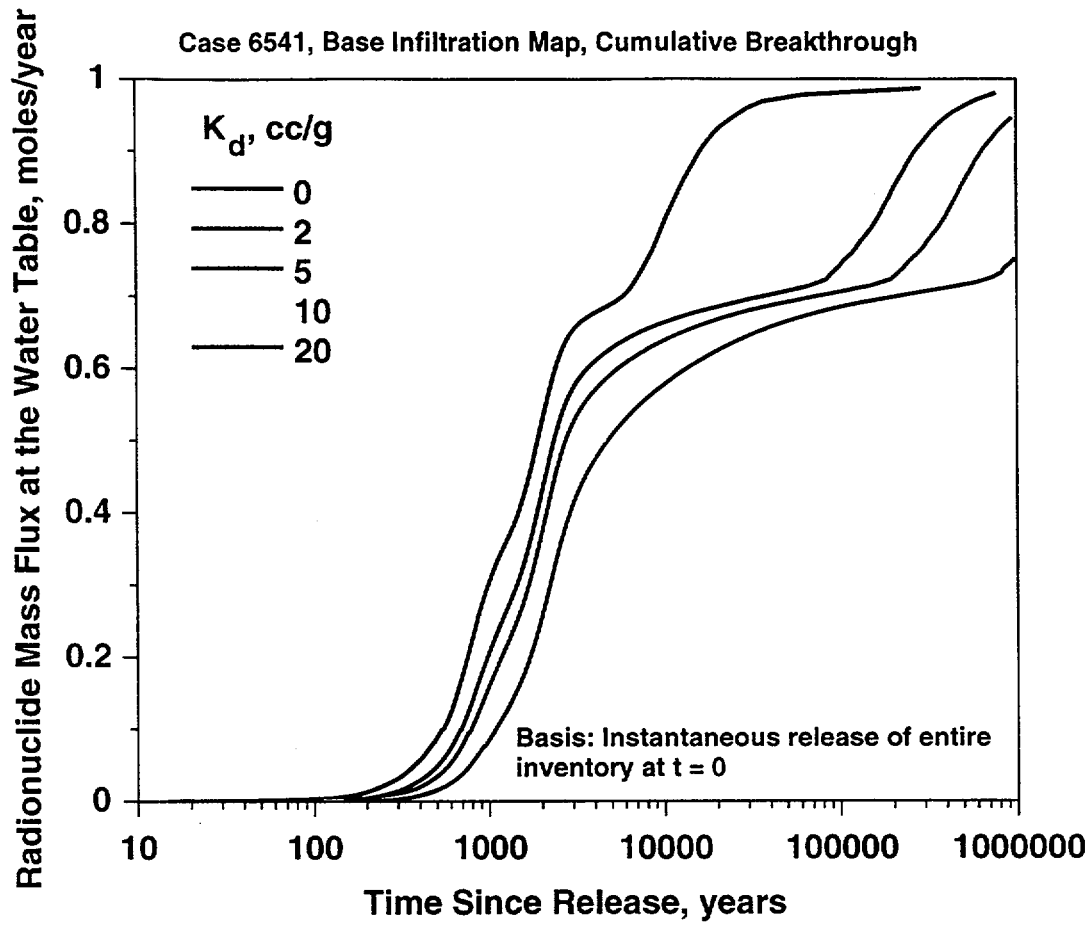

Figure 8-3. Cumulative residence time distributions for transport of radionuclides in the two-dimensional site scale model. Property set 6541, base infiltration map.

Before presenting the sensitivity analyses for the uncertain parameters discussed, the water table breakthrough curve for a more typical release scenario is presented. For this calculation particles at a uniform rate across the repository starting at 1,000 years for a period of 30 ky are released, after which the inventory is depleted and the releases stop. This case simulates a 1,000 year canister lifetime and solubility-limited release thereafter. This release scenario and a zeolite K_d of 2 cc/g is a typical scenario for ^{237}Np. Figure 8-4 shows the results for this simulation for the base case. Breakthroughs at the water table commence at slightly greater than 1,000 years, and plateau to a constant value 5 to 10 ky. This plateau persists until the releases stop at 31 ky. During this period, all fast pathways associated with the first peak in the Green's function are supplying

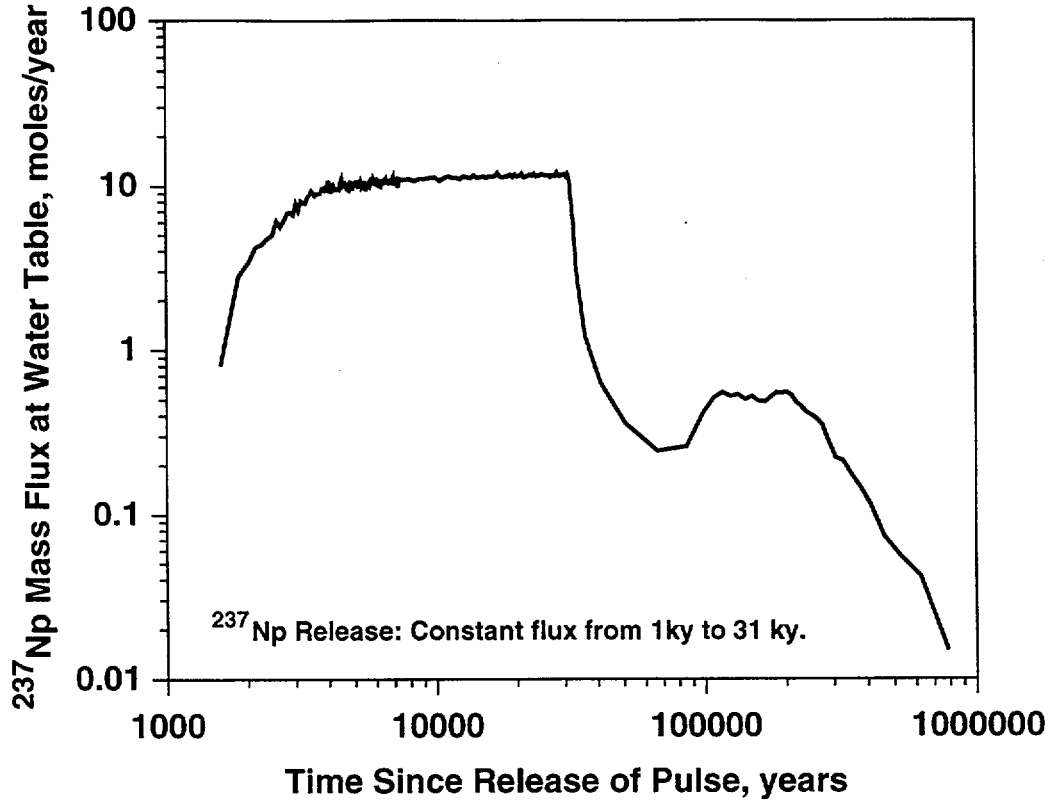

Figure 8-4. Water table breakthrough of ^{237}Np for the base case. Parameter set 6541, base infiltration map, $k_d = 2$ cc/g, constant release rate from 1 ky to 31 ky.

radionuclides at the water table, and the breakthrough curve, thus, resembles the first plateau of the cumulative breakthrough curve shown in Figure 8-3. Once the inventory is depleted, these pathways no longer are supplied with radionuclides, and are in essence flushed out with fresh water. The remaining portion of the breakthrough curve comes from contributions to the slower moving pathways. Since the duration of the source term (30 ky) is much shorter than the spread in travel times associated with these pathways, the breakthrough of this portion of the inventory resembles the Green's function response (Figure 8-2, red curve), in contrast to the early breakthroughs.

Since this curve is the source term for the saturated zone transport system, we can foresee the ramifications of the current unsaturated zone flow model predictions on total system performance. Namely, if waste packages degrade on the order of 1,000 years after waste emplacement and the system's flow partitioning between fractures and matrix is as predicted with the current model parameters (6541), then the peak mass flux at the water table for radionuclides, such as ^{237}Np, will be reached within 10 ky. For this scenario, any parameter or process in the unsaturated zone (NFE, waste package, unsaturated zone system) that reduces release rates will directly influence total system performance. In addition, saturated zone flow or transport processes will be critical to characterize for their ability to dilute this initial breakthrough. The breakthrough of the second peak would appear to not be important for determination of peak dose for radionuclides, such as ^{237}Np, unless the first peak becomes significantly diluted and the compliance period is extended to 100,000 y or greater. This conclusion is based on radionuclide sorption onto zeolites (and no sorption elsewhere), and does not apply to other more sorptive radionuclides.

For non-sorbing radionuclides such as ^{99}Tc, the breakthrough of the second peak occurs within 10,000 y (Figure 8-2, $K_d = 0$ case). Because this residence time is of the same order of magnitude as the time period over which radionuclides are released from the potential repository, the breakthrough curve will not exhibit the distinct bimodal character predicted for ^{237}Np. Rather, the entire inventory breaks through to the water table within about 50 ky, and the distinction between the fracture peak and the matrix peak becomes blurred. Thus, the influence of sorption for ^{237}Np is to delay the arrival of the matrix transport portion of the inventory. This is in effect a dispersion mechanism that lowers the peak dose to levels below what would be obtained in the absence of sorption.

Finally, we note that small portions of the inventory travelling through very fast pathways (less than 100 year travel times) have an insignificant impact on the water table breakthrough curves. If indeed the observations of bomb-pulse ^{36}Cl at the ESF represent only a small fraction of

the total flow, this analysis shows that these flow paths are mitigated by the small proportion of radionuclide mass travelling through them, as well as by slow release rates. In addition, the saturated zone will tend to dilute any rapid-moving radionuclide in the unsaturated zone system, as long as the proportion of mass travelling through these paths is small.

8.6 The Influence of Hydrologic and Geochemical Parameter Sets

The LBNL site-scale model report provided a variety of parameter sets, which were screened in Chapter 5 to eliminate redundant sets not likely to give rise to different behavior than the base case. In this section we examine two-dimensional transport for other parameter sets developed by LBNL. The goal is to determine if the method of model calibration or the form of the fracture/matrix interaction conceptual model influences radionuclide transport significantly. If it does, then this conceptual model uncertainty should be reflected in total system performance analyses since it would represent an important uncertainty.

Case 6412b: The Green's function curves for different sorption coefficients and the cumulative residence time distribution curves for this case are shown in Figures 8-5 and 8-6, respectively. The response curves are not significantly different than the base case. Recall that case 6412b employs a constant reduction factor in each unit as the multiplier in the fracture/matrix interaction model. At steady state, it is expected that the constant reduction factors obtained by parameter estimation should be similar to the weighting factor obtained with the alternative interaction models used for the base case, since both data sets were made to fit the available saturation data. Under transient conditions, the models could perhaps yield different results, but for steady state flow fields, it is not surprising that the breakthrough curves are quite similar.

Case 6531b: The Green's function curves for different sorption coefficients and the cumulative residence time distribution curves for this case are shown in Figures 8-7 and 8-8, respectively. Breakthrough occurs earlier and at higher levels in this case, and the bulk of the inventory travels rapidly to the water table within 10 ky. The only significant difference in the breakthrough curves

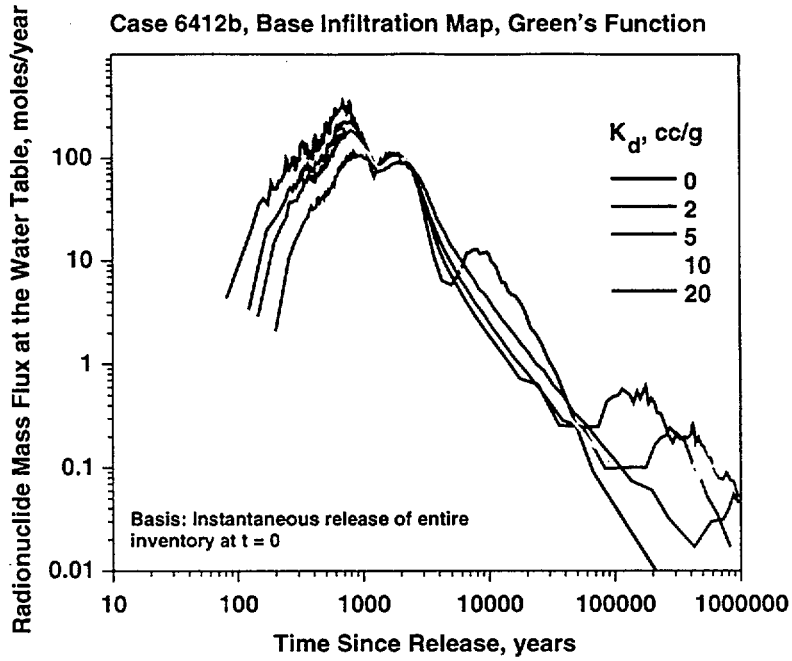

Figure 8-5. Green's function residence time distributions for transport of radionuclides in the two-dimensional site scale model. Property set 6412b, base infiltration map.

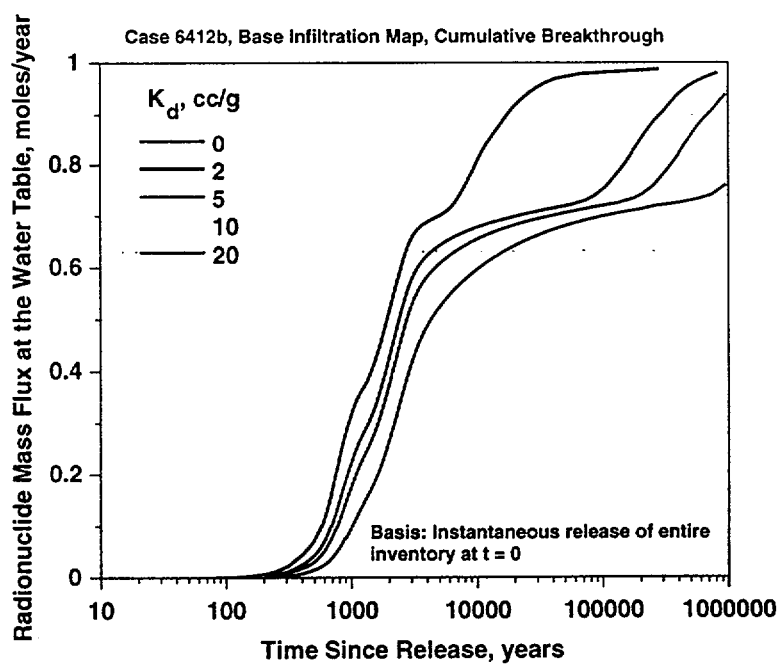

Figure 8-6. Cumulative residence time distributions for transport of radionuclides in the two-dimensional site scale model. Property set 6412b, base infiltration map.

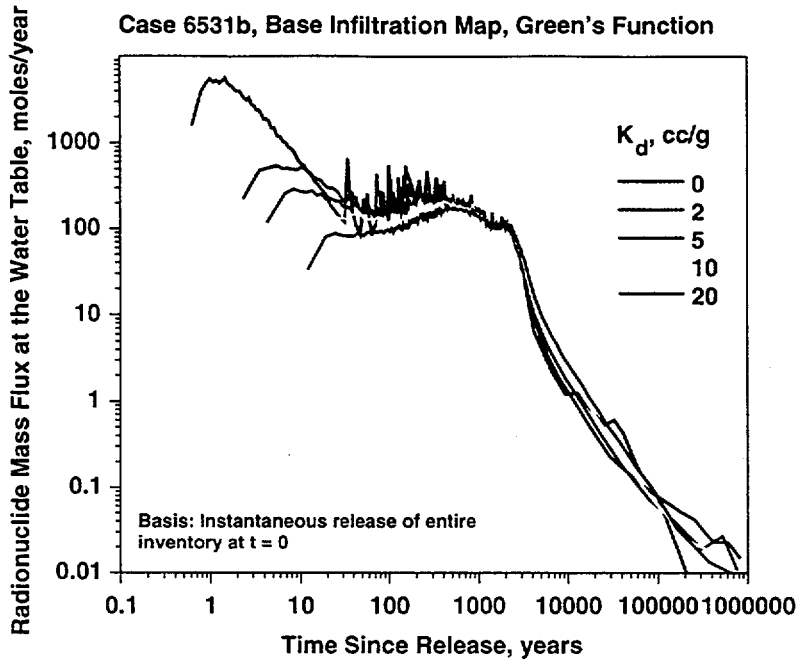

Figure 8-7. Green's function residence time distributions for transport of radionuclides in the two-dimensional site scale model. Property set 6531b, base infiltration map.

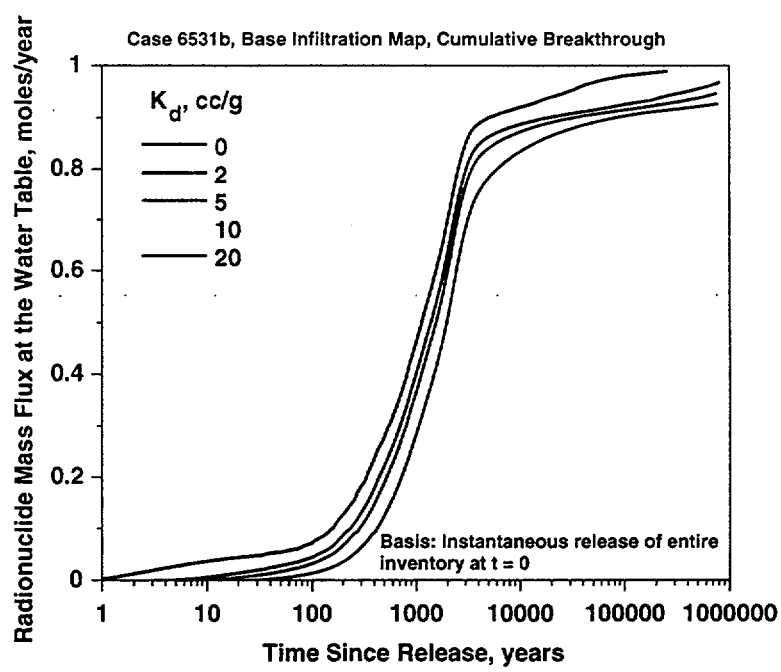

Figure 8-8. Cumulative residence time distributions for transport of radionuclides in the two-dimensional site scale model. Property set 6531b, base infiltration map.

as a function of sorption coefficient is at early times, where the no-sorption case has a higher mass flux than the sorbing radionuclide cases. This is a characteristic of a system in which matrix transport is limited to the high permeability vitric units, and flow through the zeolites is almost exclusively fracture flow and transport. Therefore, sorption on zeolites has a relatively minor impact on the results for this case. In contrast to case 6412b, case 6531b exhibits significantly different behavior than the base case. It represents the extreme of fracture-dominated flow through the zeolites, with little influence of sorption. Of course, radionuclides that sorb onto the vitric units would be delayed relative to nonsorbing species.

These three cases represent how, under base-case infiltration conditions, the range of uncertainty in hydrologic parameter values results in different performance for the unsaturated zone. In general, zeolite permeabilities in these parameter sets are too low to transmit a large fraction of the flow. This minimizes the degree to which sorption of radionuclides such as ^{237}Np and uranium are retarded by sorption onto the zeolitic rocks. It must be recognized that the permeability of the zeolites are model-derived quantity, albeit constrained by measured data. If the upscaled permeability of a zeolitized region of rock exhibits a higher permeability than the averaged values obtained by parameter estimation techniques, then significantly more retardation is to be expected. The study of matrix hydrologic and transport properties in a heterogeneous region of varying zeolitic abundance is presented in Chapter 12. In that chapter, we demonstrate that if permeability is correlated with degree of alteration, greater matrix flow and, hence, retardation onto zeolites is predicted than occurs in this chapter's simulations.

8.7 The Effect of Percolation Flux

Percolation flux is one of the key uncertainty parameters that will influence the mass flux values and arrival time distributions at the water table. Strictly speaking, to simulate the flow field assuming a different percolation flux, a new set of hydrologic parameters should first be developed. However, given that matrix saturations are relatively insensitive to percolation flux

over the range of uncertainty at Yucca Mountain (about a factor of three higher or lower than the base case map), we assume that the hydrologic parameter sets developed using the base-case map can be applied directly for fluxes a factor of three higher or lower than the base case. This concept is demonstrated in Figure 8-9, a plot of the difference in predicted fluid saturations in the matrix

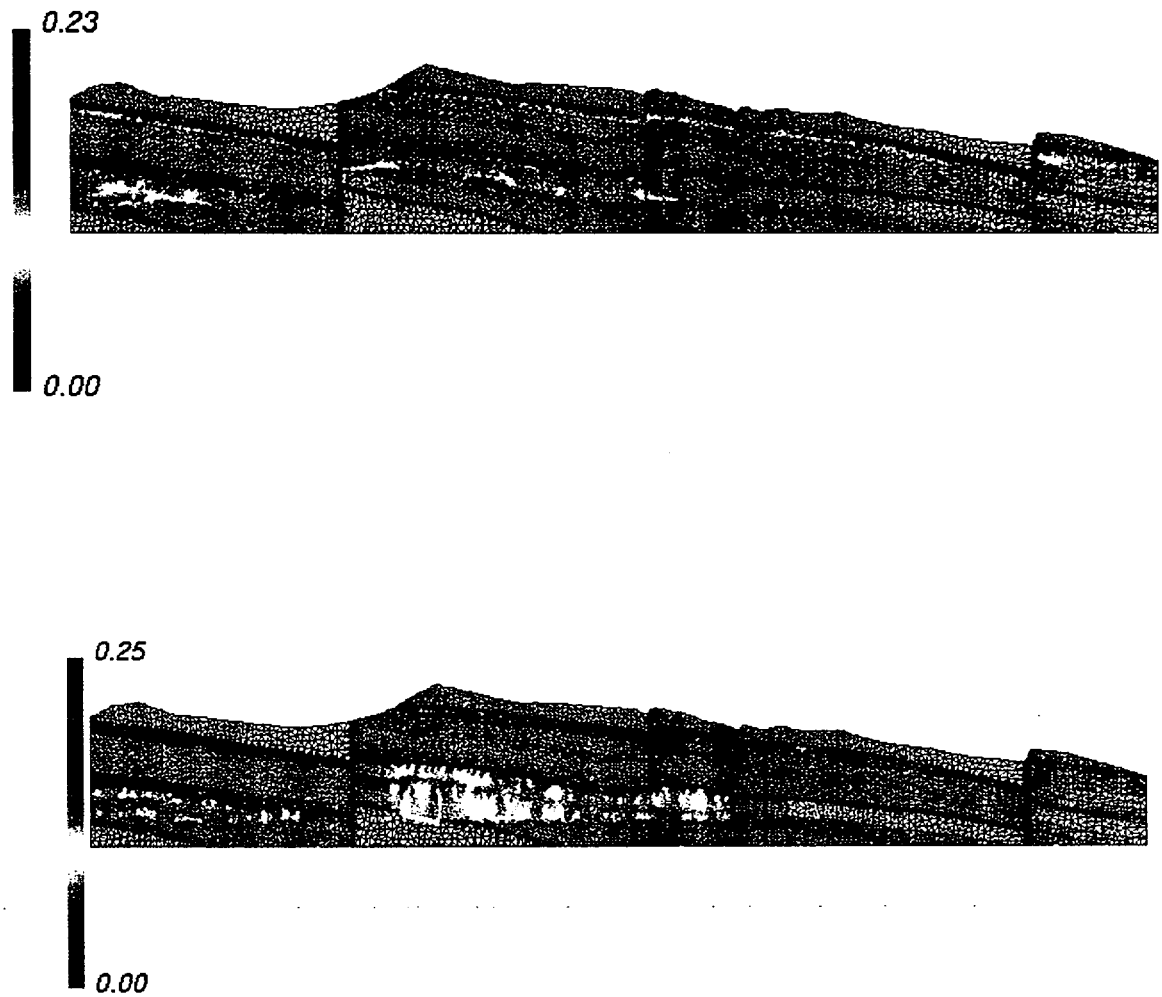

Figure 8-9. Difference in predicted fluid saturations from an increase in the base-case percolation flux map by a factor of three at all locations. Top figure: matrix saturation difference; bottom figure: fracture saturation difference.

(top figure) and fractures (bottom figure) for an increase in percolation flux of a factor of three at all locations on the base infiltration map. The matrix saturations, the only ones for which data are available, exhibit changes of less than 0.05 at almost all locations, with differences of 0.1 only in

a few locations. At the higher percolation rate, the fracture saturations increase more dramatically, a characteristic of increased fracture flow. Nevertheless, we conclude from this comparison that as a first approximation, the use of the parameter values determined with the base map is warranted for this range of percolation flux values.

This analysis begins with a set of calculations for the base case parameter set (case 6541) assuming an increase by a factor of three (called the "3 x I" case) and a decrease by a factor of three (I/3). Figures 8-10 and 8-11 show the Green's function and cumulative breakthrough curve for the

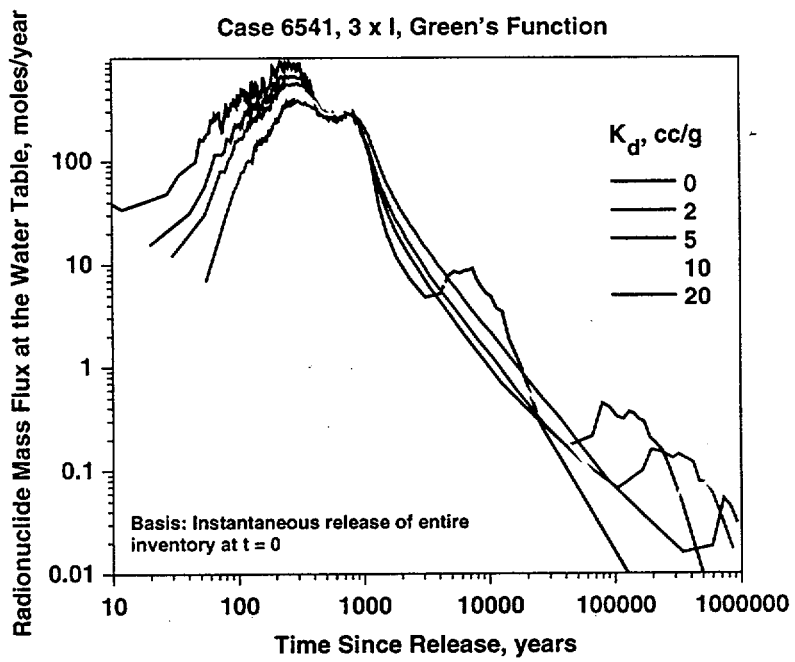

Figure 8-10. Green's function residence time distributions for transport of radionuclides in the two-dimensional site scale model. Property set 6541, 3 x I infiltration map.

3 x I case, and Figures 8-12 and 8-13 are the same curves for the I/3 case. As expected, the percolation flux is a key parameter controlling the transport response. At the higher percolation flux, the first peak of the breakthrough curve occurs much earlier (less than 1000 years), and perhaps more importantly, a greater fraction of the inventory travels through the fast pathways, thereby bypassing the zeolites. This observation is most easily seen in Figure 8-11 for the 3 x I case

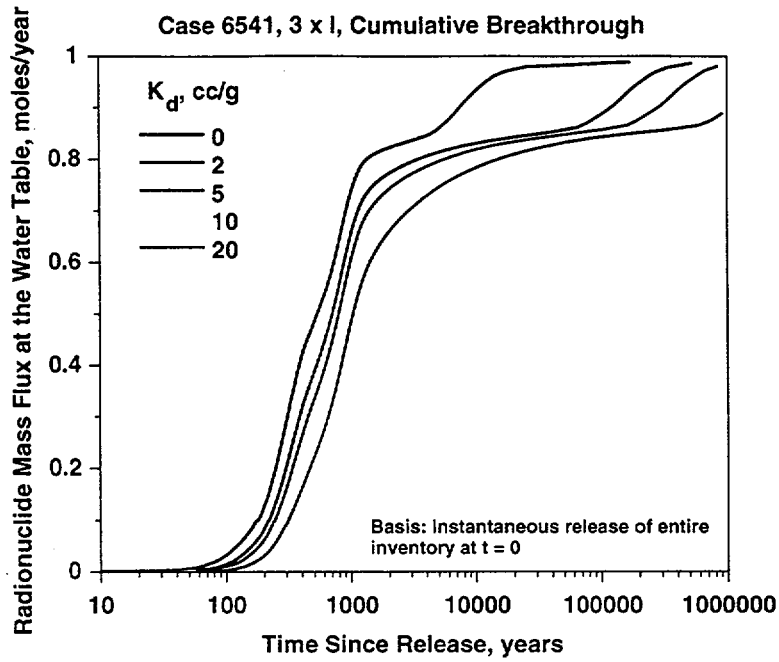

Figure 8-11. Cumulative residence time distributions for transport of radionuclides in the two-dimensional site scale model. Property set 6541, 3 x I infiltration map.

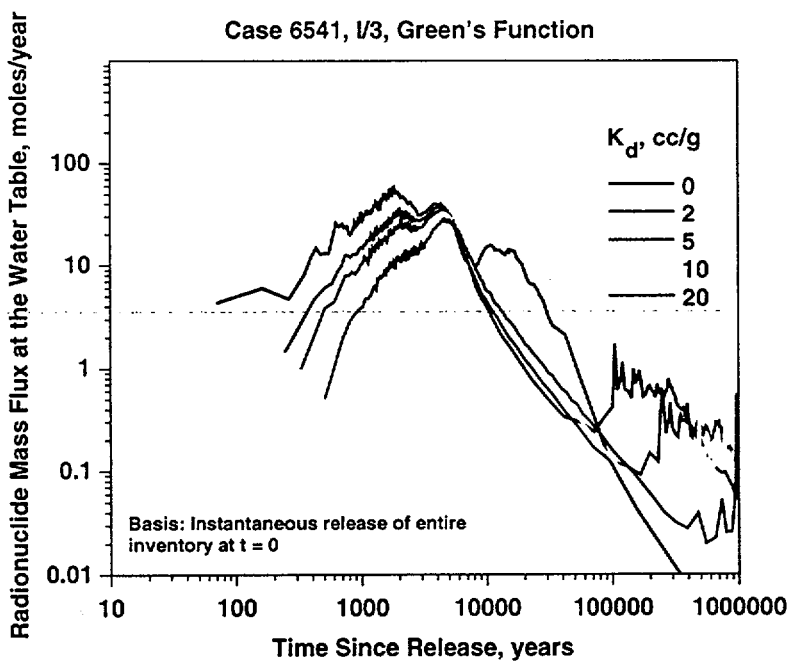

Figure 8-12. Green's function residence time distributions for transport of radionuclides in the two-dimensional site scale model. Property set 6541, I/3 infiltration map.

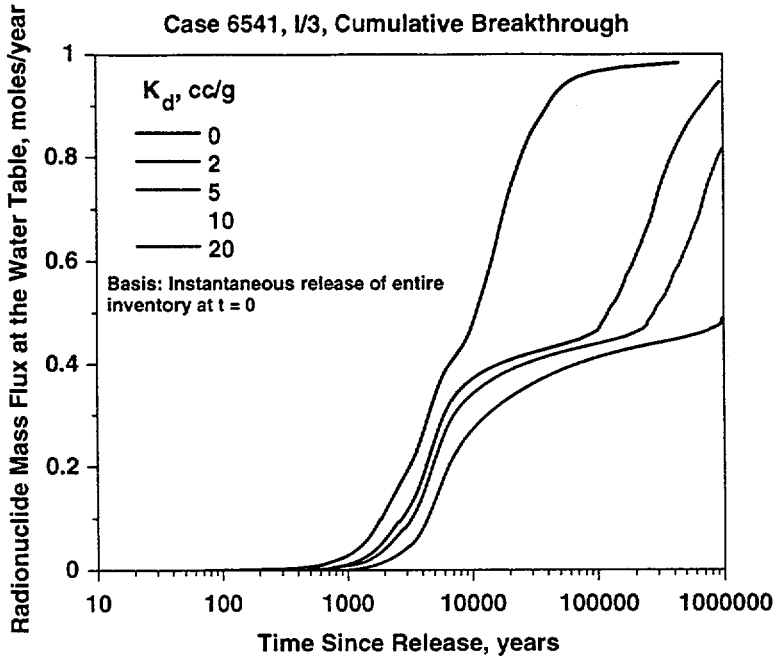

Figure 8-13. Cumulative residence time distributions for transport of radionuclides in the two-dimensional site scale model. Property set 6541, I/3 infiltration map.

(the converse is true for the I/3 case in Figure 8-13), the cumulative breakthrough curve. For this parameter set, even the I/3 case predicts a significant fraction of radionuclides traveling through the faster pathways. This is caused by the low zeolite permeabilities derived in the parameter estimation simulations combined with the still high percolation flux values predicted above the potential repository (up to 6 mm/yr).

Since the possibility exists for lower percolation flux values than predicted by the base case map, we continue to explore the ramifications of lower percolation for the other parameter sets. It is important to realize that higher infiltration is also possible, as in the 3 x I case, but given the behavior of each parameter set for the base case map, there is little point in further testing at the higher values. At higher flux values, the unsaturated zone transport is dominated by fractures, and travel times are short. We conclude that unless these parameter sets underestimate significantly the permeability of the zeolitic rocks, fracture flow through these horizons dominates transport at the

base infiltration rate or higher rates. If bulk fracture permeability is also low in the zeolites, then lateral flow would be induced.

For comparison, we present transport results for the I/3 infiltration map for the remaining parameter sets in Figures 8-14 and 8-15. The results presented in this figure, when compared to the base-case results, illustrate the degree of uncertainty in transport caused by the various parameter sets and conceptual models. Comparing cases 6412b and 6412c, we note that the adjustment of parameter values in the vitric units below the potential repository has minor effect on the transport behavior. This effect is in spite of a difference in the simulated matrix saturations of the two models, shown in Figure 8-16, in plots of the matrix saturations, and the difference in saturations for the two models. Although the property values resulted in lower saturations in these units (apparently more in keeping with the measured data), the distribution of flux in fracture and matrix in these units and the zeolitic rocks apparently did not change significantly.

Case 6522 parameters were developed by Bodvarsson et al. (1997) assuming that the infiltration rate is one-fifth that of the base-case map. It is being used here for the I/3 case, assuming that the somewhat different infiltration rates have little influence on the calibration. The Green's function is also similar to the previous cases, except for a somewhat greater fraction of the inventory travelling through the faster pathways. The only case to exhibit significantly different behavior for the I/3 infiltration scenario is case 6531b, the upstream saturation weighting parameter set. This set exhibited significantly more rapid transport than the others in one dimension and at the base infiltration rate. This trend continued to hold for this infiltration rate as well.

8.8 Grid Refinement Study

An accurate transport solution requires that the numerical grid be discretized finely enough to capture accurately the details of the flow and transport system. Two types of grid errors are possible. First, a coarse grid can smear the details of a complex, heterogeneous flow and transport

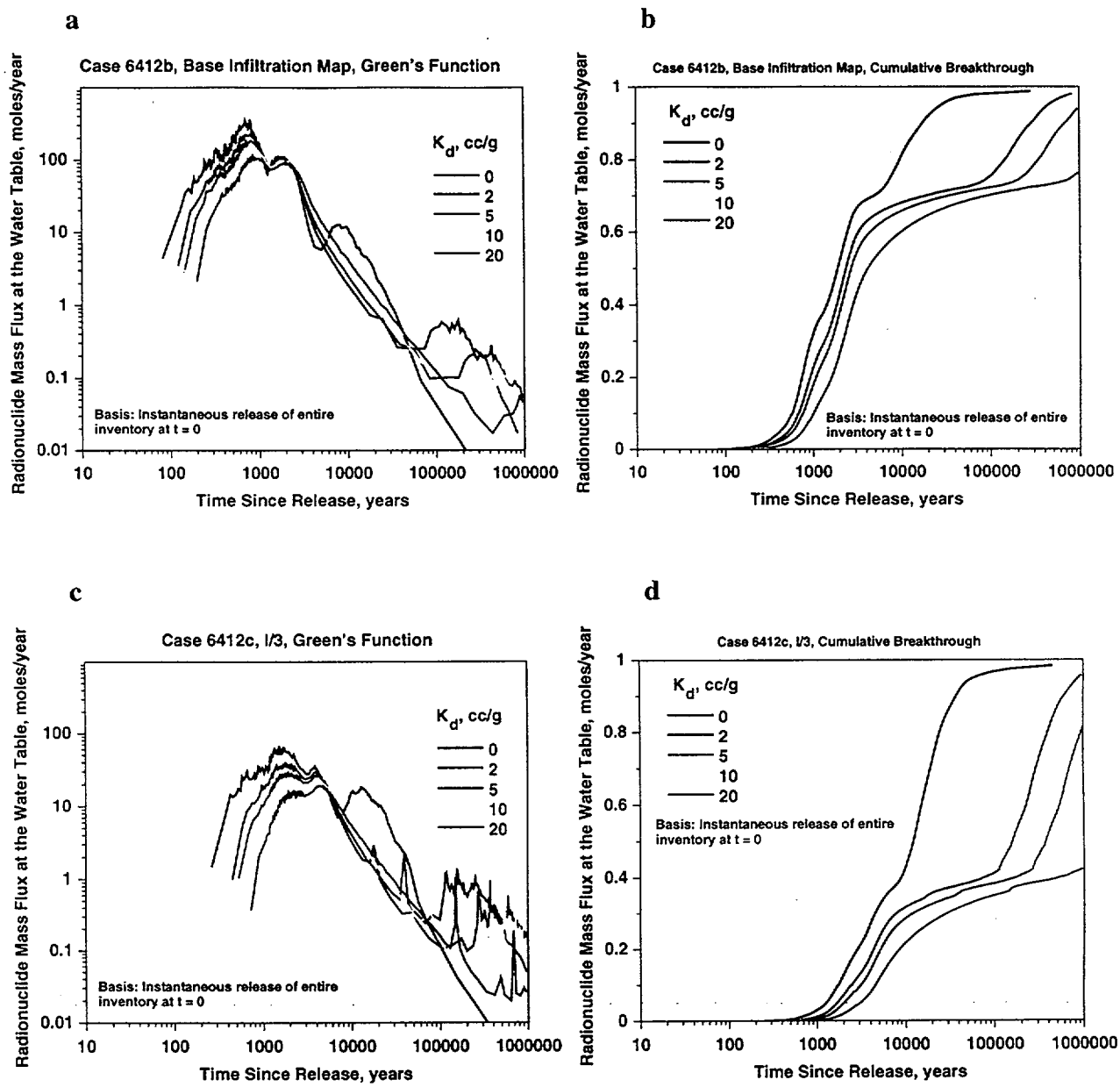

Figure 8-14. Green's function (left column of figures) and cumulative residence time distributions for the I/3 infiltration map for various parameter sets. a, b) 6412b; c, d) 6412c.

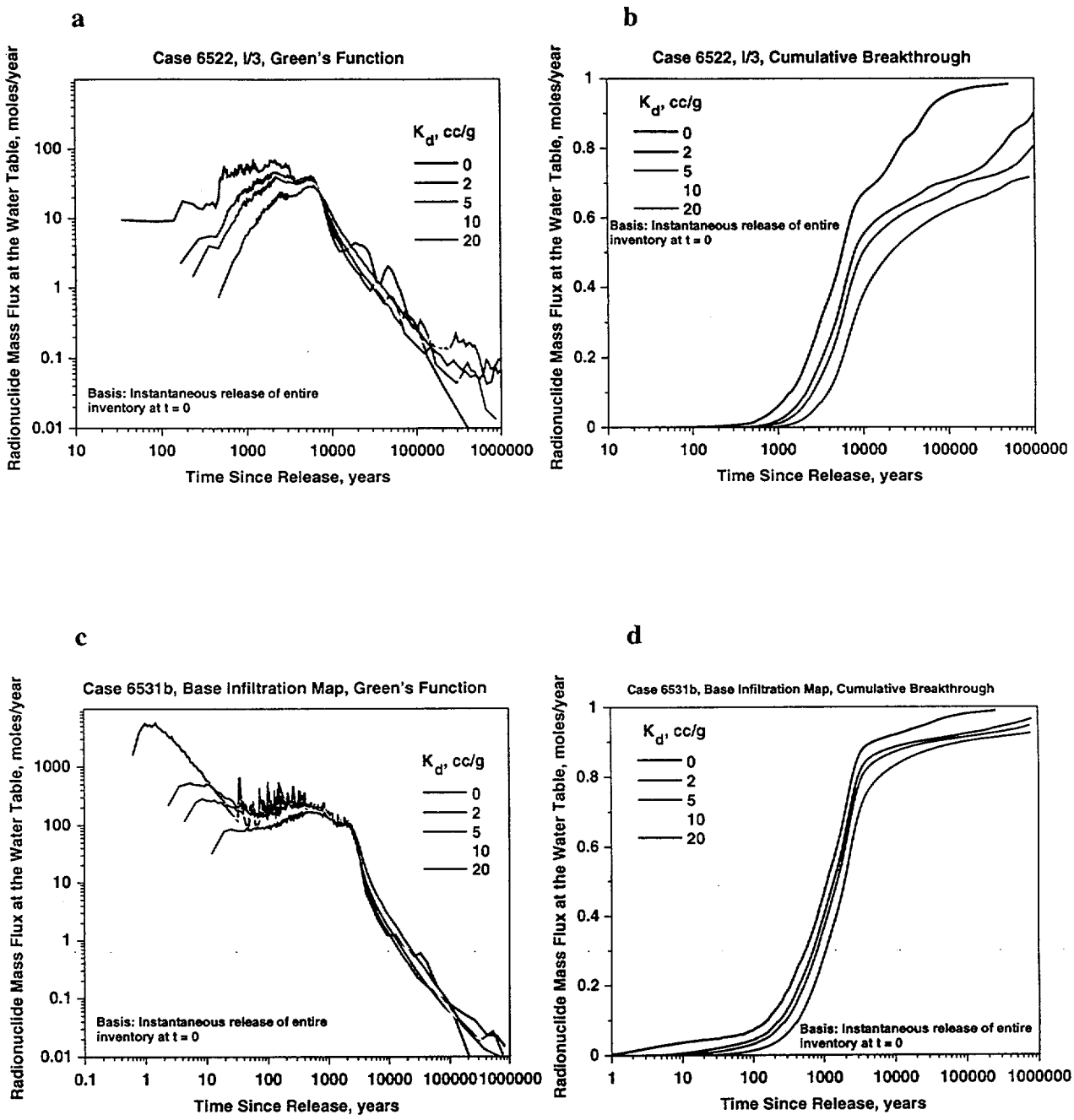

Figure 8-15. Green's function (left column of figures) and cumulative residence time distributions for the I/3 infiltration map for various parameter sets. a, b) 6522; c, d) 6531b.

parameter field, requiring spatial averaging to capture with a single set of parameters a complex system with widely contrasting parameter values within each computational grid element. Even for

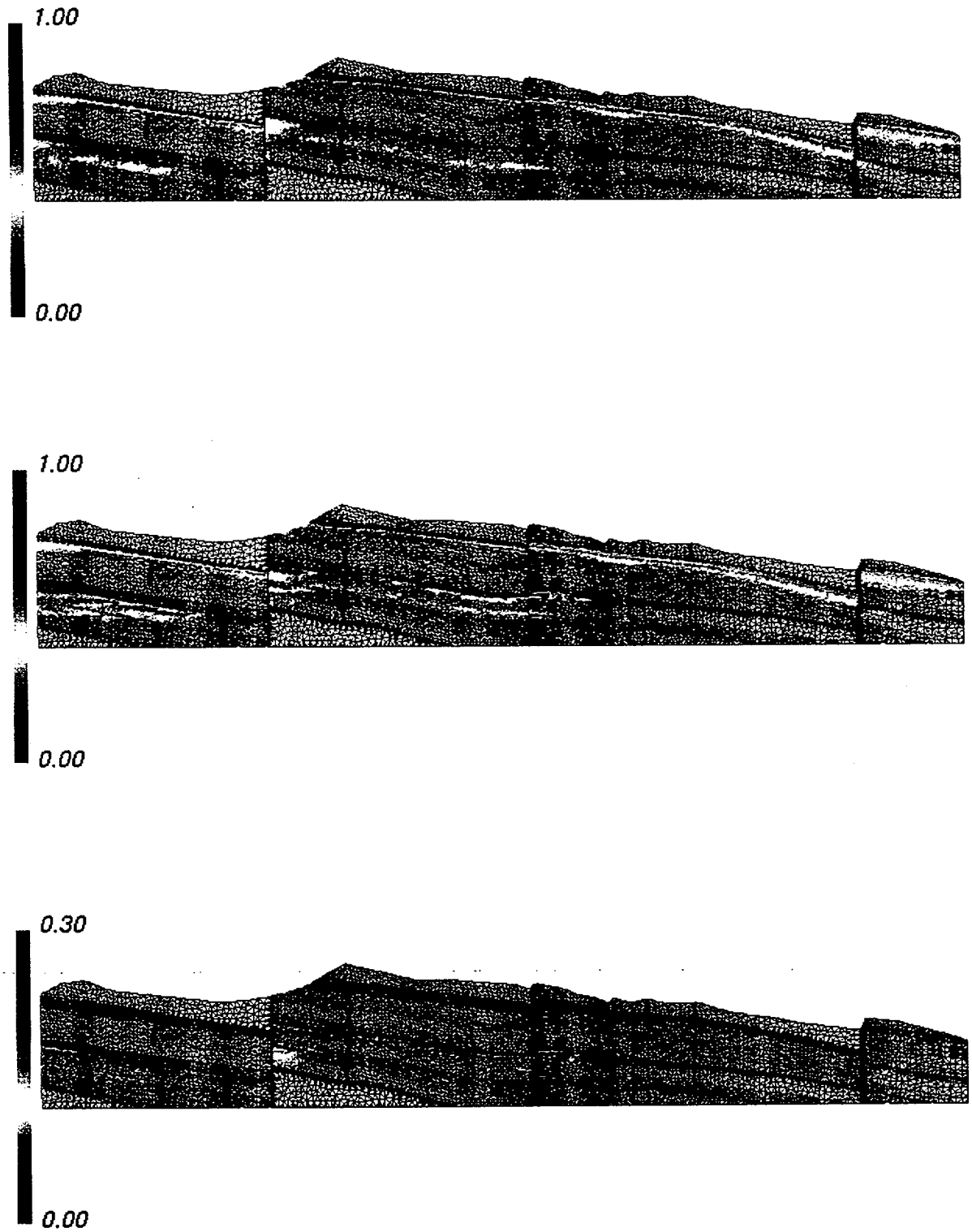

Figure 8-16. Comparison of matrix saturations for cases 6412b and 6412c. I/3 infiltration map. Top figure: 6412b; middle figure: 6412c; bottom figure: difference in saturations (6412c - 6412b).

a layered system with homogeneous properties within each unit, several computational grid points may be required to capture the details of a complex flow and transport system. This grid resolution numerical accuracy issue is examined here, for the ten percent zeolite map on the same refined grid used in Chapter 12 for the heterogeneity study where all zeolite alteration percentages are considered.

In this calculation we map the zeolite distribution defined as the 10% zeolite case onto each grid, and compute steady state fluid flow transport to the water table for both cases. Therefore the only difference is the numerical grid in the region at and below the potential repository. Figures 8-17 and 8-18 show the results for the two models for K_d values of 0, 2, and 10 cc/g. The responses

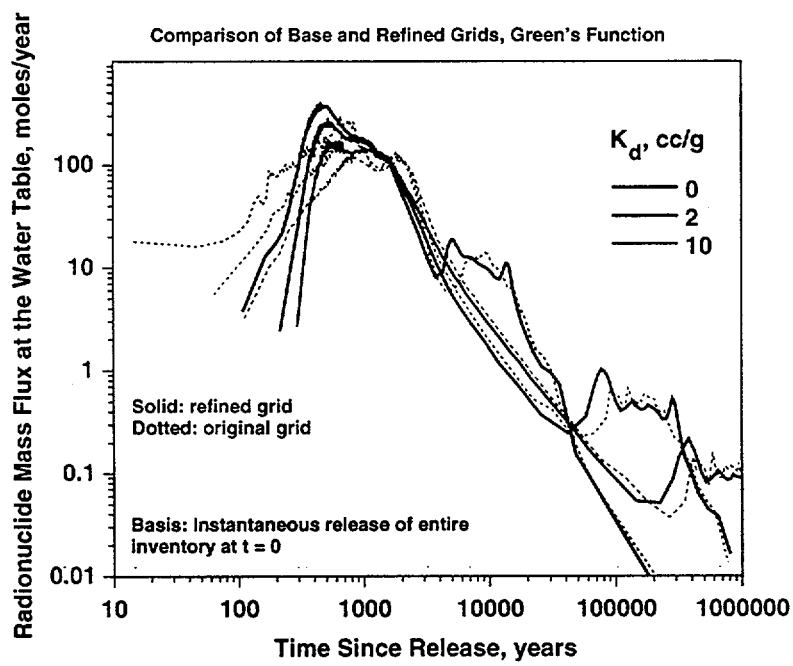

Figure 8-17. Comparison of Green's functions (base-case grid and refined grid) for transport of radionuclides in the two-dimensional site scale model. Property set 6541, base infiltration map.

are quite similar for the two cases in terms of the peak arrival times and general shapes. The refined grid exhibits a slightly higher peak value with less dispersion. However, recall that when an actual NFE source term is applied in these models, the area under this peak (or the plateau value in the

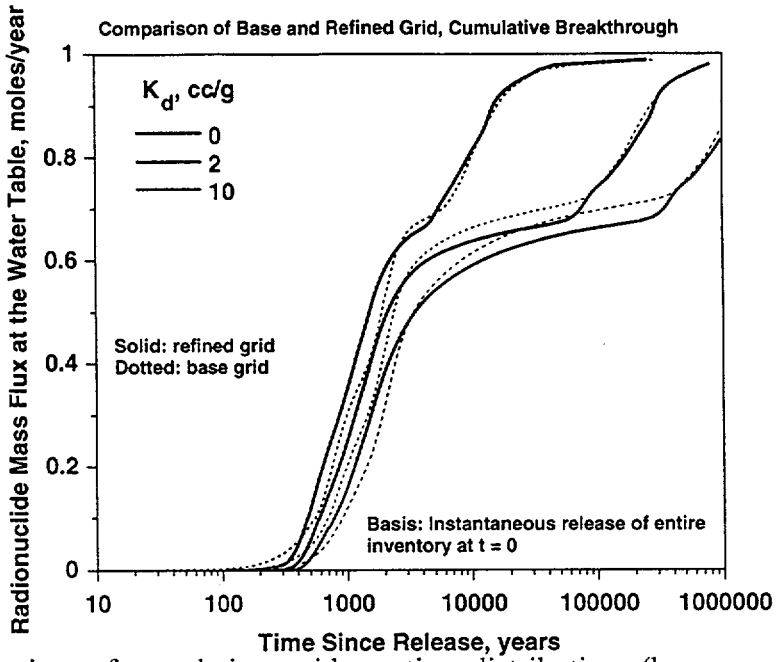

Figure 8-18. Comparison of cumulative residence time distributions (base-case grid and refined grid) for transport of radionuclides in the two-dimensional site scale model. Property set 6541, base infiltration map.

cumulative breakthrough curve) is more important than details regarding the shape. Figure 8-18 shows that, based on this criterion, the responses are quite similar. Therefore, we conclude that the coarser grid is adequately resolved for the purposes of this study. The refined grid is still necessary for the study of the impact of heterogeneities presented in Chapter 12.

8.9 Uncertainties in Zeolite Distributions and Property Variations

No parameter in the site-scale flow model is known to a high degree of precision. Therefore, it is important to understand the impact of uncertainty in key parameters on the performance of the unsaturated zone as a barrier to radionuclide migration. One aspect of the system that has presented itself most noticeably in this version of the site-scale radionuclide transport model is the prediction that a significant portion of the inventory may bypass the zeolites through fractures. This result has occurred due to the low matrix permeabilities and the weak coupling between fractures and matrix brought on by the new fracture/matrix coupling models.

The implications are important for both nonsorbing and sorbing radionuclides. Nonsorbing species, such as ^{99}Tc, travel more rapidly to the water table because of the increased velocities in the fractures of the zeolitic units, rather than slow matrix percolation. Radionuclides, such as ^{237}Np and uranium, also sorb onto zeolites, so the impact of fracture flow is even more pronounced. Therefore, one of the critical uncertainties is the distribution and hydrologic property values for zeolitic tuffs.

To study the influence of property value uncertainty, we simulated a case in which the parameter set 6412c was revised to increase the matrix permeability of each zeolitic unit by a factor of five. We call this simulation case 6412d. Both property sets are described in Table 5-2. The justification for this level of increase is that the measured values easily spans a range that encompasses this variation, and that the LBNL parameter estimation results imply that a rather wide range of zeolite matrix permeabilities could fit the data almost equally as well. Of course, this logic would imply that either an increase or decrease is warranted. We choose to study only the increase because even for the base case values, the zeolites are being bypassed to a large extent. Lowering the zeolite matrix permeability would not fundamentally change this result.

Figures 8-19 and 8-20 show the Green's function and cumulative residence time distributions for this case assuming the I/3 infiltration map, and Figures 8-21 and 8-22 are the results for the base infiltration case. The performance of the unsaturated zone improves dramatically for this variation in property values, especially when combined with the I/3 infiltration map. The nonsorbing radionuclide has first arrivals greater than 1,000 years and the peak occurs at about 10 ky. In essence, due to matrix flow through the zeolites, the first peak in the breakthrough curve vanishes, and virtually all radionuclide travels slowly through the matrix below the basal vitrophyre. This dramatically improves the performance with respect to radionuclides that sorb to the zeolites, as shown in Figures 8-19 to 8-22. For example, peak breakthrough for the $K_d = 2$ cc/g case (a typical value for ^{237}Np) occurs at about 100 ky for this case. For the base infiltration map, performance is not as good (Figures 8-21 and 8-22), but the

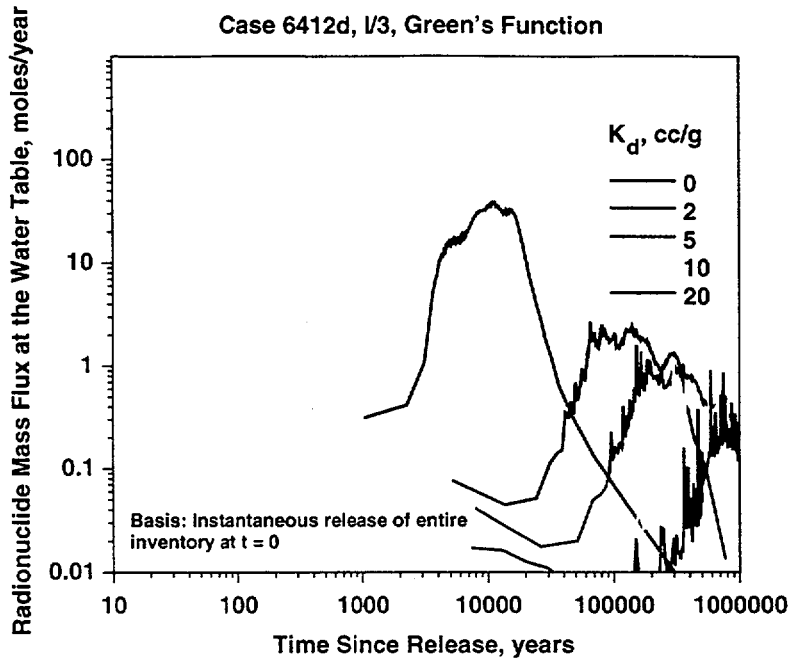

Figure 8-19. Green's function for transport of radionuclides in the two-dimensional site scale model. Property set 6412d (high-K zeolites), I/3 infiltration map.

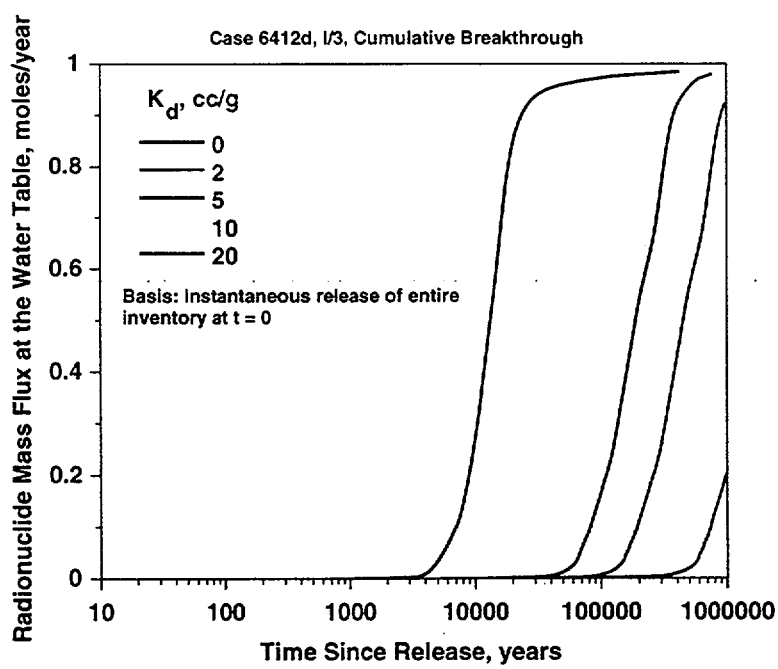

Figure 8-20. Cumulative residence time distributions for transport of radionuclides in the two-dimensional site scale model. Property set 6412d (high-K zeolites), I/3 infiltration map.

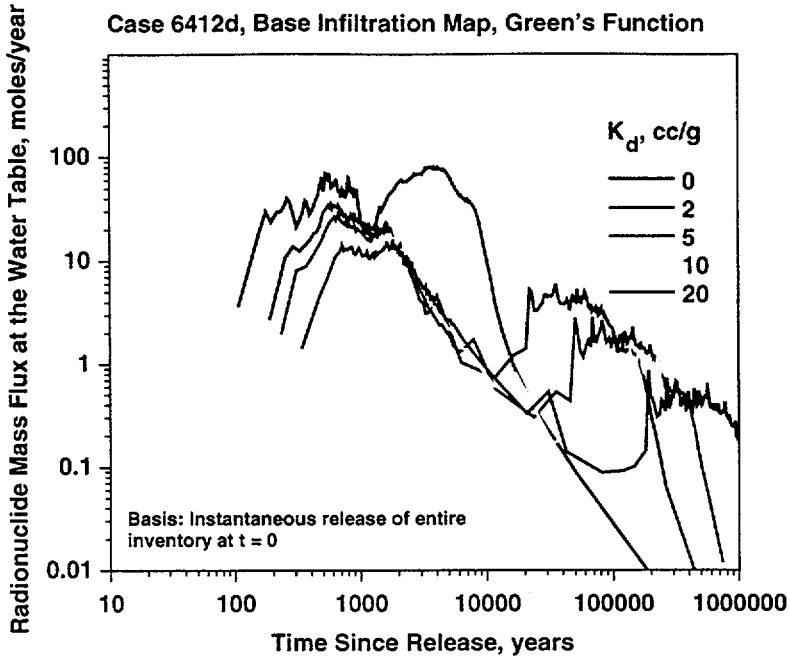

Figure 8-21. Green's function for transport of radionuclides in the two-dimensional site scale model. Property set 6412d (high-K zeolites), base infiltration map.

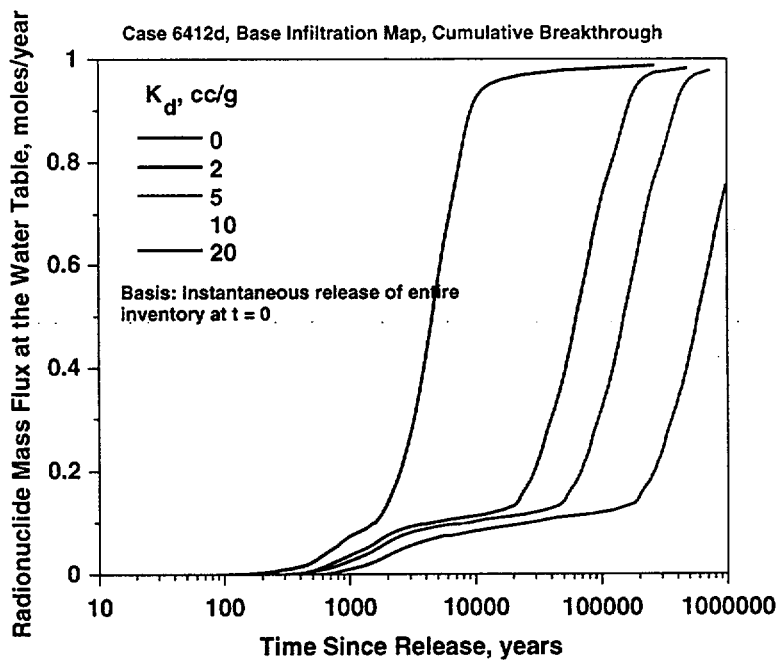

Figure 8-22. Cumulative residence time distributions for transport of radionuclides in the two-dimensional site scale model. Property set 6412d (high-K zeolites), base infiltration map.

fraction of radionuclide travelling through the rapid pathways is still greatly reduced from the base case parameter values. Clearly, the properties of the zeolites is of overriding importance to the performance of the unsaturated zone.

8.10 Plutonium Colloid Transport Analysis

In this section we expand upon a topic in which significant advances have been made recently in our ability to capture the potentially important process of colloid-facilitated transport. The Unsaturated Zone (UZ) Flow and Transport Workshop conducted by TSPA personnel identified the issue of colloidal transport as a key uncertainty in transport of radionuclides in the unsaturated zone, reiterating statements made for many years by scientists at Los Alamos and elsewhere. Specifically, the workshop participants concluded that in order to develop a credible model for plutonium movement in the UZ, transport of Pu radiocolloids and "pseudo-colloids" (Pu attached to natural colloidal material or colloids introduced in the water due to construction of the repository) must be considered. To date, process-level transport models and PA models have assumed that plutonium migrates as an aqueous component. Since sorption coefficients of aqueous plutonium on Yucca Mountain tuffs are large, plutonium has been predicted to migrate only a short distance before undergoing radioactive decay. Colloid-facilitated transport has the potential to increase transport velocities considerably, and thus must be included in future analyses. Even if the "bottom line" remains the same (i.e. that plutonium does not contribute significantly to the predicted dose at the accessible environment), including colloidal transport will add an additional degree of credibility to the analyses.

At the PA Workshop, a model of plutonium migration was proposed that included aqueous transport, kinetically controlled sorption of plutonium onto natural and man-made colloids, as well as transport as radiocolloids. However, simpler models are needed to fulfill several goals:

- scoping the problem to identifying key processes and parameters;
- providing simple analytical solutions to check against the more sophisticated models when

they are developed;

- perhaps to provide a simplified model to PA that could be used to bound the problem for TSPA-VA (this goal would be realized only if the simple model was indeed a defensible abstraction of the more complex model).

In this section we derive an analytical solution, present results of the model, and make a first attempt to quantify how different model assumptions and chemical parameters will impact the predicted transport of radionuclides for which colloid-facilitated transport is possible. This model is then incorporated into the site-scale transport model to predict plutonium migration. More sophisticated models and analyses that include estimates of specific parameters for radionuclides such as plutonium will follow at a later date.

8.10.1 Model Development

The model developed herein is a one-dimensional transport model of a contaminant travelling in a fractured medium. It is assumed that the hydrologic conditions are such that uninterrupted fracture flow pathways exist from the repository to the water table. Thus the model is an "end-member" that attempts to capture the worst-case conditions from the standpoint of colloid-facilitated transport. It must be stressed that the model would severely underestimate the retardation capacity of the unsaturated zone to radionuclides, such as plutonium, if it can be demonstrated that rock strata between the repository and the water table exhibit matrix-dominated flow and transport. This concern is demonstrated in the site-scale model calculations that follow. Nevertheless, it is a starting point for addressing performance under conditions of fracture-dominated transport, a scenario not ruled out in present site scale models.

Aqueous transport: We first consider a model available in the literature for the one-dimensional transport of an aqueous contaminant, and later revise it to include colloidal transport. This first model was developed by Tang et al. (1981). The model geometry is one of transport in a parallel-plate fracture, with the surrounding matrix block on either side of the fracture (Figure 8-23). The transport equation to be solved in the fracture assumes the one-dimensional advective-

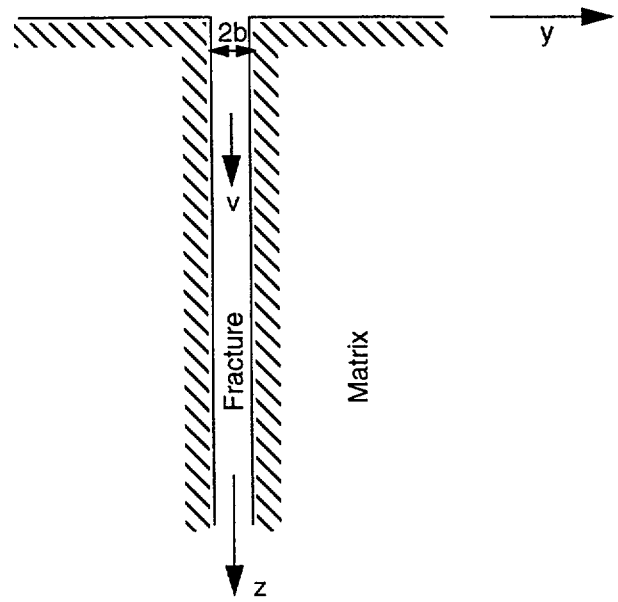

Figure 8-23. Schematic of the fracture transport model (after Tang et al., 1981)

dispersion equation, diffusion into the porous rock matrix, equilibrium, and linear sorption on the fracture surface:

$$R_f \frac{\partial C}{\partial t} = D_z \frac{\partial^2 C}{\partial z^2} - v \frac{\partial C}{\partial z} - \frac{q}{b} \qquad \text{(Eq. 8-2)}$$

where C is the concentration, t is time, z is the coordinate in the direction of fluid flow, R_f is the sorption retardation factor for the contaminant on the fracture, D_z is the axial dispersion coefficient, v is the fluid velocity, q is the diffusive loss term for the porous rock matrix, and $2b$ is the fracture aperture. Assuming no advective flow of fluid in the matrix, the transport equation for the contaminant is:

$$R_m \frac{\partial c}{\partial t} = D_m \frac{\partial^2 c}{\partial y^2} \qquad \text{(Eq. 8-3)}$$

where c (lower case) is the concentration of contaminant in the matrix, y is the direction perpen-

dicular to the flow direction, R_m is the retardation factor for the matrix, and D_m is the diffusion coefficient in the matrix rock. These two transport equations are coupled through the diffusive loss term q, formulated by assuming continuity of concentration for fluid in the fracture with that in the matrix at $y = b$, such that:

$$q = -\theta D_m \frac{\partial c}{\partial y}\bigg|_{y=b} \qquad \text{(Eq. 8-4)}$$

where θ is the volumetric water content in the matrix (equal to porosity for a saturated matrix, or porosity times saturation for an unsaturated matrix). Tang et al. (1981) derived a full transient solution to this system of equations for any position in the fracture or matrix. In this paper, we give the result for a position $z = L$ in the fracture, presumed to be at the water table:

$$\frac{C}{C_{in}} = \frac{2 \cdot \exp(Pe/2)}{\pi^{1/2}} \int_l^{\infty} \exp\left[-\xi^2 - \frac{Pe^2}{16\xi^2}\right] \operatorname{erfc}\left(\frac{PeA}{4\xi^2 \sqrt{\frac{t}{\tau} - \frac{PeR_f}{2\xi^2}}}\right) d\xi \qquad \text{(Eq. 8-5)}$$

where C_{in} is the concentration at the entrance to the model, ξ is the integration variable, τ is the mean residence time of fluid through the fracture, equal to L/v,

$$l = \left(\frac{\tau PeR_f}{4t}\right)^{1/2} \qquad \text{(Eq. 8-6)}$$

and

$$A = \frac{\theta(\tau R_m D_{mol})^{1/2}}{2b} \qquad \text{(Eq. 8-7)}$$

Equation 8-6 also makes use of the relation between D_z and dispersivity α, namely that $D_z = \alpha v$, from which it follows that the axial dispersion Peclet number $Pe = L/\alpha$. Additional simplifications are possible if axial dispersion is considered to be negligible. Starr et al. (1985) derived a similar model for this case, showing that

$$\frac{C}{C_{in}} = \mathrm{erfc}\left(\frac{A}{\sqrt{t/\tau - R_f}}\right) t > R_f\tau \qquad \text{(Eq. 8-8)}$$

with $C/C_{in} = 0$ for $t \le R_f\tau$. Although the finite dispersion model Equation 8-5 will be used for the simulations presented below, Equation 8-8 provides a useful simplification to examine the dependencies in the model. The main parameters are the fracture retardation factor R_f, which provides a sorptive delay in the breakthrough times from that of water flow in the fracture, and the dimensionless group A, which can be used to assess the relative importance of advective transport in the fracture to diffusion in the rock matrix. High values of A lead to the case in which interaction of contaminant with the rock matrix is important, and would result from any of the following conditions: high matrix porosity, large water travel times in the fracture, high matrix diffusion coefficient, large matrix sorption coefficient, or small aperture.

Colloid-facilitated transport: In this section we include a simplified colloidal transport model equation to derive a combined aqueous/colloidal transport model. The key assumptions of the colloidal transport sub-model are:

- the contaminant sorbs reversibly to the colloids in addition to interacting with the rock matrix and fractures;
- the colloids are isolated to the fracture, and possess dispersive properties equivalent to that of an aqueous solute;
- the colloids interact reversibly with the fracture surface.
- Given these assumptions, a transport equation for contaminant attached to colloids can be written as

$$R_c\frac{\partial C_c}{\partial t} = D_z\frac{\partial^2 C_c}{\partial z^2} - v\frac{\partial C_c}{\partial z} \qquad \text{(Eq. 8-9)}$$

where C_c is the concentration of contaminant attached to colloids, and R_c is a retardation factor

that captures the details of colloid attachment/detachment and filtration processes.

To couple the transport equation for contaminant on colloids (Equation 8-9) to the aqueous transport equation (Equation 8-2), reversible, linear sorption of contaminant onto colloids is assumed:

$$C_c = K_c C \qquad \text{(Eq. 8-10)}$$

where K_c is the distribution parameter relating the concentrations. Since both C and C_c are expressed as moles contaminant per unit fluid volume, K_c is a dimensionless parameter expressing the ratio of contaminant mass residing on colloids to the mass present in aqueous form. In terms of more commonly defined and measured quantities, K_c is the product of the distribution coefficient for contaminant on colloids and the concentration of colloidal material available for sorption (mass of colloids per unit fluid volume). Adding Equations 8-2 and 8-9, and making use of Equation 8-10, we obtain for the concentration of the contaminant in the aqueous phase for the fracture:

$$\left(\frac{R_f + K_c R_c}{1 + K_c}\right)\frac{\partial C}{\partial t} = D_z \frac{\partial^2 C}{\partial z^2} - v\frac{\partial C}{\partial z} - \frac{q}{b(1 + K_c)} \qquad \text{(Eq. 8-11)}$$

The coupling between the fracture and matrix is identical to the case without colloids, since we assume no mobility of colloids into the matrix rock. Inspection of Equations 8-11 and 8-2 reveals that the forms of the transport equations are identical, with different constants in the accumulation and diffusive loss terms. Therefore, the solutions developed thus far (Equations 8-5 to 8-8) need only be modified slightly to include colloid contaminant transport. To do this, we define revised constants $\hat{R}_f$ and $\hat{A}$ as follows:

$$\hat{R}_f = \frac{R_f + K_c R_c}{1 + K_c} \qquad \text{(Eq. 8-12)}$$

$$\hat{A} = \frac{\theta(\tau R_m D_{mol})^{1/2}}{2b(1 + K_c)} \qquad \text{(Eq. 8-13)}$$

Using these expressions instead of their counterparts R_f and A allow us to consider colloidal

transport under dispersive conditions (Equation 8-5) or plug-flow fracture conditions (Equation 8-8). One final note is that the inlet concentration C_{in} must include contributions from both colloidal and aqueous contaminant, and therefore should be considered to be a total mass of contaminant (aqueous and colloidal) per unit fluid volume.

8.10.2 Results of Colloid Transport Simulations

One-Dimensional Simulation Results: This discussion begins with a general description of the features of the model for an aqueous contaminant traveling through a fracture, and then examine the differences between aqueous-only and colloid-facilitated contaminant transport. We use parameter values that we regard as possible for unsaturated zone transport through a fracture system directly connecting the repository to the water table. The range of values of each parameter are listed in Table 8-2 below:

Table 8-2. Potential ranges of hydrologic and transport parameter values

Parameter	Range	Note
τ	0.1-10 y	Example: 350 m flow distance, 3.5 mm/y through fractures, fracture volumetric water content of 10^{-5}: τ = 1 year.
Dispersivity	1 - 100 m	0 is no dispersion (Equation (Eq. 8-8))
R_f	1-100	1 is no fracture sorption, 100 is possible for a strongly sorbing radionuclide
R_m	1-1000	1 is no fracture sorption, 1000 would result from K_d = 100 cc/g, rock density of 2 cc/g, and θ = 0.2
D_{mol}	10^{-12}-10^{-10} m^2/s	Low values are indicative of diffusion into low-water content matrix. High values are typical of measured values under saturated conditions.
b	0.1-10 mm	Poorly known parameter
θ	0.1-0.3	0.1 is the matrix water content for a welded, nearly saturated rock or nonwelded, partially saturated rock. 0.3 would be typical for a saturated, zeolitic rock. 0.2 used for all simulations in this report.
K_c	0-1000	0 no colloids or minimal sorption, 1000 is the equivalent of 999 parts out of 1000 residing on colloids

Table 8-2. Potential ranges of hydrologic and transport parameter values(Continued)

Parameter	Range	Note
R_c	1-100	Little known about colloid filtration or sorption in fractures

Some of these parameters should be considered to be correlated, even though the sensitivity analysis treats them as separate. Examples include the fact that fracture fluid travel time should be related to the aperture, and that diffusion coefficient is a strong function of matrix volumetric water content. Because the parameters are here assumed to be uncorrelated, the calculations presented below are to be considered a first step toward an understanding of the important parameters, rather than a sensitivity analysis that could be used directly in Performance Assessment activities.

Aqueous transport without colloids: To place the colloid transport calculations in perspective, we first present results of the transport model without colloids present. All transport results are presented as dimensionless breakthrough curves at the water table to a constant-concentration release at the repository. Figure 8-24 shows the results of the model for different

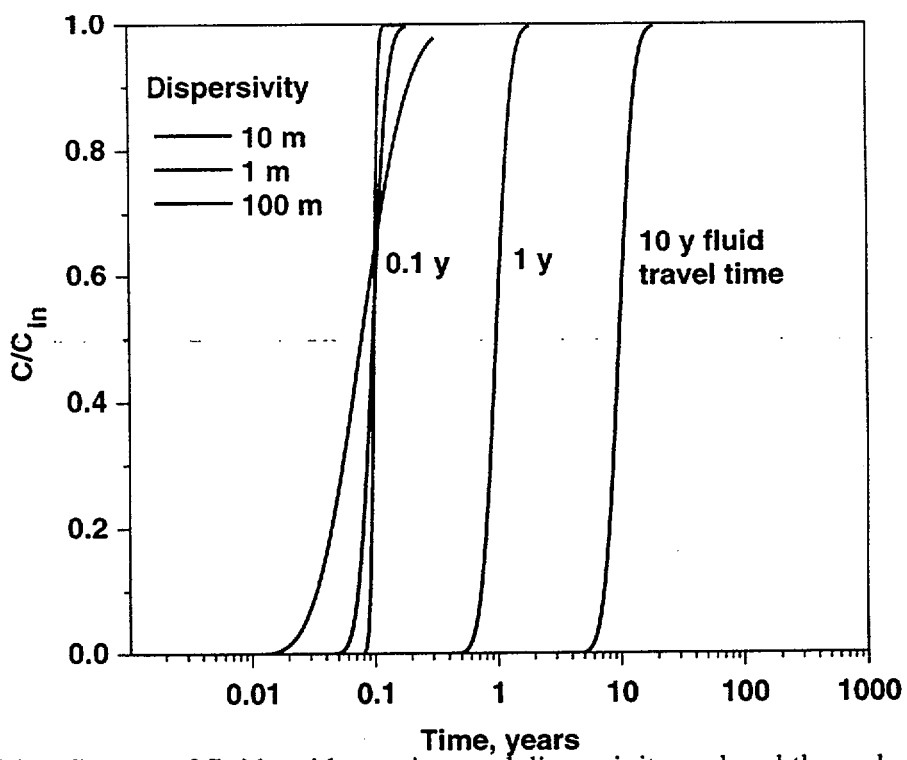

Figure 8-24. Influence of fluid residence time and dispersivity on breakthrough at the water table. No matrix diffusion or sorption.

fluid residence times in the absence of matrix diffusion. As expected, if retardation effects are neglected, the model reduces to conventional convective-dispersive behavior with a mean travel time equal to the fluid travel time. The dispersivity is varied from 1 m to 100 m for the 0.1 y fluid travel time case, and is shown to have very little impact on the breakthrough curve. Therefore, 10 m dispersivity is assumed for all subsequent simulations. If travel times are indeed this short, no amount of dispersion in the fractures will spread the transporting radionuclide significantly. Figure 8-25 illustrates the influence of sorption on fracture surfaces, which of course delays the breakthrough even in the absence of matrix diffusion.

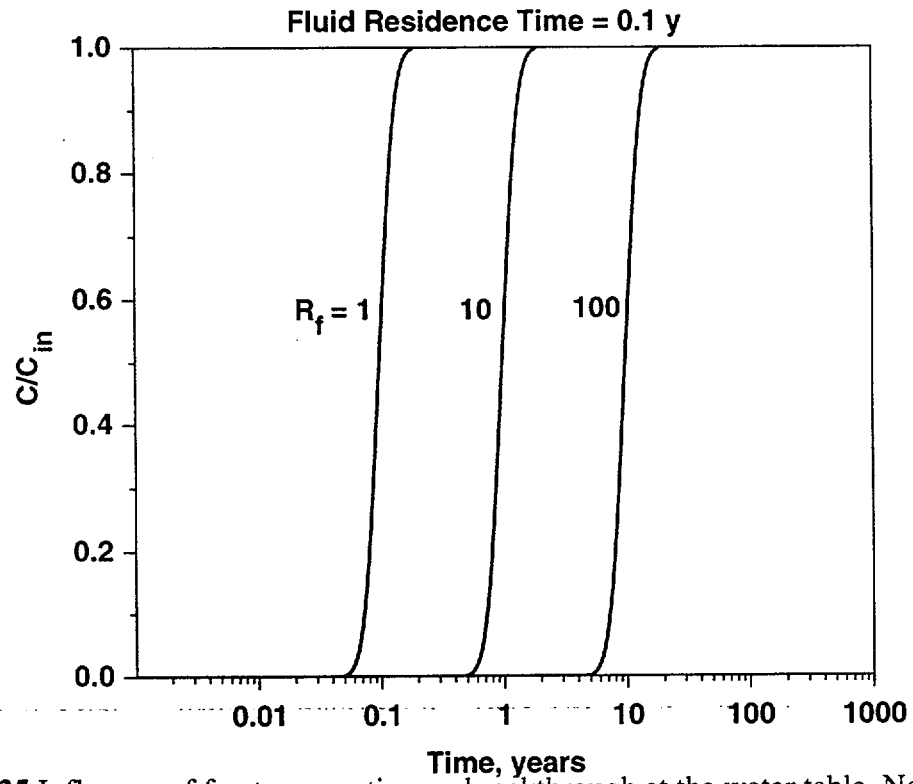

Figure 8-25. Influence of fracture sorption on breakthrough at the water table. No matrix diffusion or sorption. Fluid travel time = 0.1 y.

When matrix diffusion is included in the model, increased travel times and greater apparent dispersion of the breakthrough curves are predicted. Figure 8-26 illustrates the influence of matrix diffusion coefficient on the breakthrough curves over the range selected to represent uncertainty in the unsaturated zone. Significant increases in travel times are predicted, even for the case of 1 y

fluid travel time. The influence of the matrix sorption retardation factor is identical to the effect of

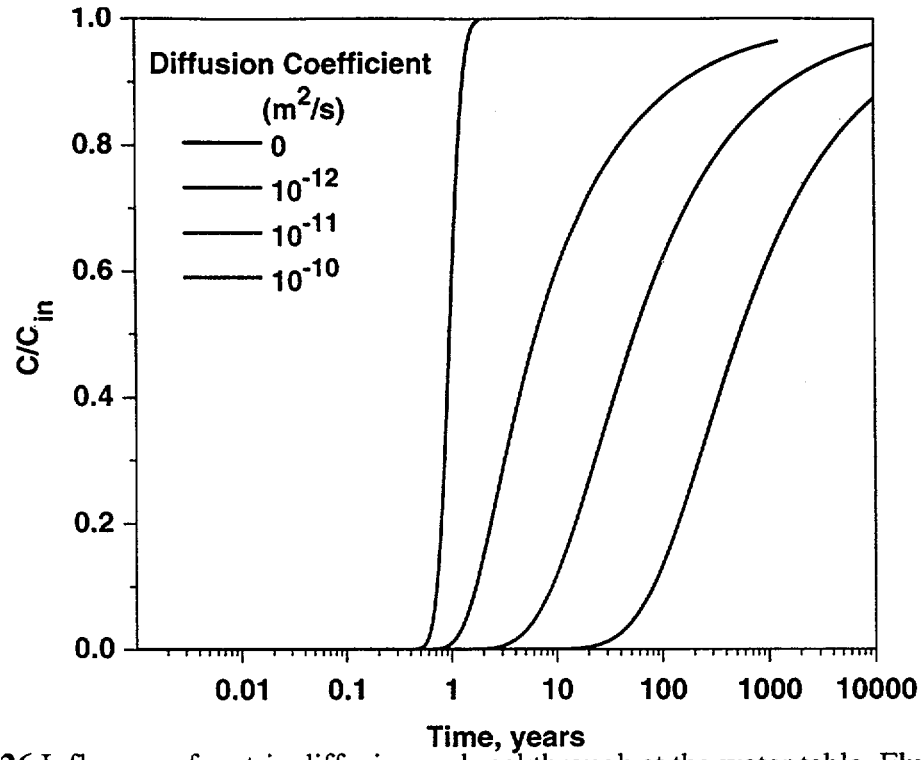

Figure 8-26. Influence of matrix diffusion on breakthrough at the water table. Fluid travel time = 1 y. No matrix or fracture sorption.

diffusion coefficient, as seen by comparing the results of Figure 8-27 with those of Figure 8-26. This similarity is due to the equivalent roles played by R_m and D_{mol} in the mathematical development in the model (they appear as a product in the expression for A in Equation 8-5).

Colloid-Facilitated Transport: Colloid-facilitated transport due to sorption on existing colloid particles is suspected to be most important for strongly sorbing radionuclides such as plutonium. To illustrate the extent to which colloids could increase the mobility of plutonium, we examine the case in which the predicted large retardation of plutonium (the $R_m = 1000$ case in Figure 8-27) are influenced by colloids. In the absence of sorption of aqueous plutonium or retardation of colloids in the fracture itself, the fracture retardation factor $\hat{R}_f$ of Equation 8-12 is 1, regardless of the colloid distribution parameter K_c. However, the diffusion parameter $\hat{A}$

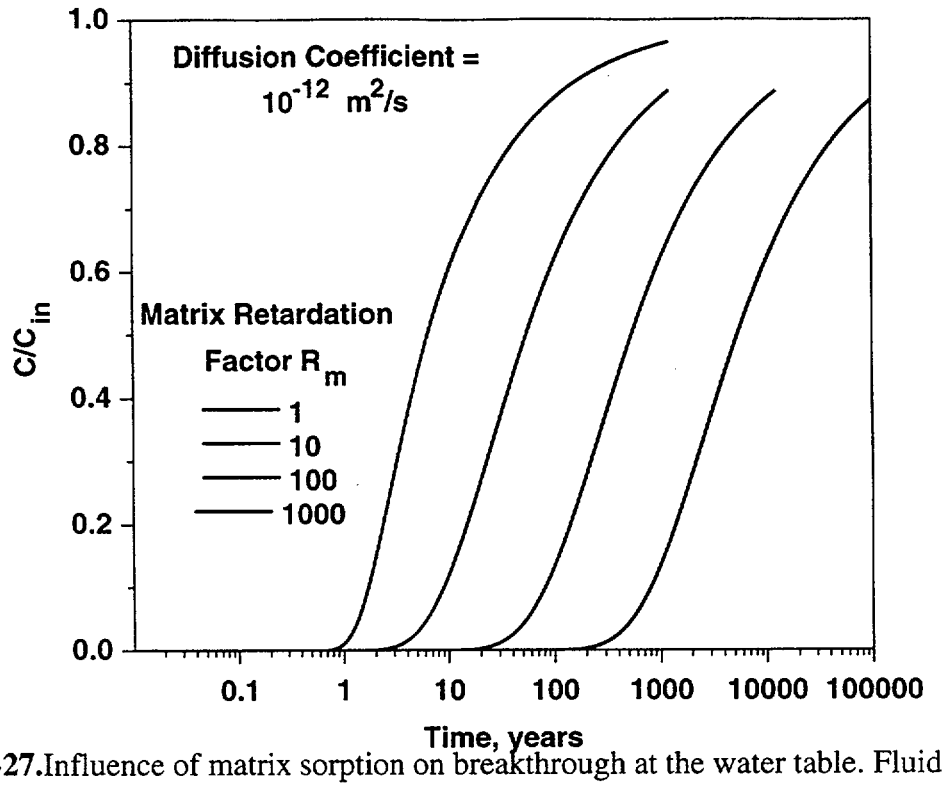

Figure 8-27. Influence of matrix sorption on breakthrough at the water table. Fluid travel time = 1 y. D_{mol} = 10^{-12} m²/s. No fracture sorption.

decreases with increasing K_c, so that sorption on colloids reduces significantly the travel times and apparent dispersion of the breakthrough curves (Figure 8-28). One way to assess the relative impact of colloid and matrix diffusion/sorption qualitatively is to compare the matrix retardation factor R_m to the term $1 + K_c$ in the denominator of Equation 8-13. If diffusion and strong sorption to the rock matrix is predicted to be important in the absence of colloid-facilitated transport, as is the case with plutonium when modeled as an aqueous radionuclide, then Equation 8-13 implies that colloid-facilitated transport will negate the benefits of matrix sorption as $1 + K_c$ approaches or exceeds $\sqrt{R_m}$. For plutonium, a K_d of 100 cc/g roughly corresponds to $R_m = 1000$, or $\sqrt{R_m} \approx 30$. For K_c values less than 1 (equal amounts of radionuclide on colloids and as an aqueous solute), the role of colloids in reducing matrix diffusion and sorption will be slight. Conversely, if 90% or more of the plutonium resides on the colloids ($K_c = 10$), the performance benefit of

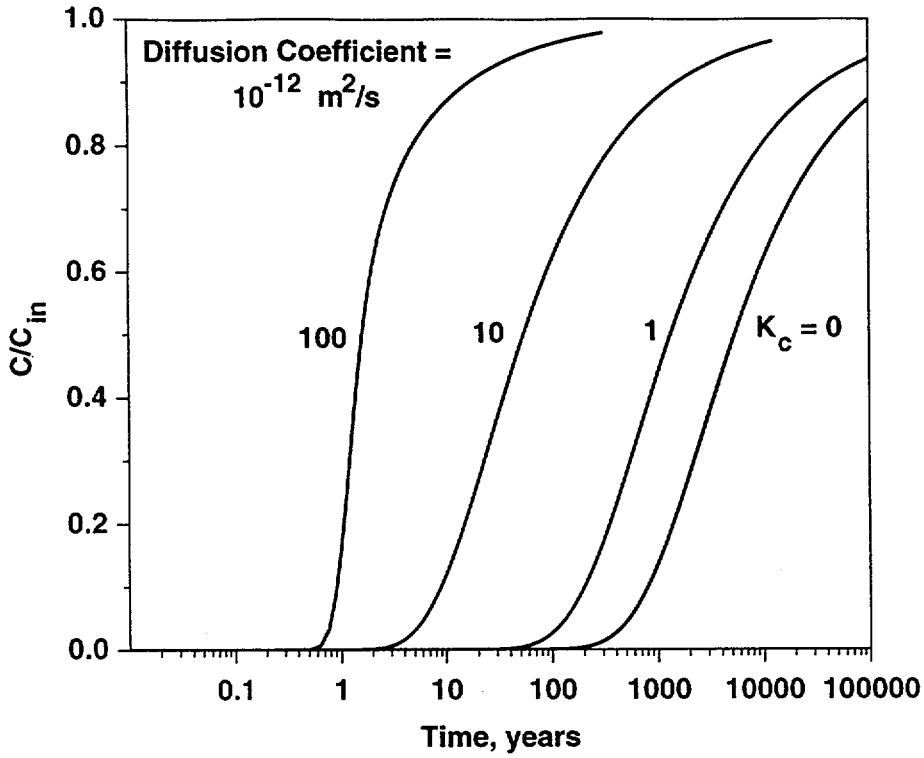

Figure 8-28. Influence of colloid-facilitated transport on breakthrough at the water table. Fluid travel time = 1 y. D_{mol} = 10^{-12} m²/s. R_m = 1000. No fracture sorption.

matrix diffusion and sorption will be largely negated, and fracture transport will resemble that of a solute with little or no access to the rock matrix.

This analysis has so far neglected any retardation of aqueous or colloidal contaminant in the fracture itself. Equation 8-12 shows the interplay between sorption of aqueous plutonium on fractures and sorption on colloids. When fracture retardation factors are large ($R_f \approx 100$ or more), the earliest arriving radionuclide is delayed somewhat relative to the case of no fracture sorption (Figure 8-29). Also, Figure 8-29 also shows the performance benefit of assuming retardation of the colloids during transport. The effect of increased R_c appears small for this simulation, but the nature of the model suggests that the benefit of delay in colloids is present no matter how high the value of K_c. In other words, filtration or attachment/detachment processes is the last transport "barrier" to mitigate the deleterious performance brought on by colloid-facilitated transport.

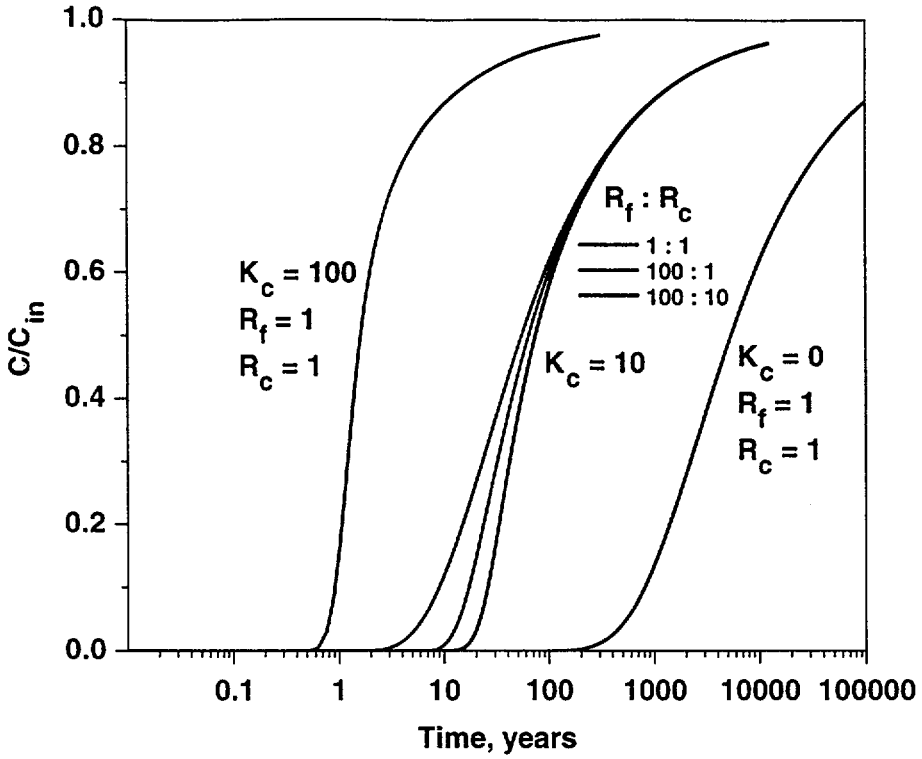

Figure 8-29. Influence of colloid-facilitated transport on breakthrough at the water table. Fluid travel time = 1 y. D_{mol} = 10^{-12} m^2/s. R_m = 1000. Varying fracture sorption, colloid attachment, colloid sorption.

8.10.3 Discussion of Colloid-Facilitated Transport Results

This section examines the potential role of colloids in facilitating transport of strongly sorbing radionuclides such as plutonium. Although the hydrologic and transport model assumptions are simplistic, the analysis places the relative importance of colloids and aqueous radionuclides in perspective by examining the case for which colloid-facilitated transport is deemed to be most problematic, namely fracture flow and transport. For this situation, we must still consider aqueous transport processes that serve to retard the movement of radionuclides, such as matrix diffusion and sorption on fractures and in the matrix. Not doing so will lead to poor predictions of repository performance due to the overly conservative assumption that colloids result in a direct, rapid migration to the water table. Although this may be the case for radionuclides that form stable radiocolloids, the influence of introduced colloids must consider the interaction between the colloids and aqueous radionuclide.

The importance of colloid-facilitated transport is discussed with respect to the movement of aqueous radionuclide through the fractured tuff, so that the primary results are presented in terms of possible degradation in repository performance from the "base case" of aqueous transport. Colloid-facilitated transport is shown to severely reduce travel times and apparent dispersion when the fraction of radionuclide residing on colloids approaches that present as an aqueous solute. Colloids reduce the diffusive loss of radionuclide to the rock matrix by preventing radionuclide from leaving the fracture via diffusion and sorption to the rock matrix. Furthermore, if sorption onto fractures is important, colloids reduce the effective retardation factor in a manner analogous to aqueous speciation effects in which nonsorbing complexes form at the expense of sorbing complexes. Conversely, fracture sorption can be considered a transport process that "competes with" colloid-facilitated transport if the colloid distribution parameter K_c is of order 1. Thus the key parameter needed to constrain this problem of colloid transport is K_c, a parameter controlled by the sorption coefficient of radionuclide and the amount of colloidal material present. The next step will be to update this study with estimated values of K_c based on field measurements of colloid concentrations and estimated or measured values of the sorption coefficient.

There are additional processes and proposed scenarios that are not directly handled with this model. One important scenario not discussed is the migration of plutonium radiocolloids, which are thought to be extremely stable in Yucca Mountain groundwater. This scenario can be handled by separating plutonium radiocolloids into their own category, one in which, in the absence of filtration, a radionuclide travels essentially at the fluid velocity in the fractures. The key parameter will then be the source concentration of radiocolloid. For both radiocolloids and pseudocolloids, a key uncertainty is the nature of the interaction of colloids with the rock, captured in the present model in the R_c term. It is perhaps too early to devote much effort to constrain R_c, given that the chemical interactions of radionuclides with colloids and the radiocolloid source term may be too small to degrade performance significantly. If future analyses uncover scenarios in

which performance is significantly impacted by colloids, then colloid filtration studies would be warranted.

Although the model is idealized, it can be used quite simply as a building block of a more sophisticated hydrologic model. We now present results of plutonium migration in the unsaturated zone that includes the influence of colloid-facilitated transport. The model developed here assumes fracture flow and transport for the fracture domain, with interaction with the surrounding matrix. In the matrix, the sorption coefficient of aqueous plutonium is assumed to be reduced by a factor of $1 + K_c$, and there is no filtration of colloids in the matrix even for advective transport through high-permeability units like the vitric Calico Hills unit. Thus the model is conservative in its assumptions on the migration of colloids through the unsaturated zone.

The form of the mathematical model is identical to the fracture transport sub-model employed by the particle tracking module of FEHM. Therefore, with literally no changes to the code, colloid-facilitated transport can be included. Of course, the underlying conceptual model assumptions must be acceptable (valid, or at least bounding) in order for this approach to be used. The main assumption that must be justified is reversible, linear interaction between radionuclide and colloids. Irreversible or kinetically limited sorption onto colloids (or the rock) would limit the applicability of this model, although this could perhaps be handled approximately through adjustment of K_c. The benefits of using the same code, model hydrostratigraphy, and hydrologic flow fields for colloid-facilitated and aqueous transport of radionuclides are great enough that further work to justify the model assumptions or to determine that the assumptions are bounding is advisable.

When 2- or 3-dimensional site-scale transport simulations are performed with the dual permeability model formulation, the predicted partitioning of flow between fractures and matrix is treated, rather than the overly conservative assumption of pervasive fracture flow directly to the water table. Since in some units matrix flow predominates, model parameters characterizing colloid transport through the rock matrix are required. Sensitivity analyses are likely to show that

if colloid-facilitated transport is important, filtration during transport through the matrix of the CHn would be a key barrier to the movement of colloids. In future studies we will investigate this issue using the UZ flow and transport model. If colloids are deemed to degrade performance under assumptions of minimal filtration, then additional work will be required. Ultimately, an unsaturated zone field transport test using particulate tracers, such as was done in the saturated zone at the C-Wells, could provide critical information on filtration. For TSPA-VA, we will be at the stage of being able to address these uncertainties in models; these uncertainties could be reduced with a field-scale transport test, with results available in time for the Licence Application.

Figure 8-30 shows the Green's function for plutonium transport to the water table for case

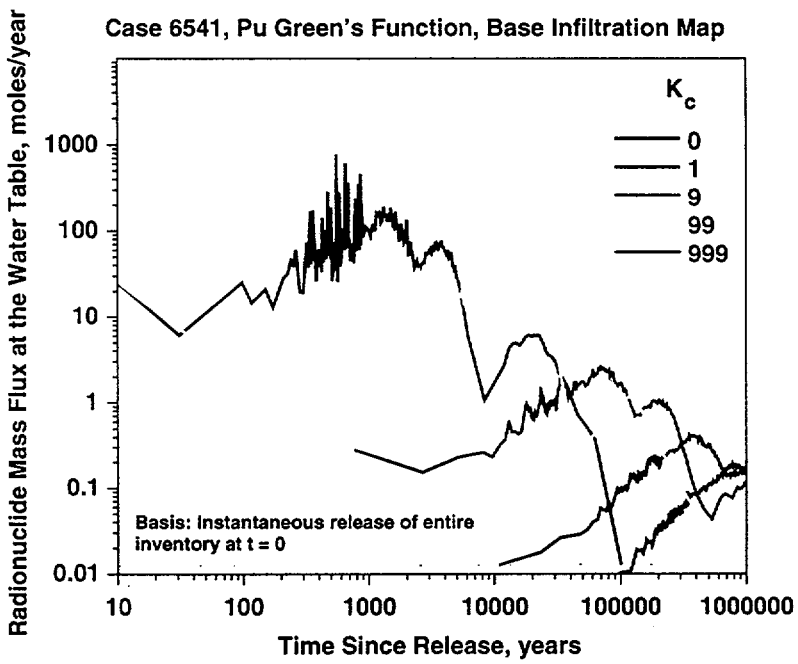

Figure 8-30. Green's function for Plutonium transport through the unsaturated zone for different values of K_c. Case 6541, base infiltration map, aqueous plutonium K_d = 100 cc/g, all units.

6541, base infiltration map. The impact of the colloidal plutonium partitioning coefficient K_c is dramatic, with very little radionuclide even reaching the water table for $K_c = 0$ (no colloid-

facilitation). For progressively higher values of K_c, the breakthroughs occur at earlier times, and at much higher mass flux values. The effect is equivalent to lowering the sorption coefficient from its assumed aqueous value of 100 cc/g to values of 1 or less. Clearly, if most of the plutonium present travels in colloidal form, the impact on performance is substantial. When more than half of the plutonium is aqueous ($K_c < 1$), the predicted migration potential of plutonium is small, and the impact on overall system performance will be minimal. The cumulative breakthrough curves for this case are shown in Figure 8-31, Although there is some tendency toward very short travel times

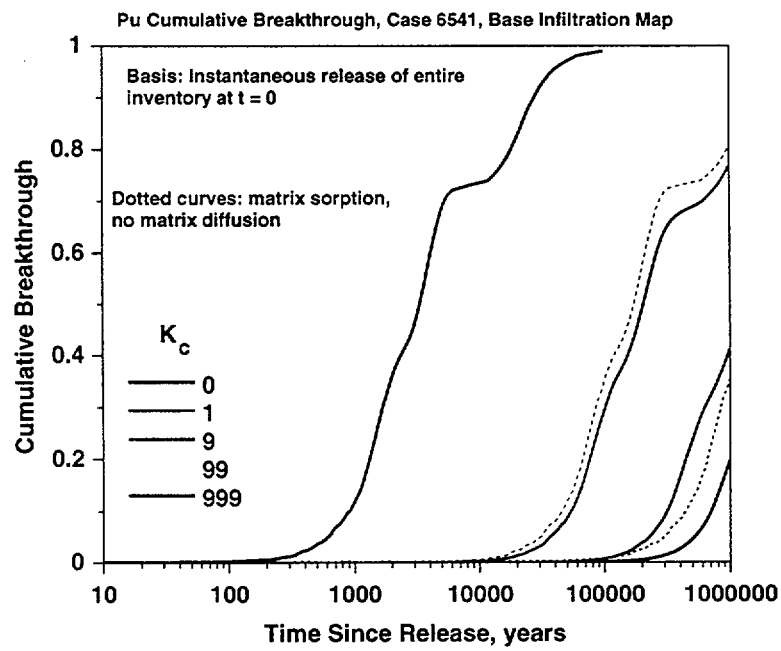

Figure 8-31. Cumulative breakthrough curves for plutonium transport through the unsaturated zone for different values of K_c. Case 6541, base infiltration map, aqueous plutonium K_d = 100 cc/g, all units. Dotted curves are simulations with no matrix diffusion.

in the Green's function (on the order of 1 year to the water table), the cumulative curves indicate that this is only a very small portion of the plutonium inventory. Also plotted in this figure are simulations in which the effective sorption coefficient for matrix flow and transport is reduced due to colloids, and the fractures are assumed to exhibit no matrix diffusion. The close agreement

between these curves and their equivalent curves with matrix diffusion illustrates that the primary effect of colloid-facilitated transport is in reducing the effective sorption coefficient in units exhibiting matrix flow and transport, such as the vitric Calico Hills units. It is these units that provides the migration barrier to plutonium migration, rather than the units exhibiting fracture-dominated flow. Therefore, a conservative assumption of no matrix diffusion in fractures can be made, since the key uncertainties in the transport results reside in matrix-flow units.

Studies are underway to evaluate the possibility of colloid-facilitated transport of plutonium, with respect to the physical and chemical parameters that are likely to influence the parameter K_c (Triay et al., 1997). The stability and mobility of colloids in groundwater depend most strongly on the chemical conditions and less so on the fluid temperature. Higher ionic strength fluid tends to reduce the stability of colloids, floculation being the principle mechanism reducing the concentration of colloids in solution. As quantitative results from these studies become available, they will be incorporated into the modeling effort through reduction in the uncertainty in K_c.

8.11 Transient Analyses

Considerations

Most flow and transport calculations of the unsaturated zone have assumed steady state flow conditions. There is good reason to believe that short-term transients at the time scale of individual precipitation events are damped in the nonwelded PTn unit, so that the flow field in the underlying units experience a much smoother input of flux than what occurs at the surface. This is examined in greater detail in Chapter 6 where sensitivity of this assumption to parameter sets and PTn thickness is evaluated. With regard to longer term transients such as climate-change induced variations in percolation flux, there has been considerably less effort devoted to determining the influence of such events and the validity of the steady state assumption for computing flow

distributions and for making transport predictions. The practical reasons for considering steady state flow as the starting point is that the computational burden of transient fluid flow and solute transport calculations is much greater. Furthermore, it could be argued that if a simpler steady state model does a good job at explaining the data at Yucca Mountain, it should be favored over a more complex, transient flow model.

Even if steady state models prove to be sufficient for explaining present-day conditions, there is a need to compute the impact of long-term transients on the ability of the unsaturated zone to impede the transport of radionuclides. There is ample evidence in the record of long-term variations in climate, which in turn led to changes in percolation rate and flow characteristics. Earlier we showed that percolation rate is a controlling parameter on radionuclide transport, so capturing the changes likely to occur in the future is important. Ultimately, the method to be used in TSPA-VA analyses to capture long-term transients is likely to be some form of a quasi-steady state model in which the flow is assumed to jump instantaneously from one steady state flow field to another. For this type of model to be valid, we must first show, through transient analyses, that the simplifying assumption does not significantly change the results. Furthermore, to provide added confidence, we must demonstrate an understanding of the time scales and magnitudes of the changes occurring in the transient simulation. In this section we present an analysis of flow and transport in a transient system is presented that should provide the basis for making the simplifying assumptions just discussed.

Transport Results

We start with an analysis of the magnitude and time scale of changes in the flow field in response to long-term changes in the percolation rate. The three cases considered are;

- Case 1: increase in percolation rate from the base map to the 3 x I case;
- Case 2: decrease in percolation rate from the base map to the I/3 case;
- Case 3: increase in percolation rate from the I/3 case to the base map.

Hydrologic parameter set 6412b was chosen to perform this analysis.

Figure 8-32 shows the water flow rate exiting the two-dimensional model domain versus

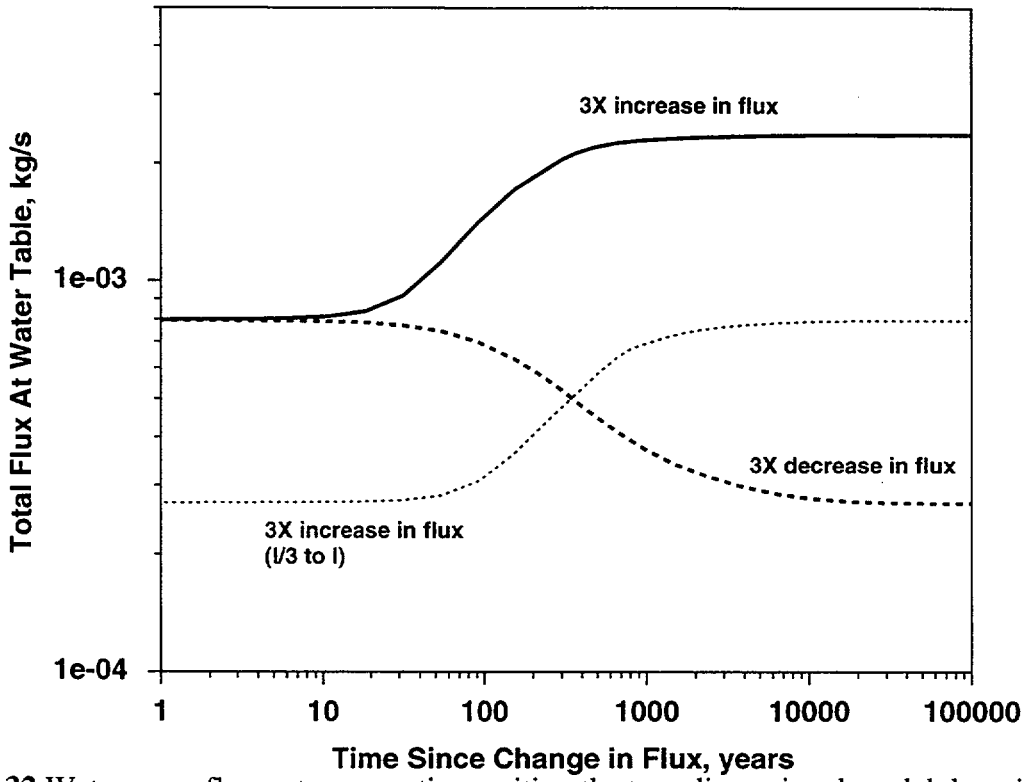

Figure 8-32. Water mass flow rate versus time exiting the two-dimensional model domain for the three transient cases considered. Changes in percolation rate occur at t = 0.

time for the three cases. The fluid flow response at the water table in response to a flux increase begins to be seen after only about 50 to 200 years, depending on the absolute level of the starting infiltration rate. this rapid response is due to flow through permeable fracture pathways which, because of their low storativity, take very little time to adjust to the flow rate increase. The ramp to the eventual water mass flow rate takes longer, from 500 to 5000 years. There is a very gradual rise to the plateau values at long times, probably due to the filling of matrix pores to their new, higher saturation values. The time scale for that process is governed by the fracture/matrix interaction parameter. The infiltration rate decrease scenario (Case 3) exhibits similar time scales as Case 2, the increase between these same two infiltration values.

The matrix saturations for four locations below the crest of Yucca Mountain are shown in Figures 8-33 (Paintbrush tuff non-welded unit ptn3 and vitric Prow Pass tuff ch4v) and 8-34

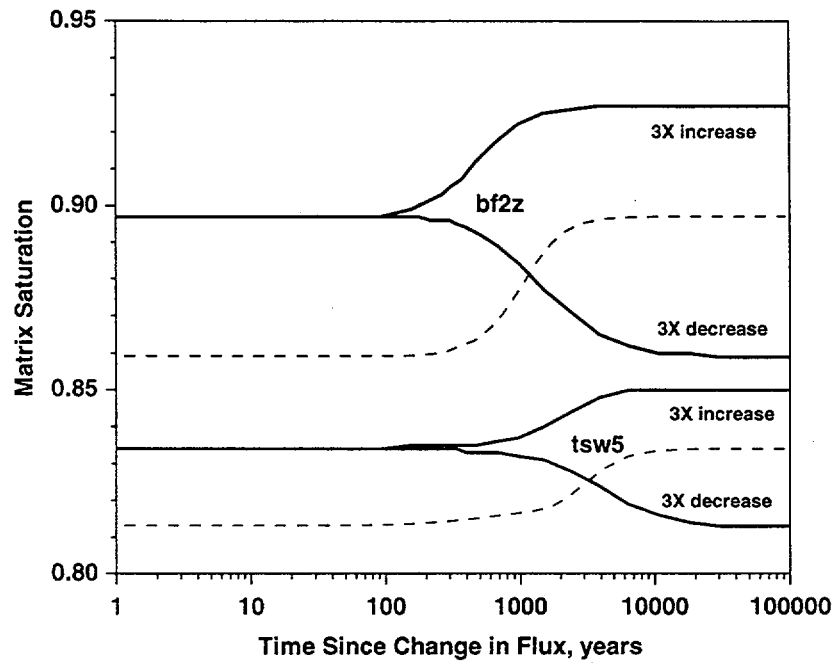

Figure 8-33. Matrix saturations in the ptn3 and ch4v units in response to the long-term transients in percolation flux. Black curves: ptn3; Blue curves: ch4v.

(Topopah Springs lower lithophysal tuff tsw5 and zeolitic Bullfrog tuff bf2z). Two effects are giving rise to the transient response. First, the infiltration changes are felt first in the units closest to the ground surface, as expected. However, in addition to the transient reaching a given location, the rate of imbibition or drainage between the fractures and matrix is a strong function of the fracture/matrix interaction term. In a welded unit such as tsw5, fluid transfer is slow because of the large reduction factor for the fracture/matrix interaction term. Therefore, rock in this unit responds to changes in percolation rate more slowly than the underlying ch4v and bf2z units. The time scale for the changes to take place in the matrix saturations of tsw5 are between 1 and 10 ky, depending on the infiltration scenario. This result provides evidence that if the climate last changed about 10 ky ago, the matrix saturations have probably had enough time to equilibrate to their new saturation

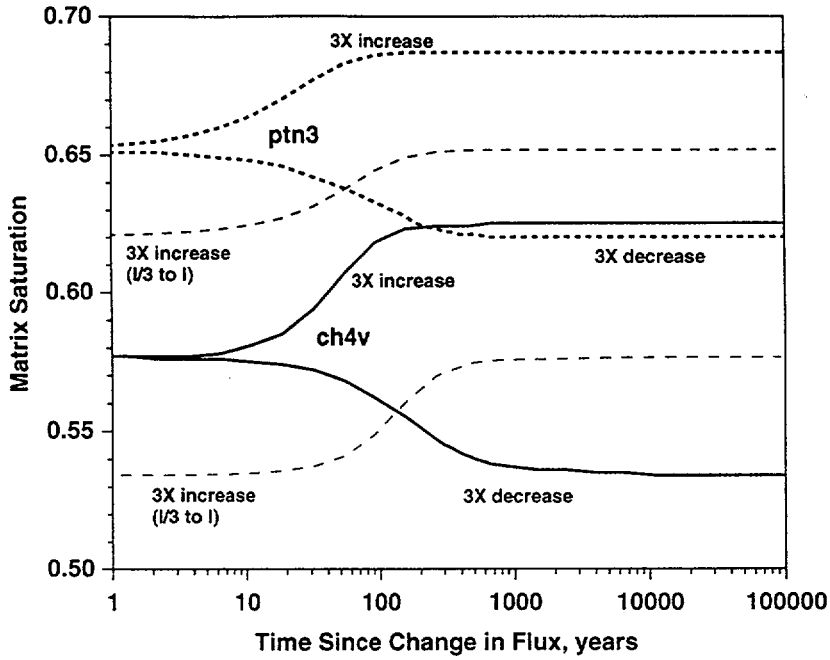

Figure 8-34. Matrix saturations in the tsw5 and bf2z units in response to the long-term transients in percolation flux. Black curves: bf2z; Red curves: tsw5.

values, rather than being reflective of a past climate scenario. For the welded units, this conclusion can be made with less confidence than for the nonwelded units, given the different time scales involved. Finally, note that the absolute magnitude of the changes in matrix saturation are quite small. This result shows that it is acceptable to use hydrologic parameter values from parameter estimation simulations at one infiltration rate for simulations at other fluxes within a factor of three of the original value without significantly affecting the fit to the matrix saturation data.

The nature of radionuclide transport during a long-term transient is examined with the following scenario. The radionuclide ^{237}Np is simulated with $K_d = 2$ cc/g in the zeolitic tuff, with a constant release rate from the NFE from 1 ky to 31 ky, after which it was assumed that the entire inventory was depleted. At 5 ky after waste emplacement, we assume a climate-change-driven increase in the infiltration rate from the base map to the 3 x I map, after which the flux remains constant for the duration of the simulation. Particle tracking simulations in fully transient mode

were used to simulate the radionuclide breakthrough curve at the water table. This result is shown in Figure 8-35, along with other simulation results used for comparison. The radionuclide mass

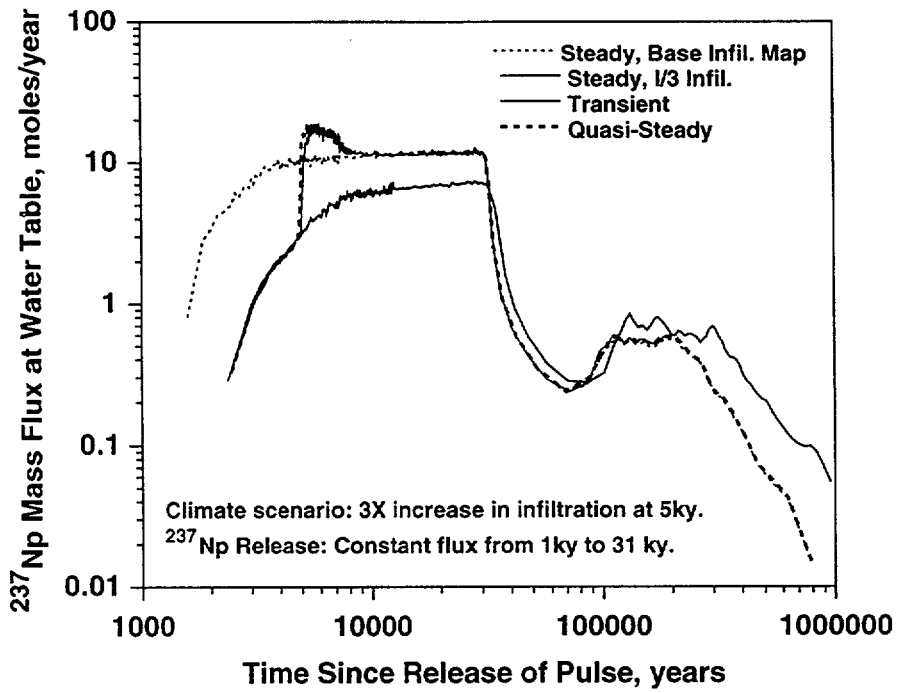

Figure 8-35. Breakthrough curve of ^{237}Np at the water table for the long-term transient scenario. Also shown are the steady state curves for the two infiltration rates, and the quasi-steady state method.

flux in the transient simulation tracks the base-map result exactly for the first 5 ky, rises sharply as the repository horizon flux responds to the higher infiltration, and then tracks the 3 x I result closely after about 10 ky. The rise in the flux value to levels greater than the upper steady state curve is the result of the radionuclide mass resident in the flowing water at the time the flow rate increase occurs. Since the release rate is assumed constant despite the change in flow rate for this simulation, the concentration within the fluid at the time of the flow rate change is greater than values thereafter. The higher infiltration rate carries this solution to the water table at a greater rate, thereby temporarily increasing the mass flux to levels greater than even the 3 x I steady state curve. Once the concentrated fluid is flushed from the unsaturated zone, the breakthrough curve reverts to the curve predicted for the higher infiltration rate case. Note that if a more realistic scenario of

infiltration-dependent release rate were simulated, the result presented here would probably be masked the increased radionuclide flux from the repository. Nevertheless, the simulation shows that except for the transient effect, the flux at the water table is closely approximated by the appropriate steady state curve (base case curve before 5 ky, 3 x I thereafter).

The final comparison in this transient analysis is to examine the quasi-steady state assumption, comparing it to the full transient simulation. As shown previously in Figure 8-35, the agreement is extremely good, even during the transient period. The differences are shown on an expanded scale in Figure 8-36. The quasi-steady state assumption was run assuming that the new,

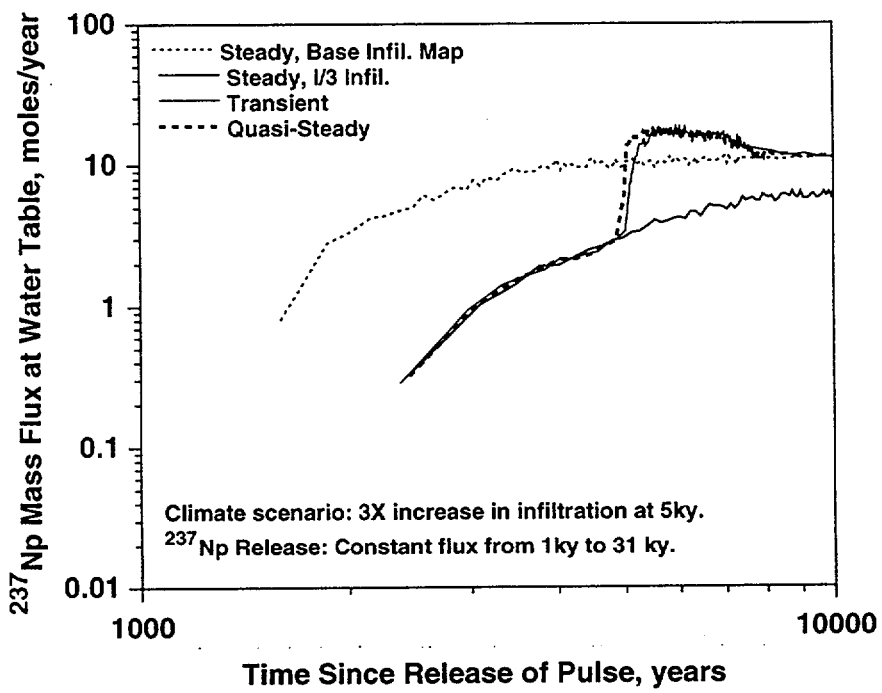

Figure 8-36. Breakthrough curve of ^{237}Np at the water table for the long-term transient scenario, shown on an expanded scale near the time of the change in percolation flux.

high-flux flow field took effect exactly at 5 ky. Instead of the finite time required to reach the steady state at the higher percolation flux, the influence of the transient appears immediately at the water table. However, we showed earlier that the flow field achieves a steady state at a higher infiltration rate within 100 to 1000 years, a very short time interval in a simulation of this scale.

This is the reason that the quasi-steady assumption works as well as it does. Although further testing with different parameter sets, radionuclides, and NFE release rates should be carried out, it appears that the quasi-steady state assumption is an excellent approximation to the full transient solution.

One other climate-related effect that must be considered is the possibility of a rise in the water table due to a future wetter climate. For the unsaturated zone model, the elevation of the water table is set as an imposed boundary condition, and thus is not a computed result. Estimates based on mineralogic studies and saturated zone modeling efforts have placed the water table as roughly 100 m above the present-day elevation in the past. In this model, we can easily assign the water table a higher elevation by specifying all nodes below a certain elevation as water table nodes. In a sensitivity study of water table elevation, we assume a water table elevation of 830 m, and perform the simulation with the base infiltration map and parameter set 6541. Figures 8-37 and

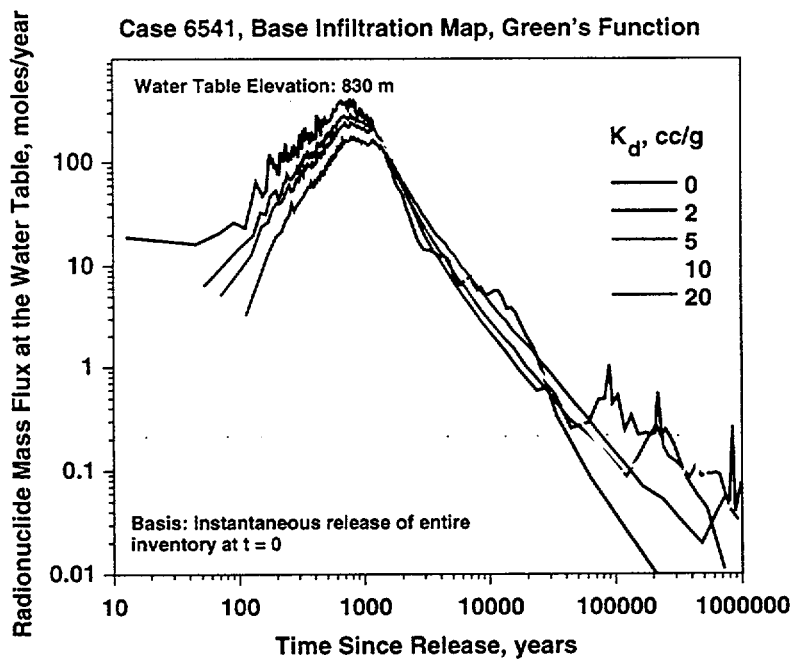

Figure 8-37. Green's function for transport of radionuclides in the two-dimensional site scale model. Property set 6541, base infiltration map, elevated water table.

8-38 are the resulting Green's function and cumulative residence time distribution curves for this system. Arrival times at the water table are somewhat higher for the elevated water table compared

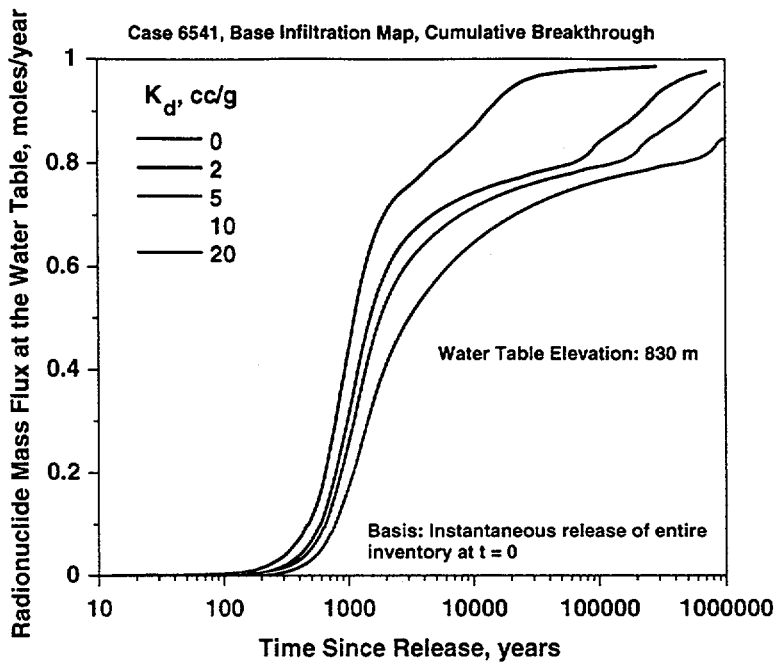

Figure 8-38. Cumulative residence time distributions for transport of radionuclides in the two-dimensional site scale model. Property set 6541, base infiltration map, elevated water table.

to the base case (Figures 8-2 and 8-3), as expected. The higher water table places more of the CHn and underlying units under the water table. This includes some of the zeolitic units that provide retardation of radionuclides. This effect, combined with the negative impact of higher percolation rate on unsaturated zone transport, makes the unsaturated zone perform considerably more poorly as a barrier under a future, wetter climate scenario.

8.12 Conclusions

In most of the two- and three-dimensional simulations presented in this study, steady state flow fields are generated using FEHM, and then radionuclide transport is computed for various transport parameters. The steady state assumption allows us to compute generic breakthrough curves in response to a pulse of radionuclide injected at time 0. This simulation provides the basis for computing, external to the FEHM simulation, the actual response to a realistic near field release

scenario. Numerical convolution is employed for this purpose. In this section we present the results of the generic response curves for a variety of flow and transport parameter sets and scenarios.

Multiple parameter sets from the LBNL site-scale flow model and variations on the USGS infiltration map are used in the simulation of radionuclides from the potential repository to the water table. For most of these parameter sets, radionuclides tend to bypass the zeolites of the Calico Hills via fracture transport when base-case infiltration conditions are simulated. When the infiltration rate is scaled by 1/3, significant fracture flow in the zeolites is still simulated with most parameter sets. A modification increasing CHn zeolite matrix permeabilities by a factor of 5 leads to substantially greater matrix flow and, hence, retardation of sorbing radionuclides. This process leads to dramatic improvement in the performance of the unsaturated zone. These studies demonstrate the overriding importance of proper characterization of the zeolitic units for performance assessment. Presently, there is significant uncertainty in the characteristics of these units due to data limitations. Enhanced characterization efforts, including the planned field test at Busted Butte, would reduce the uncertainty in these calculations and lead to a better understanding of the true nature of the hydrologic and transport behavior of the CHn.

Colloid-facilitated transport of otherwise immobile radionuclides like Plutonium is also addressed in this chapter. As very little data are currently available for Plutonium sorption onto colloids, we present a sensitivity analysis of the significant processes to mobility. In the absence of sorption onto the mobile colloids, Plutonium migration is limited due to large sorption coefficients. Assuming reversible sorption, when partitioning onto colloids approaches 99% or more, Plutonium mobility becomes potentially important to performance. If sorption of Plutonium onto colloids is irreversible, any colloid transport would directly affect performance assessment.

Long-time transients capturing climate change related phenomena are also simulated in this chapter. The results show that the flux of radionuclide at the water table under transient conditions is closely approximated by a quasi-steady state model. Thus multiple steady-state simulations can be used to predict the effects of wetter or drier future climates on radionuclide flux at the water

table. The effect of potential water table rise due to wetter, future climates is also considered. The combined effect of a shorter travel distance to the water table and high fluxes under a wetter climate scenario yield prediction of poorer unsaturated zone performance than for the present climate conditions.

Chapter 9 - Three-Dimensional Radionuclide Transport

9.1 Abstract

The two-dimensional approach presented in the last chapter is extended to the three-dimensional site-scale model of radionuclide transport. With the full three-dimensional transport model, implications of lateral flow, spatial variability of flux, and underlying strata thickness are examined. Compared to the two-dimensional model, greater spreading in the travel time distribution curve is simulated due to the additional flow paths sampling a greater range of property variability that occur in three dimensions. This variability leads to cumulative breakthrough curves at the water table spanning the range from 10 years to 10,000 years. Regarding spatial variability in releases, radionuclides released from the northern end of the repository are more likely to experience rapid transport to the water table than radionuclides released in the southern portion of the potential repository. As in the two-dimensional simulations, slightly higher matrix permeability in the zeolites leads to substantially greater retardation of radionuclides. The diffusion coefficient influences the breakthrough curves simulated with the three-dimensional model, especially for the portion of the inventory with the shortest travel times. By contrast, the dispersion coefficient is shown to have very little impact on the unsaturated zone transport.

9.2 Software and Data QA Status

The FEHM code is used to perform all flow and transport calculations in this report. The code is qualified in accordance with Los Alamos quality assurance requirements and is documented in (Zyvoloski et al., 1992, 1995a, 1995b). The QA status of the data used in this report is shown in Table 9-1.

Table 9-1. QA Status of Data used in this Chapter			
REFERENCE	Q Status	DTN	COMMENT
Bodvarsson et. al., 1997 "The Site-Scale Unsaturated Zone model of Yucca Mountain, Nevada, For the Viability Assessment, LBL Technical Report LBNL-40378	Q	LB970601233129.001	No DTN assigned. Hydrologic property sets computed in this report are used throughout the present study.
Flint et. al., 1996, Conceptual and numerical model of infiltration for the Yucca Mountain Area, Nevada", USGS WRIR MOL 19970409.0087	Q	GS960908312211.003/ NA	USGS DTN 3GUI623M
Triay et. al., 1996a, "Summary and Synthesis Report on Radionuclide Retardation for the Yucca Mountain Site Characterization Project, Los Alamos National Laboratory YMP Milestone Report 3784	Q	LAIT831341AQ96.001	

9.3 Introduction

In the previous chapter, we presented transport results on a representative two-dimensional, East-West cross section model. Many of the uncertainties of the flow and transport model were investigated, including different hydrologic parameter sets, infiltration rates, and transport parameters. A great number of processes and parameters can be examined quickly in two dimensions without compromising the validity of the result through dimensionality reduction. However, there are some issues that can only be examined thoroughly in three dimensions. These include any heterogeneities that vary in the direction not modeled in the two-dimensional simulation (the North-South direction in the present study), variations in hydrologic layer thicknesses or mineralogic thicknesses, and spatial variability in infiltration. In addition, lateral flow effects can only really be studied thoroughly in three dimensions.

In this chapter we use the three-dimensional model to investigate these and other issues. In addition, we present results of variations in transport properties not examined explicitly in the two-

dimensional results, such as diffusion and dispersion parameters. The process for incorporating the three-dimensional geologic framework model into a numerical grid was described in Chapter 3. As with the two-dimensional simulations, zeolite abundance from the min-pet model was mapped onto the three-dimensional numerical grid using a cut-off value approach (described in Chapter 2). Locations with zeolite abundance greater than 10% are given zeolite properties. At other locations in the model, the unaltered properties of the geologic units are used to populate the model with property values that are homogeneous within a layer.

9.4 Radionuclide Simulations, Base Infiltration Rate

In this set of simulations, we compute the radionuclide transport functions for the base case hydrologic property set, Case 6541 (see Table 5-3), with the base-case infiltration map from Flint et al. (1996) which is shown in Figure 6-7. For sorption, we examine the behavior assuming sorption only in zeolitic rocks, where the K_d value is varied from 0 (no sorption anywhere in the model) to 20 cc/g. As discussed earlier, this series of simulations covers the nonsorbing radionuclides (^{99}Tc, ^{129}I, ^{14}C, and ^{36}Cl) and sorbing radionuclides ^{237}Np and the various isotopes of uranium. The Green's function, or response of the system to a pulse of radionuclide released instantaneously at time 0, is used to characterize transport through the three-dimensional model to the water table. Figure 9-1 shows the results of the simulations for this case. With the current hydrologic property set, there is a tendency for some fraction of the inventory to travel rapidly through fractures to the water table. This fracture transport is through the zeolitic rocks where, for the current property sets, the matrix permeability is insufficient to transmit the flow. There is a hint of a bimodal distribution of transit times in the $K_d = 0$ curve, but, in general, the overall response exhibits a wide range of residence times without much tendency of clustering into distinct arrival times. This behavior is due to the wide range of hydrogeologic conditions present across the repository. The three-dimensional model samples the entire range of this variability, rather than

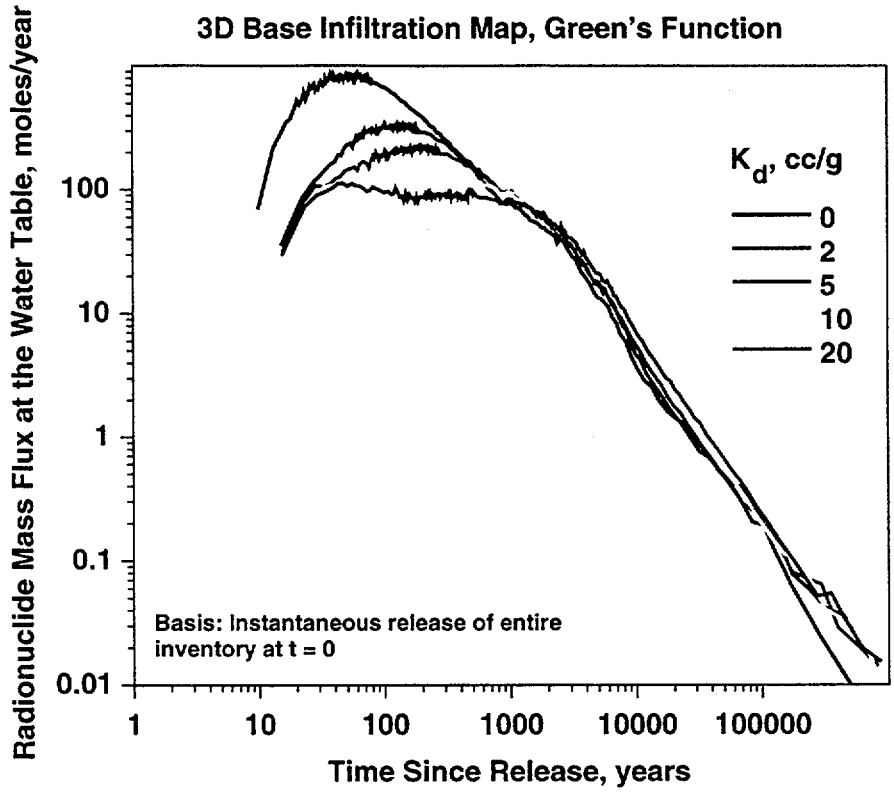

Figure 9-1. Green's function for radionuclide transport in the three-dimensional site scale model. Property set 6541, base infiltration map.

biasing the results through the selection of a particular cross section. The spatial variability issue is addressed further in a moment.

As sorption coefficients in the zeolitic tuffs are increased, retardation reduces the amount of early arriving radionuclide through the matrix diffusion/sorption process. In addition, radionuclide percolating through the zeolite matrix is delayed. The result is a reduction in peak concentration in the Green's function, and a shift to longer residence times of a larger portion of the inventory. This effect is seen more readily in the integrated cumulative breakthrough curves in Figure 9-2. The portion of the inventory with transit times less than 100 years is small, and the distribution of times for different fractions of the radionuclide inventory to reach the water table spans a range of 10 years to greater than 10 ky. This variability is greater than for the two-dimensional simulations presented previously, and is an essential feature that must be captured in

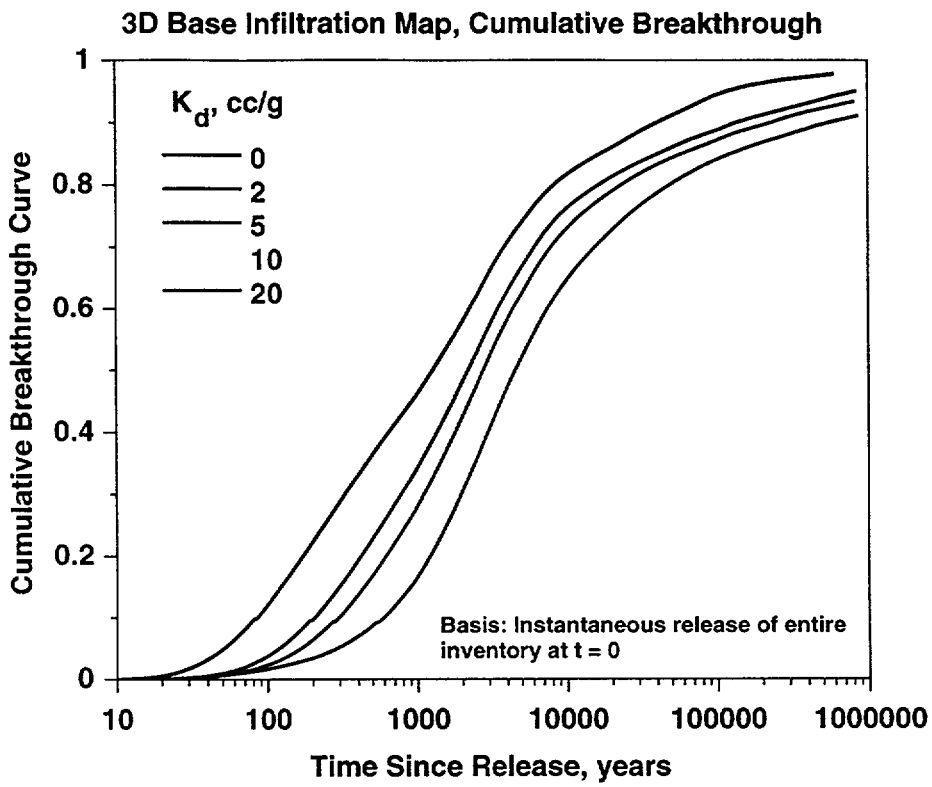

Figure 9-2. Cumulative breakthrough curves for radionuclide transport in the three-dimensional site scale model. Property set 6541, base infiltration map.

any total system performance assessment. Sorption onto zeolites shifts the curves to longer residence times, which means that for a given time such as a hypothetical 10 ky compliance period, less of the radionuclide is predicted to reach the water table. Thus the benefit of sorption onto zeolites is present in the three-dimensional model to perhaps a greater degree than for the two-dimensional simulations.

9.5 Radionuclide Simulations, I/3 Infiltration Map

In this section we examine the influence of infiltration rate on the performance of the unsaturated zone transport system. Property set 6541 is used as in the previous section, but with an infiltration map in which the flux is reduced by a factor of three from the base map at all locations. The resulting Green's function is shown in Figure 9-3, and the cumulative breakthrough curves are

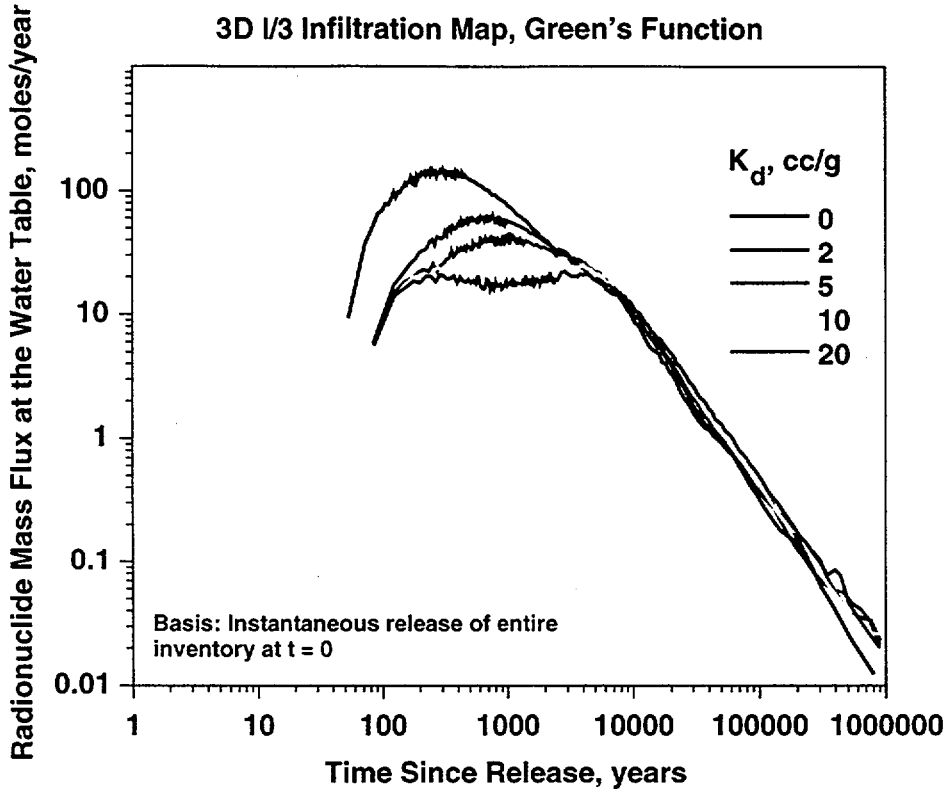

Figure 9-3. Green's function for radionuclide transport in the three-dimensional site scale model. Property set 6541, I/3 infiltration map.

presented in Figure 9-4. Relative to the base infiltration map, transport times and peak values for the Green's function curves differ by more than the factor of three that would be expected in this comparison, all else being equal. Lower infiltration rates allow a greater fraction of the radionuclide inventory to travel through the zeolitic tuffs, thereby increasing the travel times. This is the case even for nonsorbing radionuclides such as ^{99}Tc. The cumulative breakthrough curves exhibit a wide range of transit times as before, but the values are from several hundred to tens of thousands of years for nonsorbing radionuclides, and from one thousand to one hundred thousand years for radionuclides that sorb to the zeolitic tuffs. Clearly, the uncertainty in infiltration rate must be captured in total-system performance analyses or else the full range of possible behaviors will not be captured in the unsaturated zone model.

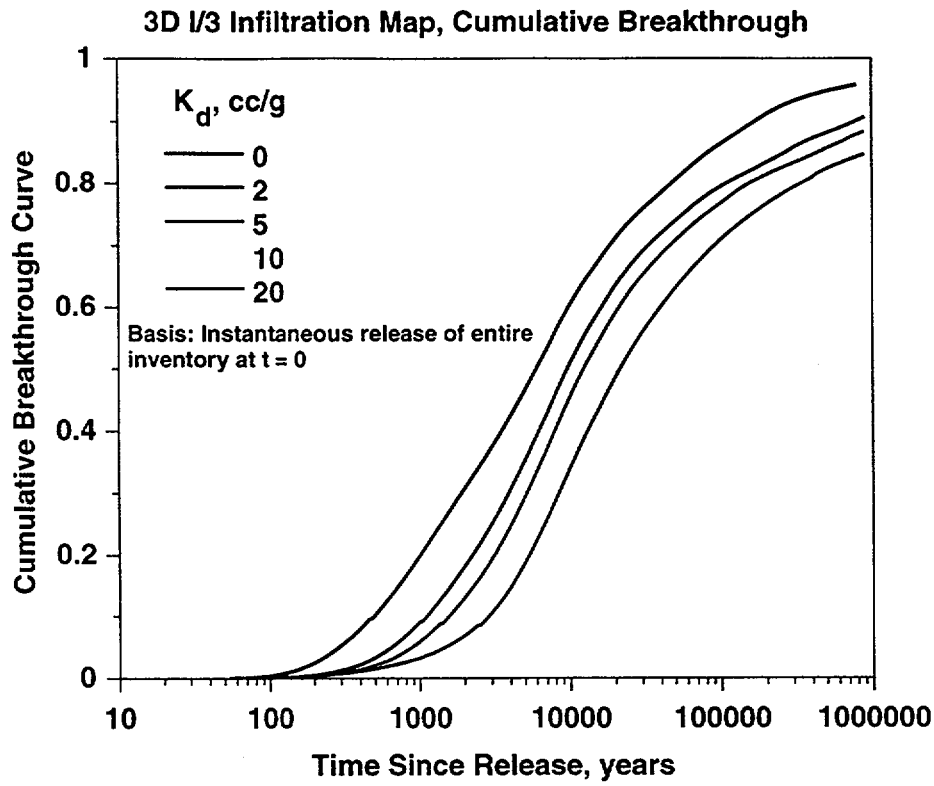

Figure 9-4. Cumulative breakthrough curves for radionuclide transport in the three-dimensional site scale model. Property set 6541, I/3 infiltration map.

9.6 Large Scale Spatial Variability in Radionuclide Transport

Variability across the repository horizon in the stratigraphic thicknesses, mineralogic abundances, and infiltration rates, as well as possible lateral diversion effects, could all play a role in the overall behavior of the unsaturated zone. One way to further understand the integrated transport results just presented is to examine the difference in travel time distributions as a function of position in the repository. To do this, we break the nodes representing the repository into five patches of nodes, each section representing approximately a rectangle comprising one fifth of the repository. The divisions were made from north to south to examine variability with respect the northing location of the release. One fifth of the total radionuclide inventory is released from each

of these patches, and the individual response curve for each patch is recorded. For all simulations presented in this analysis, the $K_d = 2$ cc/g case is used for the analysis.

Figure 9-5 shows the Green's function for each of the five individual sections of the

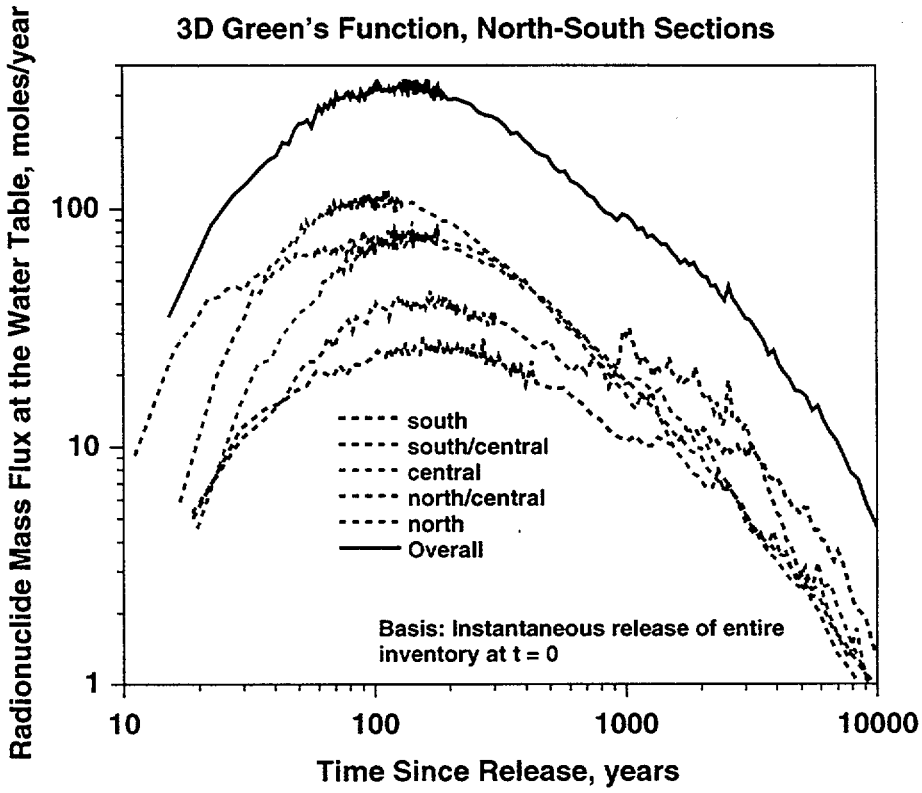

Figure 9-5. Green's function for radionuclide transport from five subsections of the repository in the three-dimensional site scale model. Property set 6541, base infiltration map.

repository along with the total integrated curve. Figure 9-6 shows the cumulative breakthrough curves for these same simulations. Radionuclide released in the northern end of the repository tends to have a greater tendency for rapid transport to the water table. The southern release points, by contrast, exhibit greater matrix flow and transport and a greater tendency toward longer residence times. We attribute this behavior to a more sporadic distribution of zeolites below the southern section of the repository. With the current property values, zeolites are effectively barriers to flow and transport, so that radionuclides travel through fractures in regions of high zeolitic alteration, such as areas in the north sections below the repository. We must point out, however,

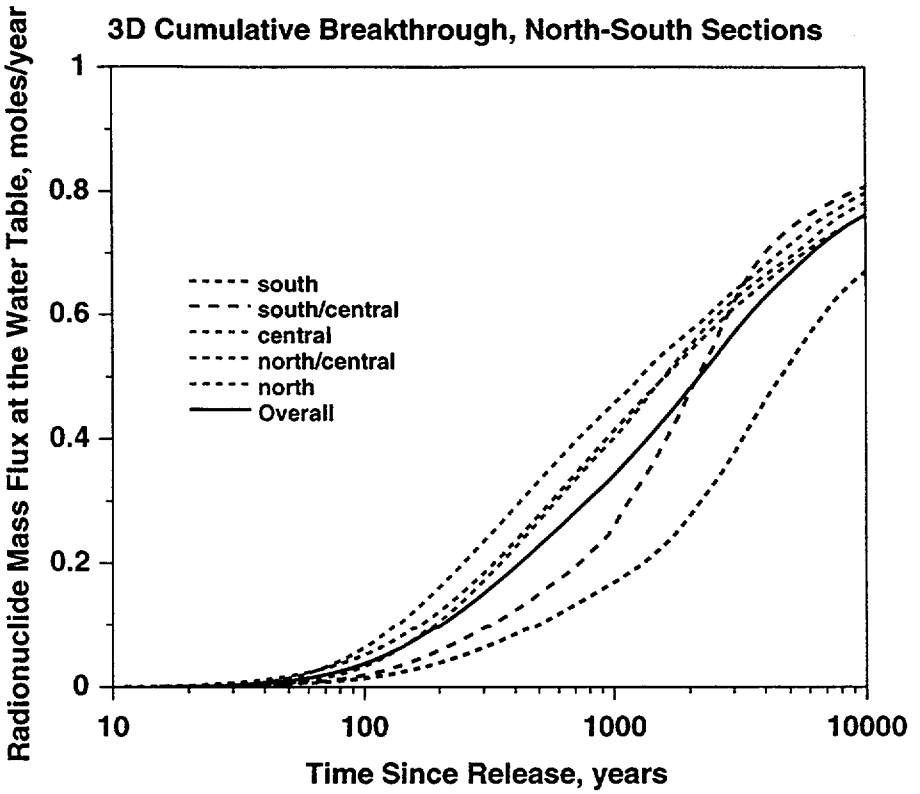

Figure 9-6. Cumulative breakthrough curves for radionuclide transport from five subsections of the repository in the three-dimensional site scale model. Property set 6541, base infiltration map.

that if the hydrologic property values of zeolites had been set somewhat higher, and matrix flow and transport through zeolites had occurred to a greater degree, this situation would have been reversed, i.e., zeolites would be a benefit to performance rather than a detriment, and releases from the northern end of the repository would have the longer residence times. This analysis points out the critical importance in characterizing the hydrologic properties of units with zeolitic alteration. A similar pattern emerges for the I/3 case, as shown in Figures 9-7 and 9-8. The tendency for rapid transport to the water table is decreased at the lower infiltration rates, but the general pattern of more rapid transport times for northern release points is still present.

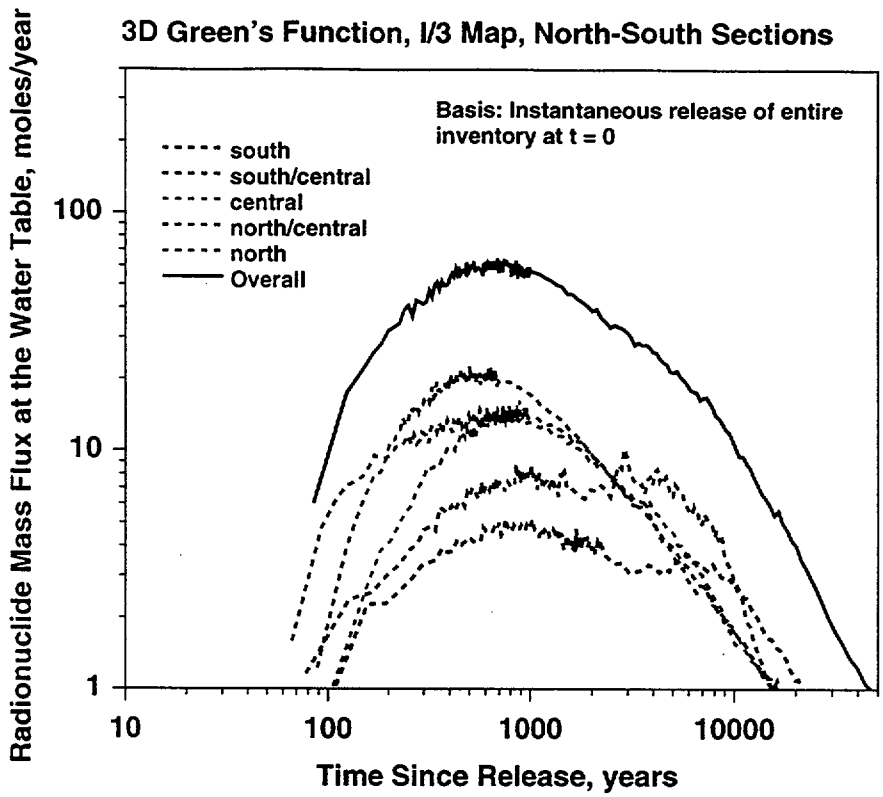

Figure 9-7. Green's function for radionuclide transport from five subsections of the repository in the three-dimensional site scale model. Property set 6541, I/3 infiltration map.

9.7 Transport parameter sensitivity studies

Earlier in this chapter, the influence of hydrologic parameter value uncertainty and the influence of sorption coefficient in the zeolitic tuffs was discussed. For each case, we assumed a diffusion coefficient in the matrix diffusion model of 1×10^{-11} m^2/s, and no dispersivity. In this section we examine the importance of transport properties not yet examined, namely the matrix diffusion coefficient and dispersivity. We perform these calculations using the three-dimensional model because these processes, in a sense, "compete with" large-scale dispersion processes to influence the overall breakthrough curves. Therefore, the most accurate information of the importance of these parameters on system performance is gained by running the three-dimensional model, where large scale heterogeneities such as those discussed earlier are captured most directly. In all cases, we use the base infiltration map to perform this sensitivity study.

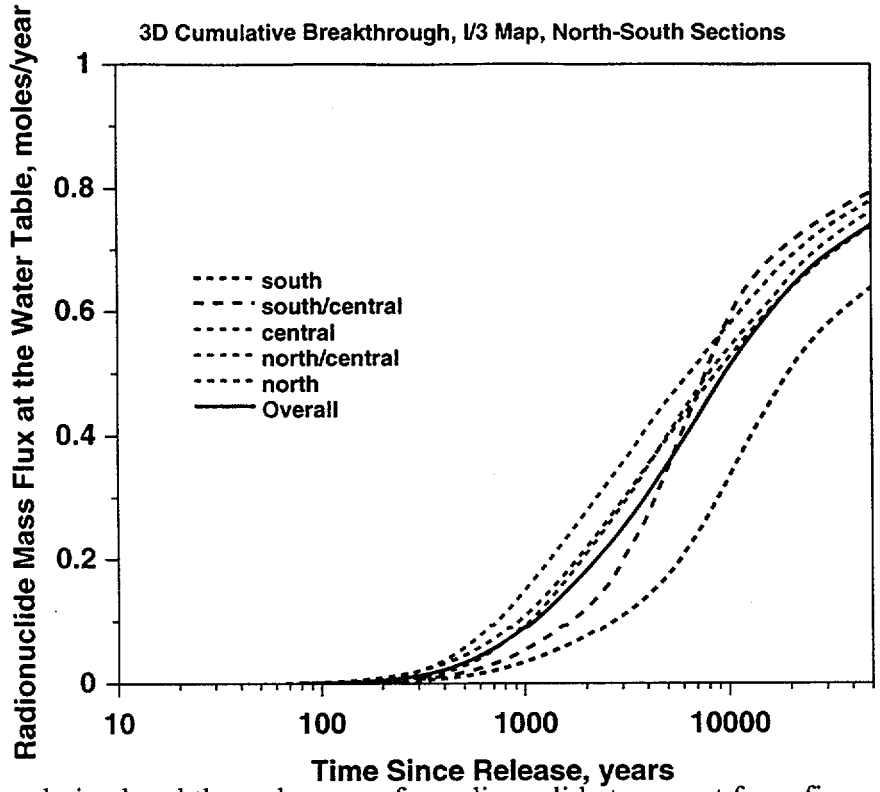

Figure 9-8. Cumulative breakthrough curves for radionuclide transport from five subsections of the repository in the three-dimensional site scale model. Property set 6541, I/3 infiltration map.

To examine the influence of the matrix diffusion coefficient, we performed simulations both for conservative radionuclides and the zeolite $K_d = 2$ cc/g case, a typical value for ^{237}Np. Figure 9-9 shows the results for conservative radionuclide breakthrough (Green's function) as a function of diffusion coefficient, and Figure 9-10 shows the cumulative breakthrough curves for the same simulations. The impact of the diffusion coefficient on the early arriving radionuclides is dramatic. This is due to the fact that this portion of the inventory is predicted to travel rapidly to the water table through fractures throughout the entire unsaturated zone. Under these circumstances, matrix diffusion is the only retardation process that delays the arrival times significantly. The range of values from 10^{-12} to 10^{-10} m^2/s spans the range of measured values for solutes diffusing through the saturated matrix. This is a close approximation in the zeolitic tuffs, which typically exhibit saturations very close to one. The cumulative breakthrough curves indicate

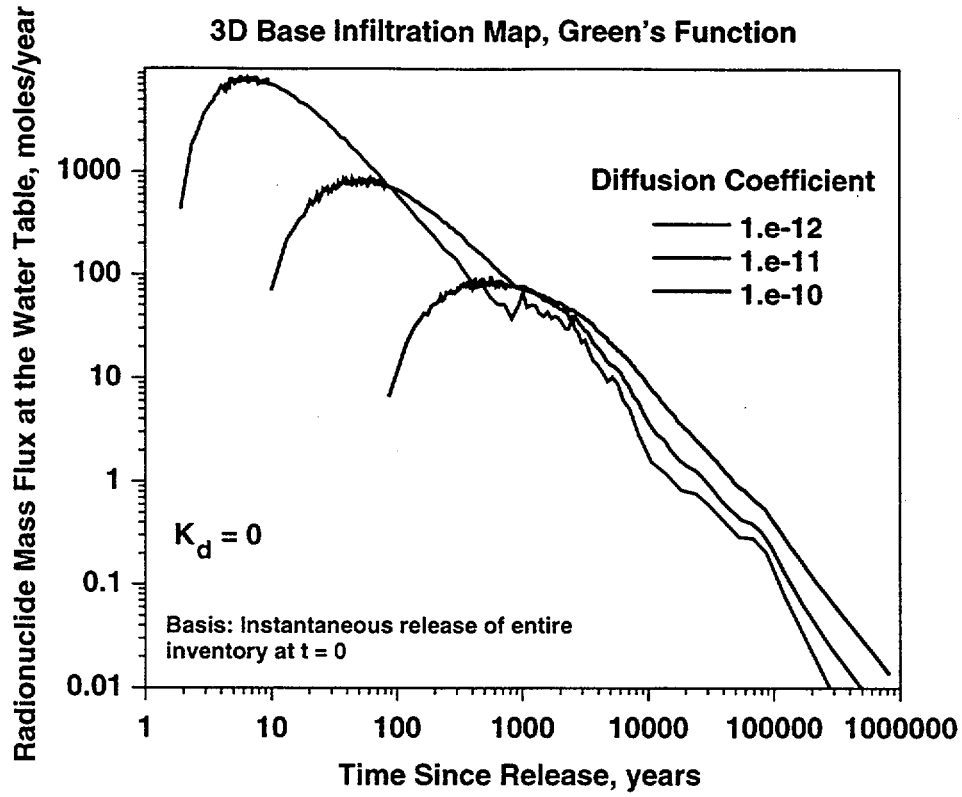

Figure 9-9. Green's function for radionuclide transport in the three-dimensional site scale model. Property set 6541, base infiltration map, no sorption, different diffusion coefficients.

that, without matrix diffusion, roughly 70% of the transport pathways have residence times of less than 10 years in the absence of matrix diffusion effects. This percentage seems large, and may be due to the current parameter sets, which simply do not allow significant fluid flow through the zeolite matrix.

Although the importance of the matrix diffusion concept in the unsaturated zone seems obvious from these results, recall that these results are for the instantaneous release scenario, and must be convoluted with an actual NFE source term to compute the arrival of radionuclides in an actual transport prediction. In Chapter 10, we show that radionuclide mass with extremely early arrivals at the water table, though counter to the notion of the unsaturated zone as a barrier to radionuclide migration, do not necessarily result in poorer overall system performance than a case with travel times on the order of 1000 years. For example, the 10^{-11} m^2/s diffusion rate curve in

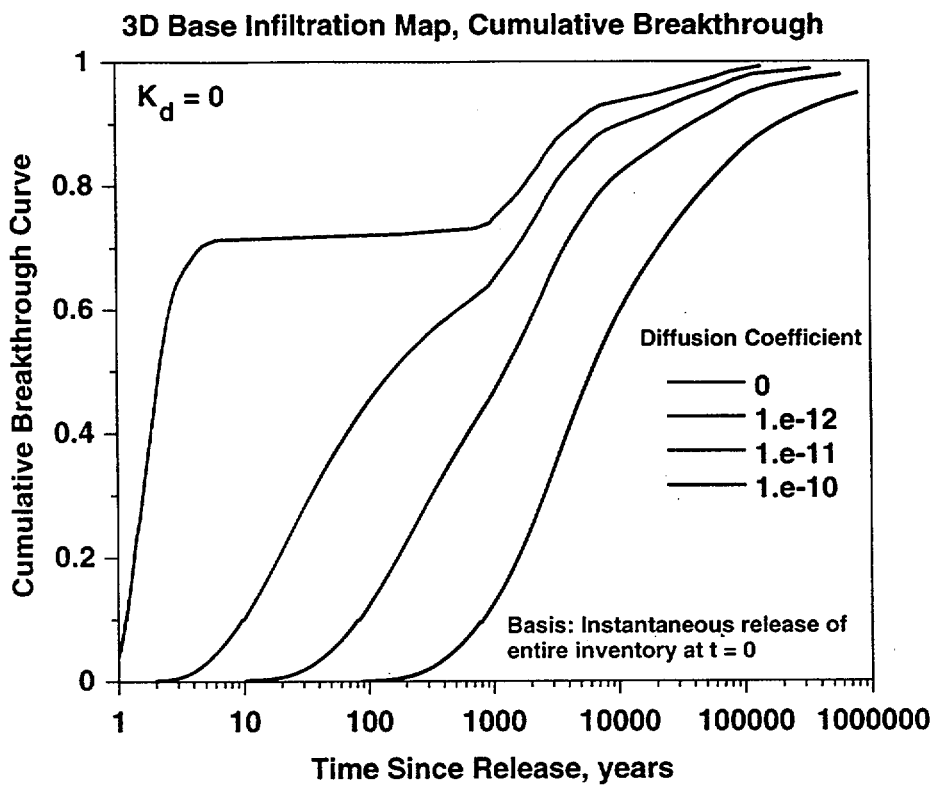

Figure 9-10. Cumulative breakthrough curves for radionuclide transport in the three-dimensional site scale model. Property set 6541, base infiltration map, no sorption, different diffusion coefficients.

Figure 9-10 still transmits about half the radionuclide inventory to the water table within a few thousand years. Under a 10 ky performance criterion, this system would probably not perform significantly more poorly than the case with no diffusion, the difference being primarily in the arrival times at the saturated zone, rather than in the peak concentration at the accessible environment. Nonetheless, at high enough values of diffusion coefficient, significant retardation occurs, and should be captured in models of unsaturated zone performance.

When matrix diffusion is coupled to sorption in the matrix, the impact of the diffusion coefficient is greater. Figure 9-11 shows the Green's function calculation for different diffusion coefficients for the $K_d = 2$ cc/g case, and Figure 9-12 plots the simulations for the cumulative breakthrough curves. Without matrix diffusion, the early arriving portion of the inventory cannot

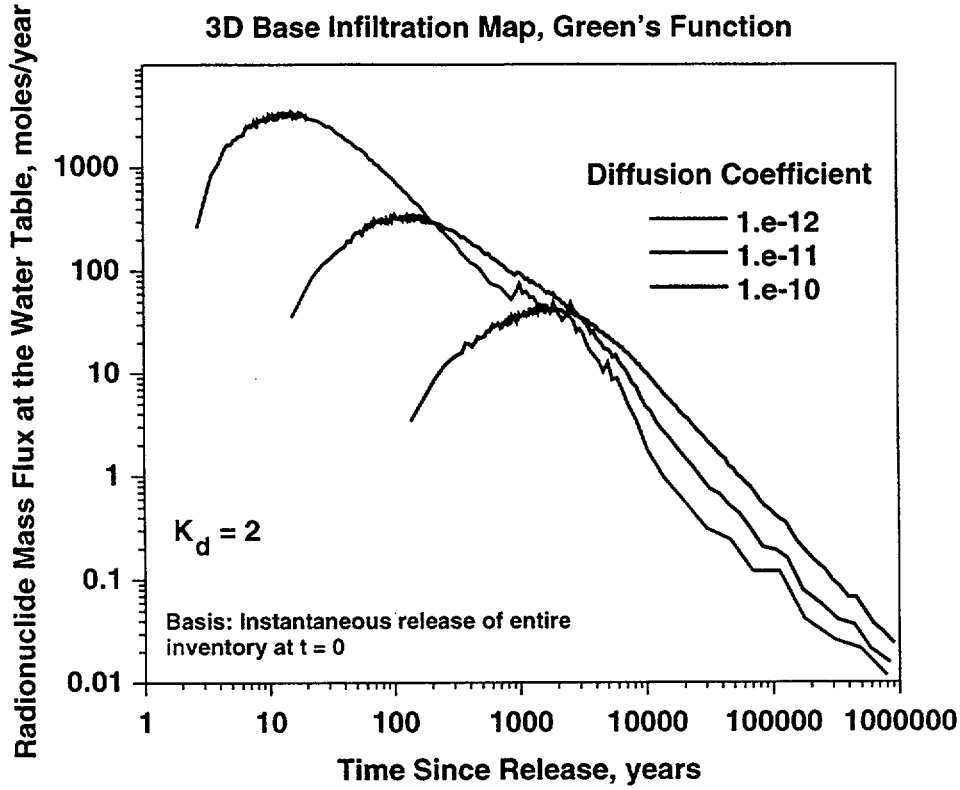

Figure 9-11. Green's function for radionuclide transport in the three-dimensional site scale model. Property set 6541, base infiltration map, zeolite K_d = 2 cc/g, different diffusion coefficients.

contact the zeolite matrix, and the breakthrough is virtually identical to that of the conservative radionuclide case presented earlier. For moderate amounts of matrix diffusion, the combined effect of matrix diffusion and sorption delays the arrivals even more than for the $K_d = 0$ case. Thus one of the most important aspects of matrix diffusion is that the process allows contact of radionuclides with the sorptive minerals that would otherwise be bypassed through fractures.

As mentioned above, all calculations presented so far have assumed no hydrodynamic dispersion of radionuclides. In Figure 9-13, we plot the Green's function curves for a conservative radionuclide for different values of the dispersivity. This dispersivity is a local hydrodynamic parameter that captures all dispersive processes occurring at scales smaller than the grid cell size. As indicated in Figure 9-13, small scale dispersion has very little effect on the overall response of

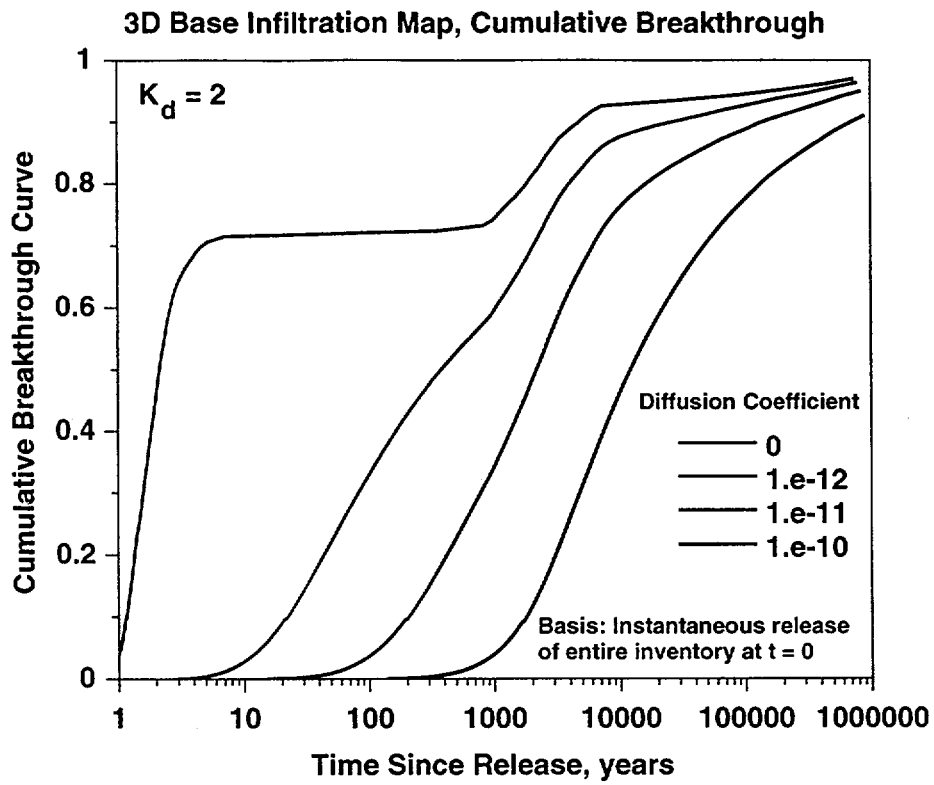

Figure 9-12. Cumulative breakthrough curves for radionuclide transport in the three-dimensional site scale model. Property set 6541, base infiltration map, zeolite $K_d = 2$ cc/g, different diffusion coefficients.

the unsaturated zone. The only significant differences occur at early times, where dispersion results in somewhat earlier (and later) arrivals due to spreading of radionuclide through dispersion in the fracture domain. The differences are small, and thus not likely to have much impact on the overall performance of the unsaturated zone. Large scale processes and variability in thicknesses of units and spatial variability of infiltration rate have much more significance as processes that spread the arrival time distribution at the water table.

9.8 Conclusions

In this chapter, the two-dimensional approach presented in the last chapter is extended to the three-dimensional site-scale model of radionuclide transport. Variations in additional transport

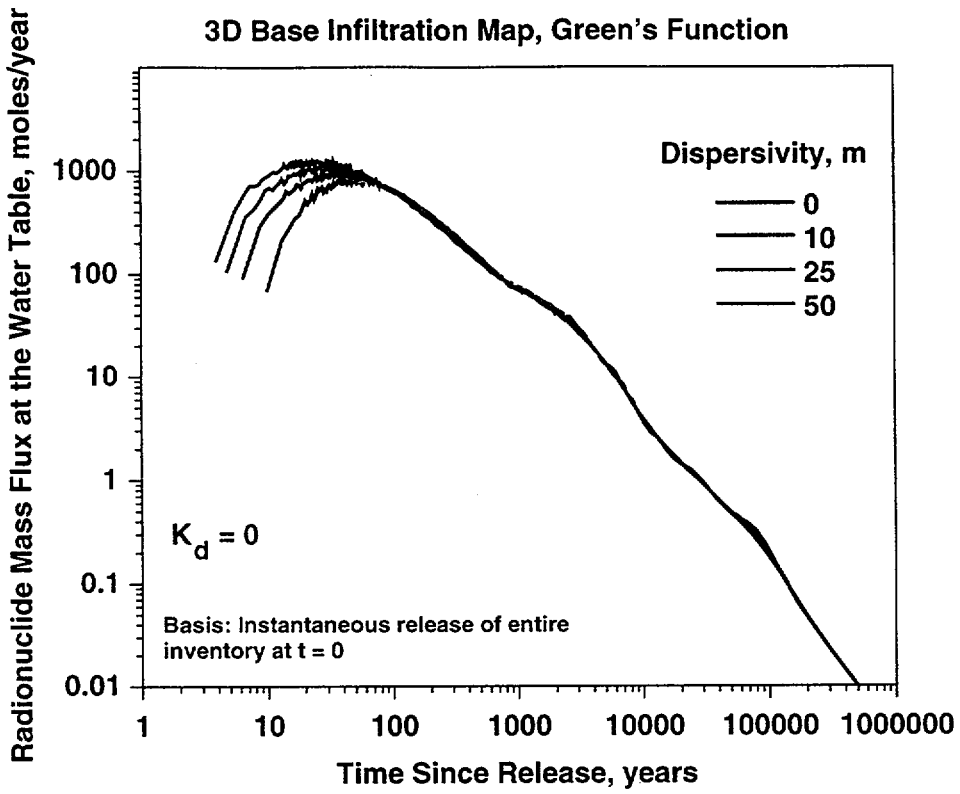

Figure 9-13. Green's function for radionuclide transport in the three-dimensional site scale model. Property set 6541, base infiltration map, no sorption, different dispersivity values.

properties such as the diffusion coefficient and the dispersion coefficient are also examined in this chapter. With the full three-dimensional transport model, implications of lateral flow, spatial variability of flux, and underlying strata thickness are examined. Compared to the two-dimensional model, greater spreading in the travel time distribution curve is simulated due to the additional flow paths sampling a greater range of property variability that occur in three dimensions. This variability leads to cumulative breakthrough curves at the water table spanning the range from 10 years to 10,000 years. The three-dimensional model predicts some sorption on the zeolites as did the two-dimensional model. However, pathways bypassing the zeolites still exist and may lead to peaks in the mass flux at the water table which are not affected by retardation in the zeolites.

The three-dimensional transport model was used to examine the difference in travel time distribution as a function of the release position in the potential repository. Radionuclides released

from the northern end of the repository are more likely to experience rapid transport to the water table than radionuclides released in the southern portion of the potential repository. The behavior is attributed to less uniform distribution of zeolites in the southern portion of the domain. This results in slower matrix flow in the nonzeolitic units in the south compared to fracture dominated flow in the zeolitic units in the north. As with the two-dimensional simulations, this finding highlights the critical need to develop greater certainty on the material properties assigned to the zeolitic units. A slightly higher matrix permeability in the zeolites leads to substantially greater retardation of radionuclides.

The diffusion coefficient influences the breakthrough curves simulated with the three-dimensional model, especially for the portion of the inventory with the shortest travel times. Diffusion into the rock matrix and sorption onto zeolites retard the transport of ^{237}Np traveling in fractures. The dispersion coefficient is shown to have very little impact on the unsaturated zone transport.

Chapter 10 - Unsaturated Zone Performance Predictions

10.1 Abstract

This chapter describes the process of convolving NFE models with far-field transport simulations. With this approach, the differences in response due varying hydrologic conditions near waste emplacement drifts, different engineered barrier designs, time varying thermodynamic effects on canister corrosion, differing models of release due to dissolution of waste, and uncertainty in transport processes in backfill and invert material can all be evaluated. For nonsorbing radionuclides like ^{99}Tc, there is no retardation in any material between the potential repository and the water table. For all of the different property sets developed by LBNL, fracture flow through the zeolitic Calico Hills and underlying units results in bypassing of most of the unsaturated zone matrix material for the USGS infiltration estimates. NFE release rates control the maximum concentration flux at the water table. Releases that occur over longer periods of time lead to lower peak mass fluxes at the water table. Reducing the infiltration rate in these predictions also leads to lower peak mass flux rates at the water table, and they occur significantly later in time. As with nonsorbing radionuclides, those that do sorb to zeolites like ^{237}Np still show early arrivals at the water table after release begins for these parameter sets due to the simulated fracture bypass of the zeolites. However, relatively small changes from the LBNL parameters lead to vastly improved performance with respect to sorbing radionuclides. Reduction in uncertainty of the actual hydrologic properties of the Calico Hills (both fracture and matrix) would clarify whether these predictions of poor far-field barrier performance is indeed warranted or whether they are a by-product of a calibration procedure that was not well constrained by data indicating the degree of fracture flow in the units below the basal vitrophyre.

10.2 Software and Data QA Status

The FEHM code is used to perform all flow and transport calculations in this report. The code is qualified in accordance with Los Alamos quality assurance requirements and is documented in (Zyvoloski et al., 1992, 1995a, 1995b). The QA status of the data used in this report is shown in Table 10-1.

Table 10-1. QA Status of Data used in this Chapter

REFERENCE	Q Status	DTN	COMMENT
Bodvarsson et. al., 1997 "The Site-Scale Unsaturated Zone model of Yucca Mountain, Nevada. For the Viability Assessment, LBL Technical Report LBNL-40378	Q	LB970601233129.001	No DTN assigned. Hydrologic property sets computed in this report are used throughout the present study.
Flint et. al., 1996, Conceptual and numerical model of infiltration for the Yucca Mountain Area, Nevada", USGS WRIR MOL 19970409.0087	Q	GS960908312211.003/ NA	USGS DTN 3GUI623M
Triay et. al., 1996a, "Summary and Synthesis Report on Radionuclide Retardation for the Yucca Mountain Site Characterization Project, Los Alamos National Laboratory YMP Milestone Report 3784	Q	LAIT831341AQ96.001	
Triay et. al, 1996b, "Radionuclide Sorption in Yucca Mountain Tuffs with J-13 Well Water,: neptunium, Uranium, and Plutonium, Los alamos National Laboratory Yucca Mountain Site Characterization Project" Milestone 3338, Technical Report LA-12956-MS	Q	LAIT831341AQ96.001 *	* DTN supersedes DTN LA000000000104.001
Triay et. al., 1996c, "Batch Sorption Results for neptunium transport through Yucca Mountain tuffs, Los alamos National Laboratory Yucca Mountain Site Characterization Project Milestone 3349, Technical Report LA-12961-MS	Q	LAIT831341AQ96.001 *	*DTN supersedes DTN LA000000000090.001

Triay et. al., 1996d, "Comparison of Neptunium Sorption Results using batch and column techniques, Los Alamos National laboratory Yucca Mountain Site Characterization Project Milestone 3041, Technical Report LA-12958-MS	Q	LA000000000106.001	DTN Accession No. MOL.19950630.0300

10.3 Introduction

In the previous two chapters, we simulated the transport of radionuclides from the repository to the water table for a variety of different hydrologic parameter sets and infiltration rates, determining the behavior for both steady state and transient flow fields. In those analyses we made extensive use of the Green's function, or response of the system to a pulse of radionuclide released from the repository at time 0. For steady state flow fields, we showed how this curve can be converted by numerical convolution into a breakthrough curve for an arbitrary input function of radionuclide from the near field environment (NFE). In this chapter a series of sensitivity analyses of radionuclide migration for various NFE release scenarios is performed. The convolution approach allows us to rapidly assess the interplay between release scenarios and unsaturated zone transport, so that an individual unsaturated zone simulation need not be performed for each scenario. The purpose of these analyses is to examine the interplay between expected performance of the unsaturated zone transport system with different NFE performance scenarios. This allows us to examine the importance of various aspects of the unsaturated zone system, including:

- the existence of very rapid transport paths (less than 100 year travel time);
- the flow split between fractures and matrix in the CHn units as a function of infiltration scenario;
- the extent to which the unsaturated zone provides travel time delays approaching the proposed 10,000 year time frame proposed as a regulatory compliance period, as well as longer periods.

This section is not a total-system performance analysis, as it omits key elements that must be included in such studies. These factors include:

- Detailed models of the NFE release rate of radionuclides.The release rate is approximated with very simple functions designed to capture the correct trends.
- Spatial variability in release rate within the repository region due to differences in repository heat effects and variability in local percolation rate. These factors are lumped into a single source term that applies to the repository as a whole. The convolution approach could have been applied to various sections of the repository and the results combined by superposition, but this approach was not carried out in the present study.
- The lack of coupling to a saturated zone model to compute concentrations at the accessible environment that can then be converted to a dose. The computation of concentrations in the saturated zone is treated in Zyvoloski et al. (1997).

Thus, this chapter is designed to elaborate on the combined behavior of the NFE source term/unsaturated zone transport system. The output from this combined model is in the form of mass flux at the water table versus time, which is the feed to a saturated zone model. The influence of various parameters and model uncertainties on the breakthrough curves will be demonstrated and explained. As such, this section provides the underlying explanations and understanding of how the unsaturated zone transport system, in combination with typical NFE source term models, is likely to transmit radionuclides to the water table.

10.4 Radionuclide Transport Properties

The radionuclides examined in this chapter include the actinides ^{237}Np, ^{233}U, ^{242}Pu, as well as ^{99}Tc. The nonsorbing ^{99}Tc can be thought of as a surrogate for other conservative radionuclides such as ^{36}Cl, ^{14}C, and ^{129}I, so the others are not modeled explicitly in the present study even though they are potentially important to total system performance. Transport properties for these radionuclides and others have been discussed in detail in other studies (Triay et al., 1996a, Robinson et al., 1995, 1996) and will be summarized briefly here. Sorption coefficients for these

radionuclides have been measured on a variety of tuff types at different chemical conditions. The radionuclides ^{99}Tc, ^{14}C, and ^{129}I are all assumed to be conservative, nonsorbing radionuclides in the unsaturated zone, based on measurements and their presumed oxidation states in the Yucca Mountain fluids. ^{14}C is perhaps better described by a multi-phase model that includes partitioning between the liquid and gas phases, and precipitation as calcite on the rock. Viswanathan (1996) modeled the gas-liquid partitioning as a function of fluid chemistry to describe the behavior of natural gas-phase ^{14}C in the unsaturated zone. However, the most conservative approach is to assume liquid-phase only transport, as gas-phase partitioning would disperse radionuclide to the atmosphere, thereby reducing the dose associated with groundwater transport.

The actinides exhibit small to moderate amounts of sorption onto the Yucca Mountain tuffs, especially to zeolites such as clinoptilolite and mordenite, which are present beneath the potential repository. ^{237}Np and ^{233}U sorption appear to be minimal onto vitric and devitrified tuffs that have not been altered by secondary mineralization. The sorption coefficient of ^{237}Np onto zeolitic tuff is discussed in detail in Chapter 8. An appropriate value for this radionuclide is about 2 cc/g on zeolitic tuff; we conservatively assume a value of 0 elsewhere, although measurable sorption has been observed on other tuff samples. Uranium exhibits somewhat higher sorption coefficients on zeolites (3-20 cc/g, depending on concentration), but similarly small values onto unaltered tuff samples. Plutonium sorbs to all types of tuff at Yucca Mountain; for this radionuclide we use a nominal value of 50 cc/g on all tuffs. Ordinarily, this degree of sorption would imply very slow migration. However, colloid-facilitated transport of plutonium is considered in this version of the model: details of this process are described in a subsequent section as well as in Chapter 8.

The matrix diffusion model for fracture transport requires the input of a diffusion coefficient for each radionuclide into the tuff. Values in the range of 10^{-10} to 10^{-11} m^2/s have been measured under saturated conditions (Triay et al., 1997). In addition, fracture coatings do not appear to inhibit the diffusion into the rock matrix. Given the rather small sensitivity to diffusion coefficient of the Green's functions computed previously, we choose a fixed diffusion coefficient

of 10^{-11} m^2/s for all simulations in this section. Dispersivity also had a relatively small impact on the results presented earlier. Therefore, to simplify the interpretation, we conservatively assume no hydrodynamic dispersion. When this assumption is made, all spreading of radionuclide is caused by large-scale heterogeneities captured explicitly in the model, such as flow partitioning between the fractures and matrix and variations in vitric and zeolite thicknesses with position beneath the repository.

10.5 Abstracted Models for NFE Source Term

A comprehensive representation of the release of radionuclides from the near-field environment (NFE) is beyond the scope of the present study, which focuses on unsaturated zone flow and radionuclide transport processes. The factors that enter into the rate of radionuclide release from the NFE include:

- hydrologic conditions near waste-emplacement drifts, including the probability of seepage into the drift and dripping onto the waste canisters;
- the presence and effectiveness of engineered barriers built into the near-field system, such as backfill and drip shields;
- the time-varying thermodynamic conditions at waste packages (temperature, pressure, relative humidity), which control the corrosion rate of the canisters;
- the dissolution rate of the waste form, depending in turn on the ability of liquid water to contact the surface of the spent fuel rods;
- the transport of radionuclides in the aqueous phase through the failed waste package, backfill (if present), and invert material;
- the solubility of radionuclides in the near-field environment.

The incorporation of these factors into NFE models has typically been the purview of researchers studying the near-field system, and the models developed have been analyzed and abstracted in

past TSPA analyses (e.g. Wilson et al., 1994, Andrews et al., 1995). The complexity of these models and the unsaturated zone flow and transport model requires that each be dissected to determine which factors are the most important ones affecting system performance. Otherwise, the overall analysis is not "transparent," i.e. there is not a clear, understandable picture of the key factors and parameters that control the performance of the overall system. Therefore, there is value in adopting simplifications in some aspects of the system while retaining the complex behavior in other parts, so that the role of the uncertainties in the complex model can be highlighted.

In the present study, we accomplish this goal for the unsaturated-zone transport barrier by abstracting the NFE source term model. By using simple parameterizations for the NFE system, we can examine the role of critical assumptions and uncertainties of the unsaturated zone transport system, discovering which processes and parameters are important under different regimes of NFE behavior. The NFE source terms, though simple, are designed to capture the range of possible release scenarios. The first function we use to describe the NFE is a constant release of finite duration, beginning at a minimum time, t_{can}, and lasting until all radionuclide has been leached from the repository region (Figure 10-1a). The duration before any releases captures whatever minimum lifetime is assumed for the waste packages before corrosive degradation allows contact of water onto the waste form. Once releases start, the constant release rate occurs over a time period that will depend on near-field conditions and the type of radionuclide. For example, for solubility-limited radionuclides, such as ^{237}Np, the solubility is thought to control the release from the near-field environment, so that even if waste form dissolution supplies radionuclide to the fluid at rates that imply concentrations greater than the solubility, precipitation in the near-field will occur, thereby, placing a maximum on the release rate. By contrast, the rate for a dissolution-rate-limited radionuclide such as ^{99}Tc will depend on the kinetics of dissolution. Release rates for either radionuclide will also be a function of the water flow rate through the waste package, since liquid water is the carrier fluid. Typically, t_{rel}, the time over which releases occur, will be shorter (faster rates) for dissolution-rate-limited radionuclides, but the value is a function of the many factors

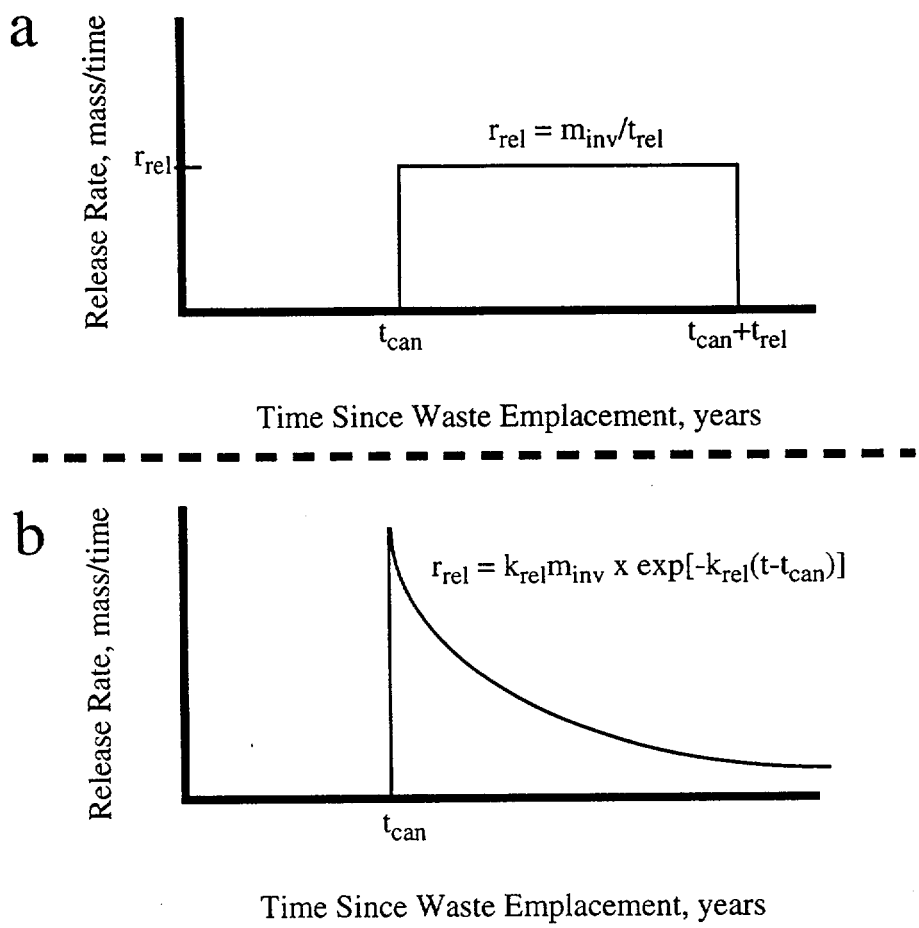

Figure 10-1. Schematic of abstracted rate models for radionuclide release from the NFE. a) constant-release-rate model; b) exponential-release-rate model.

listed above, so in this study we examine the performance of the unsaturated zone for a range of t_{rel} values.

The second model in Figure 10-1 assumes that after the initial period of no release, the rate starts at an initial maximum value and decays exponentially in time, such that at long times, the entire inventory is leached from the near field. The time dependence is intended to capture the variability in lifetime of individual waste packages, which in turn is likely to depend strongly on variability in fluid flux associated with dripping on individual canisters. For example, an order of magnitude difference in fluid flux translates to a similar magnitude difference in the local radionuclide release rate. Some waste packages will be unfavorably located within regions of high flux; other packages will reside in zones of lower risk where little or no dripping occurs. Still others

may be damaged by rockfall or other failure scenarios in the engineered system. To capture this variability, an exponential decay in total release rate is assumed. In previous TSPA analyses such as Andrews et al. (1995), the published release rates, which did attempt to capture these effects, appear to tail off over long times in this fashion, thus justifying the use of this sort of simplified release model to examine the unsaturated zone system. Like the constant rate model, the exponential model has a parameter k_{rel} that scales the time frame over which the majority of releases occur, i.e. $1/k_{rel}$ is a characteristic time over which a radionuclide is released from the NFE. After about three times this characteristic time, most of the inventory is depleted.

The subsections that follow examine the behavior of radionuclides ^{99}Tc and ^{237}Np in greatest detail because of their importance in previous TSPA analyses. ^{242}Pu is described in its own section because of the possibility of colloid-facilitated transport. Finally, more limited modeling studies are presented for ^{233}U, ^{14}C, and ^{129}I.

10.6 Transport Predictions for ^{99}Tc

We first examine the predicted transport of ^{99}Tc under an assumed release scenario of 1000 years of no release, followed by constant release rate for 3000 years. In all cases that follow we hold t_{can} at 1000 years, since the influence is merely as a delay time, with no other impact on the breakthrough curve. The 3000 year time for complete release represents a relatively rapid dissolution of the waste form and mobilization of the radionuclide. Figure 10-2 shows the resulting breakthrough at the water table (radionuclide mass flux versus time) for four of the hydrologic parameter sets assuming the base infiltration map. After the 1000 year minimum lifetime of the waste package/near-field system, breakthroughs at the water table occur well within 10 ky, regardless of which parameter set is chosen. The peak values of about 100 moles/y are controlled mostly by the release rate, rather than by details of the unsaturated zone transport system. This occurs because for these parameter sets, the fracture flow predicted in the CHn units provides

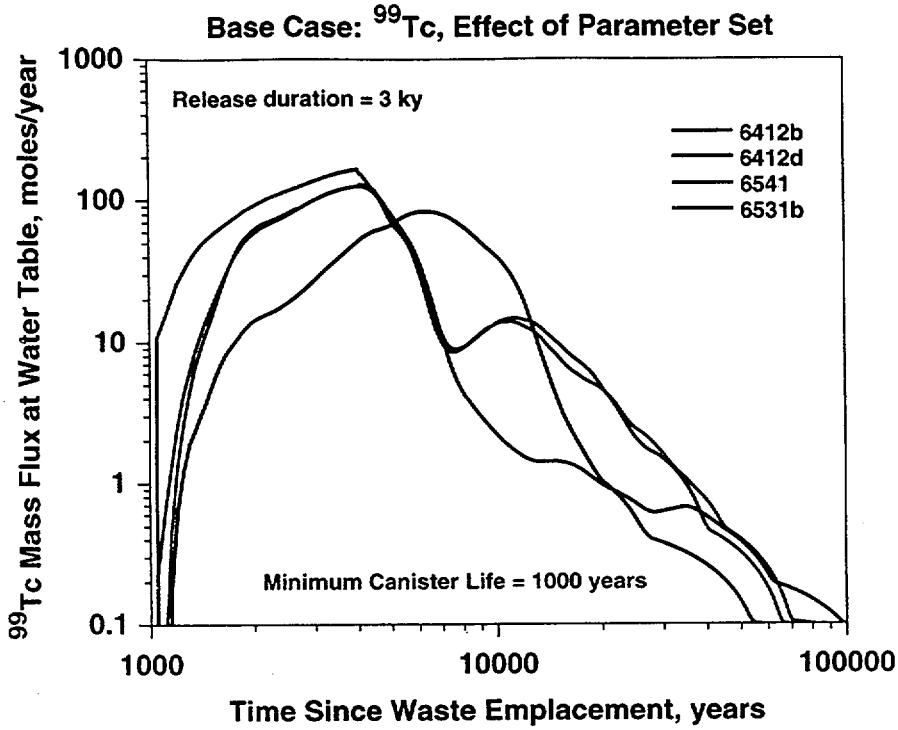

Figure 10-2. Breakthrough of ^{99}Tc at the water table for different hydrologic parameter sets. Base infiltration map, t_{can}=1000 y, t_{rel}=3000 y.

minimal barriers to radionuclide migration. This conclusion can be stated in a general way as follows: *for all of the property sets developed by LBNL using parameter estimation techniques, fracture flow through the zeolitic Calico Hills and underlying units results in bypassing of most of the unsaturated zone through fractures at the assumed infiltration rates used here. Even without considering the retardation due to sorption, this results in only minimal effectiveness of the unsaturated zone transport barrier.* The exception in Figure 10-2 is case 6412d, which assumed higher zeolite permeability. For this case, the peak is extended to about 5000 years, and its value is lower.

Regarding rapid transport through fractures in time periods of less than 100 years, recall that parameter set 6531b exhibited the greatest amount of fast-pathway flow. However, notice that this effect is not predicted to be important for predicting mass fluxes at the water table, since the quantity traveling through such paths is predicted to be small, and finite release durations (as

opposed to the instantaneous release used for the Green's function calculation) tend to negate the influence of small quantities of fast-path transport.

To illustrate the influence of NFE release rate on breakthrough curves, we plot breakthrough curves for a 10 ky release duration in Figure 10-3. All curves plateau at about the

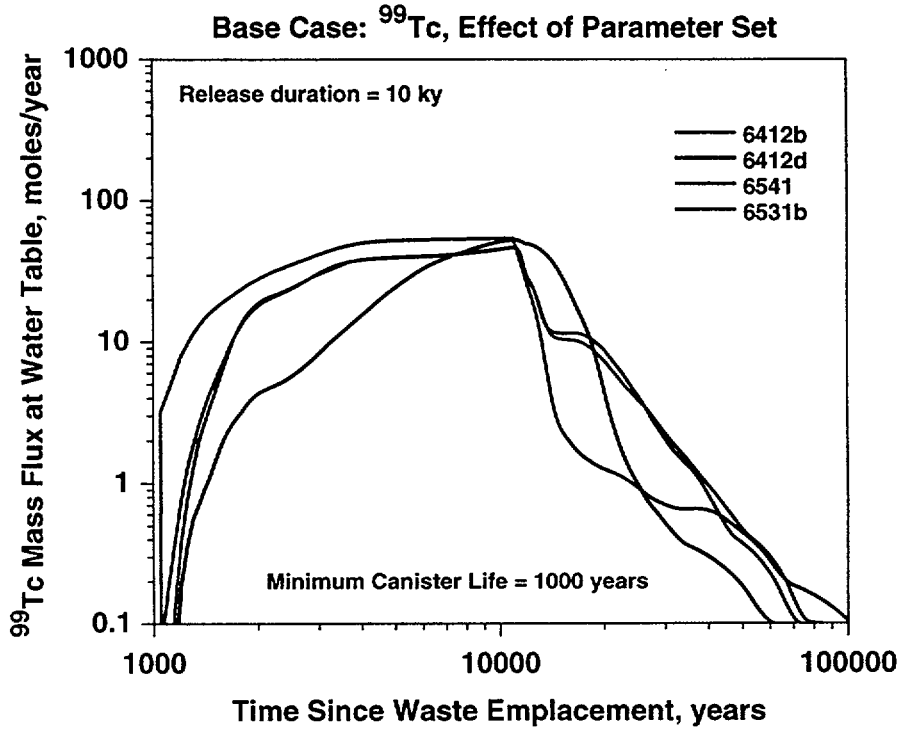

Figure 10-3. Breakthrough of ^{99}Tc at the water table for different hydrologic parameter sets. Base infiltration map, t_{can}=1000 y, t_{rel}=10000 y.

same level, namely the release rate at the repository. Only for one case, parameter set 6412d, does this maximum occur over times approaching 10 ky. The others reach this level within 5,000 years. A more complete examination of the influence of release rate on the base case (6541) parameter set is shown in Figure 10-4, in which the duration of release is varied from 3 to 50 ky. The plateau in each case is at the release rate from the NFE.

For unsaturated zone performance predicted from the base case, the NFE release rate will control the maximum release rate; under these conditions the unsaturated zone is a relatively poor barrier to transport for nonsorbing radionuclides. This conclusion applies only to parameter sets

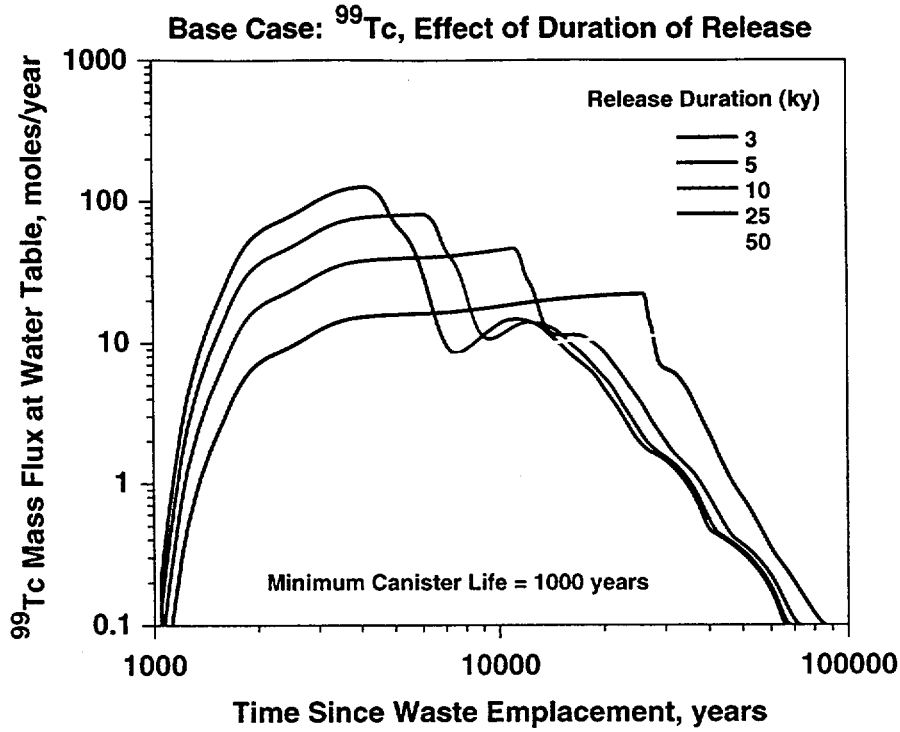

Figure 10-4. Breakthrough of ^{99}Tc at the water table for different durations of release. Base infiltration map, t_{can}=1000 y, parameter set 6541.

and infiltration rates similar to the base case. The unsaturated zone transport system provides a more robust barrier under somewhat different assumptions, as shown below.

Infiltration rate plays a key role in the predicted mass flux at the water table. Figure 10-5 shows the influence of infiltration rate on the ^{99}Tc breakthrough curve (3 ky duration of release) for case 6541, and Figure 10-6 is a similar plot for the high-k zeolite case, 6412d. For case 6541, the peak values are reached before 10 ky, but the peak mass flux is a function of the infiltration rate, even though the duration of release, and hence the NFE release rate, was constant in each case. This difference reflects the lower flow fraction flowing through fractures at the lower infiltration rates. A similar effect is seen for case 6412d (Figure 10-6), but in addition, travel times approaching 10 ky are predicted at the lower infiltration rate. Note also that these simulations probably underestimate the importance of infiltration rate, since the NFE release rate was held fixed despite changes in flux. A more realistic scenario would be a lower release rate (longer

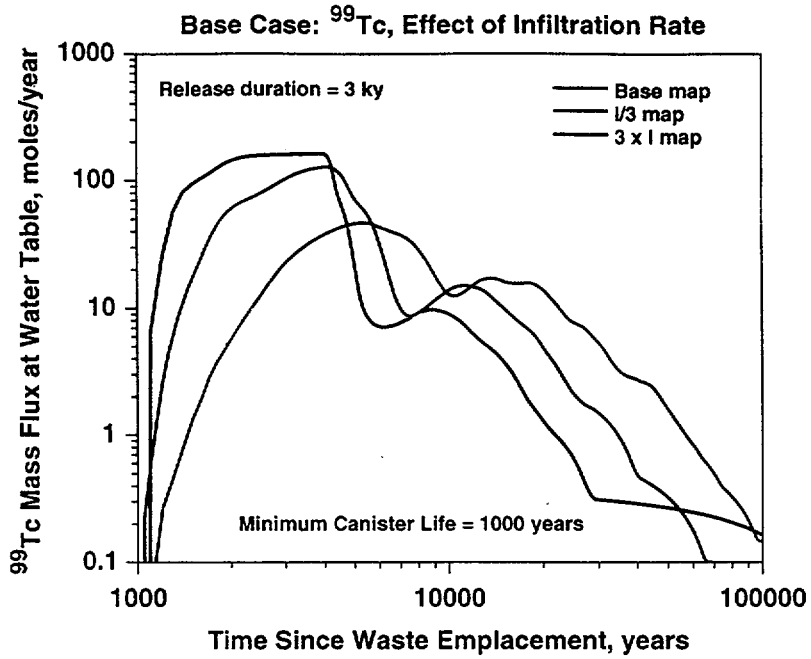

Figure 10-5. Breakthrough of ^{99}Tc at the water table as a function of infiltration rate. t_{can}=1000 y, t_{rel} = 3000 y, parameter set 6541.

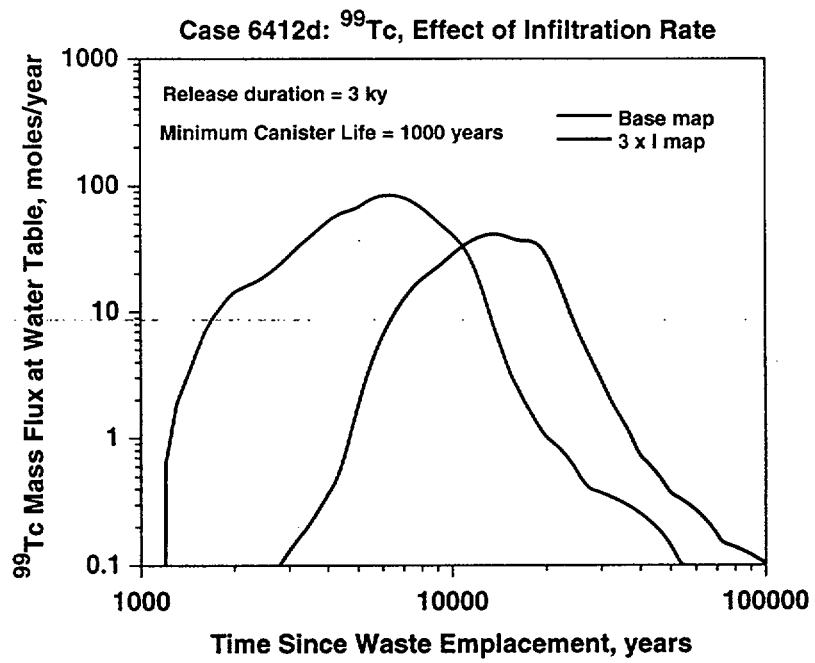

Figure 10-6. Breakthrough of ^{99}Tc at the water table as a function of infiltration rate. t_{can}=1000 y, t_{rel} = 3000 y, parameter set 6412d.

release duration) for the low infiltration rate case. Building these interrelationships into model predictions is the subject of TSPA analyses, and is beyond the scope of the present study.

It is unlikely that the NFE release rate will be uniform until the inventory is depleted, but rather should be a function of the time-history of waste package failures, the spatial distribution of percolation flux, and other factors. Therefore, the exponential release scenario discussed above was developed. This function appears to roughly capture the complexities built into previous TSPA analyses of release rate from the near field. For ^{99}Tc, we assume that the exponential decay time ($1/k_{rel}$) spans a similar range as the times chosen for the constant release case above, namely 3 ky to 50 ky. Figure 10-7 shows the results of the simulations. Qualitatively, the conclusions are similar

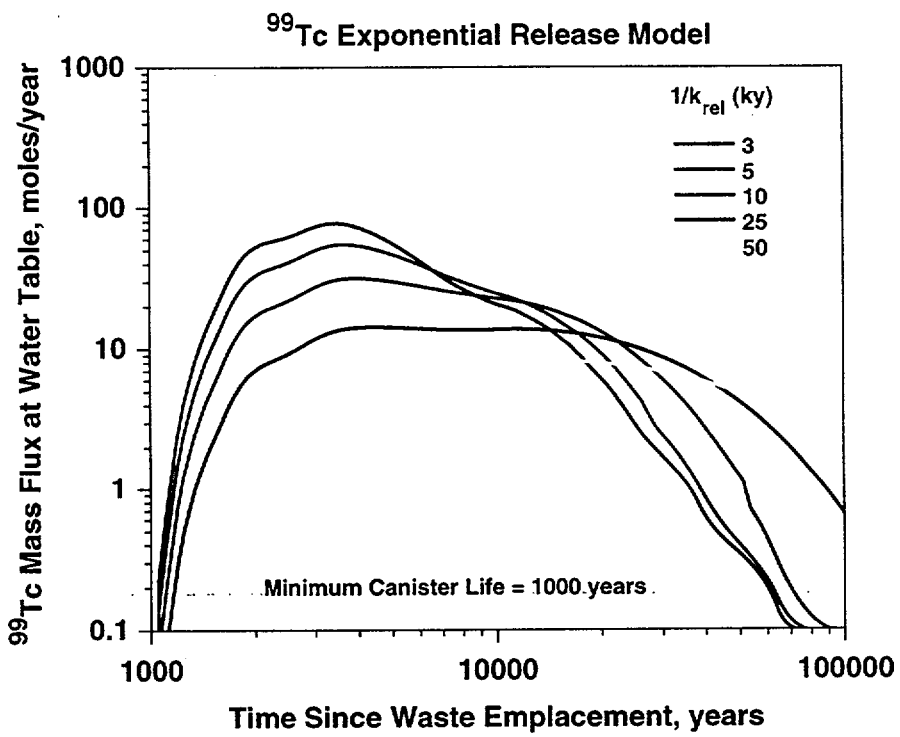

Figure 10-7. Breakthrough of ^{99}Tc at the water table for different values of k_{rel} for the exponential release scenario. Base infiltration map, t_{can}=1000 y, parameter set 6541.

to the constant release scenario in that the peak mass flux is controlled by the maximum value issuing from the near field. In other words, the unsaturated zone provides a meager barrier to radionuclide migration for this property set. However, the peak flux value and the shape of the

response curve at the water table are different than those obtained with the constant source model. In particular, the peak mass flux values tend to be somewhat lower for the exponential release scenario with the same time scale as the constant release case because the exponential model spreads some releases to much longer times, presumably because of a distribution of failure times and release rates for individual canisters. Therefore, the details of the failure scenarios for the NFE model will be important for predicting total system performance.

Finally, we compare the two-dimensional and three-dimensional integrated transport simulations for ^{99}Tc in Figure 10-8. The transport predictions in three dimensions appear to be

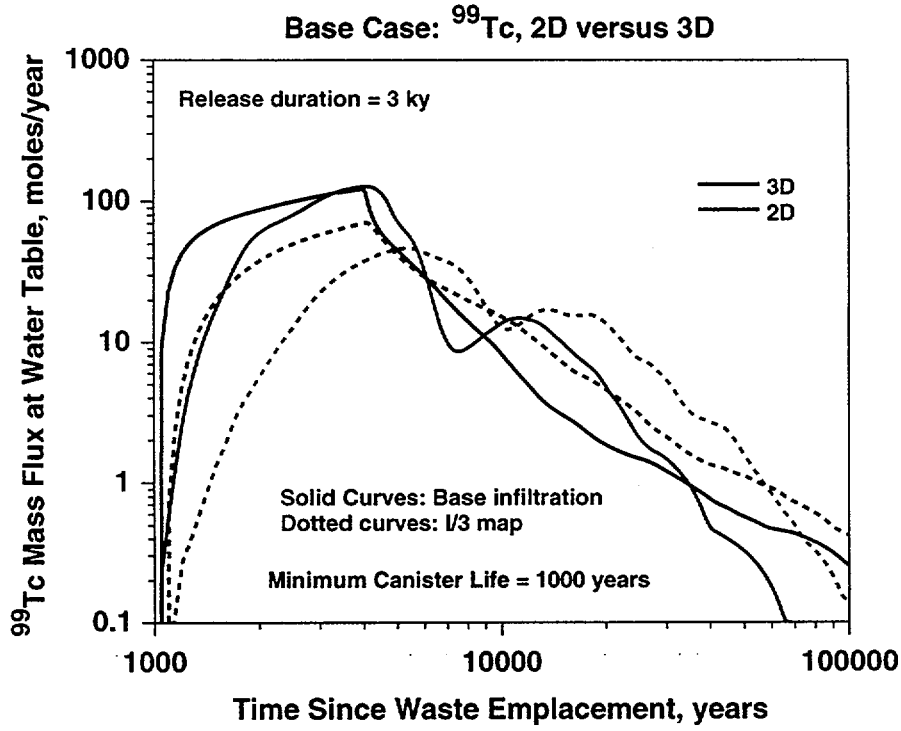

Figure 10-8. Breakthrough of ^{99}Tc at the water table comparing the two-dimensional and three-dimensional models. Base infiltration map and I/3 map, t_{can}=1000 y, parameter set 6541

adequately approximated by the two-dimensional prediction for conservative radionuclides. The fundamental reason for this is the predominantly downward flow and transport through fractures simulated in each model. Subtle differences in flow appear to be relatively unimportant for ^{99}Tc.

10.7 Transport Predictions for ^{237}Np

The key differences in the behavior of ^{237}Np relative to ^{99}Tc arise due to sorption of ^{237}Np (taken as 2 cc/g in this section) and the longer duration of release (lower release rate) of this solubility-limited radionuclide. The water table breakthrough curves for the various parameter sets are shown for various durations of release in Figures 10-9 (10 ky duration of release), 10-10 (30

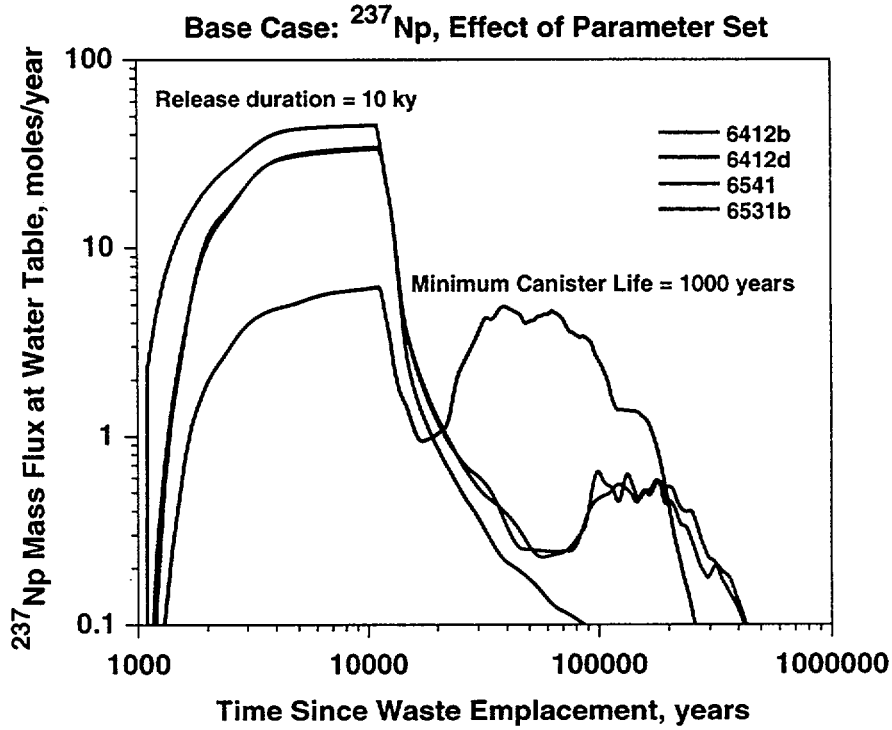

Figure 10-9. Breakthrough of ^{237}Np at the water table for different hydrologic parameter sets. Base infiltration map, t_{can}=1000 y, t_{rel} = 10 ky, parameter set 6541.

ky duration of release), and 10-11 (100 ky duration of release). As before, a 1000 year minimum canister life is assumed. A distinct bi-modal response is predicted for ^{237}Np, due to fracture flow bypassing the zeolites. The fraction that travels through the zeolite matrix sorbs and is delayed to times on the order of 100 ky. The level of the plateau at earlier times is controlled by the flow fraction that bypasses the zeolites through fractures. The one parameter set that yields significantly better performance is case 6412d, the high-k zeolite case (Table 5-3). This result highlights the importance of characterizing the nature of flow and transport in zeolitic tuff. As with ^{99}Tc, the

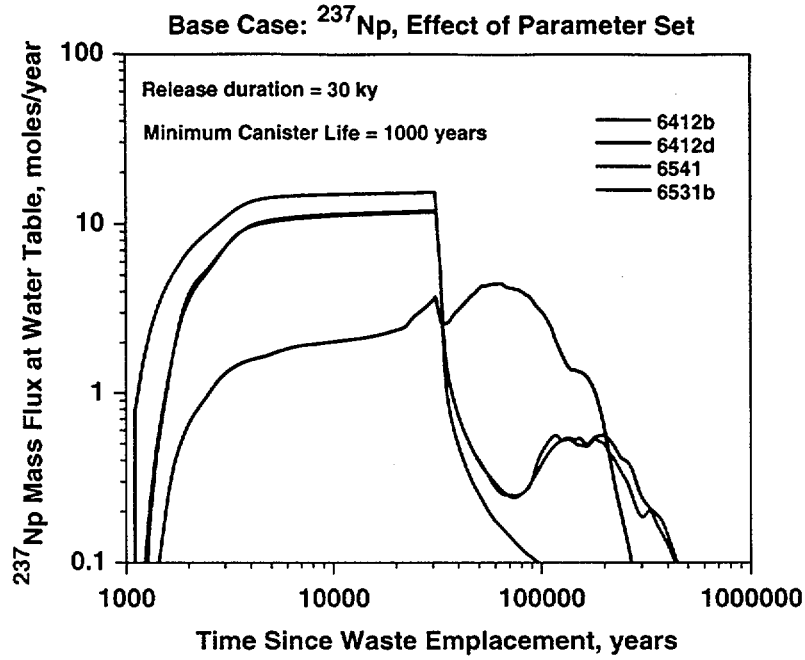

Figure 10-10. Breakthrough of ^{237}Np at the water table for different hydrologic parameter sets. Base infiltration map, t_{can}=1000 y, t_{rel} = 30 ky, parameter set 6541.

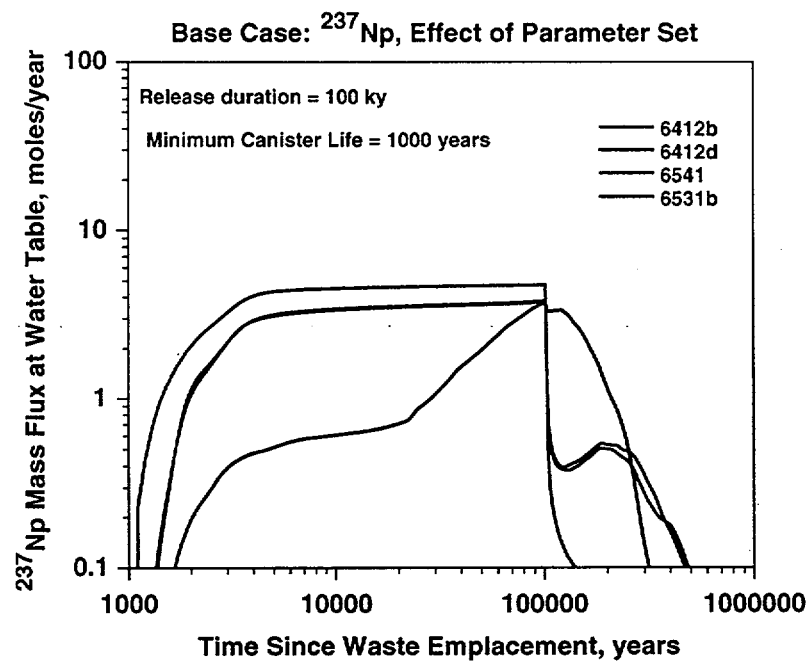

Figure 10-11. Breakthrough of ^{237}Np at the water table for different hydrologic parameter sets. Base infiltration map, t_{can}=1000 y, t_{rel} = 100 ky, parameter set 6541.

early arriving portion of the inventory results in the peak mass flux at the water table for all cases except 6412d, where, for the shortest release duration (10 ky), the mass fluxes of the two sets of pathways are almost equal, and for longer release periods, the long-residence-time peak at 100 ky is the larger one.

For the base case, the effect of duration of release is shown in Figure 10-12. The curves

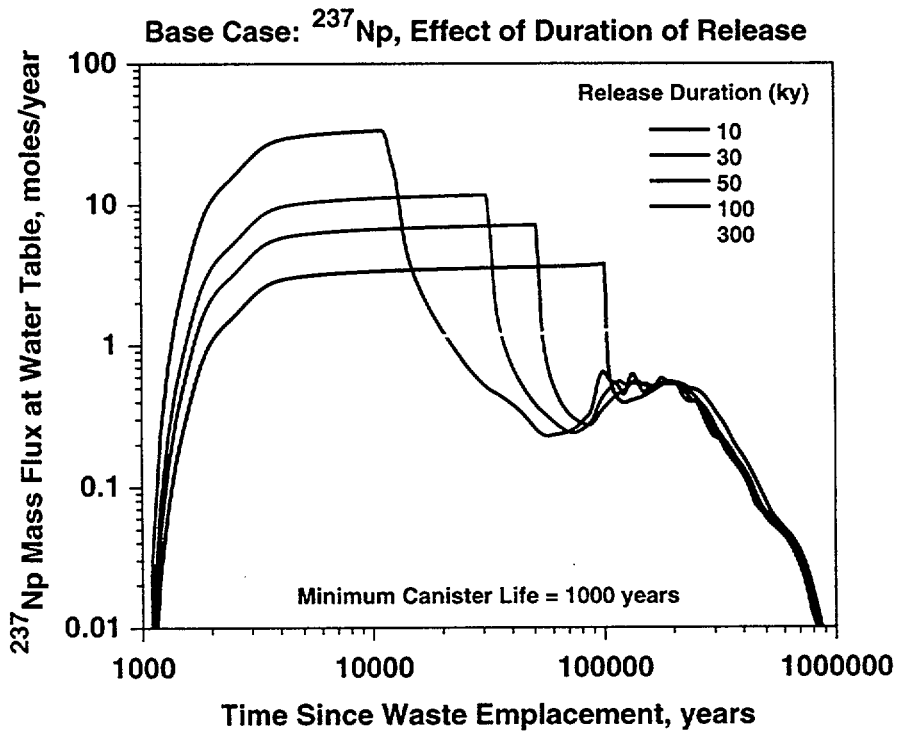

Figure 10-12. Breakthrough of ^{237}Np at the water table as a function of duration of release. t_{can}=1000 y, base infiltration map, parameter set 6541.

plateau at a value that depends on the NFE release rate and the fraction of the inventory that bypasses the zeolitic tuffs through fractures. Infiltration rate also influences the results markedly, as shown for parameter set 6541 for the 30 ky release duration in Figure 10-13. Progressively lower percentages of fluid travel through the matrix at higher infiltration rates, resulting in higher peak mass flux values associated with the early-arriving portion of the inventory. The extreme case of this situation is at the low infiltration for parameter set 6412d (Figure 10-14), where the I/3 map results in no bypassing of zeolites. For this case, no ^{237}Np reaches the water table before 40 ky,

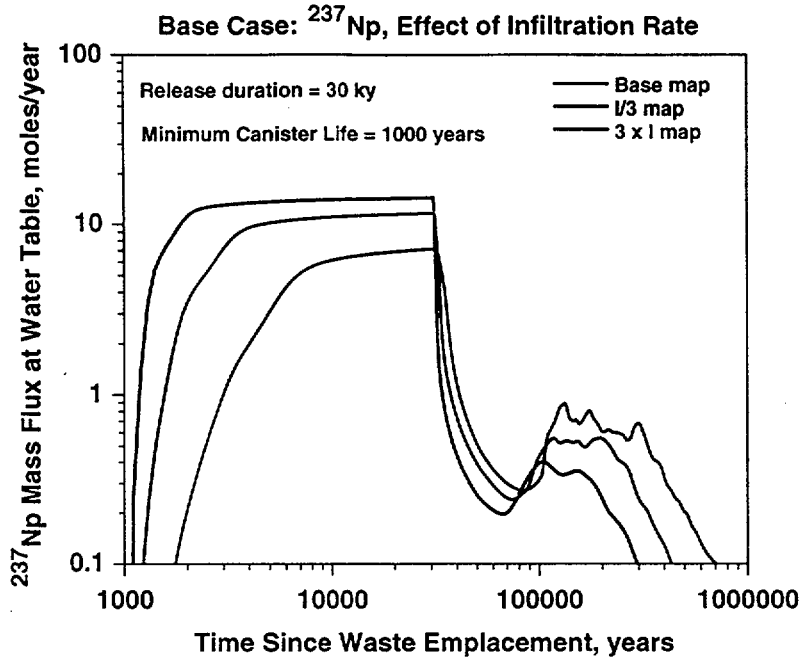

Figure 10-13. Breakthrough of ^{237}Np at the water table as a function of infiltration rate. t_{can}=1000 y, t_{rel} = 30 ky, parameter set 6541.

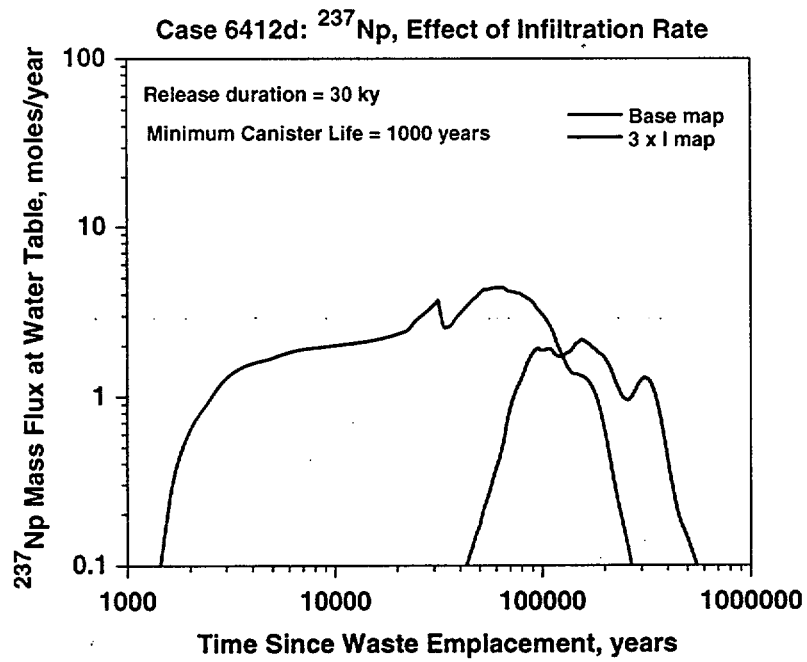

Figure 10-14. Breakthrough of ^{237}Np at the water table as a function of infiltration rate. t_{can}=1000 y, t_{rel} = 30 ky, parameter set 6412d.

and the peak occurs between 100 and 150 ky. Clearly, relatively small changes from base case conditions can lead to vastly improved performance with respect to radionuclides such as ^{237}Np. Nevertheless, under base case conditions with the parameter sets supplied by LBNL, the unsaturated zone does not provide a significant barrier to radionuclide migration. For ^{237}Np, the NFE source term, which will depend strongly on solubility and near field hydrologic conditions, is likely to control the mass flux of this critical radionuclide.

Breakthrough curve results for the exponential release scenario for case 6541, base infiltration map are shown in Figure 10-15. As was the case with ^{99}Tc, the general conclusions are

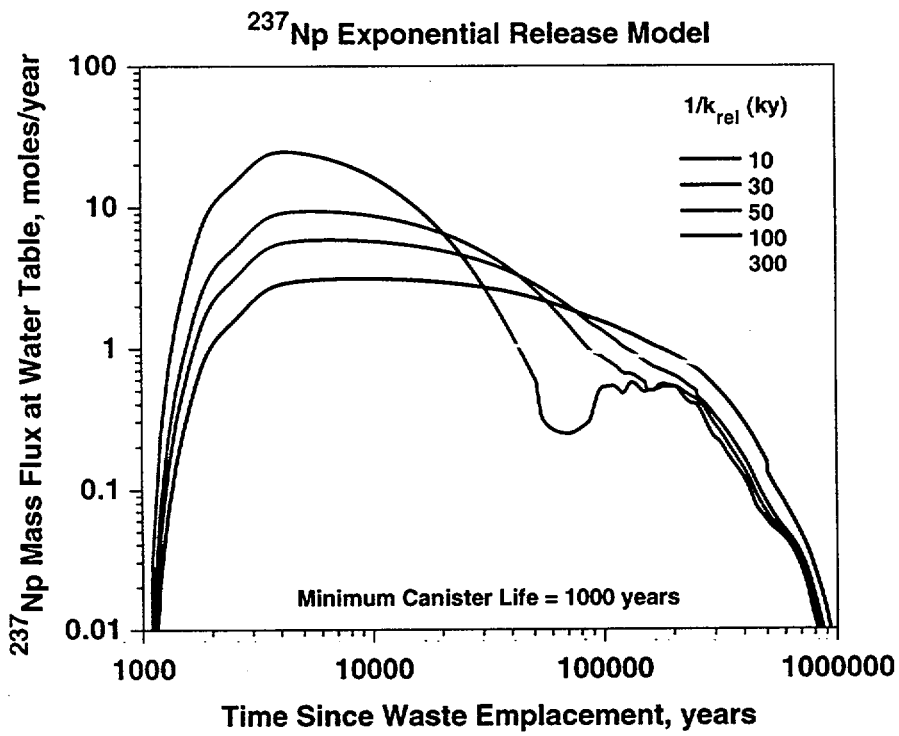

Figure 10-15. Breakthrough of ^{237}Np at the water table for different values of k_{rel} for the exponential release scenario. Base infiltration map, t_{can}=1000 y, parameter set 6541.

unchanged by the form of the release scenario, but the exact predictions of mass flux versus time are different for the exponential release scenario. Specifically, the peak mass flux values are somewhat lower for the exponential release scenario with the same time scale as the constant release case, for reasons explained above with regard to ^{99}Tc.

A comparison of the two-dimensional and three-dimensional integrated transport prediction is shown in Figure 10-16. As with ^{99}Tc, the three-dimensional simulation is adequately

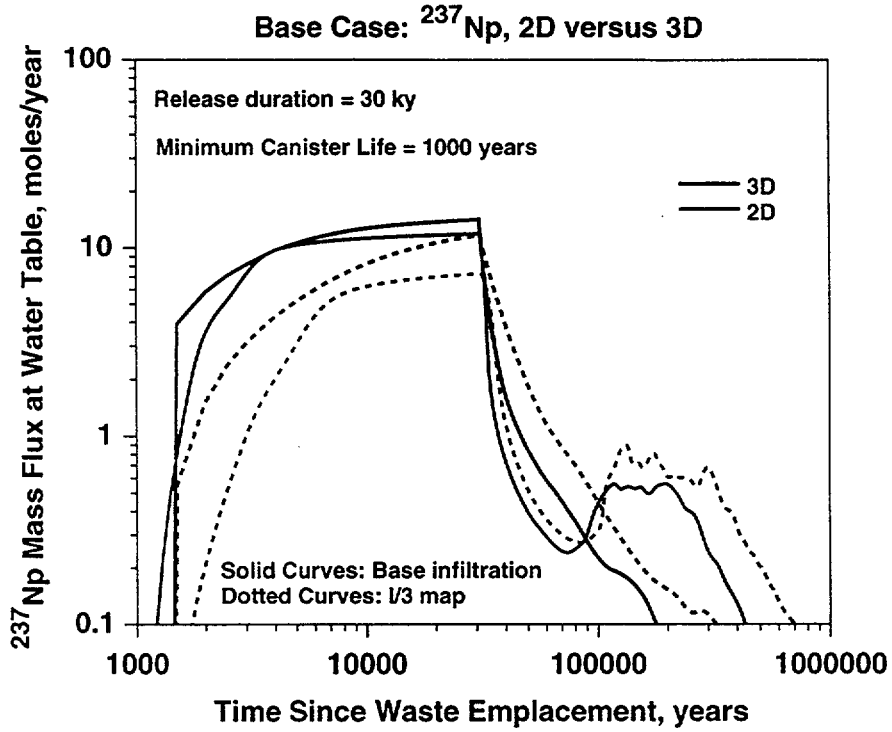

Figure 10-16. Breakthrough of ^{237}Np at the water table comparing the two-dimensional and three-dimensional models. Base infiltration map and I/3 map, t_{can}=1000 y, parameter set 6541.

approximated by the two-dimensional model, except perhaps for a significant deviation for the I/3 infiltration scenario. The two-dimensional model predicts somewhat more matrix flow through the zeolites, which shifts more of the inventory to longer residence times, when compared to the three-dimensional simulation. Overall, however, the differences are fairly small compared to other uncertainties in the models.

10.8 Transport Predictions for Uranium Isotopes

As mentioned in the previous chapter, Triay et al. (1996a) determined that uranium exhibits significant sorption only onto the zeolitic tuffs at Yucca Mountain for the geochemical conditions

likely to be present. A nonlinear sorption isotherm behavior was determined, with K_d values of about 20 cc/g at 8 x 10^{-8} mol/l, compared to 3 cc/g at 10^{-4} mol/l. Robinson et al. (1996) used the nonlinear Langmuir and Freundlich isotherm models to simulate uranium transport. However, in the present study, we use the linear sorption model embodied in the particle tracking model to bound the behavior. This requires that we examine a broad range of sorption coefficients to assess the likely effects of nonlinear isotherm behavior.

The appropriate source term for uranium was also discussed in Robinson et al. (1996) and will be briefly reviewed here. The isotopes of uranium present in the inventory consist of several long-lasting isotopes, the most plentiful of which is ^{238}U. Figure 10-17 shows the predicted

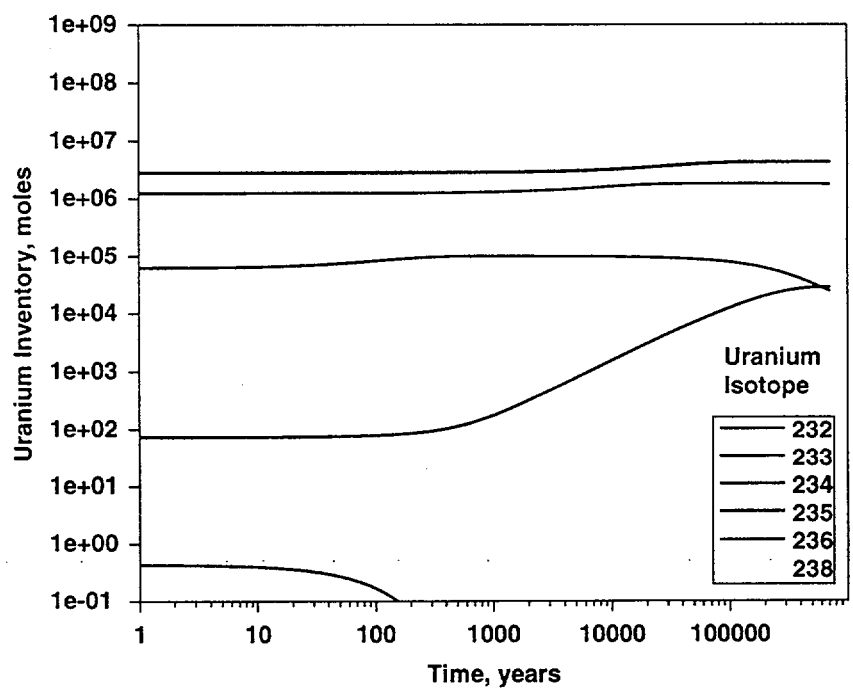

Figure 10-17. Uranium isotope inventory as a function of time for a 70,000 MTU repository and -- add description of inventory assumptions (initial inventory data from Wilson et al., 1994).

proportions of the different uranium isotopes with time generated by Robinson et al. (1996) using the initial inventory figures of Wilson et al. (1994) and decay-chain models to track the ingrowth and decay of all isotopes of uranium and other radionuclides. The initial inventory data, half-lives

of radionuclides, and relevant decay chains are presented in Appendix A, along with a brief description of the calculation method for determining the isotope distribution with time.

This proportion of uranium isotopes represents the relative amounts of each isotope, regardless of where these isotopes are located in space. If all isotopes were present at the repository and available for mobilization, then a reasonable assumption would be that the release rate of each isotope would be proportional to the fraction of each present at any given time. However, production of ^{233}U occurs due to decay of ^{237}Np, most of which will probably have escaped the near-field environment by the time significant quantities of ^{233}U are generated. Therefore, special provisions are required for ^{233}U; this special case is discussed below. For all isotopes except ^{233}U, we assume that the release rate is proportional to the fraction of each present at time 0 (e.g. congruent dissolution), and that the total NFE source term for uranium is governed by the solubility of uranium, assumed to be about one order of magnitude larger than ^{237}Np (Triay et al., 1997). A key difference with uranium relative to ^{237}Np is the much larger inventory of uranium in the waste form, resulting in much longer times for complete dissolution and mobilization of the waste.

For ^{233}U, we assume that the majority of this isotope is mobilized as the parent ^{237}Np, and that decay produces ^{233}U, which then transports with properties similar to that of ^{237}Np. In the unsaturated zone, we showed that for the current property values, the influence of zeolite K_d, the only significant difference between uranium and ^{237}Np, was relatively minor since fracture transport is the controlling feature of transport in this system. Under these assumptions, ^{233}U breakthrough curves can be generated simply from the ^{237}Np results with a post-processing calculation to account for ^{237}Np decay to ^{233}U.

Transport predictions for uranium isotopes are shown in Figure10-18. This calculation assumed solubility-limited release at a rate ten times faster than the 30 ky release scenario for ^{237}Np, though for uranium this implies only 6.7% of the uranium inventory is released after 100 ky. The constant release rate presumed using this model is reflected at the water table after about

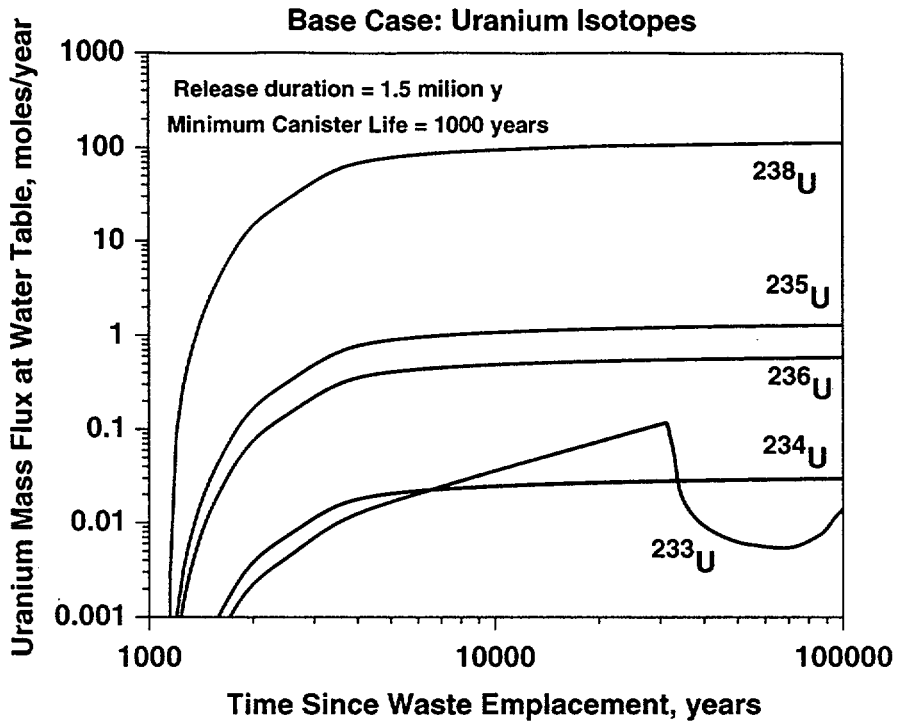

Figure 10-18. Water table breakthrough curves for Uranium isotopes. Property set 6541, base infiltration map, release rate similar the ^{237}Np case with 30 ky release scenario (for Uranium only --% is released after one million years).

5000 years, and the relative proportion of each isotope is controlled by the fraction of each present in the inventory, as discussed above. The exception is ^{233}U, which tracks the behavior of ^{237}Np, but at a level that increases with time due to the decay of the parent. Note also that radionuclides that reach the saturated zone as ^{237}Np will still decay to ^{233}U in the saturated zone, thereby adding to the amount of the daughter product reaching the accessible environment.

10.9 Transport Predictions for Plutonium Isotopes

In Chapter 8 we presented a model for colloid-facilitated transport of plutonium. We showed that even for the current hydrologic property values, with fracture-dominated flow through a large portion of the unsaturated zone, that retardation in nonwelded vitric tuff provides a very robust barrier to migration of this strongly sorbing radionuclide, as long as the plutonium remains primarily in the aqueous phase. When plutonium is assumed to sorb to mobile colloids, the

situation is akin to a more weakly sorbing radionuclide, and significant releases to the water table are predicted. In this section we convolute these results with a range of NFE release rates for plutonium to predict the mass flux at the water table for some specific scenarios.

As was the case for uranium, several isotopes of plutonium are present in the waste form. Figure 10-19 shows the quantity of each isotope present versus time. In contrast to ^{233}U, there is

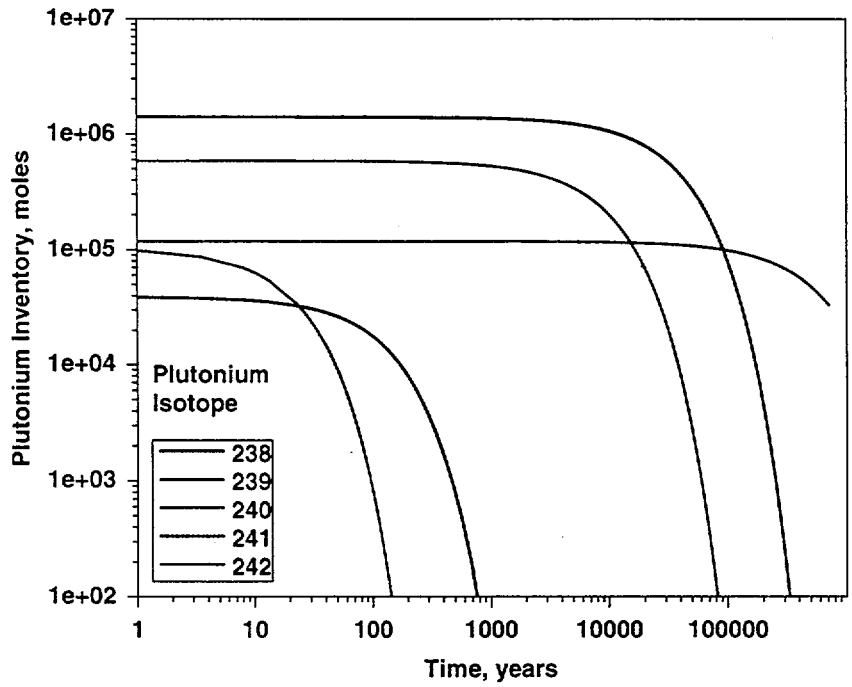

Figure 10-19. Plutonium isotope inventory as a function of time for a 70,000 MTU repository and --- add description of inventory assumptions (initial inventory data from Wilson et al., 1994).

no ingrowth from a mobile radionuclide to complicate the prediction of dissolution in the near field. After a few hundred years, the remaining isotopes are ^{239}Pu, ^{240}Pu, and ^{242}Pu, which are, as was the case with uranium, assumed to be released in proportion to their relative proportions in the inventory.

Plutonium is a very insoluble radionuclide under the geochemical conditions present in the unsaturated zone. Triay et al. (1997) report values at 25°C ranging from 5×10^{-8} mol/l to 1×10^{-8}

mol/l in the pH range of 5.9 to 8.5. These solubilities are roughly three orders of magnitude lower than those of ^{237}Np. Therefore, to a first approximation, NFE release rates would be predicted to be three orders of magnitude lower under similar hydrologic conditions if the limiting factor for release rate is the solubility in the aqueous phase. This is one end-member that we consider in this set of calculations. The other extreme is to consider the total fluid phase ^{242}Pu as governed by radionuclide present either in the aqueous phase or sorbed to colloids. For this extreme, we assume that the aqueous phase plutonium is at the solubility limit, but that an additional portion of the inventory is also mobilized on colloids, so that the effective "solubility" (moles plutonium present in either the aqueous or pseudo-colloidal form) equals $C_S K_c$, where C_S is the aqueous solubility and K_c is the partitioning coefficient for sorbed plutonium defined in the previous chapter. For example, the $K_c = 999$ case raises the effective solubility, and presumably the release rate from the NFE, by three orders of magnitude from the value in the absence of colloids. Under these extreme conditions, release rates similar to those predicted for ^{237}Np would occur.

Figure 10-20 shows the predicted water table breakthrough curves obtained by convoluting the results of the Green's function calculation of total plutonium for the hydrologic base case (property set 6541, base infiltration map) with different durations of release corresponding to different K_c values. The parameter K_c has a multiplicative effect on the predicted mass flux at the water table. With little or no sorption to colloids, transport is slow, as shown earlier, and furthermore the NFE releases are limited by the low aqueous solubility of plutonium. At high K_c values, transport is enhanced and the NFE release rate is increased, resulting in much earlier and much higher mass fluxes a the water table. Because of this combined effect, the partitioning parameter K_c essentially controls the predicted breakthrough flux at the water table for this radionuclide. Further work to assess the importance of ^{242}Pu in total system performance should therefore focus primarily on estimating this key parameter. The influence of dimensionality is also fairly unimportant, as shown by the three-dimensional model result for $K_c = 999$ shown as the dotted curve on Figure 10-18.

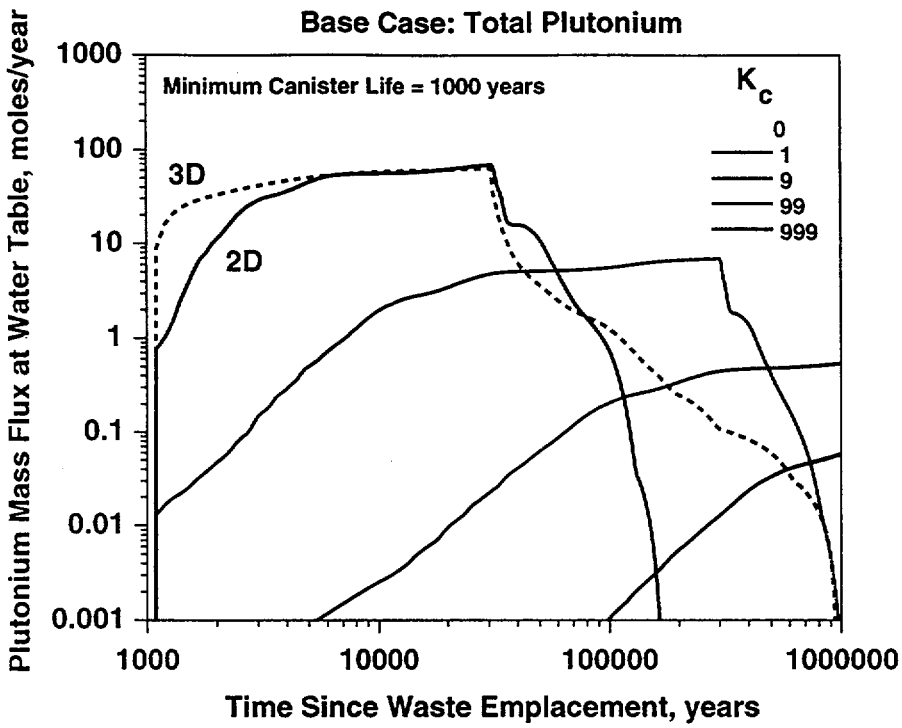

Figure 10-20. Water table breakthrough curves for total plutonium. Property set 6541, base infiltration map, different durations of release. Duration of release is directly proportional to effective solubility, which in turn is proportional to K_c.

Figure 10-21 shows the individual breakthrough curves for the various isotopes of plutonium for the $K_c = 99$ case. Because the release is solubility-limited, and congruent dissolution of the various isotopes is assumed, the quantity of long-lived isotopes such as ^{242}Pu increases as radioactive decay of ^{240}Pu and ^{239}Pu reduce the mass of each present in the near field.

10.10 Conclusions

Predicting the response at the water table to the large variety of near field environment (NFE) release scenarios is done most efficiently by decoupling the far-field and near-field models. This chapter describes the process of convolving NFE models with far-field transport simulations. With this approach, the differences in response due varying hydrologic conditions near waste emplacement drifts, different engineered barrier designs, time varying thermodynamic effects on canister corrosion, differing models of release due to dissolution of waste, and uncertainty in

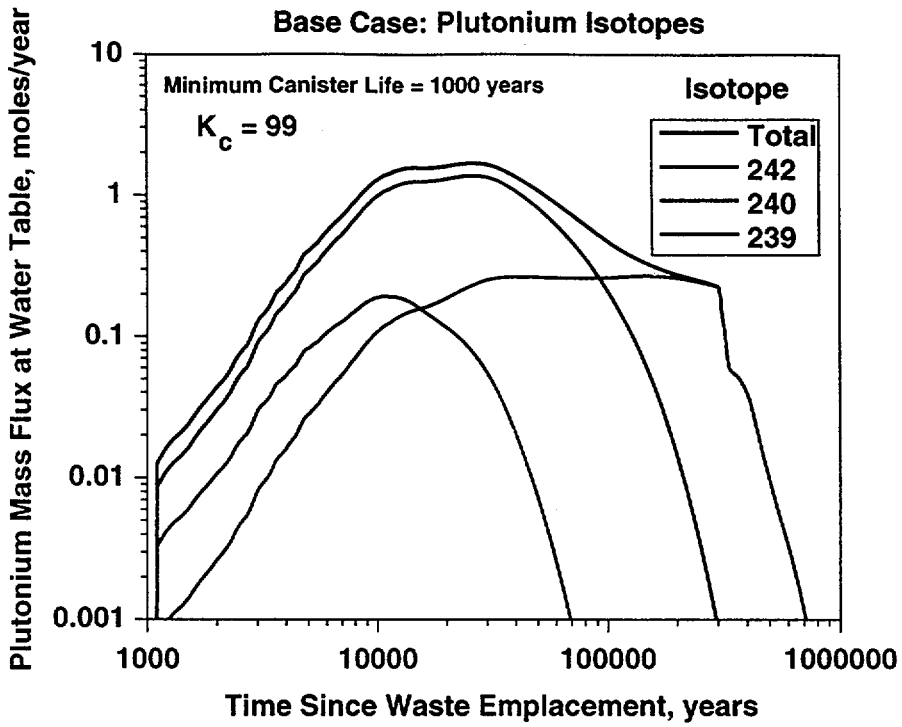

Figure 10-21. Water table breakthrough curves for individual isotopes of Plutonium. Property set 6541, base infiltration map, durations of release corresponding to $K_c = 99$.

transport processes in backfill and invert material can all be evaluated. The present study focuses on the unsaturated zone transport barrier; simplified NFE source term functions are used.

For nonsorbing radionuclides like ^{99}Tc, there is no retardation in any material between the potential repository and the water table. For all of the different property sets developed by LBNL, fracture flow through the zeolitic Calico Hills and underlying units results in bypassing of most of the unsaturated zone matrix material for the USGS infiltration estimates. NFE release rates control the maximum concentration flux at the water table. Releases that occur over longer periods of time lead to lower peak mass fluxes at the water table. Reducing the infiltration rate in these predictions also leads to lower peak mass flux rates at the water table, and they occur significantly later in time.

As with nonsorbing radionuclides, those that do sorb to zeolites like ^{237}Np still show early arrivals at the water table after release begins for these parameter sets due to the simulated fracture bypass of the zeolites. This early arrival appears to control the peak mass flux as well. Under these

conditions, two factors control the magnitude of the peak mass flux at the water table. First, the NFE release scenario directly influences the actual peak mass flux; rapid releases over short time periods yield higher peaks. Second, any parameter that influences the relative flow fraction through fractures has a direct impact on peak mass flux.

Relatively small changes from the LBNL parameters lead to vastly improved performance with respect to sorbing radionuclides. However, without modification, those parameter sets lead to predictions of very little mitigation of releases from the near field by the unsaturated zone. Reduction in uncertainty of the actual hydrologic properties of the Calico Hills (both fracture and matrix) would clarify whether these predictions of poor far-field barrier performance is indeed warranted or whether they are a by-product of a calibration procedure that was not well constrained by data indicating the degree of fracture flow in the units below the basal vitrophyre.

Chapter 11 - Reactive Transport of ^{237}Np with Repository Heat

11.1 Abstract

Characterization and performance assessment studies for the potential high-level nuclear waste repository at Yucca Mountain have identified ^{237}Np as a radionuclide of concern for the proposed repository. To predict the migration of neptunium after a repository breach, an understanding of the relevant hydrologic and geochemical processes is required. The hydrologic flow in the unsaturated zone at Yucca Mountain is dependent on the infiltration rate, stratigraphy of the vadose zone, and the heat generated by the decaying radioactive waste. The geochemical processes that strongly affect ^{237}Np migration include: solubility-limited release of ^{237}Np from the near-field environment, aqueous speciation of neptunium into non-sorbing carbonate/hydroxy complexes and the sorbing NpO_2^+ cation, sorption of neptunium onto the zeolitic tuffs via an ion exchange mechanism, and radioactive decay. We investigate the coupled effects of chemical interactions and heat on neptunium transport from the potential repository to the water table. The selective coupling method is introduced to solve these reactive transport problems. The simulations indicate that in the absence of irreversible changes in the hydrologic and transport properties, the heat pulse does not significantly affect the migration of neptunium, as the time scale of heat pulse propagation is shorter than the time scales associated with neptunium release and migration. Water chemistry, particularly pH and calcium and sodium concentrations, significantly affect the retardation of neptunium by the zeolitic rocks between the repository and the water table.

11.2 Software and Data QA Status

The FEHM code is used to perform all flow and transport calculations in this report. The code is qualified in accordance with Los Alamos quality assurance requirements and is

documented in (Zyvoloski et al., 1992, 1995a, 1995b). The QA status of the data used in this report is shown in Table 11-1.

Table 11-1. QA Status of Data used in this Chapter

REFERENCE	Q Status	DTN	COMMENT
Bertetti et al., 1996 "Neptunium (V) Sorption Behavior on clinoptilolite, Quartz, and Montmorillonite, Mat. Res. Soc. Symp., Proc., Vol. 412, 631-638, 1996	non-Q		
Flint et. al., 1996, Conceptual and numerical model of infiltration for the Yucca Mountain Area, Nevada", USGS WRIR MOL 19970409.0087	Q	GS960908312211.003/ NA	USGS DTN 3GUI623M
Nitsche et. al., 1993, "Measured Solubilities and Speciations of Neptunium, Plutonium, and Americium in a Typical Groundwater (J-13) from the Yucca Mountain Region", Los Alamos National Laboratory Report Number LA-12562-MS, July 1993	non-Q non-Q	LA000000000012.001 LA000000000012.002	Accession Nos. MOL.19950705.0241 NNA.19930507.0136, and MOL.19950621.0265, and MOL.19950711.0329
Ogard and Kerrisk, 1984, "Groundwater Chemistry along flow paths between a proposed repository site and the accessible environment, Los Alamos National Laboratory Report LA-10188-MS, 1984	non-Q	LA000000000038.001	Accession No. NNA.19870406.0021
Tait et. al., 1996, "Sorption as a function of groundwater chemistry to elucidate sorption mechanisms, Los Alamos National Laboratory Yucca Mountain Site Characterization Project Milestone 3219, 1996	Q Q	LAIT831341AQ95.001 LAIT831341DQ95.002	
Triay et. al., 1996a, "Summary and Synthesis Report on Radionuclide Retardation for the Yucca Mountain Site Characterization Project, Los Alamos National Laboratory YMP Milestone Report 3784	Q	LAIT831341AQ96.001	

Triay et. al, 1996b, "Radionuclide Sorption in Yucca Mountain Tuffs with J-13 Well Water,: neptunium, Uranium, and Plutonium, Los alamos National Laboratory Yucca Mountain Site Characterization Project" Milestone 3338, Technical Report LA-12956-MS	Q	LAIT831341AQ96.001 *	* DTN supersedes DTN LA000000000104.001
Triay et. al., 1996c, "Batch Sorption Results for neptunium transport through Yucca Mountain tuffs, Los alamos National Laboratory Yucca Mountain Site Characterization Project Milestone 3349, Technical Report LA-12961-MS	Q	LAIT831341AQ96.001 *	*DTN supersedes DTN LA000000000090.001
Triay et. al., 1996d, "Comparison of Neptunium Sorption Results using batch and column techniques, Los Alamos National laboratory Yucca Mountain Site Characterization Project Milestone 3041, Technical Report LA-12958-MS	Q	LA000000000106.001	DTN Accession No. MOL.19950630.0300

11.3 Introduction

In addition to the hydrologic processes that are important in controlling radionuclide migration, transport processes such as advection and dispersion, along with geochemical processes such as precipitation-dissolution, adsorption, and aqueous speciation reactions, will also affect the movement of radionuclides. For all but the most soluble radionuclides, the solubility determines the amount of radionuclide that will be mobilized after a canister breach. Many radionuclides participate in aqueous speciation reactions, resulting in the formation of numerous aqueous complexes. These complexes often differ in their adsorption behavior. The interaction among these various geochemical processes may play an important role in radionuclide migration. In general, a numerical model must account for these hydrological, transport and geochemical processes in order to be credible.

In this chapter, we investigate the migration of ^{237}Np from the potential repository to the water table (Viswanathan et al., 1997). Because of its long half life (2.14×10^6 years), relatively high solubility under oxidizing conditions, low dose limits, and predicted low sorption,

performance assessment models have identified ^{237}Np as a radionuclide of concern for the proposed repository at Yucca Mountain (Wilson et al., 1994; Andrews et al., 1995). We utilize FEHM (Zyvoloski et al., 1992) to study ^{237}Np transport. The reactive transport model for FEHM simulates the important geochemical processes that affect ^{237}Np migration. An equilibrium formulation is used for aqueous speciation reactions, because the time scale of such reactions are typically much shorter than groundwater transport time scales, making the local equilibrium assumption valid (e.g. Steefel and Lasaga, 1994). By contrast, rock-water interactions such as adsorption and precipitation-dissolution reactions often exhibit kinetic limitations in groundwater systems (e.g. Steefel and Lasaga, 1994). Therefore, we utilize a kinetic formulation for these rock-water reactions.

Previous studies (Birdsell et al., 1994; Robinson et al., 1995) have modeled the transport of ^{237}Np using linear equilibrium adsorption models which may have oversimplified these geochemical processes. The transport calculations of this chapter examine the migration of ^{237}Np as a function of groundwater chemistry and composition. Batch and column sorption experiments (Triay et al., 1996a, b, c; Tait et al., 1996) along with speciation and solubility experiments (Wolery, 1992; Nitsche et al., 1993; Bertetti et al., 1996; Efurd et al., 1996) are used to construct the reactive transport model. We then apply the model to the two-dimensional site-scale simulations.

The flow system is in part constrained by recent published data (Flint et al., 1996; Paces et al., 1996; Triay et al., 1996a; Robinson et al., 1996) used to estimate infiltration rate and bound the percolation flux through the unsaturated zone. Furthermore, we extend previous transport model predictions to non-isothermal conditions brought on by radioactive decay waste heat. Several studies have addressed the impact of heat on the thermohydrologic conditions in the near field (Buscheck et al., 1996) and at the site scale (Buscheck and Nitao, 1993) for the purpose of establishing the conditions to be experienced by waste packages. These packages are being designed to withstand a potentially corrosive environment for up to 10,000 years. The site-scale

thermohydrologic calculations of the present study are designed to study the possible impacts on ^{237}Np migration after waste canisters are breached and radionuclides escape the near-field environment.

The overall goal of this chapter is to examine the combined effects of infiltration rate, repository heat, and reactive transport processes on the migration of ^{237}Np from the potential repository to the water table. Including these effects will allow us to assess the validity of assumptions embodied in previous studies such as isothermal conditions and linear equilibrium sorption. Furthermore, such simplifications, if valid, will greatly facilitate future performance assessment calculations, which typically involve hundreds of Monte Carlo simulations in which numerous uncertain parameters are varied in an attempt to capture the overall uncertainty of the system.

11.4 Model Description

11.4.1 Flow and Energy Formulations

Detailed derivations of the governing equations for two-phase flow including heat transfer have been described by several investigators (e.g. Brownell et al., 1975; Mercer and Faust, 1975; Zyvoloski, 1983). The FEHM code is a two- or three-dimensional finite element code suitable for simulating systems with complex geometries that arise when modeling subsurface flow and transport. In the unsaturated zone, the system of governing equations arises from the principles of conservation of water and air, as well as conservation of energy. Darcy's law is assumed to be valid for the movement of each phase. In most simulations in this chapter, the relative permeability curves for the fractured rock are assumed to be adequately represented by an equivalent continuum model (ECM). The primary assumption in the model is that the capillary pressure in the fractured medium equals that in the matrix. Assuming the fractured and matrix domains can each be described using the characteristic curve model introduced by van Genuchten (1980), the composite permeability of the medium at a given matrix saturation (and capillary pressure) can be represented

as a weighted average of the permeabilities of the two media. From this treatment, a single value can be obtained for the relative permeability. Because fractures are predicted to be dry until the capillary pressure in the matrix reaches a low value (at high saturation), the permeability is dominated by matrix properties until almost complete saturation of the matrix, after which fracture saturations and liquid permeabilities rise due to fracture flow. Limits of applicability of the ECM model were explored for fluid flow by Pruess et al. (1990).

For transport calculations, these assumptions are less likely to be applicable than for the case of fluid flow because of the longer time scales of solute transport relative to transmission of a fluid pressure difference within a matrix block as described in Chapters 4 and 5. Therefore, we also include a series of one-dimensional scoping calculations using a dual permeability model (DKM). In this model formulation, fractures and matrix are treated as two overlapping continua, with appropriate properties assigned for each continuum. Additionally, there is a transfer term describing fluid flow between the two continua at each location in space. An additional parameter, a characteristic length scale for transport of heat, mass, and solutes between the two continua, is also required. When this length is small, the model reverts to ECM behavior. For larger lengths, the coupling between the fracture and matrix domains is weak, and flow in the two media becomes more independent. Because fracture-dominated flow and transport is expected to be present in some stratigraphic units, it is essential to consider the relative flow fractions in the two media as demonstrated in Chapter 5. Current limitations in the model preclude simulations of the full reactive transport system with heat effects in dual permeability. Therefore, we use these dual permeability scoping calculations as a guide to adjusting an ECM model to capture the influence of fracture flow and radionuclide transport. Provisions for correcting the model for transport are developed in section 11.8.1.

11.4.2 Reactive Transport Equations

The equations in the reactive transport model are coupled to the heat and flow system because the flow and energy equations are used to obtain flow velocities and temperature-dependent transport properties. However, we assume that transport has a negligible effect on fluid

properties, permeability, and the heat balance and do not consider possible effects on rock properties due to the mineralogic alteration of rocks and the redistribution of dissolved minerals. Furthermore, the alteration and recrystallization of minerals to phases that are either more sorptive or less sorptive is not addressed here.

FEHM uses aqueous, immobile, and vapor components as the primary dependent variables (PDVs) in the reactive transport equations. A set of chemical components is defined as the minimum number of species that uniquely describe the chemical system (Mangold and Tsang, 1991). In FEHM, the secondary dependent variables (SDVs) are uncomplexed aqueous component concentrations and aqueous complex concentrations. We assume that all aqueous phase speciation reactions are at equilibrium (known as the local equilibrium assumption), resulting in the following relationship between PDVs and SDVs:

$$C_j = c_j + \sum_{i=1}^{N_x} a_{ij} x_i \qquad j = 1, \ldots, N_c \qquad \text{(Eq. 11-1)}$$

where C_j is the total aqueous concentration of component j, c_j is the uncomplexed concentration of component j, x_i is the concentration of complex i, a_{ij} is the stoichiometric coefficient representing the number of moles of component j in complex i, N_c is the number of aqueous components and N_x is the number of aqueous complexes (Yeh and Tripathi, 1989).

Applying the local equilibrium assumption to aqueous phase speciation reactions greatly reduces the number of PDVs in the transport equations and is generally accepted to be a valid assumption (e.g. Steefel and Lasaga, 1994). Given the total aqueous concentration of each aqueous component, the SDVs can be calculated using a set of nonlinear algebraic equations derived from chemical equilibrium theory (e.g. Lichtner, 1996). To obtain the total aqueous concentrations, the reactive transport equations for aqueous, immobile, and vapor components must be solved. There are no SDVs for either vapor or immobile components, because the model as currently formulated

treats only aqueous speciation. Reactions involving vapor and immobile components are treated with a kinetic formulation, with kinetic reactions represented as reaction source-sink terms in the reactive transport equations.

11.4.2.1 Governing Equations for the PDVs

For transient fluid flow, the generalized version of the reactive transport equation for an aqueous component is

$$\frac{\partial A_j}{\partial t} = \nabla\bullet(\phi S_l D_j \nabla \rho_l C_j) - \nabla\bullet f_c + R_j \qquad j = 1, \ldots, N_c \qquad \text{(Eq. 11-2)}$$

where $A_j = \phi C_j S_l \rho_l$ is the solute mass storage per unit total volume for aqueous component liquid concentration C_j (units of concentration are moles/kg fluid); $f_c = \rho_l C_j u_l$ is the advective mass flux of solute; D is the hydrodynamic dispersion tensor; S_l is the saturation; u_l is the Darcy velocity vector; ϕ is the porosity; S_l is the liquid saturation; and R_j is the kinetic reaction source-sink term. The porosity is an effective porosity for transport, which in the code can be assigned different values than the values used for fluid flow. This provision allows us to simulate the case in which fracture flow results in a low transport porosity due to the small pore volume available for transport within the fractures. To simplify the notation for the remainder of the chapter, we define the advection-dispersion operator:

$$L_l(C) = \nabla\bullet f_c - \nabla\bullet(\phi S_l D_j \nabla \rho_l C_j) \qquad \text{(Eq. 11-3)}$$

Equation (Eq. 11-2), the reactive advection dispersion equation, can then be rewritten as:

$$\frac{\partial A_j}{\partial t} + L_l(C_j) = R_j \qquad j = 1, \ldots, N_c \qquad \text{(Eq. 11-4)}$$

The reaction transport equation for a vapor component takes on a similar form to Equation 11-4 and is given by

$$\frac{\partial B_k}{\partial t} + L_v(G_k) = R_k \qquad k = 1, \ldots, N_v \qquad \text{(Eq. 11-5)}$$

where B_k is the solute mass per total volume of component k, G_k is the vapor concentration of component k, u_v is the vapor Darcy velocity vector and N_v is the number of vapor components. The hydrodynamic dispersion tensor is assumed to reduce to longitudinal and transverse components (e.g. Lichtner, 1996).

Immobile components are not transported and are therefore treated using a simple mass balance given by

$$\frac{\partial M_m}{\partial t} = R_m \qquad m = 1, \ldots, N_{im} \qquad \text{(Eq. 11-6)}$$

where M_m is the immobile concentration (mass solute per unit mass rock matrix) of component m and N_{im} is the number of immobile components.

The reaction rate terms in Equations 11-4, 11-5, and 11-6 originate from the kinetic reactions in the system and may be nonlinear functions of the concentrations of the total aqueous components, uncomplexed aqueous components, aqueous complexes, immobile components and vapor components. FEHM is capable of modeling the following kinetic processes: linear adsorption, nonlinear Langmuir adsorption, ion/surface exchange, precipitation-dissolution and liquid-vapor interchange of solute. The specific kinetic models used to model ^{237}Np adsorption and dissolution will be provided in the application section. Equations 11-4, 11-5, and 11-6 result in a system of $(N_c + N_m + N_v)N_n$ nonlinear coupled partial differential equations (PDEs) where N_n is the number of spatial grid points. FEHM's method for solving this system of coupled PDEs will be discussed in the solution procedure section.

11.4.2.2 *Governing Equations for the SDVs*

Given all of the aqueous component concentrations, the uncomplexed aqueous component concentrations and aqueous complex concentrations can be calculated using chemical equilibrium theory. The chemical equilibrium calculations performed by FEHM are similar to the techniques

used in batch geochemical software such as EQ3/6 (Wolery, 1992). A chemical reaction describing aqueous speciation can be written in the following general form

$$\sum_{j=1}^{N_c} a_{ij}\hat{C}_j \Leftrightarrow \hat{X}_i \qquad i = 1, \ldots, N_x \qquad \text{(Eq. 11-7)}$$

where $\hat{C}_j$ is the chemical formula for the aqueous component j, and $\hat{X}_i$ is the chemical formula for the aqueous complex i. FEHM assumes that all aqueous speciation reactions are at local equilibrium. The mass action expression for an aqueous component is given by

$$K_i = x_i \prod_{j=1}^{N_c} (\gamma_j c_j)^{-a_{ij}} \qquad \text{(Eq. 11-8)}$$

where K_i is the equilibrium formation constant for complex i and γ_j is the activity coefficient for aqueous component j. In these calculations, we neglect ionic strength corrections. For example, for Yucca Mountain well UZ-14, the chemical analyses (Figure 2) yield a range of ionic strengths from 0.004 to 0.013 mol/l, for which the Davies equation for activity coefficients yields γ_j values that are very close to 1. Equations 11-1 and 11-8 can be combined to express the total aqueous concentration of component j as a function of the uncomplexed component concentrations:

$$C_j = c_j + \sum_{i=1}^{N_x} a_{ij} K_i \prod_{z=1}^{N_c} c_z^{a_{iz}} \qquad j = 1, \ldots, N_c \qquad \text{(Eq. 11-9)}$$

Equation 11-9 results in a set of N_c nonlinear algebraic equations to be solved given all of the total aqueous concentrations.

11.5 Solution Procedure

The solution of the flow and energy equations will not be discussed in this chapter. This description can be found in Zyvoloski et al. (1992).

11.5.1 Solution Method for the PDVs:

The reactive transport equations given by Equations 11-4, 11-5 and 11-6 result in a set of nonlinear coupled PDEs. Many reactive transport codes, including FEHM, utilize a two-step approach to decouple the PDEs (e.g. Cederberg et al., 1985, Narasimhan et al., 1986, Yeh and Tripathi, 1989). Two-step methods divide the solution into a transport step, in which the aqueous and vapor components are transported by advection and dispersion, and a reaction step, in which aqueous, vapor and immobile components react with one another. The transport and reaction steps are either coupled iteratively or sequentially (Walter et al., 1994). In FEHM, the transport and reaction steps are coupled iteratively. First, a trial solution for the reaction terms is computed. These reaction terms are then used in the transport step. Iteration between these two steps is performed until convergence is achieved.

The numerical implementation of the transport step can be derived by rewriting Equations 11-4, 11-5 and 11-6 in fully implicit time-discretized form:

$$\frac{C_j^{n+1} - C_j^n}{\Delta t} + L(C_j)^{n+1} = R_j^{n+1} \qquad \text{(Eq. 11-10)}$$

$$\frac{G_k^{n+1} - G_k^n}{\Delta t} + L(G_k)^{n+1} = R_k^{n+1} \qquad \text{(Eq. 11-11)}$$

$$\frac{M_m^{n+1} - M_m^n}{\Delta t} = R_m^{n+1} \qquad \text{(Eq. 11-12)}$$

where n indicates the time step level. The reaction rate terms in these equations can be estimated using a Taylor series expansion to linearize the reaction rate term

$$R_i^{n+1,p+1} = R_i^{n+1,p} + \sum_{j=1}^{N_c} \left(\frac{\partial R_i}{\partial C_j}\right)^{n+1,p} (C_j^{n+1,p+1} - C_j^{n+1,p}) +$$

$$\sum_{k=1}^{N_v} \left(\frac{\partial R_i}{\partial G_k}\right)^{n+1,p} (G_k^{n+1,p+1} - G_k^{n+1,p}) + \qquad \text{(Eq. 11-13)}$$

$$\sum_{m=1}^{N_{im}} \left(\frac{\partial R_i}{\partial M_m}\right)^{n+1,p} (M_m^{n+1,p+1} - M_m^{n+1,p}) + \ldots$$

where p is the iteration level and i represents either an aqueous, vapor or immobile component. The iterative methods in the literature differ in the number of terms evaluated in this Taylor series expansion. Expanding each term on the left hand side of equations 11-10, 11-11 and 11-12 in a Taylor series and substituting the expanded reaction rate given by Equation 11-13 results in a set of linear algebraic equations which constitute a single iteration of the Newton-Raphson method. However, the Newton-Raphson method results in a large system of coupled linear equations stemming from the derivative terms of R_i with respect to other aqueous, vapor, or immobile components. The approximate iterative approaches in the reactive transport literature often drop terms in the Taylor series expansion to decouple the linear equations into smaller equations sets that are solved sequentially. The sequential iterative approach described by Engesgaard and Kipp (1992) and Kinzelbach et al. (1991) use only the first term in the Taylor series ($R_i^{n+1,p}$). We will refer to this method as the SIA-0 method. We have found that this method works efficiently for relatively slow kinetic reactions but becomes inefficient for faster kinetic reactions. It is possible to improve the SIA-0 method by including additional terms in order to improve the convergence of SIA. The SIA-1 method estimates the reaction term as:

$$R_i^{n+1,p+1} = R_i^{n+1,p} + \left(\frac{\partial R_i}{\partial C_i}\right)^{n+1,p} (C_j^{n+1,p+1} - C_j^{n+1,p}) \qquad \text{(Eq. 11-14)}$$

The SIA-1 approach seeks to improve the estimate of $R_i^{n+1,p+1}$ by considering the relationship between R_i and C_i only. That is, the relationships with other aqueous, vapor and immobile components are neglected, and the linear equations arising from the individual components are solved separately. We have found that the SIA-1 greatly improves convergence for large Damkohler number systems, when kinetics are fast compared to the transport time scale (Tebes-Stevens et al., 1997). However, for certain reactions, the SIA-1 approach becomes quite inefficient because some of the cross derivative terms ($\partial R_i / \partial C_j, i \neq j$) that are neglected by SIA-

1 are significant. Physically, this can occur when aqueous, vapor, or immobile components that are, in fact, coupled to one another are treated as though they were independent. In an extension of the SIA methods, we selectively include additional derivative terms that couple a subset of the components to one another to improve convergence. Since cross derivative terms, $\partial R_i / \partial C_j$, are now included in the calculation, sets of components must be solved simultaneously. We note in passing that in the extreme case in which only $\partial R_i / \partial C_i$ are calculated, the method reduces to the SIA-1 method. At the other extreme, in which all components are coupled, a global implicit solution scheme (Steefel and Yabusaki, 1996) is effectively obtained. We say effectively because in this implementation, a reaction iteration is still required to include the aqueous speciation reactions. Nonetheless, only a few iterations (less than 5) are typically required when the reactive transport equations for components that are strongly coupled through reaction terms are solved simultaneously.

The linear equation solver in FEHM was developed primarily for the solution of coupled fluid flow and heat transport. The solver makes use of well-tested numerical techniques that take advantage of the block structure of the coupled equations for pressure, temperature, and fluid saturation (e.g. Zyvoloski, 1983; Behie et al., 1985). Here, we use the same solver technologies for the transport solution step. In essence, for N_{dof} (where N_{dof} is the number of "degrees of freedom," in this context equal to the number of components solved simultaneously) unknowns per grid point, the same operations on the overall matrix of a single-unknown solution are carried out, but multiplications of individual matrix elements now become matrix multiplications involving the $N_{dof} \times N_{dof}$ submatrices, and divisions are carried out as multiplications by the inverse of the submatrix. Since such operations become memory and cpu intensive for large problems, it is important to employ efficient numerical techniques. FEHM uses numerical methods suitable for the nonsymmetric matrices that arise from the finite element solution of reactive transport equations on unstructured numerical grids. The solver software uses incomplete factorization with variable fill-in level (Zyvoloski, 1986) as a preconditioner, and a generalized minimum residual

(GMRES) acceleration technique (Saad and Schultz, 1986) for the iterative solution. Details of this method as applied to heat and mass transport problems may be found in Zyvoloski et al. (1992). In a typical reactive transport solution with FEHM, the heat and mass transfer solution is also being performed, so the initial bookkeeping associated with the method is already being carried out, and the memory allocated for the solution is shared between the heat and mass solution and the transport solution.

There are definite trade-offs in computational efficiency and memory utilization between the SIA techniques and methods involving coupling of the transport equations of individual components. Coupling requires more time per iteration and more memory than typical SIA methods. However, components strongly coupled by reaction may not converge using SIA methods without using small time steps. Since flexibility is required in a general purpose code, the transport iteration in FEHM was developed with a provision we call Selective Coupling to solve the component concentrations in groups of one or more at a time, so that only those components that need to be coupled are solved simultaneously. It is necessary to solve a set of equations for each component present in the system, but the order of solution and the nature of the coupling are set by the user at run-time. This allows the user, on the basis of his knowledge of the reactive transport system, to couple only those components that are required for efficient solution of the system of equations. Selective Coupling of components linked to each other through kinetic chemical reactions allows a given problem to be solved in the fastest, yet most memory efficient manner possible (Viswanathan, 1996). The use of this provision in the solution of the neptunium transport chemical system is demonstrated in the application section of this chapter, however, the methods used should have wider applicability in the field of reactive chemical transport. Details of the computational performance of this method will be explored in a future publication.

11.5.2 Solution Method for the SDVs

Every time a trial solution for the reaction terms is calculated in a transport iteration, the SDV's must be solved for. The Newton-Raphson method is used to perform these calculations at each grid point. The solution procedure is similar to batch geochemical codes such as EQ3/6 (e.g.

Wolery, 1992). The techniques used to handle pH calculations are presented in Tebes-Stevens et al. (1997).

11.6 Yucca Mountain Unsaturated Zone Hydrology and Geochemistry

11.6.1 Hydrogeologic Setting

Characterization of the hydrostratigraphy of the unsaturated zone at Yucca Mountain generally follows from the delineation of major stratigraphic units and structural features such as faults. The stratigraphic structure of the unsaturated zone of Yucca Mountain is comprised of alternating layers of welded and nonwelded volcanic tuff that are tilted, uplifted, fractured, and faulted. Information from boreholes, the Exploratory Studies Facility (ESF), a shaft currently under construction, and surface studies has led to various classification schemes for the stratigraphy at the site (e.g. Scott and Bonk, 1984; Buesch et al., 1996). The repository, if constructed, will be located approximately 350 m above the water table and roughly 200 to 300 m below ground surface, depending on the local topography, within the nonlithophysal portion of the Topopah Springs welded (TSw) unit (Figure 11-1d). From the surface, the highly fractured Tiva Canyon welded (TCw) unit (not present at well UZ-14 in Figure 11-1d) is the first major stratigraphic unit encountered under a largely unconsolidated alluvial cover that varies in thickness from zero to more than 50 m. Below the TCw is the Paintbrush tuff nonwelded (PTn) unit, with a higher permeability in the rock matrix, but lower bulk permeability due to lower fracture density. The TSw unit consists mainly of highly welded and fractured subunits of devitrified tuff, some of which contain a high density of lithophysal cavities. The TSw extends about 100 to 150 m below the potential repository before the Calico Hills nonwelded (CHn) unit is reached. The CHn is a less fractured tuff that contains both vitric sections and a horizon that exhibits extensive zeolitic alteration. In the cross section chosen for calculations, the underlying Prow Pass and Bullfrog units also lie above the water table, and both have zones of zeolitic alteration. In general, the major hydrostratigraphic units dip to the East at angles of 5 to 10° (Figure 11-2a), creating the possibility

of lateral flow at the interfaces of units of contrasting hydrologic properties. The predominant modes of fracturing are cooling joints and fractures and faults induced by past tectonic activity. Experimental laboratory and field measurements, as well as conceptual and numerical models (Montazer and Wilson, 1984; Wittwer et al., 1995; Altman et al., 1996; Robinson et al., 1996), suggest that some of these features may be associated with complex subsurface flow patterns. In this set of calculations, the major stratigraphic units were further subdivided to capture important differences within the units such as the low porosity vitrophyre at the base of the TSw. Hydrologic property values for each unit (listed for all units in Robinson et al., 1996) were derived from Wittwer et al. (1995) for the units from the surface to the TSw and Loeven (1993) for the CHn units.

11.6.1.1 *Unsaturated Zone Geochemistry*

The major ion chemistry of fluids in the unsaturated zone will impact many aspects of repository behavior, including the corrosion of waste packages, dissolution rate of the waste form, and solubilities, speciation, and sorption of radionuclides. In addition, the chemical data provides important insights on the hydrologic system of the unsaturated zone. The use of chloride and other ions to characterize the unsaturated zone hydrology is the subject of ongoing studies, and will be treated only very briefly here. Figure 11-1(data published in Yang et al., 1996) shows the important anions (11-1a), cations (11-1b), and pH (11-1c) of the unsaturated zone fluids in samples extracted from non- to partially welded tuffs in wellbore UZ-14.

The chloride mass balance method (Allison et al., 1985, Scanlon, 1991) can be used to estimate the infiltration rate. The method assumes that the deposition of chloride onto the surface occurs at a constant rate both in precipitation and as dry fallout. Evapotranspiration serves to concentrate the infiltrating fluid in chloride by a factor that is proportional to the amount of evapotranspirative loss of water in the soil zone. Given this conceptual model, we obtain I using $I = C_p P / C_s$, where C_p is the concentration in precipitation (estimated to be 0.4 ppm by Triay

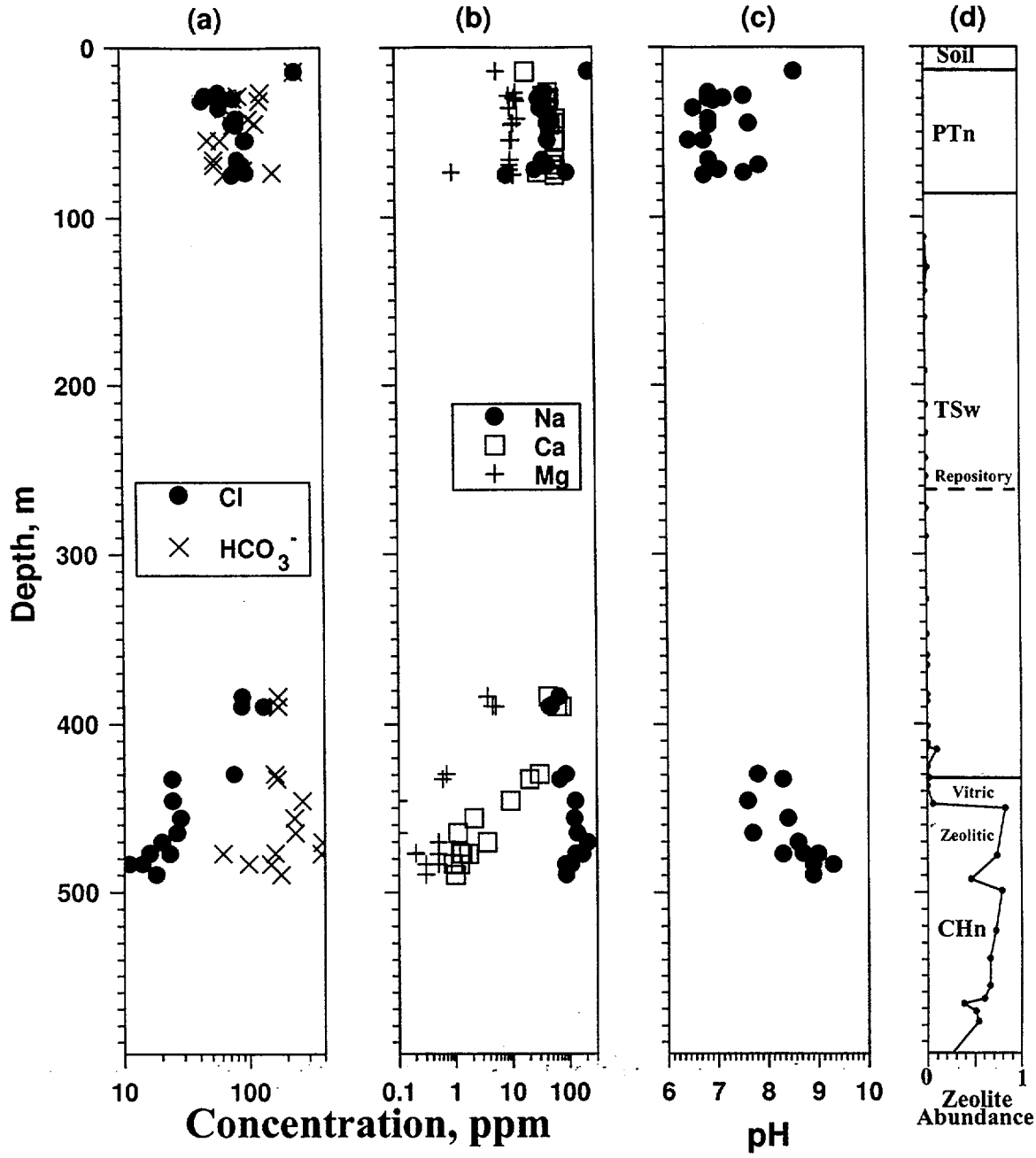

Figure 11-1. Geochemistry and stratigraphy of well UZ-14 (aqueous chemical data from Yang et al., 1996). (a) Chloride and bicarbonate concentration, (b) sodium, calcium, and magnesium concentration, (c) pH and (d) stratigraphy and zeolite abundance

et al., 1996a), C_s is the concentration in the sample (for example, 87 ppm for the PTn samples in UZ-14, Figure 11-1a), and P is the precipitation rate (taken to be 170 mm/y, from Hevesi and Flint, 1996). This method yields an estimated percolation rate of 0.8 mm/y in the vicinity of UZ-14, with

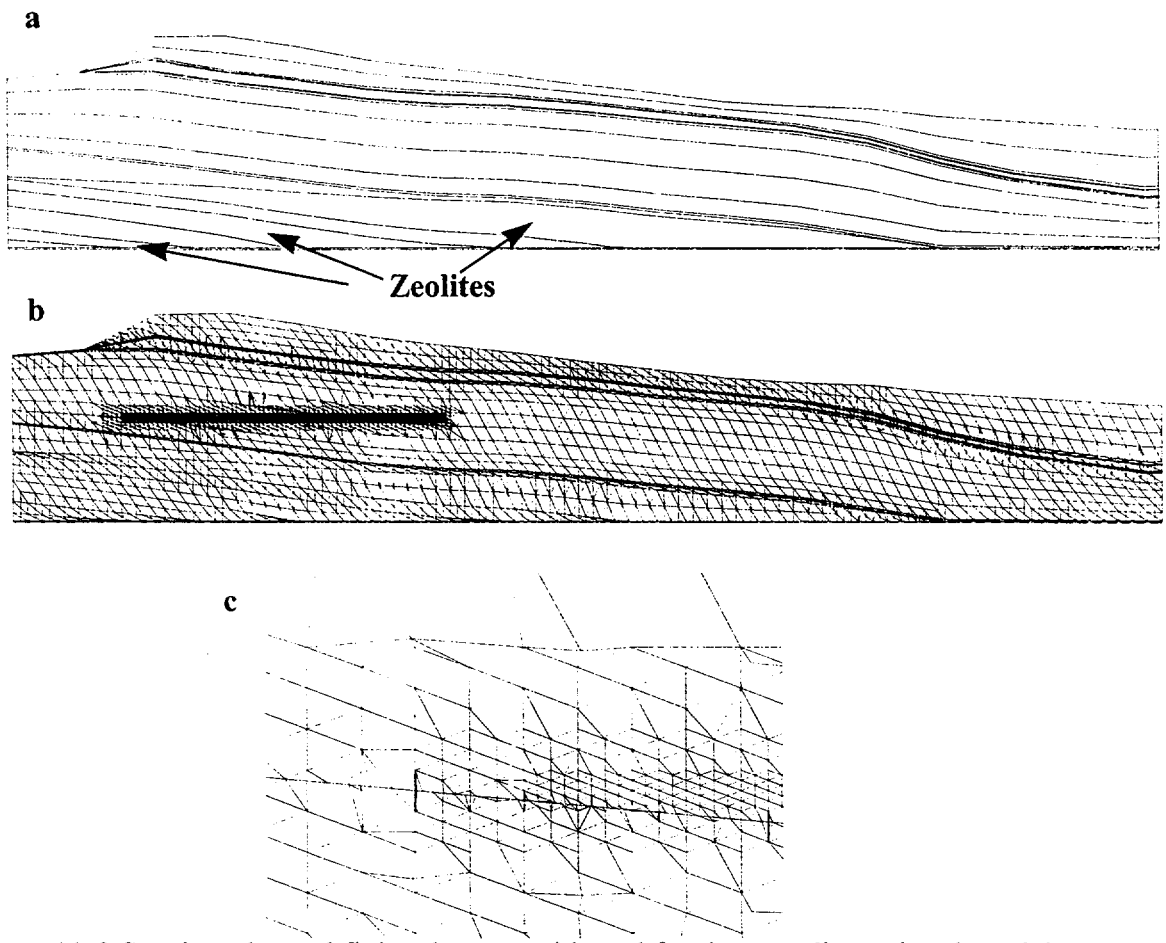

Figure 11-2. Stratigraphy and finite element grid used for the two-dimensional model cross section. (a) stratigraphy, including locations of zeolitic rocks, (b) finite element grid, (c) close-up of a small portion of the grid near the repository.

estimates based on the individual samples ranging from 0.3 to 1.4 mm/y. This range is lower than the current average infiltration rate in the vicinity of UZ-14 of 3 mm/y cited by Flint et al. (1996), but the agreement is adequate when considered in the context of a spatially varying infiltration model with a range of values from 0 to over 20 mm/y (see the next section).

The chloride concentration at greater depths is significantly lower than the values in the PTn. This result is consistent with either lateral diversion of fluid originating at a higher infiltration region at the surface, or a climate change scenario, in which a wetter climate during the Pleistocene Epoch (about 10 ky ago) resulted in higher infiltration rates and fluids of lower chloride concentration that have taken roughly 10 ky to percolate to this depth. In these simulations, we use

the latter explanation to justify the examination of the neptunium transport system assuming a future wetter climate scenario, in which infiltration rates increase as dissolved ion concentrations decrease.

The cation chemistry in UZ-14 (Figure 11-1b) and other wells at Yucca Mountain are used in the present study to obtain ranges of concentrations to use in simulations and to justify the use of an ion exchange model of neptunium sorption. In the section titled Neptunium Chemistry below, we show that the available sorption data are consistent with ion exchange on zeolitic tuffs. Zeolites are located above the water table in the Calico Hills unit (Figure 11-1d) and the underlying Crater Flats tuffs (located below the water table in UZ-14). With a conceptual model of local one-dimensional downward percolation of fluid, the cation concentrations in Figure 11-1b suggest a dynamic system of ion exchange within the zeolitic horizons, with Na^+ competing with K^+ (data not available for UZ-14), Ca^{2+}, and Mg^{2+}. As with chloride, the profiles are consistent with a transient hydrogeochemical system, in which the relative cation concentrations entering the zeolites are different than in the past. It appears that at the present time, divalent cations are sorbing at the top of the zeolitic horizon at the expense of Na^+, which is transported to greater depths at higher concentrations than the fluid entering the horizon. Current modeling efforts are directed toward using the ion exchange system to understand the transient hydrologic and chemical system. For now, we use data from wellbores UZ-14 (Figure 11-1), UZ-16, and NRG-6 to bound the range of concentrations of cations in the neptunium ion exchange model. The ranges for the unsaturated zone fluids are 50-200 ppm for Na^+, 1-50 ppm for Ca^{2+}, 0.1-20 ppm for Mg^{2+}, and 7 to 9 for pH (Figure 11-1c).

11.6.2 Fluid Percolation Rate

The percolation rate of water through the unsaturated zone will control the migration rate of radionuclides to the water table, and thus is of critical importance in these simulations. Of the estimated 170 mm/y average precipitation rate at the site, only a small fraction is expected to escape evapotranspiration and run-off and percolate deep into the subsurface rock layers. The

nature of the infiltration at the surface is likely to be episodic, associated with individual storms and seasonal differences in average precipitation. Infiltration is also almost certainly spatially variable, a result of differing near-surface hydrogeologic conditions. Estimated maps of temporally averaged infiltration rates have been constructed based on models of surface soil hydrologic processes, calibrated with measurements of moisture content in shallow boreholes (Flint et al., 1996). The deep percolation rates derived from these measurements are uncertain due to difficulties in developing a comprehensive model for the evapotranspirative processes that control the results. Nonetheless, estimates vary spatially from zero net infiltration (typically in zones of extensive alluvial cover) to 20 mm/y infiltration. The highest estimates tend to occur at greater elevations and in regions of thin soil layers. The average infiltration rate in the modeled area for this 0 to 20 mm/y range is about 5 mm/y.

Geochemical methods to estimate the rate of deep fluid percolation have recently been compared to the near-surface moisture profile monitoring studies. Estimates using the chloride mass balance method discussed above, yield site-wide estimates of infiltration rate ranging from 0.4 to 22 mm/y (infiltration estimates reported by Triay et al., 1996a). Fabryka-Martin et al. (1996b) illustrate that measurements of ^{36}Cl in samples collected in the ESF are consistent with an average infiltration rate in excess of about 1 mm/y, and perhaps as high as 10 mm/y. Robinson et al. (1996) present results of modeling of the ^{14}C liquid age measurements of Yang et al. (1996), concluding that the data are consistent with percolation rates between 1 and 5 mm/y. Finally, Paces et al. (1996) use a conceptual model of continuous deposition of calcite to estimate the infiltration rate that is consistent with the total estimated quantity of calcite present in the vadose zone. A 2 mm/y infiltration rate is predicted using this method.

The results of these studies illustrate the difficulty of obtaining precise estimates of average infiltration rate through the unsaturated zone. Some of the variability of the estimates is the result of the approximations and lack of sensitivity of the estimation techniques, but the wide range no doubt also reflects true variability in space and time of the infiltration process. In this chapter, we

deal with this variability and uncertainty through sensitivity analyses, in which different infiltration rate scenarios are selected for study. Spatially uniform infiltration rates of 1 and 4 mm/y were selected as representative of the average ranges discussed above, and a spatially variable infiltration rate based on the work of Flint et al. (1996) is used to investigate the impact of spatial variability. For this case, the average infiltration rate at the cross section (Figure 11-2a) selected is 4.8 mm/y, with values ranging from 0 to 18 mm/y. The variable infiltration scenario which is discussed in forthcoming sections refers to this work by Flint et al. (1996).

11.6.3 Computational Domain

The domain selected for the transport calculations is a two-dimensional, East-West cross section through Antler Ridge. Figure 11-2a shows the East-dipping stratigraphy at this cross section, including the zeolitic horizons important to the transport of neptunium, the location of the potential repository and major fault zones that intersect the cross section. Although there are variations in thicknesses of stratigraphic units in the North-South direction, this cross section is a representative slice through the three-dimensional system that allows the issues relevant to transport of neptunium to be studied. The finite element grid for the entire cross section is shown in Figure 3b. The X3D grid generator (Trease et al., 1996) was used to develop this grid. The grid generator is capable of honoring the stratigraphic boundaries, while providing regions with fine discretization, such as the repository region (Figure 11-2c). This allows heat to be applied to a node representing an individual drift (a tunnel containing the waste canisters) in the repository with several nodes in between to capture the heat transfer and fluid flow behavior between drifts in the near-field region. Furthermore, the neptunium inventory can be placed only at nodes representing the drifts. For this grid, the nominal node spacing in the near-field region is 3 m.

11.7 Neptunium Chemistry

The sorption coefficient K_d for ^{237}Np measured on core samples in the laboratory varies from effectively 0 to values of order 5 cc/g, over the range of geochemical conditions found in

Yucca Mountain fluids and rocks. This range has sufficient impact on performance to motivate the development of a reactive transport model that predicts the adsorption of ^{237}Np as a function of water composition. Considerable experimental work has been done to characterize ^{237}Np solubility, speciation and sorption over the range of conditions expected at the Yucca Mountain site (e.g. Nitsche et al., 1993; Bertetti et al., 1996; Efurd et al., 1996; Triay et al., 1996a). We have combined these experimental results with studies of the Yucca Mountain groundwater and pore-water geochemistry (Ogard and Kerrisk, 1984; Triay et al., 1996a; Yang et al., 1996) to develop a reactive transport model for ^{237}Np that includes dissolution, speciation and sorption of ^{237}Np as a function of groundwater composition.

The experimental program for studying ^{237}Np sorption, solubility, and speciation was designed under the assumption that fluids from the saturated zone in wells J-13 and UE-25 p#1 (Table 11-2) can be used to bracket the composition of the Yucca Mountain fluids in the unsaturated zone (UZ) (Meijer, 1992). J-13 water is a dilute sodium bicarbonate water from the shallow saturated zone. Calcium, potassium, and magnesium are the major cations, and bicarbonate, sulfate, chloride and fluoride are the major anions, in order of decreasing concentration. Silica is the only other major constituent (Ogard and Kerrisk, 1984). UE-25 p#1 water is obtained from the saturated zone from the deeper Paleozoic carbonate aquifer, and has higher concentrations of most of these chemical species.

Table 11-2. Groundwater Compositions (ppm) of Unsaturated Zone Fluids and Fluids Used in Sorption Studies

Species(mg/L)	J-13 Ogard and Kerrisk (1984)	UE25 p#1 Ogard and Kerrisk (1984)	UZ Fluids Yang et al. (1996)
Ca	11.5	87.8(10)*	1-50
Mg	1.8	31.9	0.1-20
Na	45	171	50-200
HCO3	143	698	50-300
pH	6.9	6.7	7-9

*Ca concentration after degassing and precipitation of $CaCO_3$ is shown in parenthesis. The lower value is typical of values in sorption studies (Triay et al. 1996a).

11.7.1 Solubility and ^{237}Np Inventory

Solubility establishes an upper limit for the concentration of aqueous neptunium in the source term for radionuclide migration from the near-field environment. Nitsche et al. (1993) and Efurd et al. (1996) measured the solubility of ^{237}Np from groundwaters representative of the Yucca Mountain region. The more recent measurements of Efurd et al. (1996) are considered to be more representative since they employed refined experimental techniques for adjusting solution pH. Solubilities for J-13 groundwaters are shown in Table 11-3.

Table 11-3. Solubility of ^{237}Np (Efurd et al. (1996))

Temperature, °C	pH 5.9	pH 7	pH 8.5
25	6.5×10^{-4}	3.1×10^{-5}	1.5×10^{-5}
60	9.4×10^{-4}	1.6×10^{-5}	1.7×10^{-5}
90	9.0×10^{-4}	7.9×10^{-6}	5.5×10^{-6}

We model the precipitation-dissolution of neptunium at the repository with a first order kinetic expression (e.g. Lasaga, 1984). The solubility product data at 25, 60, and 90°C are used by the model to estimate the value of the solubility product as a function of temperature using polynomial interpolation. Neptunium dissolution has proven to be fast in comparison to the transport time scales associated with Yucca Mountain (Nitsche et al., 1993). Therefore, we select the kinetic parameter value to ensure that the reaction proceeds to equilibrium.

The solid component represents the total amount of ^{237}Np present at a given repository node and is the source term for any aqueous neptunium released into the system. The neptunium inventory for the simulations was computed assuming the initial quantities of individual radionuclides given by Wilson et al. (1994) assuming a 70,000 Metric Tons Uranium (MTU) total inventory. To calculate the mass of neptunium at each repository node in the two-dimensional

cross section, we divide the total inventory equally into each drift node and divide by the thickness of the repository in the unmodeled direction to place the calculations on a one-meter-thick basis. In the transport simulations, we assume that once the drift node rewets, the canisters immediately are breached and radionuclides escape the near-field environment at the solubility limit of ^{237}Np. Therefore, for simplicity and in the interest of conservatism, we assume no retardation effect of the near-field engineered barrier once water contacts the waste packages. If this assumption proves to be overly conservative, similar calculations could be performed, in which the dissolution reactions are initiated after an additional time lag to simulate the performance benefits of the engineered system.

11.7.2 Speciation

Neptunium released into the aqueous phase participates in speciation reactions. These speciation reactions are given in Table 11-4. The three total aqueous components chosen to model these reactions are NpO_2^+, HCO_3^-, and H^+.

Table 11-4. Reactions and Log Equilibrium Coefficients for Np Speciation

Reaction	0°C	25°C	60°C	100°C	150°C	200°C
$H_2CO_3(aq) \Leftrightarrow HCO_3^- + H^+$	-6.58	-6.34	-6.27	-6.39	-6.72	-7.24
$HCO_3^- \Leftrightarrow CO_3^{2-} + H^+$	10.62	10.33	10.13	10.08	10.20	N/A
$H_2O \Leftrightarrow OH^- + H^+$	-14.93	-14.17	-13.04	-12.26	-11.64	-11.26
$NpO_2^+ + H_2O \Leftrightarrow NpO_2(OH)^0(aq) + H^+$	N/A	8.9	8.2	7.6	7.2	N/A
$NpO_2^+ + 2H_2O \Leftrightarrow NpO_2(OH)_2^- + 2H^+$	N/A	20.2	N/A	18.0	17.0	N/A
$NpO_2^+ + HCO_3^- \Leftrightarrow NpO_2(CO_3)^- + H^+$	6.85	5.73	4.48	3.40	2.39	N/A
$NpO_2^+ + 2(HCO_3^-) \Leftrightarrow NpO_2(CO_3)_2^{3-} + 2H^+$	14.59	13.66	12.57	11.53	10.36	N/A
$NpO_2^+ + 3(HCO_3^-) \Leftrightarrow NpO_2(CO_3)_3^{5-} + 3H^+$	23.58	22.49	21.11	19.59	17.69	N/A

To demonstrate chemical speciation behavior of the system, a series of one-element, batch FEHM simulations were performed. Since there is no flow or transport in these simulations, the results are similar to those of a batch geochemical code such as EQ3/6 (Wolery, 1992). Calculations were performed at 5 x 10^{-6} mol/l of neptunium, a typical value of solubility. The total carbonate concentration in solution was taken to be either that of J-13 or UE-25 p#1 fluid. Figure 11-3 shows the speciation results for neptunium in J-13 water at 25°C. At low pH values, the dominant species is NpO_2^+, with carbonate and hydroxy complexes becoming significant at pH values of about 8 and higher. In the higher carbonate UE25 p#1 water, the results are similar, but the transition to the carbonate and hydroxy complexes occurs at pH values closer to 7. Also, the specific species that are important at higher pH values tend to be the carbonate rather than the hydroxy complexes. As will be demonstrated below, the fraction of total neptunium present as the NpO_2^+ species is presumed to play an important role in the sorption behavior since experiments show that NpO_2^+ sorbs whereas the carbonate and hydroxy complexes do not sorb. Figure 11-4 shows the model calculations of fraction NpO_2^+ versus pH for J-13 fluids at various temperatures, and UE-25 p#1 fluid at 25°C. For the UE-25 p#1 fluid (higher carbonate concentrations) at 25°C, the shift to species other than NpO_2^+ occurs approximately one-half of a pH unit lower than for J-13 fluid. Potentially larger effects are predicted for the temperature dependence, which shifts the predicted curves up to two pH units from 25 to 90°C. This effect is due to the temperature dependence of the equilibrium constant of the mono-carbonate complex reaction (the fifth reaction in Table 11-4). If the temperature-dependence of this reaction is properly captured in the equilibrium constant values in the table, and if the temperatures in the zeolites are elevated during the period in which neptunium is travelling through the zeolites, then the temperature dependence will have a significant impact on performance predictions.

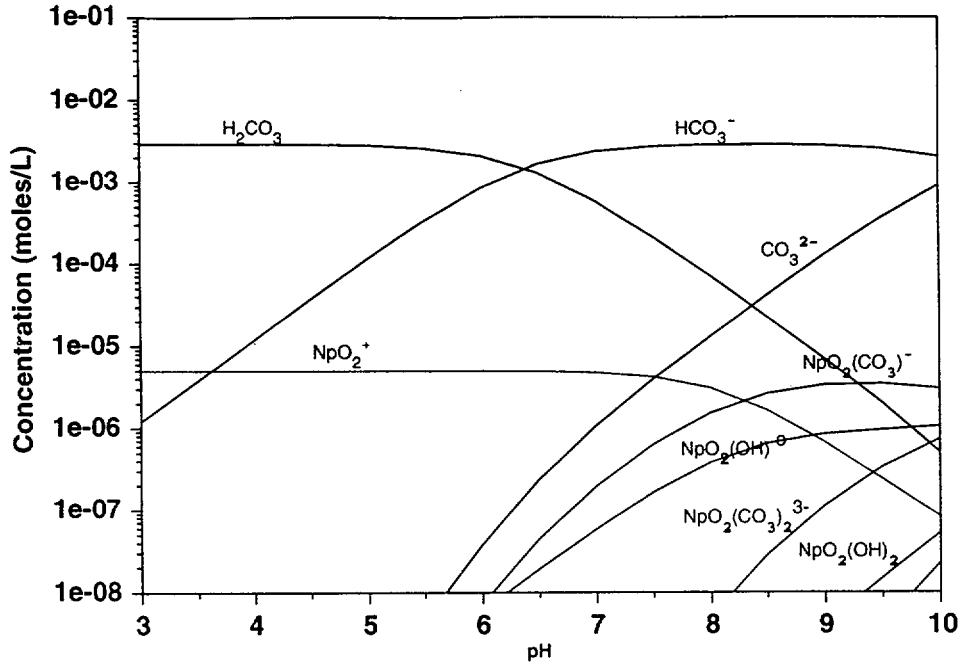

Figure 11-3. ^{237}Np speciation in J-13 water at 25°C with a solubility of 5×10^{-5} mol/l.

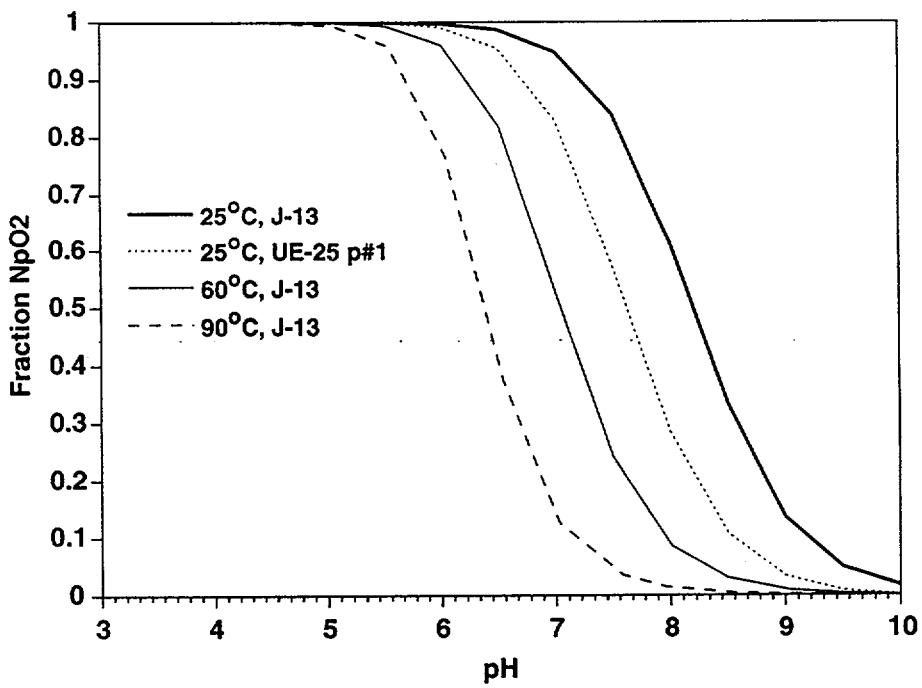

Figure 11-4. Predicted fraction of ^{237}Np as NpO_2^+ cation as a function of temperature and fluid composition (J-13 fluid versus UE-25 p#1 fluid).

11.7.3 *Sorption Data*

A comprehensive set of laboratory studies have been performed to characterize the sorption of neptunium on Yucca Mountain tuffs (Thomas, 1987; Bertetti et al., 1996; Tait et al., 1996; Triay et al., 1996a, b). In the first phase of experiments, sorption was shown to be minimal ($K_d < 0.4$ cc/g) on the vitric and devitrified tuffs in the pathways from the repository to the water table. Small but appreciable sorption (K_d values of 2.5± 1.4 cc/g for 46 batch sorption measurements in J-13 water in the pH range 8.25± 0.5 reported by Triay et al., 1996c) was found on rocks that have undergone zeolitic alteration. The presence of minor amounts of highly sorptive minerals such as hematite does not appear to translate to higher sorption in the whole rock samples. Triay et al. (1996a) postulate that this lack of enhanced sorption compared to single mineral sorption measurements could be due to passivation of the mineral surface. In fractures, coating minerals such as calcite, iron oxides, and manganese oxides exhibit significant sorption of neptunium (Triay et al., 1996a). However, in these simulations, we assume that matrix flow predominates in the nonwelded to partially welded units below the potential repository for the infiltration rates chosen. Therefore, sorption on fracture surfaces is not considered, although under different sets of hydrologic conditions, fracture flow and sorption on fracture surfaces could become important.

The mineral responsible for the sorption of neptunium on zeolitic tuffs at Yucca Mountain is clinoptilolite. Triay et al. (1996b) showed that the sorption behavior of zeolitic Yucca Mountain tuff was essentially equivalent to that of pure clinoptilolite when the experiments are carried out under similar chemical conditions and that differences can be understood quantitatively on the basis of the relative surface areas of the samples.

11.7.4 Sorption Models

To develop a quantitative geochemical model of neptunium sorption on zeolitic tuffs as a function of groundwater composition, we rely on the batch sorption data cited above (Triay et al., 1996c), as well as directed laboratory studies examining the impact of fluid chemistry (Tait et al., 1996; Triay et al., 1996a). The models developed in the present study are used to simulate the

sorption of NpO_2^+, where the aqueous concentration of NpO_2^+ is computed via the speciation reactions in Table 11-4. Recall that Figure 11-4 illustrated the effects of the speciation calculations in a plot of the fraction of neptunium present as NpO_2^+ as a function of fluid composition and temperature. The figure shows that as pH increases, the fraction of NpO_2^+ decreases, resulting in a lower effective sorption coefficient K_d. An estimate of the effective sorption coefficient $K_{d,eff}$ in the zeolitic Calico hills units is given by $K_{d,\,eff} = f_{NpO_2} \cdot K_{d,\,max}$, where $K_{d,\,max}$ is the maximum distribution coefficient in a system consisting of 100% neptunyl cation, and f_{NpO_2} is the fraction of total neptunium present as neptunyl cation. For the J-13 fluid at 25°C, the speciation results will predict a reduction in f_{NpO_2} and $K_{d,\,eff}$ by a factor of 2.9 from pH 7 to pH 8.5. These chemical calculations are in good agreement with the recently published sorption data of Triay et al. (1996c) of a decrease in K_d in J-13 water by a factor of 2 from 3 cc/g to 1.5 cc/g in this pH range (Figure 4 of that report).

The transition to neptunium carbonate complexes occurs at a lower pH value for UE-25 p#1 water, consistent with the low measured sorption coefficients in the fluid even at pH 7. There is some discrepancy between the speciation calculations and the observed sorption data, since the experiments show essentially no sorption even at pH 7, while the speciation calculations predict significant amounts of NpO_2^+ are present up to a pH of about 9 for UE-25 P#1fluid. Nonetheless, the trends are correct and the pH ranges over which transitions occur are within one pH unit of what is consistent with the batch sorption data. Therefore, we feel that the reactions of Table 11-4 provide a consistent explanation for the impact of pH on the observed sorption behavior of ^{237}Np.

To simulate the sorption of NpO_2^+ cation, we couple the speciation results presented above with an ion exchange model for NpO_2^+. Ion exchange models for clinoptilolite have been studied by many authors including Viani and Bruton (1993), Pabalan (1994), and Triay et al. (1996a). The ion

exchange model developed in the present study is patterned after a model first proposed by Triay et al. (1996a). Figure 11-5 shows the measured sorption coefficient on pure clinoptilolite as a function of Na^+ concentration in pure sodium bicarbonate solutions (data from Tait et al., 1996). These data indicate an ion exchange mechanism with a restricted number of sorption sites, as shown by Triay et al. (1996a). The following set of ion exchange reactions are assumed in the present study:

$$NpO_2^+ + tAl\text{-}Na^+ \Leftrightarrow tAl\text{-}NpO_2^+ + Na^+ \quad \log_{10}K = -1.58 \qquad \text{(Eq. 11-15)}$$

$$Ca^{2+} + 2tAl\text{-}Na^+ \Leftrightarrow (2tAl)\text{-}Ca^{2+} + 2Na^+ \quad \log_{10}K = 1.5 \qquad \text{(Eq. 11-16)}$$

where tAl represents a tetrahedral aluminum sorption site. The first reaction alone is used to model the data of Figure 11-5. The waters at Yucca Mountain contain divalent cations like Ca^{2+} that compete for the available ion exchange sites. The equilibrium constants listed in Eqns. 11-15 and 11-16, along with the cation exchange capacity (CEC) for neptunyl cation of 5×10^{-4} equiv/L, produce a good match to the data of Figure 11-5. The resulting K_d is 3 cc/g in J-13 water at pH 7, which is consistent with the J-13 sorption data. As shown earlier, as pH increases, the speciation reactions decrease the relative amount of NpO_2^+ in solution, resulting in lower apparent K_d's.

There is significant variability in the measured K_d values for zeolitic tuffs that is not captured with a single set of sorption model parameters. We assume that the range of apparent K_d values is due to different surface areas and, hence, surface sites available for sorption. This same variability is likely to be a reality in the field, since the fraction of clinoptilolite measured in field samples within the zeolitic horizons varies significantly (Vaniman and Bish, 1995). We handle this variability in the field simulations by assuming a range of surface site densities, while keeping the exchange coefficients constant.

In UE-25 p#1 water, the measured K_d values are considerably lower than in J-13 water. In the model developed here, this result is reproduced as the combined effect of a greater tendency for the formation of non-sorbing neptunium-carbonate complexes due to the higher carbonate

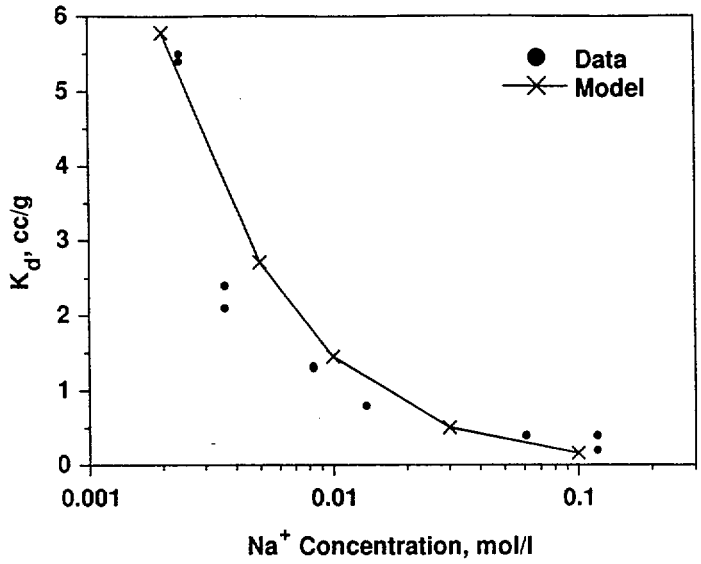

Figure 11-5. ^{237}Np sorption coefficient versus Na+ concentration in pure sodium bicarbonate solutions (data from Tait et al., 1996). The X's with accompanying curve is the predicted ion exchange model result.

concentrations and the higher concentrations of competing cations for the small number of available sorption sites. The best available data for comparison are column sorption experiments, which are more accurate for measuring low apparent K_d values than are batch experiments. The values of 0.2 to 0.4 cc/g determined in column studies by Triay et al. (1996d) are somewhat higher than the value of essentially 0 predicted by the model. This discrepancy is acceptable when making repository performance predictions, since the model errs on the conservative side (i.e. no sorption). Triay et al. (1996a) suggest a surface complexation sorption reaction (not included in the present study) that could explain the difference. One area in which the model may yield non-conservative predictions is in fluids with low pH (<8) but high concentrations of dissolved cations such as UE-25 p#1 fluid. For example, at pH 7, the model predicts an apparent K_d of roughly 1 cc/g, whereas experiments at these conditions yield K_d values of essentially 0. Thus, we must view the model results carefully in the regime of low pH and high cation concentrations. Additional experiments carried out under carefully controlled conditions with varying cation concentrations are needed to

further refine the model. Nonetheless, the current model allows us to examine the sensitivity of the system to different chemical compositions in the range measured in the field.

11.7.5 Column Studies

FEHM simulations using data from columns studies of Triay et al. (1996d) to examine whether ^{237}Np sorption may be kinetically limited under flowing conditions. The suite of column experiments analyzed were conducted using crushed zeolitic tuff with J-13 well water at a pH of 8.3. Crushed tuff was used to overcome mass transfer limitations in the column experiments. In the numerical analyses, the data for tritium, a conservative tracer, was used to fit the dispersivity of the column. The tritium breakthrough emerges from the column at one pore volume, as expected. Using the dispersivity obtained from the tritium simulation, ^{237}Np transport experiments were analyzed using a linear kinetic sorption model. The linear kinetic model was chosen over the competitive ion exchange model, since there were constant chemical conditions in the column. The K_d and the kinetic parameter were fit to the experimental data, yielding a good fit with a K_d of 1.25 cc/g and a kinetic parameter of 8 hr^{-1}. The K_d of 1.25 cc/g is consistent with the batch sorption coefficients for J13 water at a pH of 8.3 (Figure 11-4). Next, to check for kinetic control, the kinetic parameter was set to a large number (greater than 100 hr^{-1} in this system) so that the linear kinetic model would simplify down to an equilibrium model. Figure 11-6 shows that in the column studies, the sorption process is captured more accurately with a kinetic model, rather than an equilibrium formulation. Another ^{237}Np sorption experiment was analyzed using the same column at a different flow rate (2.99 ml/hr). This additional experiment confirmed that the K_d and kinetic parameters are independent of flow rate. The result agrees with the findings Pabalan (1994), who reported that the ion exchange reactions controlling ^{237}Np sorption onto Clinoptilolite equilibrate after one or two days. Despite the slight kinetic control of sorption in the laboratory, no kinetic limitations are expected in the field due to the much longer time scales of transport in the natural system.

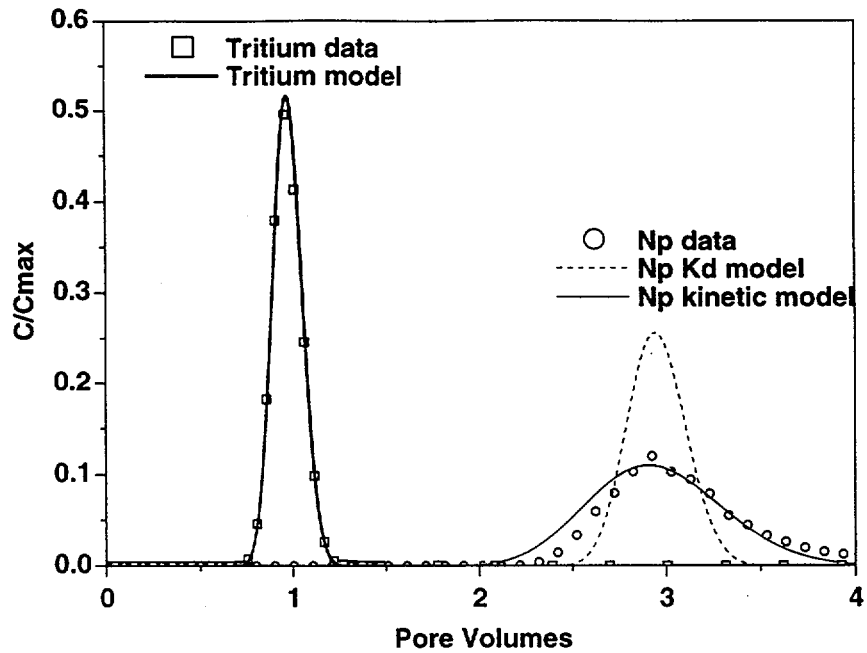

Figure 11-6. Tritium and ^{237}Np sorption column study using J-13 well water at a pH of 8.3. The curves represent fits to the data for equilibrium and kinetic sorption models

11.8 Model Results

11.8.1 Preliminary One-Dimensional Flow and Transport Simulations

The unsaturated zone at Yucca Mountain consists of alternating layers of welded and non-welded tuffs with wide contrasts in the matrix permeability and fracture density. This hydrogeologic complexity gives rise to variations in the predicted nature of flow through the unsaturated zone, ranging from fracture-dominated to matrix-dominated flow, depending on the unit. In this section, we develop a one-dimensional isothermal model domain to investigate the nature of flow through the various rock units. The same hydrologic and transport properties are used in these calculations as the forthcoming site-scale simulations. In particular, we address the question of whether it is possible to approximate the radionuclide transport behavior using a single continuum model. In this section we demonstrate that as a first approximation, the relative flow fractions in the fractures and matrix as predicted by a DKM model allow us to assign appropriate effective porosities in the units below the potential repository for transport of radionuclides.

Therefore, an ECM model can be used for transport calculations of heat, fluid, and solute. Specifically, if the flow is predicted to be within the fracture domain, the fracture porosity is used in transport calculations, whereas if matrix flow predominates, the matrix porosity is used. Since the fracture porosity is typically several orders of magnitude smaller than the matrix porosity, this approximation will result in very rapid transport velocities through units controlled by fracture flow, and the overall performance of the unsaturated zone will then be dominated by the behavior of those units predicted to be controlled by matrix flow.

The one-dimensional model used for this analysis extends from the surface to the water table using the stratigraphy of the unsaturated zone at wellbore SD-9, located near the northeast corner of the potential repository. Figures 11-7a and b show the fracture and matrix flow fractions at 1 and 4 mm/y, respectively using the DKM model. Above the potential repository, the flow is fracture-dominated in the TCw, transitions to matrix-dominated flow in the PTn, and back to fracture-dominated (>50% flow) in the TSw. Of greatest importance for radionuclide transport is the flow below the repository, where at 1 mm/y the flow is predicted to convert to matrix flow in the vitric CHn unit and remain as matrix flow to the water table, including in the zeolitic CHn where sorption of ^{237}Np is predicted. Therefore, at relatively low infiltration rates, transport is expected to be controlled by the much larger matrix porosity of the CHn. In contrast, the TSw can be approximated as fracture-dominated flow and transport, obtained by setting the porosity in a single continuum transport model to the fracture porosity.

The situation at 4 mm/y is more complex. For the parameter values selected as the base case, the permeability of the zeolitic CHn matrix is too low to support the entire 4 mm/y flux. Therefore, the rock in the CHnz is predicted to exhibit significant fracture flow (about 60% in Figure 11-7b). There is considerable variability in the measurements of matrix permeability of all of the tuffs, including the CHnz, and this variability will have a significant impact on the prediction of the flow split between fractures and matrix. Figure 11-7c shows that a zeolite permeability a factor of 3 greater (well within the range of measured values) results in a prediction of matrix-

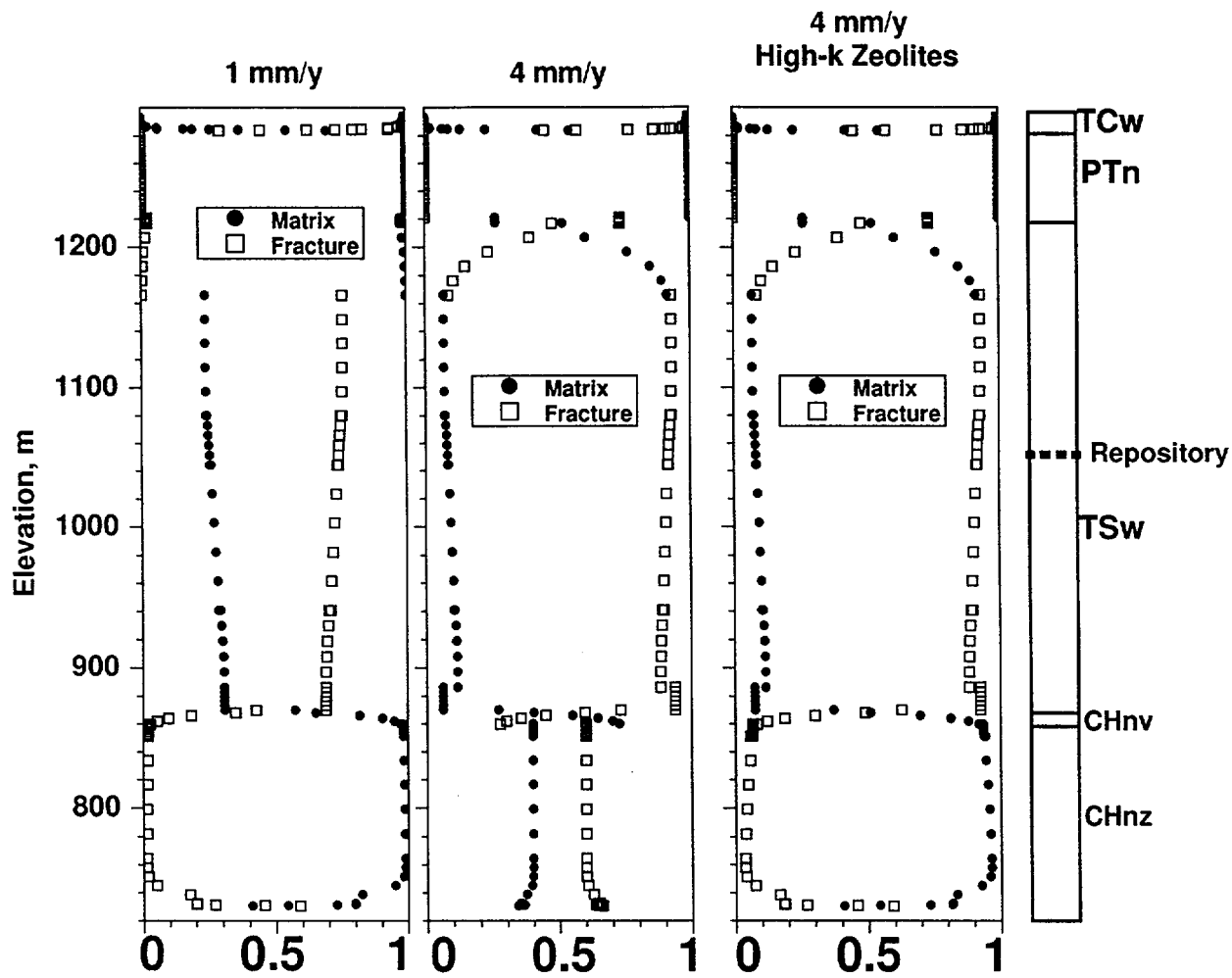

Figure 11-7. The fraction of flow residing in the matrix and fracture for the DKM model.

dominated flow throughout the CHn, as was the case at 1 mm/y. This analysis points out the uncertainty in the nature of flow through the zeolitic CHn unit. This uncertainty is treated by establishing bounds on the type of transport behavior, as discussed below.

Before developing the two-dimensional models of heat and mass transport, we present one-dimensional transport model results using the DKM results just presented, along with ECM results for comparison. For this analysis we use the particle tracking transport module of FEHM because of its efficiency in handling DKM systems with widely contrasting flow velocities in the two continua. For details of the particle tracking method, see Chapter 4. Figure 11-8 shows the breakthrough of ^{237}Np at the water table versus time in the one-dimensional model. At 1 mm/y,

the ECM and DKM models result in virtually equivalent breakthrough curves, a consequence of the matrix-dominated flow through the CHn predicted by the DKM model (Figure 11-8a). A very small fraction of the mass arrives early in the DKM model, but the majority of the radionuclide travels through the matrix, and the two models give very similar results. At 4 mm/y, the situation is similar for the high-permeability zeolite case. However, for the base-case properties, the DKM model predicts a significant portion of the ^{237}Np inventory traveling through fractures. The resulting breakthrough curve at the water table is bimodal, with a large flux arriving within the first 30,000 years of the simulation. Clearly, an ECM model is not capable of reproducing this behavior, except in a bounding sense. In most of the two-dimensional ^{237}Np transport simulations, we assume that flow is matrix-dominated throughout the zeolitic units since this assumption facilitates the investigation of the effect of chemical and thermal conditions on sorption and transport. However, to assess the role of the uncertainty of the flow field on predicted transport of ^{237}Np, we also present a simulation in Section 11.8.3 in which the fracture porosity is assumed for transport through the zeolites, thereby bounding the behavior.

11.8.2 Thermohydrologic Simulations

In this section, we describe the fluid flow and heat transport behavior of the model to set the stage for presenting the neptunium transport results. Current reference design conditions for the heat load issuing from the repository are assumed: the inventory of waste totalling 70,000 Metric Tons Uranium (MTU) with an 83 MTU/acre initial heat load, with waste emplaced in drifts that are 22 m apart. At the repository portion of the model, heat is supplied to individual nodes of the grid along a series of nodes spaced 22 m apart, so that in these calculations, there are roughly four unheated nodes between each node representing an emplacement drift. In the unmodeled direction, the heat load is assumed to be uniform, so that the appropriate heat load in the two-dimensional cross section (taken by convention to be 1 m thick) can be applied. The time-varying heat load exhibits a sharp drop from its initial value within the first 100-1000 years. The heat load declines to 30% of its initial heat load after 100 years and 7% after 1000 years. Infiltration rate boundary

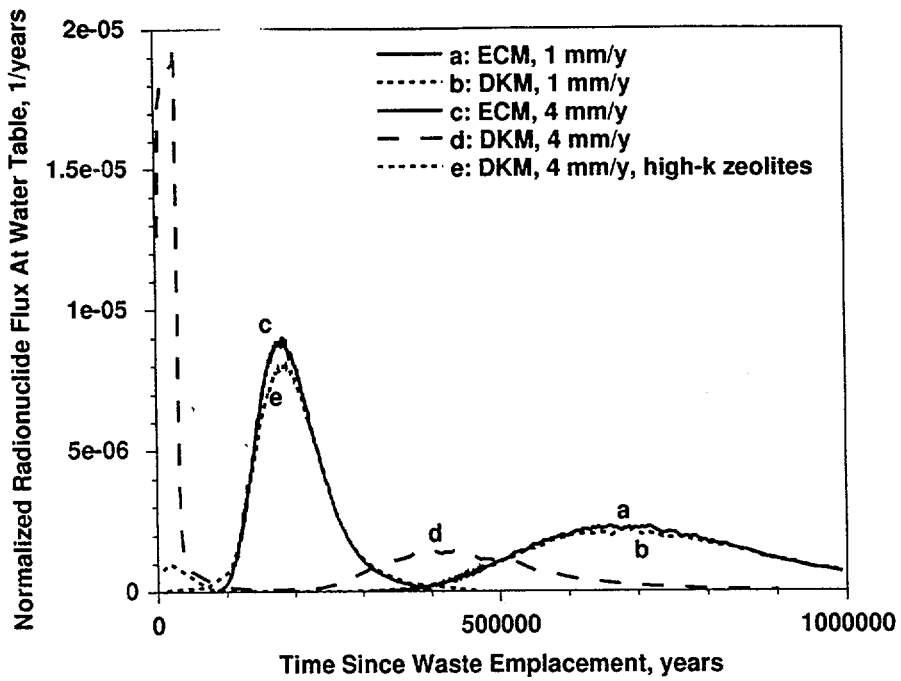

Figure 11-8. Breakthrough of ^{237}Np at the water table in the one-dimensional model. Comparison of the ECM and DKM models for different flow scenarios.

conditions were described earlier, and the fluid flow boundary condition at the bottom of the model domain is a fluid saturation of one to represent the water table.

Thermal and air pressure boundary conditions are also required as input to the model. At the surface, temperature and pressure are assigned according to the surface elevation; time-invariant values are based on a method developed by Ross et al. (1992) which captures the elevation dependence of air properties. The bottom and side boundaries are no-flow air boundaries. The thermal boundary condition at the water table is a flux-based boundary condition for the heat flux Q_b which takes the form $Q_b = \Omega(T - T_b)$ where T_b is the temperature outside of the model boundary at which the heat exchange is taking place and Ω is a scaling parameter. Adjustment of Ω allows us to examine a range of thermal conditions at the water table ranging from isothermal to the approximate behavior assuming conduction-limited heat transfer in the saturated zone. Figure 11-9a shows the predicted fluid saturation response of the system after 500 years for a

uniform 4 mm/y infiltration rate. Over a period of roughly 10,000 years, the model predicts dry-out, followed by rewetting, near the emplacement drifts. A two-phase, countercurrent flow zone develops above the potential repository, with buoyant and pressure-gradient-driven vapor movement in the upward direction counterbalanced by downward fluid percolation, the primary source of which is condensed steam. The resulting heat transfer mechanism, called a heat pipe, is much more efficient than thermal conduction alone, and results in an extended two-phase region of enhanced heat transfer at about 1 atm and 100°C (Figure 11-9b). This heat pipe sets up regions of net boiling and condensation that in turn impact the concentrations of dissolved ions. Figure 11-9c shows the predicted concentration pattern of Cl^- ion (assumed to be conservative), along with the general movement of vapor at a time of 2000 years. Net vaporization at the edges and below the repository concentrates the fluid in those zones, and net condensation directly above the repository dilutes the fluid. This pattern evolves through time, changing the chemical composition from its initial state. When the heat from the repository region is insufficient to maintain the two-phase zone, the zone collapses, and fluid reenters the repository region. The rewetting of the repository and return of the system to its ambient conditions occurs within 10,000 years of waste emplacement.

The temperature and fluid saturation near the emplacement drifts control the hydrologic and gas-phase moisture conditions that in turn control the degradation of the protective waste package containers, the dissolution of the solid radioactive waste, and the solubility of neptunium. At all infiltration rates selected, the model predicts complete dry-out of the rock near each drift, with the duration of complete dry-out conditions depending on position within the repository. Closer to the middle of the repository, dry-out regions associated with the individual drifts are predicted to merge, forming a continuous region of dry rock through which fluid cannot percolate. In contrast, an "edge effect" is predicted for drifts at either end of the repository, where enhanced downward percolation and lateral cooling effects result in a lack of coalescence of dry-out zones. Figure 11-10 shows the predicted temperature versus time in the rock near two emplacement drifts

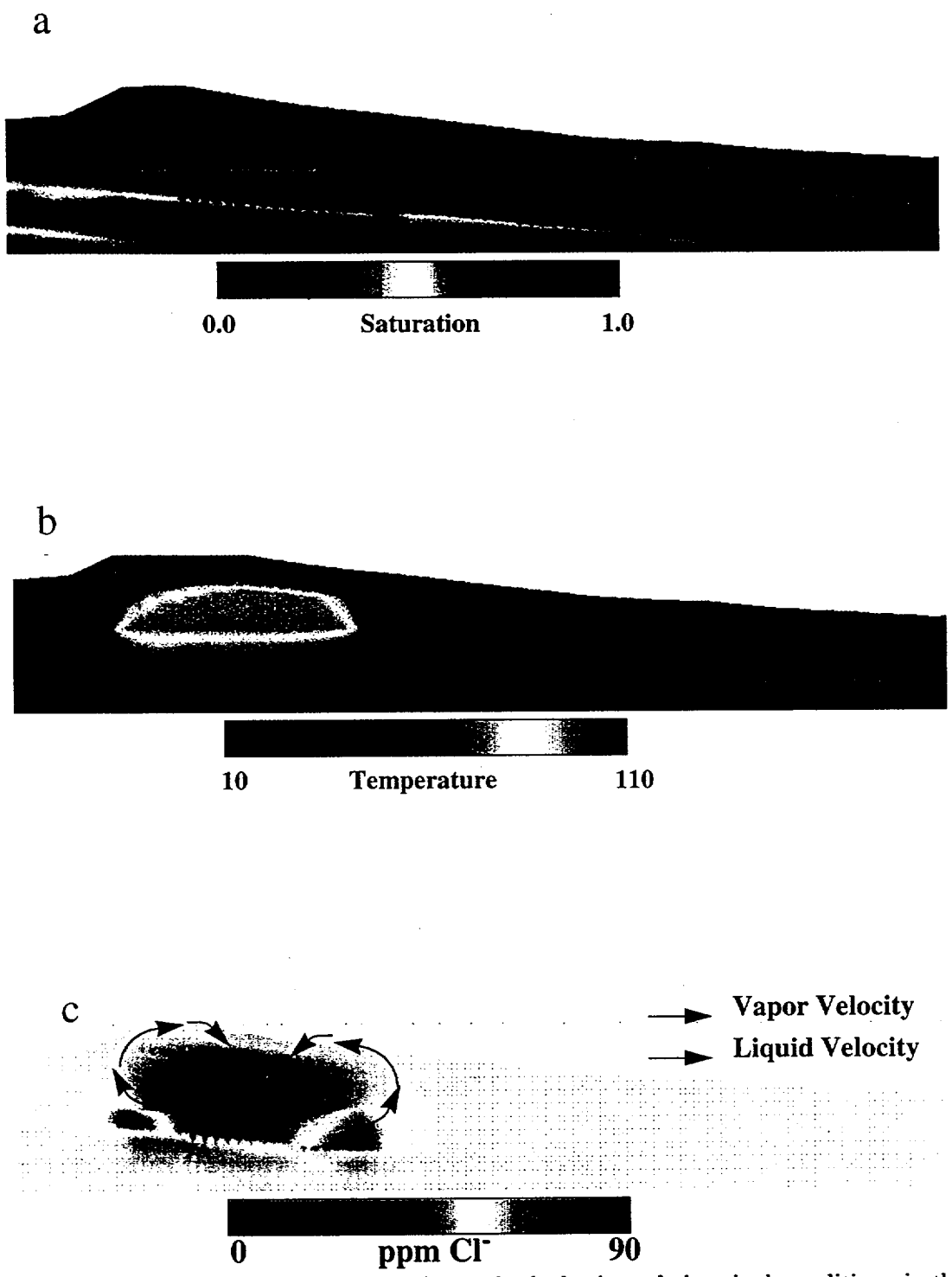

Figure 11-9. Influence of repository heat on thermohydrologic and chemical conditions in the unsaturated zone. (a) Fluid saturation profile (500 years), (b) temperature profile (500 years), (c) chloride concentration (2000 years).

(one closer to the middle of the repository, called the "center" drift, and one near the edge of the repository, called the "edge" drift) for the 4 mm/y infiltration rate scenario. In addition, the figure shows the predicted influence of infiltration rate on the temperature at the center drift. The period during which a drift is elevated to temperatures greater than 100°C corresponds to dry-out of the rock to low saturation. The period of complete dryout at a given infiltration rate depends most critically on the position of the drift within the repository. For example, for the 4 mm/y case, the onset of rewetting is predicted to occur within the first 100 years near the repository edge and between 500 and 1000 years for an inner drift. These results are in agreement with one-dimensional dual permeability simulations by Ho (1997), who predicted thermally induced increases in flux lasting for about 1000 years. Thus the choice of ECM for the model calculations appears to be acceptable from the standpoint of predicting the duration of the thermal perturbation to the flow field.

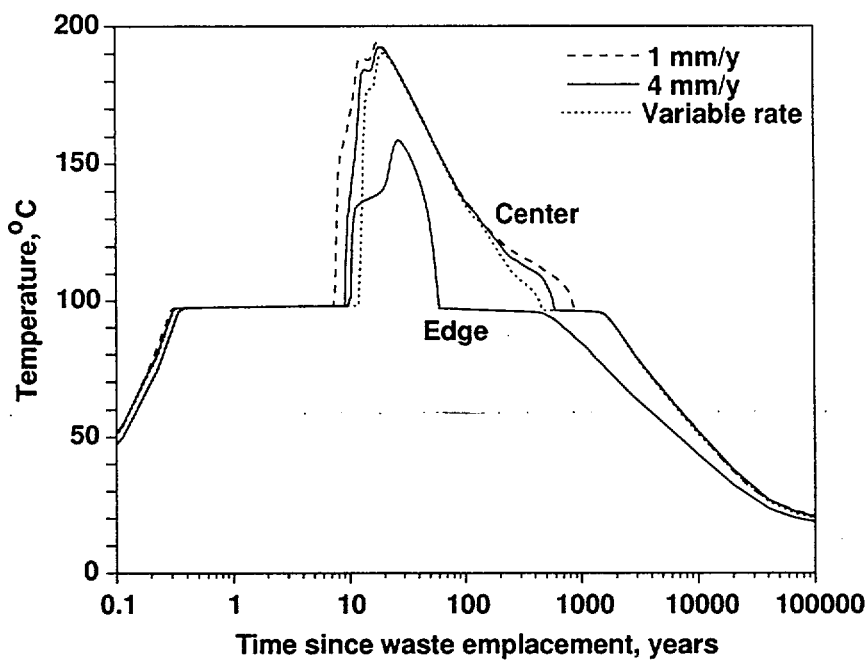

Figure 11-10. Temperature versus time in the rock near an emplacement drift in the repository. "Center"-drift near the center of the repository, "Edge" -drift near the edge of the repository. The family of curves for the "Center" drift show the influence of infiltration rate on the results.

The infiltration rate also has some influence on the model results. Figure 11-11 shows the predicted temperature-time histories at two positions in the Calico Hills unit corresponding to the top of the Calico Hills zeolitic horizon. Two comparisons are presented in the figure. First, examining the solid curves labelled "Isothermal", we note that the greater temperature rise occurs for the position that is closer to the middle of the repository heat source, despite the fact that the top of the zeolites is actually 25 m farther from the heat source than for the position below the edge of the repository. The other comparison illustrates the impact of the heat transfer boundary condition at the water table. The conduction-limited model is more insulating than the isothermal condition, resulting in a predicted rise in rock temperature at the water table (Figure 11-11) of roughly 25°C that subsequently returns to the ambient value. This effect in turn results in a higher predicted temperature rise and a longer duration of elevated temperature in all units between the water table and the repository horizon, including the zeolitic rocks.

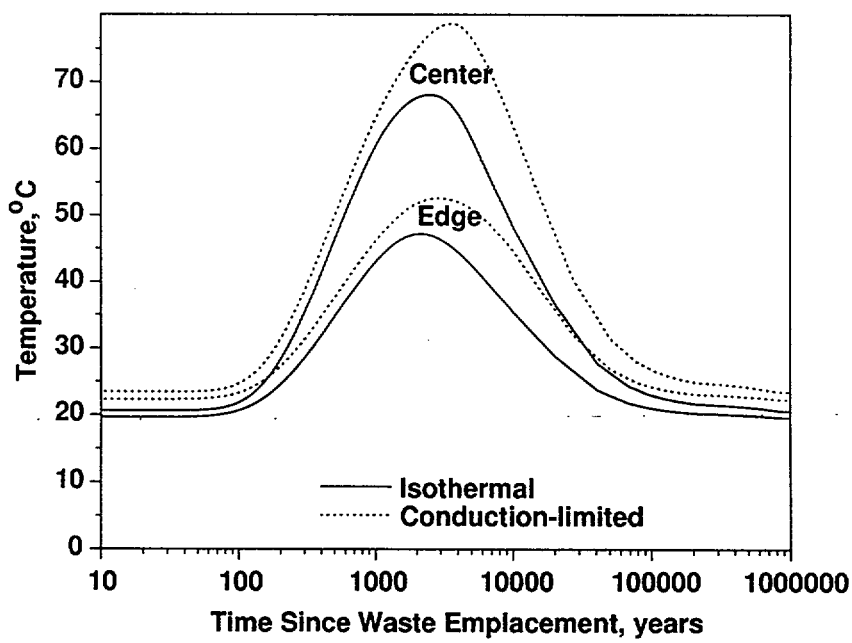

Figure 11-11. Temperature versus time at the top of the Calico Hills zeolitic horizon. "Center"-position located beneath the center of the repository; "Edge"-drift near the edge of the repository. The influence of the assumptions regarding the heat transfer at the water table boundary are also shown.

11.8.3 Neptunium Transport Simulations

In the site scale neptunium transport simulations, we study the effects of infiltration rate, temperature, pH, and bicarbonate, sodium and calcium concentrations on neptunium migration from the repository to the water table. In these simulations, we examine the rate at which ^{237}Np reaches the water table as a function of time. This measure of performance was selected because the radionuclide mass flow rate is a direct input to saturated zone transport models that predict the concentration and dose associated with ^{237}Np in the underlying groundwater system. All simulations utilize the competitive ion exchange reaction model with speciation discussed above.

Figure 11-12 shows the position of the ^{237}Np plume at various times during one of the site scale simulations. The first three profiles are total aqueous ^{237}Np concentrations (mol/kg water), and the last profile is the sorbed ^{237}Np concentration (mol/kg rock). In this simulation, the infiltration rate is 4 mm/y, pH is 8, bicarbonate concentration is 150 mg/l, sodium concentration is 125 mg/l and calcium concentration is 25 mg/l. We will refer to this simulation as the base case.

Figure 11-12a shows the repository after the waste canisters begin to cool and water begins to rewet the edges of the repository. At early times, ^{237}Np begins to dissolve and quickly flows through the Topopah Springs welded unit via fracture flow. The migration of ^{237}Np is slowed significantly by the Calico Hills nonwelded units, where matrix flow dominates. The ^{237}Np then begins a slow migration through the nonwelded tuff matrix towards the water table. Figure 13b shows the transport plume after all drifts have rewet and releases occur throughout the repository. In Figure 11-12c, the main ^{237}Np plume has reached the water table and is more dilute, mainly due to dilution with the percolating fluid and sorption to the zeolitic tuffs. Radioactive decay of ^{237}Np is considered but at the infiltration rates chosen for study, transport times are short enough that the impact of decay on concentrations is negligible. Figure 11-12d shows the sorbed ^{237}Np site concentration. The sorbed concentration profile illustrates the combined effects of the ion exchange and speciation model. For the base case, the approximate retardation factor for ^{237}Np

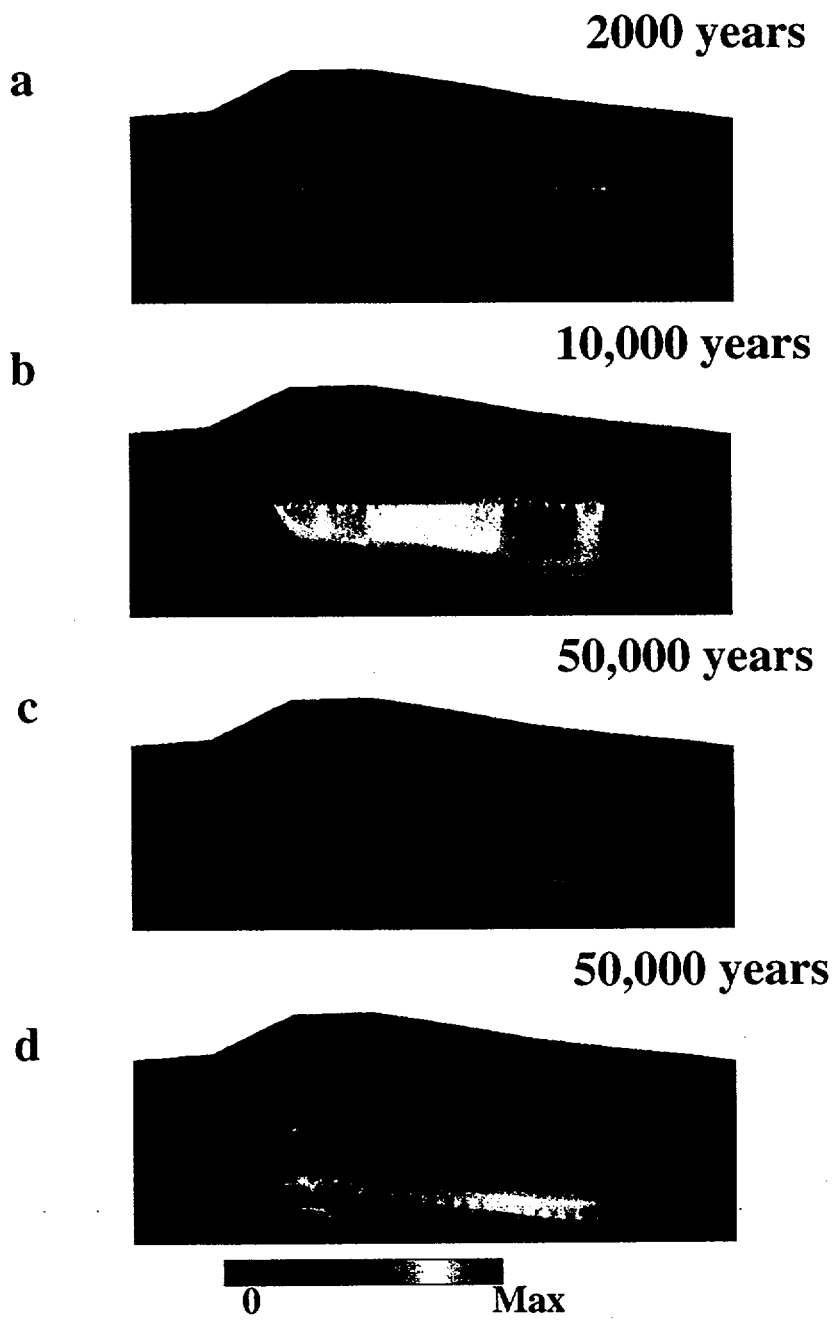

Figure 11-12. ^{237}Np transport through the unsaturated zone.(a) ^{237}Np total aqueous concentration profile after rewetting of the repository region and mobilization of ^{237}Np at all locations(10,000 years), (c) ^{237}Np total aqueous concentration profile as ^{237}Np reaches the water table (50,000 years), and (d) ^{237}Np immobile site concentration profile (50,000 years).

sorption onto the zeolitic layers is about 20. However, certain scenarios discussed below can greatly diminish the retardation of the zeolitic layers.

Figure 11-13 shows the predicted fate of ^{237}Np for infiltration rates of 1 mm/y, 4 mm/y and the variable infiltration scenario. Two sets of results are presented in the figure. First, the quantity of solid ^{237}Np remaining at the repository horizon is plotted as moles versus time (the curves that decline from their initial values to 0) during the simulation. Also, the ^{237}Np breakthrough curves at the water table are presented. Recall that the variable infiltration rate averages 4.8 mm/y at the cross section, with values ranging from 0 to 18 mm/y. As expected, the higher the infiltration rate, the faster the release of ^{237}Np from the repository resulting in a shorter travel times and higher peak concentration at water table. For the variable infiltration scenario, the inventory is completely mobilized in about 20,000 years, in contrast to 70,000 years for the 1 mm/y case. Regarding the breakthrough curves at the water table, infiltration rate has the expected result: higher fluid flow rates decrease breakthrough times and increase the peak radionuclide mass flux at the water table.

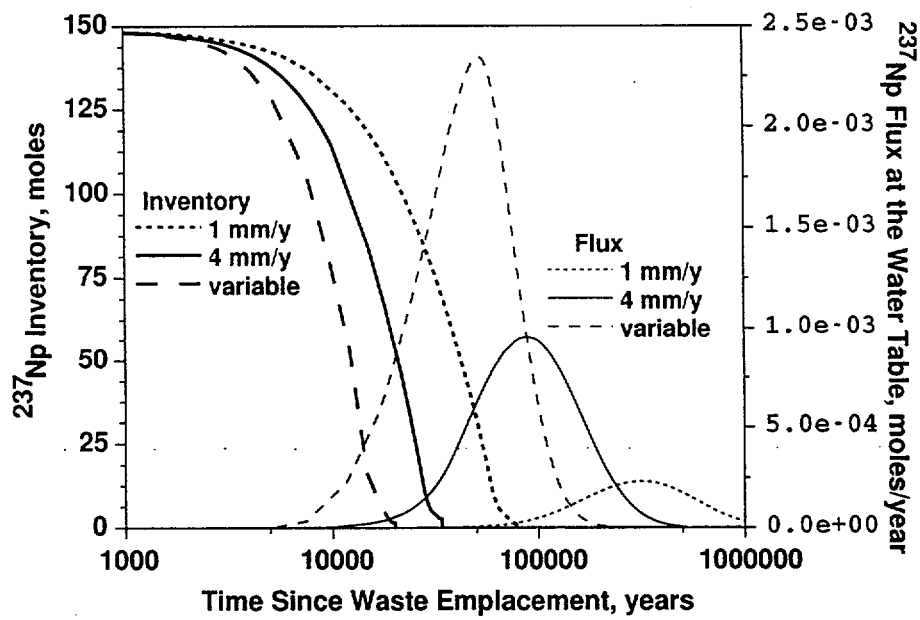

Figure 11-13. Mobilization of ^{237}Np from the near field, and breakthrough curves at the water table for different infiltration scenarios. The declining curves starting at early times represent the ^{237}Np mass remaining as a solid in the repository region (the left y-axis). The breakthrough curves exhibiting peaks are ^{237}Np flux at the water table (the right y-axis).

The matrix permeability of the nonwelded zeolitic Calico Hills units is a major uncertainty in the transport calculations. Section 6.1 showed that for a infiltration rate of 4 mm/y, the base-case zeolite permeability results in primarily fracture flow through the zeolitic Calico Hills, whereas, a zeolite permeability three times the base-case value results in matrix-driven flow. Using the DKM model for the site scale simulations is beyond the scope of this reactive transport study and is dealt with in detail elsewhere in this report. To provide a lower bound on the travel time to the water table for ^{237}Np, we simulate transport through the nonwelded zeolitic units by setting the porosity of the Calico Hills zeolitic units equal to the *fracture* porosity. In addition, we assume that the fractures do not sorb ^{237}Np. This simulation serves as a worst case scenario for the site scale model. Figure 11-14 shows that the fracture bypass case leads to ^{237}Np travel times that are significantly shorter than the base case scenario. The influence of sorption onto zeolites, shown above to result in a retardation factor of about 20 in the zeolites, is negated when fracture transport is assumed. If this is the case, significant breakthrough occurs at the water table before 10,000 years. Further experimental work and modeling will be necessary to better constrain the permeability of the zeolites to resolve the flow conditions in the Calico Hills units. To examine the influence of chemistry on ^{237}Np sorption and transport, we assume hereafter that matrix transport predominates in the zeolites, while recognizing that this uncertainty remains.

We next examine the influence of fluid pH on ^{237}Np sorption and transport. The reactions considered in the model result in little predicted change of pH with time at the zeolitic layers even during the heating phase. As recently shown by Lichtner and Seth (1996) and others, the pH is a strong function of CO_2 degassing due to heating and boiling at the heat pipe front. Rigorously modeling the geochemistry at the heat pipe front is beyond the scope of this study since the calculation would require a gas phase model of CO_2 transport. In addition, the precipitation-dissolution of minerals such as calcite and quartz would have to be considered. To approximate CO_2 degassing due to heating, we fix the concentration of CO_2(aq) throughout the model while allowing for all other components to dilute and concentrate due to heating effects. In effect, we are

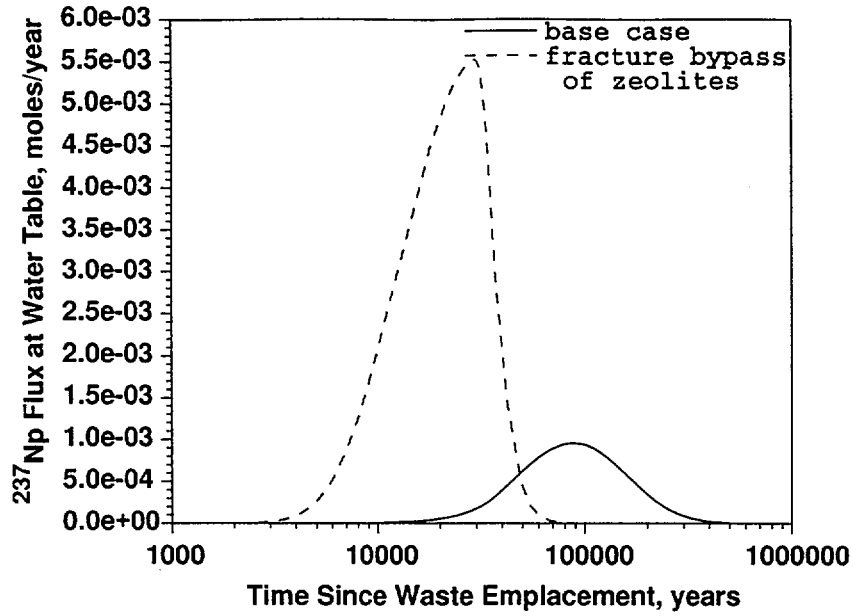

Figure 11-14. Fracture bypass of the zeolitic Calico Hills units.

assuming that the partial pressure of $CO_2(g)$ is fixed throughout the mountain. To examine the effect of heating on pH, we ran a simulation starting at a pH of 7 with J-13 geochemical conditions. As the waste heat dries out the near field, the pH sharply increases to about 11 at the heat pipe front and returns to ambient conditions as the repository cools to ambient conditions (Figure 16). This result qualitatively agrees with the one-dimensional model results of Lichtner and Seth (1996). The extent of the pH rise is perhaps overpredicted in our model, since we do not include buffering by dissolved silicic acid, which has a dissociation constant (pK_a) of 9.8. However, we show below that this simplification results in conservative model predictions since the higher the pH at the zeolites, the less sorption of ^{237}Np. Figure 11-15 shows that the pH at the top of the first zeolitic horizon, which are 150 meters away from the repository, is not affected by the drastic pH changes at the heat pipe front. Again, these model predictions agree with the Lichtner and Seth (1996) which indicates that the pH changes at the heat pipe front are primarily a near-field affect.

The effect of pH on ^{237}Np migration is more complicated than the infiltration effect, because the pH influences both the solubility and sorption behavior. As pH rises, solubility

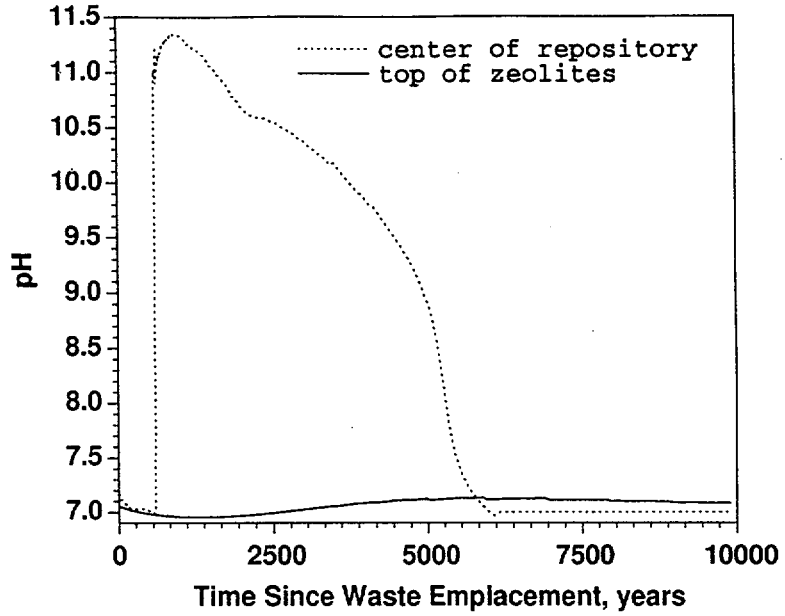

Figure 11-15. The effect of CO_2 degassing on pH at the center of the repository (heat-pipe front) and at the top of the zeolitic layers.

decreases (slower near field releases), but sorption also decreases due to the results of the speciation part of the transport model (more rapid migration). Figure 11-16 shows the ^{237}Np breakthrough for initial pHs of 7, 8, and 9 (we will discuss the "carrier plume" model results shortly). The model results indicate that effect the pH has on reducing sorption predominates over the solubility effect, which slows the release rate from the repository. Therefore, the higher the pH, the higher the peak concentration and the shorter the travel time to the repository.

We also considered a case in which a "carrier plume" or "hyperalkaline plume" of high pH migrates from the repository. The drifts of proposed repository will be lined with cement and cement-water interactions could alter the chemistry of the fluid in which ^{237}Np is transported. A detailed model for the cement-water interactions are beyond the scope of the present study, but it is well known that a transient pulse of high-pH water is expected. To study the potential effect on ^{237}Np migration, we fix the pH of the solution at the repository at a value of 10 for 5000 years. Recall that values of pH greater than 10 are unlikely due to buffering by dissolved silicic acid. After 5000 years, we assume that the cement is passivated and has no further effect on the pH. The pH

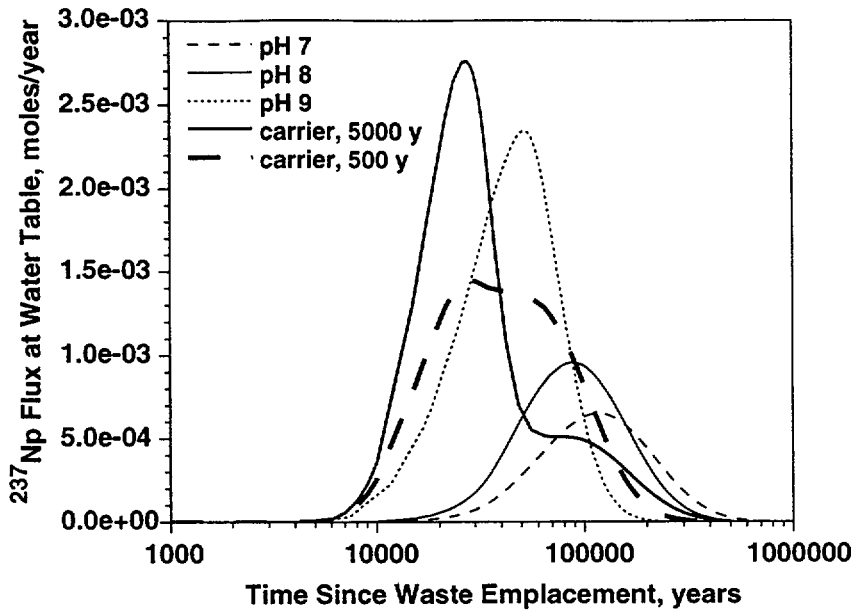

Figure 11-16. Influence of pH on the ^{237}Np breakthrough curves at the water table. The "carrier plume" result assumes an elevated pH of 10 at the repository for a period of either 500 or 5,000 years due to cement-water reactions.

perturbation results in a "carrier plume" that in these simulations allows a significant amount of ^{237}Np to traverse the zeolitic layers with no sorption. By contrast, when we limit the pH perturbation to 500 years rather than 5000 years, the early-arriving peak at the water table is much less pronounced. Further work in quantifying the influence of cement and other manmade materials must be carried out to better assess the possibility of enhanced mobility of ^{237}Np due to a carrier plume.

In contrast to the strong influence of pH on the speciation and sorption, simulations (not shown in the figure) performed over the range of bicarbonate concentrations measured in the pore fluids illustrate that bicarbonate concentration is not a significant uncertainty affecting ^{237}Np migration. Earlier, we showed that higher carbonate waters results in the formation of a higher percentage of nonsorbing carbonate complexes. Therefore, the water with a bicarbonate concentration of 300 mg/l results in slightly less sorption than the water with 50 mg/l bicarbonate concentration. However, the range of bicarbonate concentrations in unsaturated zone fluids is

significantly lower than the concentration in UE-25 p#1 fluid, where the presence of carbonates is expected to significantly lower sorption. Therefore, the influence of this parameter is not critical to the model predictions.

Variability in the concentration of cations competing for sorption sites is expected to influence the transport predictions. According to the ion exchange model, sodium and calcium concentrations play an important role in the degree of ^{237}Np sorption. However, as with bicarbonate concentration, the cation concentrations are fairly tightly constrained from the field measurements. In fact, as long as the concentrations do not evolve over time, transport predictions for the cation concentration ranges shown in Table 11-2 do not differ significantly from the results already presented. However, field evidence and climate studies indicate that infiltration rate and concentrations of dissolved ions are expected to evolve over time. Earlier we showed that the higher infiltration rate scenarios would result in a more rapid release of ^{237}Np, but in those simulations we assumed that sodium and calcium concentrations were independent of infiltration rate. We now present a transient simulation in which we assume that after 1000 years at 1 mm/y, a wetter climate prevails, and infiltration rate increases to 4 mm/y. In addition, in response to lower evapotranspiration rates relative to precipitation that is likely to prevail under a wetter climate, we assume that sodium and calcium concentrations more dilute by a factor of four during the higher infiltration period. Figure 11-17 shows that the changing climate scenario behaves more like the 1 mm/y case than the 4 mm/y case despite the fact that the 4 mm/y infiltration rate is present during the majority of the time of ^{237}Np migration. The reason for this behavior is that ^{237}Np effective K_d increases from about 2 cc/g to 5.5 cc/g at the more dilute sodium and calcium concentrations. Therefore, if higher infiltration rates are accompanied by more dilute percolating fluids, the transport predictions will underestimate sorption if a constant K_d is assumed.

The influence of repository heat on the flow field, transport properties, and ^{237}Np migration is now considered. Recall that Figure 11-4 showed that speciation and sorption could be strongly affected by temperature effects. Furthermore, the flow field itself is significantly different than that

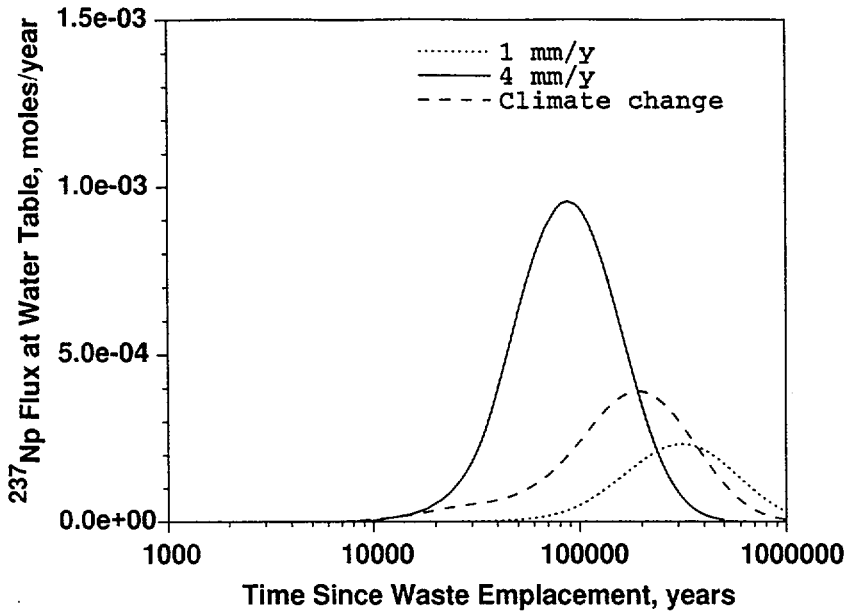

Figure 11-17. Influence of transient infiltration and chemical conditions on the ^{237}Np breakthrough curves at the water table. The "changing climate" result assumes an increase from 1 mm/y to 4 mm/y, accompanied by a four-fold decrease in cation concentrations. The 1 mm/y and 4 mm/y steady state results without geochemical transients are shown for comparison.

of the ambient system. Despite these potential complications, Figure 11-18 shows that the details of the heat transfer process have little effect on the transport of ^{237}Np. The primary reason for this result is that the temperature of the zeolites is predicted to have returned to near ambient conditions by the time the centroid of the ^{237}Np plume reaches the zeolites. Solubility is low enough to extend the period over which releases occur to greater than 10,000 years, long enough for the relatively short-term thermohydrologic transients to have abated. The only observable heat effect impacting ^{237}Np migration in the simulations is for the conduction-limited heat boundary condition. However, even this effect is insignificant. Thus, the results indicate the current model is relatively insensitive to heat effects.

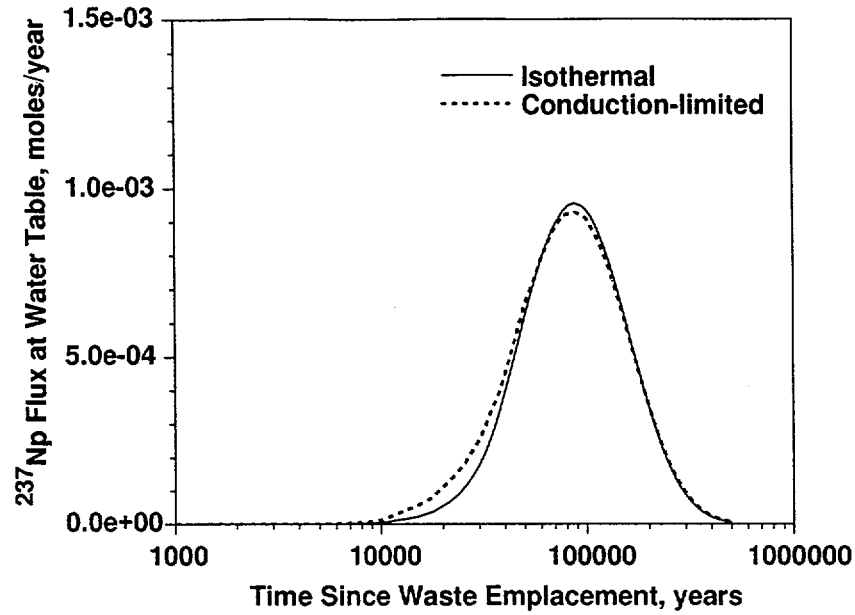

Figure 11-18. Influence of thermal boundary condition at the water table on the ^{237}Np break-through curves at the water table.

11.9 Discussion and Conclusions

The need to develop a reactive transport model for ^{237}Np migration in the unsaturated zone is motivated by its relatively weak (but significant) sorption, its high solubility, and long half-life. Considerable effort has been expended into characterizing the chemical properties of ^{237}Np in Yucca Mountain fluids, including solubility, speciation, and sorption. This chapter places these measurements into perspective for the Yucca Mountain site by combining the chemical information with the latest site characterization information on the hydrology, geochemistry, and projected thermal behavior of the unsaturated zone.

The computational intensity of performing multiple simulations of the full thermohydrologic and reactive transport behavior of ^{237}Np has led to various simplifications in previous analyses, including isothermal, steady state flow, an equivalent K_d model for sorption, and simplified source term expressions for the release of ^{237}Np from the near-field environment. Some of these simplifying assumptions will be necessary in future performance assessment

exercises due to the large number of simulations required to treat uncertainty in system parameters. As one example, the release of radionuclides from the near-field was assumed to occur as soon as rewetting of the drift takes place. In reality, time lags due to limited corrosion of the waste packages and slow transport from the packages are more realistic. To quantify the uncertainty of these and many other processes, Monte Carlo analyses are used, and thus simplifications of the full reactive transport model are required for expediency. Thus, one of the key outcomes of this work is to assess the validity of these simplifications and to propose abstractions of the complex behavior that can be used in performance assessment analyses.

The chemistry of the unsaturated zone fluids has an important influence on sorption of ^{237}Np in the zeolitic horizons, which in turn controls the transport prediction. For example, the variance in effective K_d from 0 to 2.5 cc/g translates into an order of magnitude difference in travel time through the zeolitic rocks. These travel times within the unsaturated zone are predicted to be greater than 10,000 years (one proposed regulatory time frame) for most of the ^{237}Np released. If the performance period is extended to 100,000 years or longer, ^{237}Np is predicted to reach the accessible environment in significant quantities. Thus, sorption in the zeolitic tuffs has a significant impact on predicted performance even if it is not strong enough to completely retard the migration. As expected, the percolation flux also plays a dominant role in the predicted performance, in a manner analogous to the effective K_d.

The measured variability in the chemistry of the unsaturated zone fluids, though somewhat significant, does not appear to create conditions under which effective K_d values are reduced to 0, except at pH values approaching 9. Most fluid samples have measured pH values closer to 8, creating a chemical regime in which significant sorption is predicted. Of course, bypassing of the zeolitic rock through fractures would minimize sorptive retardation; this effect is discussed further below. With regard to pH, alkaline fluid emanating from the repository region could possibly reduce sorption in the zeolites; however, for this to occur, the plume of high-pH fluid must persist to the zeolites without being buffered by the unsaturated zone fluids. Initial simulations indicate

that these effects are unlikely to impact ^{237}Np transport significantly unless the high-pH carrier plume lasts for 5000 years. Further work is required to characterize and model this possibility. The competing cations in the ion exchange model appear to be constrained enough to bound the effective K_d to values of order 2 cc/g. Though there is apt to be a range of effective K_d values due to variations in zeolite abundances and groundwater composition, it is unlikely that cation concentrations will achieve a level for which K_d values drop to lower than about 1 cc/g. Finally, the bicarbonate concentrations in unsaturated zone fluids are not high enough to result in significant carbonate complexation, as is implied by the low measured sorption in batch experiments with UE-25 p#1 fluids.

Although the ion exchange sorption model with speciation reverts to an effective K_d model under constant chemical conditions, its development was critical to examine the effect of transient hydrologic and chemical conditions brought on by repository heat effects and climate change. Chemical changes that are expected to occur during the period of ^{237}Np migration may potentially affect the sorption, creating a situation that cannot be characterized with a single K_d value. In addition to pH changes due to repository materials such as cement, climate changes are expected to result in chemical changes that in turn require the full reactive transport model, rather than a simplified K_d approach. However, the reactive transport model results can be used to justify model simplifications through a sensitivity analysis. Without the reactive transport model capability, justifying the simpler K_d approach would be much more difficult.

The impacts of waste heat and thermohydrology on the large-scale migration of ^{237}Np through the unsaturated zone appear to be relatively minor in comparison to, for example, the percolation flux through the unsaturated zone or sorption onto the zeolites for ^{237}Np. The perturbation from ambient temperature conditions has, in most simulations, subsided before the bulk of the ^{237}Np plume has reached the water table. This result is caused by several effects. First, the near-field thermohydrology (dry-out accompanied by minimal liquid flow into the drifts) is

predicted to limit releases of ^{237}Np during the period of the most vigorous thermal effects. Second, once waste packages become wet and ^{237}Np is leached, the solubility is low enough to stretch the period over which ^{237}Np escapes the near field to tens of thousands of years. This is a long enough period for the thermal wave to have returned to close to its ambient state. Although the ECM model assumption can be questioned, one-dimensional dual permeability calculations performed by C. Ho (C. Ho, pers. comm., 1997) agree with this general time scale of about 1000 years. Third, the redistribution of water in the form of vapor creates zones of concentration and dilution of dissolved species, however, the magnitude of these effects and their persistence in time are not great enough to significantly affect ^{237}Np transport. Finally, for ^{237}Np, the impact of temperature on speciation and sorption is only relevant in the zeolitic rocks, which are far enough from the heat source to minimize the potential impacts on transport. Nonetheless, under conditions of thermal-conduction-limited heat transfer in the saturated zone persists, the thermal plume persists for long enough to potentially influence the transport behavior of ^{237}Np in the zeolites. Thus, further work to bound the nature of the heat transfer coupling between the unsaturated zone and saturated zone is warranted.

Given the relative lack of significance of thermohydrology on site-scale transport, we tentatively conclude that isothermal calculations can be used in performance assessment modeling studies. However, future studies under non-isothermal conditions should address key uncertainties not treated here. The constancy of hydrologic and transport properties in the presence of wide changes in temperature is a key assumption that should be tested. Full thermohydrologic and transport simulations will also be necessary to further study the chemistry of the fluid that passes through the repository region. Nonetheless, isothermal fluid flow calculations are an appropriate platform on which to design Monte Carlo simulations in performance assessment analyses. An important aspect of the nonisothermal behavior that needs to be retained even in isothermal transport simulations is the temperature-dependence of ^{237}Np solubility, which in turn affects the duration of release. This effect can easily be included by using the rate of release from the

repository region from nonisothermal simulations as input to an isothermal simulation. Finally, the issue of fracture bypassing of the zeolites is an additional uncertainty in assessing the migration of ^{237}Np through the unsaturated zone. Using dual permeability simulations, we demonstrated that significant fracture flow through zeolites may occur, resulting in much more rapid transport to the water table and higher peak mass flux values. This uncertainty is being addressed through numerical simulations using the dual permeability model. A variety of fracture-matrix coupling models, hydrologic property data sets, and infiltration rates are being examined in two- and three-dimensional simulations, and will be the focus of a future paper. Until more definitive conclusions can be reached, our results on the influence of heat and chemical conditions must be viewed as provisional, given that, except for the zeolite bypass case, the modeling was performed under conditions in which matrix flow occurred in the zeolitic rocks.

Regarding the efficiency of the reactive transport code, the computational intensity of the simulations presented here proved to be manageable in two dimensions, allowing timely results to be obtained. The Selective Coupling method implemented in FEHM was crucial to the success of the ion exchange simulations. Ion exchange is an example of a chemical system in which chemical component concentrations are strongly coupled. In such instances, if the reaction kinetics are rapid compared to the transport time scale, convergence is difficult to attain unless the transport step is performed with coupling of the components in the ion exchange reaction. In the future, we will examine issues of computational efficiency in greater detail, determining the relative merits of Selective Coupling versus traditional SIA methods. The results of the present study suggest that the Selective Coupling method is a promising solution technique for multi-dimensional, reactive transport problems. Further development of the Selective Coupling technique will be pursued to attain additional computational and memory savings.

11.10 Conclusions

In this chapter we investigate the coupled effects of chemical interactions and heat on neptunium transport from the potential repository to the water table. The simulations indicate that in the absence of irreversible changes in the hydrologic and transport properties, the heat pulse does not significantly affect the migration of neptunium, as the time scale of heat pulse propagation is shorter than the time scales associated with neptunium release and migration. The major uncertainty in this conclusion is the possibility of rock-water interactions that permanently alter the porosity or permeability. Future investigations should focus on this possibility. Water chemistry, particularly pH and calcium and sodium concentrations, significantly affect the retardation of neptunium by the zeolitic rocks between the repository and the water table. The chemical compositions derived from field measurements appear to constrain the fluid chemistry sufficiently to allow for the estimation of sorption coefficient for ^{237}Np. Finally, the selective coupling method introduced to solve these reactive transport problems is a robust numerical technique applicable to a wide range of reactive transport problems.

Chapter 12 - Incorporation of Geostatistics into Flow and Transport Simulations

12.1 Abstract

The zeolitic threshold method used in previous chapters is replaced with more rigorous geostatistical modeling. With this more sophisticated modeling approach, we examine whether using a threshold cutoff for zeolitic abundance is an appropriate upscaling method for characterizing small scale heterogeneity. Geostatistical techniques are used to develop variograms, kriging maps, and conditional simulations of zeolitic abundance. The kriging maps are used to estimate the uncertainty in the mineralogical model. The conditional simulations result in equally probable maps of zeolitic abundance. Using the algorithms discussed in Chapters 2 and 3, a conditional simulation of zeolitic abundance was mapped on top of the geologic model. We investigate the relationship between percent alteration, permeability changes due to alteration, sorption due to alteration, and their overall effect on radionuclide transport. A key conclusion to the study is that the retardation due to sorption predicted by a conditional simulation is much larger than the retardation predicted by the zeolite threshold method. The reason for larger retardation of ^{237}Np for the conditional simulation is a small but significant K_d at locations with zeolite abundance less than 10%. For the purposes of abstracting these results, setting nonzero K_d's in the vitric tuffs may be an effective way to mimic the more rigorous conditional simulations. Rocks with high zeolitic abundance may not be as effective in retarding radionuclides such as ^{237}Np and Uranium since these rocks also in general have low permeability and contaminants can only enter these regions through molecular diffusion. In addition, any fractures in these highly zeolitized rocks will provide a mechanism for fluid and radionuclides to bypass these regions. In future studies, multiple conditional simulations will be performed using linear coregionalization models to strengthen the conclusions drawn in this study.

12.2 Software and Data QA Status

The FEHM code is used to perform all flow and transport calculations in this report. The code is qualified in accordance with Los Alamos quality assurance requirements and is documented in (Zyvoloski et al., 1992, 1995a, 1995b). The QA status of the data used in this report is shown in Table 12-1.The petroleum industry standard software packages STRATAMODEL (Stratigraphic Geocellular Modeling Reference Guide, 1995) and RC^2 (ResMod User's Manual, 1994) are used in the geostatistical analyses of heterogeneous materials. These are off-the-shelf software packages and are applied only to sensitivity studies in the present study. They are non-Q with respect to YMP and Los Alamos quality assurance requirements but they follow well documented methods for geostatistical representation of spatially varying attributes.

Table 12-1. QA Status of Data used in this Chapter

REFERENCE	Q Status	DTN	COMMENT
Altman et al., 1996, "Flow Calculations for Yucca Mountain Ground Water Travel Time (GWTT-95). Technical Report SAND96-0819, Sandia National Laboratories, 1996	non-Q	No DTN Assigned	No DTN Assigned
Bodvarsson et al., 1997 "The Site-Scale Unsaturated Zone model of Yucca Mountain, Nevada, For the Viability Assessment, LBL Technical Report LBNL-40378	Q	LB970601233129.001	No DTN assigned. Hydrologic property sets computed in this report are used throughout the present study.
Chipera et al., 1997a, "Preliminary Three Dimensional Mineralogical Model of Yucca Mountain, Nevada, YMP Milestone SP321AM4"	non-Q	Not Assigned	No DTN assigned
Chipera et al., 1997b "Mineralogic Variation in Drill Holes USW NRG-6, NRG-7-7a, SD-7, SD-9, SD-12, and UZ#14: New Data from 1996-1997 Analysis Los alamos National Laboratory YMP Deliverable SP321BM4"	Q	LADV831321AQ97.001	

Flint et al., 1996, Conceptual and numerical model of infiltration for the Yucca Mountain Area, Nevada", USGS WRIR MOL 19970409.0087	Q	GS960908312211.003/ NA	USGS DTN 3GUI623M
Flint, L. E., 1996, "Matrix properties of Hydrogeologic Units at Yucca Mountain Nevada", USGS Water-Resources Investigation Report, WRIR-96	Q	GS9609083122231.004 /NA	USGS DTN Report in Preparation.
Triay et al., 1996a, "Summary and Synthesis Report on Radionuclide Retardation for the Yucca Mountain Site Characterization Project, Los Alamos National Laboratory YMP Milestone Report 3784	Q	LAIT831341AQ96.001	
Triay et al., 1996b, "Radionuclide Sorption in Yucca Mountain Tuffs with J-13 Well Water,: neptunium, Uranium, and Plutonium, Los alamos National Laboratory Yucca Mountain Site Characterization Project" Milestone 3338, Technical Report LA-12956-MS	Q	LAIT831341AQ96.001 *	* DTN supersedes DTN LA000000000104.001
Triay et al., 1996c, "Batch Sorption Results for neptunium transport through Yucca Mountain tuffs, Los alamos National Laboratory Yucca Mountain Site Characterization Project Milestone 3349, Technical Report LA-12961-MS	Q	LAIT831341AQ96.001 *	*DTN supersedes DTN LA000000000090.001
Triay et al., 1996d, "Comparison of Neptunium Sorption Results using batch and column techniques, Los Alamos National laboratory Yucca Mountain Site Characterization Project Milestone 3041, Technical Report LA-12958-MS	Q	LA000000000106.001	DTN Accession No. MOL.19950630.0300

12.3 Motivation

Natural spatial variability in hydrologic and chemical properties can play an important role in the transport of contaminants in groundwater. Stochastic techniques to study the effects of this small-scale variability make up a large part of the groundwater literature (Gelhar, 1993). For example, reduction in sorption due to physical and chemical heterogeneity has been described by Tompson et al. (1996) and Smith et al. (1996). They suggest that for specific saturated flow

systems, significant contaminant transport will occur in zones of minimal reactivity since permeability and reactivity were found to be inversely correlated. Since we are concerned with zeolite heterogeneity in the unsaturated zone, the relationship between reactivity and effective permeability must be considered rather than the relationship between saturated permeability and reactivity.

The site-scale model of Yucca Mountain relies on averaging techniques in order to model the large scales which are of interest in the flow and transport calculations. In this chapter, we study the impact of small-scale variability in the zeolite distribution on the transport of ^{237}Np through the unsaturated zone. We develop the methodology for generating conditional simulations of zeolitic abundance to determine whether small-scale heterogeneities will significantly affect the travel times of ^{237}Np through the unsaturated zone.

Another assumption made in previous chapters was to use a threshold cutoff for zeolitic abundance. The threshold provided a method for assigning either vitric or zeolitic properties to each node since correlations did not exist between the degree of zeolitization and the hydrologic and chemical properties. In this chapter we will replace the zeolitic threshold method with more rigorous geostatistical modeling. This will allow us to determine whether using a threshold cutoff for zeolitic abundance is an appropriate upscaling method for characterizing small scale heterogeneity. Figure 12-1a shows the zeolitic distribution when a 10% threshold is used as the basis for considering a node to be zeolitically altered. The 10% threshold results in a zeolitic distribution that roughly follows the layers in Figure 2-1b of Chapter 2. A potential problem with using a simple threshold is that the zeolitic distributions change significantly as a function of the threshold. Figure 12-1b shows the zeolitic distribution for a 20% threshold: the layers loose their continuity and in some places appear as lenses. In this chapter, we examine the assumption of using a cutoff for zeolitic abundance by comparing those results to geostatistical simulations in which permeability, characteristic curve parameters for relative permeability, and reactivity are correlated to zeolitic abundance. With such correlations, the effects of chemical and physical

heterogeneity can be treated more rigorously without having to rely on a threshold cutoff for zeolitic abundance.

a

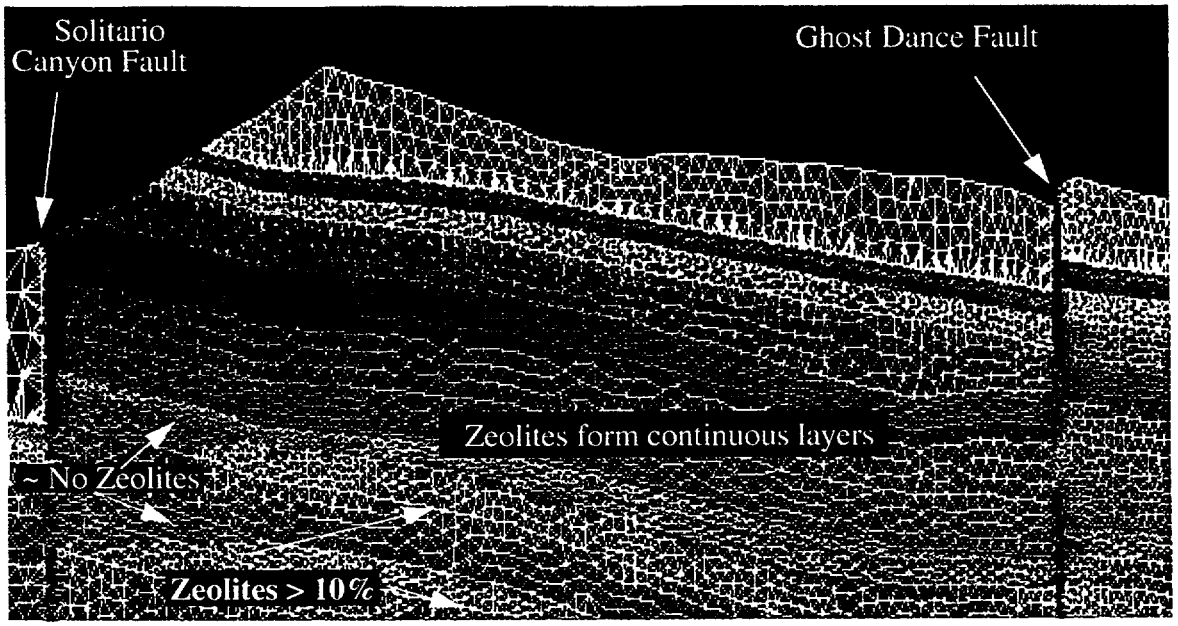

b

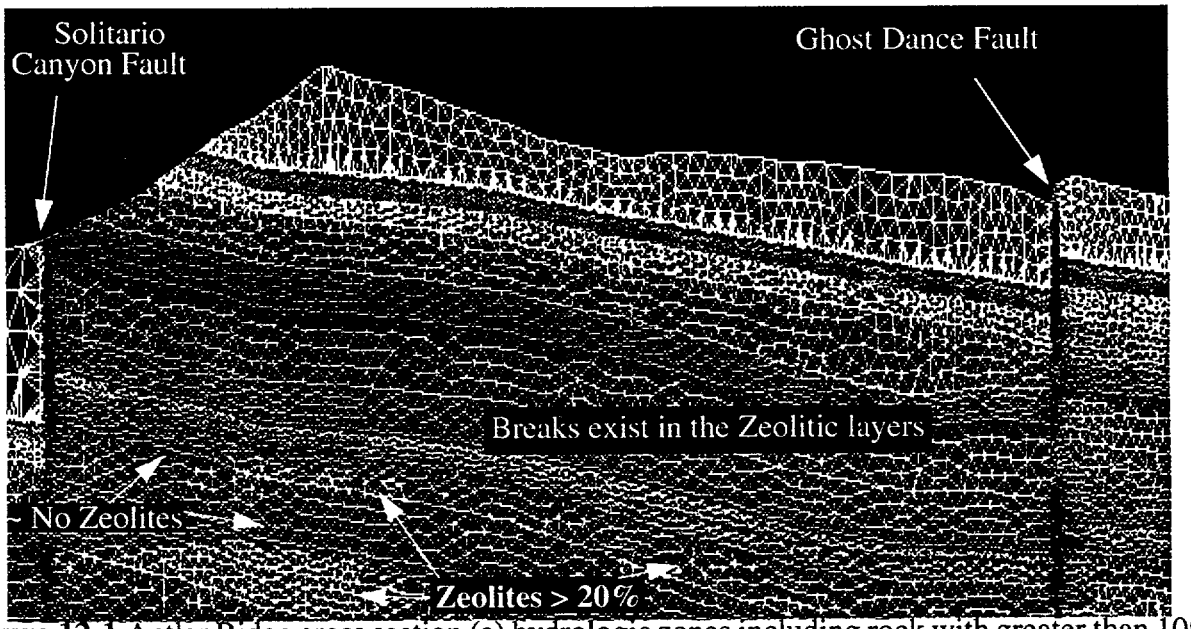

Figure 12-1. Antler Ridge cross section (a) hydrologic zones including rock with greater than 10% zeolitic abundance, (b) hydrologic zones including rock with greater than 20% zeolitic abundance.

This new 3-D framework model of fully distributed mineralogic abundances and corresponding hydrologic properties has been further improved through the application of geostatistical techniques that help characterize the uncertainties in spatial distribution of the hydrologic and chemical properties. These improvements now make it possible to refine the contaminant transport simulations. This chapter will summarize the ongoing efforts to integrate the mineralogic model and geostatistical techniques into the flow and transport simulations to better capture the effects of chemical and physical heterogeneity.

The following topics are covered in the sections of this chapter:

- Methodology for integrating geostatistical methods into the mineralogical model using a commercially available geostatistical software package (RC^2);
- A simple example to illustrate the implications of the choice of the threshold value for zeolitic cutoff;
- Field data that support a correlation between the physical and chemical properties at Yucca Mountain indicating that these correlations can have a large impact on the travel times for ^{237}Np. These correlations are used to study the relationship between zeolitic abundance, van Genuchten parameters, permeability and reactivity;
- Geostatistical techniques are used in conjunction with the mineralogical model to develop variograms, kriging maps, and conditional simulations of zeolitic abundance;
- Transport simulations are conducted with zeolitic abundance correlated to permeability, the van Genuchten model parameter α, and the distribution coefficient K_d. This simulation is used to investigate whether correlated heterogeneities can influence the travel times of ^{237}Np through the unsaturated zone, and if so, to devise abstracted models to capture the behavior.

12.4 Geostatistical Integration

Geostatistical techniques are powerful tools that can be applied to the Yucca Mountain mineralogic model because they (1) provide insight into the variability of the data; (2) characterize the uncertainty surrounding the data; and (3) help predict data values in unsampled areas. By utilizing careful geostatistical analysis of the 3-D data we can produce a fully populated stochastic site-scale numerical mineralogic model that can then be used as a basis for transport calculations.

The mineralogic model developed with STRATAMODEL (see Chapter 2) interfaces to a compatible commercially available geostatistical software package (RC^2). The regularly-spaced mineralogic data and stratigraphic surfaces output from SGM are imported by RC^2 and then analyzed by constructing experimental horizontal and vertical variograms of mineral abundance. These variograms help define the spatial continuity through a quantitative description of how data values change as a function of distance and direction. Interpretive variogram models are then used in the process of performing ordinary kriging and sequential Gaussian simulations. Ordinary kriging provides a weighted linear estimate of values at unsampled areas and is generally a smoothing technique that results in a map of the uncertainty in the data (kriging variance). Sequential Gaussian simulations, on the other hand, produce conditional simulations, given an initial random number seed. Changing the seed for each simulation yields a different realization, resulting in realistic maps of possible data values. Each simulation honors the data and always samples the same model variograms. Examples of the variograms, kriging maps, and sequential Gaussian simulations are shown in section 12.7.

12.5 Implications of Zeolite Threshold Cutoff

A simple example is developed in this section to illustrate the effect of using a threshold cutoff for zeolitic abundance on the transport of ^{237}Np. Transport through a 10 m by 10 m block of unfractured vitric tuff with a zeolitic layer will be compared to a block of vitric tuff containing

a rectangular zeolitic lens (Figure 12-2). Each block is representative of a typical element in the site-scale model for the Calico Hills unit. The layered case is analogous to a zeolitic layer shown in Figure 12-1a, whereas, the lens case is used to illustrate the case of a discontinuous zeolite distribution as shown in Figure 12-1b. In these block models, care must be taken to choose boundary conditions which will simulate a single element of the site-scale model. In the site-scale model, the water table serves as the bottom boundary condition and is thus simply set to a saturation of one. At steady state, the capillary pressure gradient and gravitational forces equilibrate to establish a saturation profile throughout the model domain. Due to the large size of the site-scale model, the capillary pressure gradient across a typical element is small. The balance between capillary pressure, which acts to retain water in the pores, and gravitational forces leads to a net downward percolation.

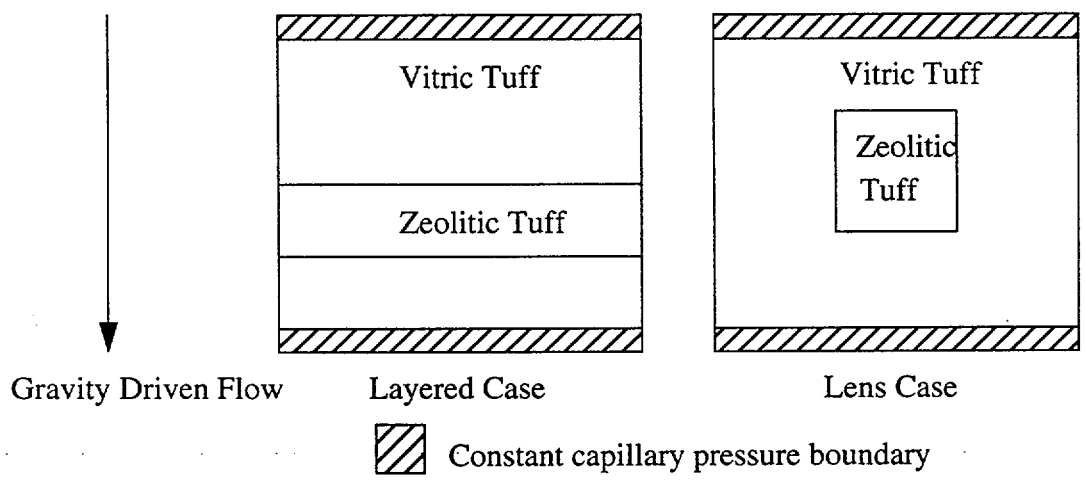

Figure 12-2. Two possible zeolitic geometries at the subgrid scale (10 m by 10 m).

In the block models, the bottom boundary cannot be set to a saturation of one as in site-scale models, because the block represents an element from the Calico Hills unit which is hundreds of meters above the water table. Therefore, we set the top and bottom boundaries of the block model to a constant capillary pressure, which results in a steady infiltration rate through the block. Lateral flow across an element can be important in the site-scale model but is not considered in this

example. The left and right sides are no-flow boundaries. We assume that these blocks are in a region of the site-scale model where downward percolation dominates.

Table 12-2 shows the properties of the vitric and zeolitic tuffs, and Figure 12-3 shows the relative permeability characteristic curves obtained from the van Genuchten model (van Genuchten, 1980). Model parameters (Flint, 1996) are given in Table 12-2.

Table 12-2. : Hydrologic and chemical properties of vitric and zeolitic tuff

Parameter	Vitric Tuff	Zeolitic Tuff
saturated hydraulic conductivity @25°C, (m/s)	4.3×10^{-9}	7.03×10^{-11}
saturated permeability, k_{sat} (m^2)	4.4×10^{-16}	7.17×10^{-18}
α of van Genuchten model (1/m)	0.0267	0.0035
n of van Genuchten model	1.386	1.495
porosity, ϕ	0.27	0.29

The quantity $k_{sat}*R_l$ is the effective permeability of the unsaturated medium. The characteristic curves of $k_{sat}*R_l$ versus capillary pressure show that, as expected, zeolitic tuff is less permeable than vitric tuff for capillary pressures less than 100 m. However, for capillary pressures greater than 100 m, the zeolitic tuff is actually more permeable than the vitric tuff. The permeability trends can be explained by the saturation-capillary pressure plot (Figure 12-3) . At low capillary pressures, the zeolitic and vitric tuffs are highly saturated and the permeabilities of the media approach the saturated permeability values. However, at a high capillary pressure, both media are drier, allowing the zeolitic tuff to actually conduct as much flow (or a little more) as the vitric tuff.

At steady state, the capillary pressure and gravitational forces equilibrate, leading to a net downward infiltration through the media. The capillary pressure at the model boundaries can therefore be chosen to obtain a given infiltration rate throughout the media. For example, setting the capillary pressure to 24 m results in an infiltration rate of about 4 mm/yr, whereas, a capillary pressure of 155 m results in an infiltration rate of about 0.1 mm/yr. Note that the infiltration rates

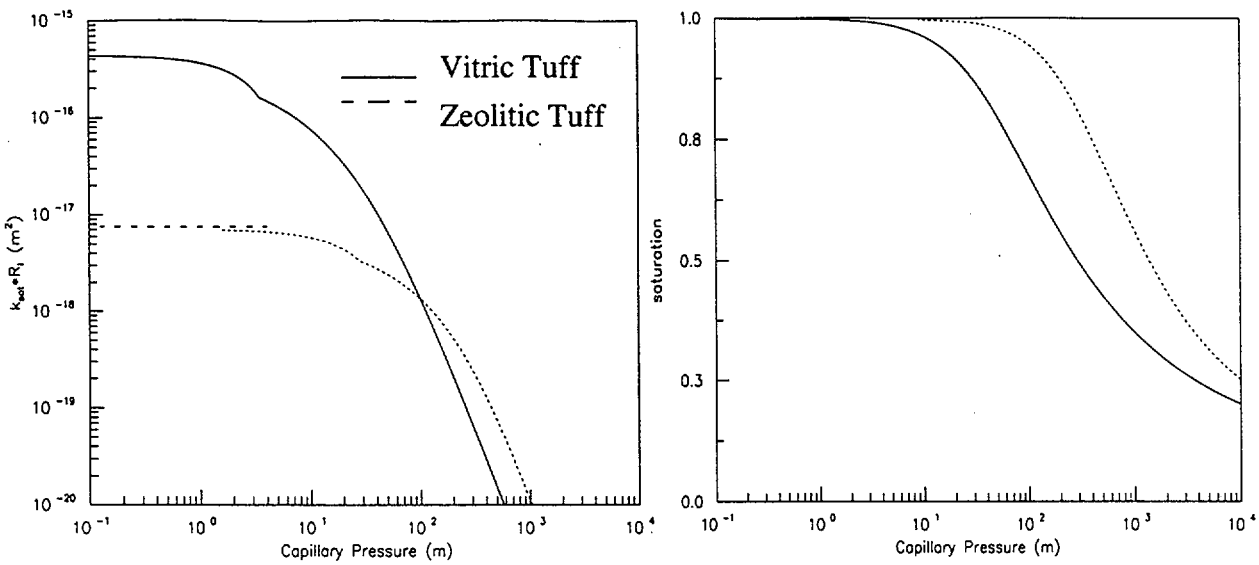

Figure 12-3. Comparison of the characteristic curves for zeolitic and vitric tuff.

are slightly different for the lens and layer cases for a given capillary pressure but are close enough for this illustrative example.

Three simulations were conducted at infiltration rates of 4 mm/yr, 1 mm/yr and 0.1 mm/yr (Figure 12-4). For the 0.1 mm/yr (P_{cap} = 155 m) simulation, the velocities are actually higher through the zeolites than through the vitric tuff, resulting in preferential flow through the zeolites. At 1 mm/yr (P_{cap} = 88 m), a slight bypass occurs around the zeolites with preferential flow through the vitric tuff. Again, the velocities through both media are similar. However, at 4 mm/yr (P_{cap} = 24 m), velocities are much higher through the vitric tuff than the zeolitic tuff. These trends are a direct result of the $k_{sat}*R_l$ vs. capillary pressure curve (Figure 12-3). Interestingly, the unsaturated permeabilities of the media change drastically over the range of infiltration rates that are expected at Yucca Mountain.

After a steady state flow field is obtained, ^{237}Np is injected uniformly along the top boundary to simulate the downward migration of ^{237}Np from the repository. For simplicity, ^{237}Np is assumed to linearly sorb to the zeolitic tuff with an equivalent K_d of 2 cm^3/g, and to not sorb to

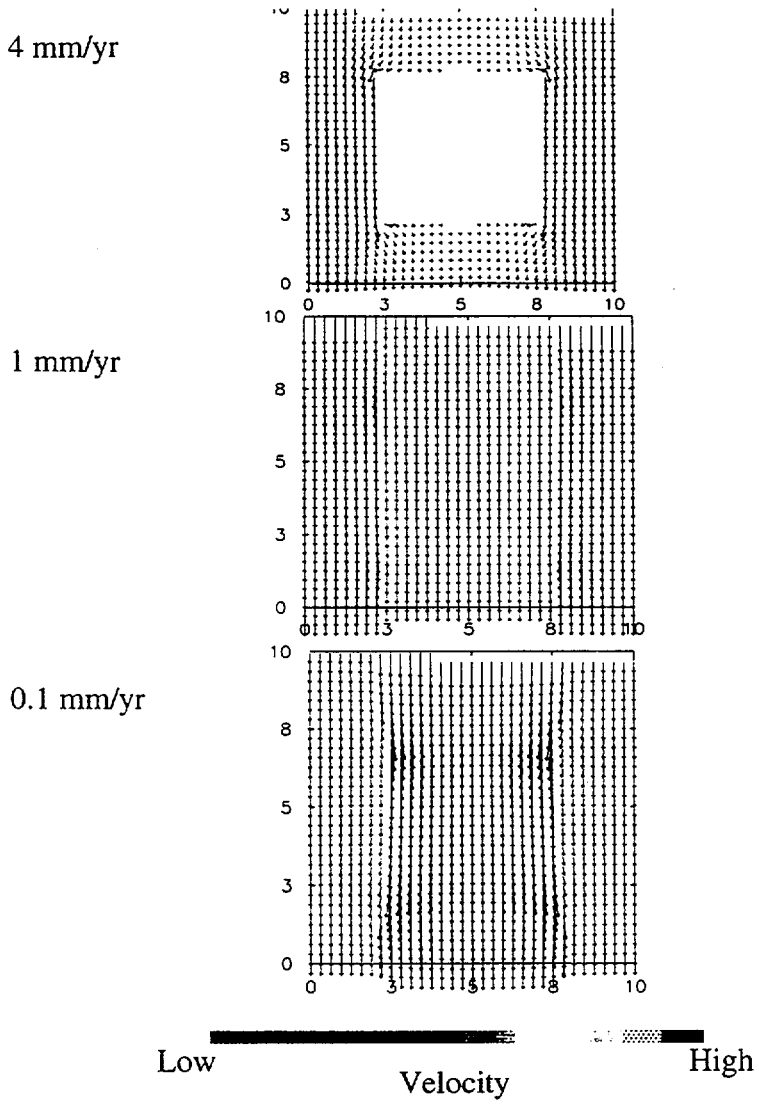

Figure 12-4. Velocity profile for the zeolitic lens case at three different infiltration rates.

the vitric tuff. In both blocks zeolites comprise 25% of the domain with the difference being the geometry of the zeolite (Figure 12-2). Table 12-3 shows the parameters used to conduct the simulations. The dispersivity and diffusion parameters are hypothetical values but are appropriate for ^{237}Np in Calico Hills tuffs.

Table 12-3. : Parameters used in the simulations

Molecular Diffusion, D^*	1×10^{-10} m^2/s
Longitudinal Dispersivity, a_l	0.01 m
Transverse Dispersivity, a_t	0.001 m
Grid spacing, Δx	0.3125 m
Time step, Δt	5,000 days

Figure 12-5 compares the cumulative mass of ^{237}Np arriving at the bottom boundary for the layered and the lens cases. At each infiltration rate, a pulse of ^{237}Np was injected into the system at the beginning of each simulation. Specifically, 166 moles of ^{237}Np at 4 mm/yr, 60 moles at 1 mm/yr and 11 moles at 0.1 mm/yr were injected over a 10 year period. For cases of lower infiltration rates, the layered case and lens case behave similarly since there are no major preferential pathways. However, for the 4 mm/yr case, the ^{237}Np is retarded to a greater extent for the layered case than for the lens case. This set of simple simulations shows that at relatively high infiltration rates, more extensive bypassing will occur if there are breaks in the zeolitic layers. Specifically, flow will preferentially avoid the zeolitic areas at relatively high infiltration rates. Section12.7 will show that zeolitically altered portions of tuff are actually correlated over length scales much larger than 10 m. Therefore, the size of the idealized flow block used in later flow and transport simulations will need to be modified. In this example, rock was assigned either zeolitic or vitric properties. This assumption is analogous to using the 10% zeolitic cutoff value. One of the questions we try to address in the rest of this chapter is whether using a zeolitic cutoff value is reasonable assumption.

12.6 Relationships Between Physical and Chemical Heterogeneity at Yucca Mountain

Figure 12-1 shows how a different threshold cutoffs for zeolitic abundance can result in significantly different zeolite distributions. A particular threshold was chosen for simplicity, and because correlations did not exist between the degree of zeolitization and the hydrologic and

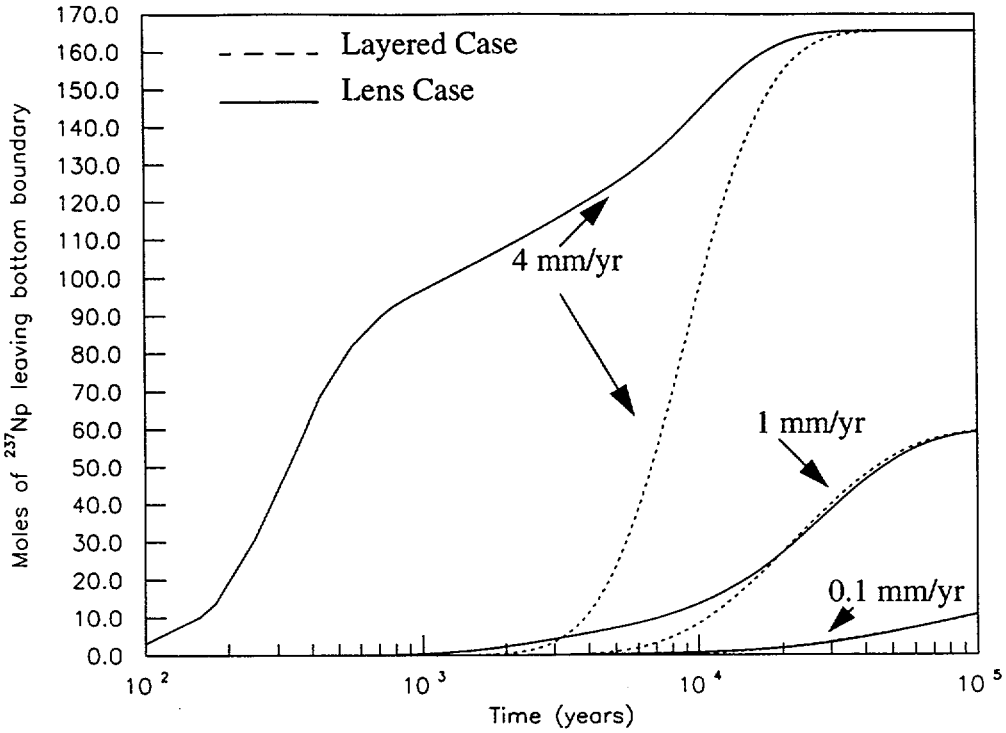

Figure 12-5. Comparison of ^{237}Np breakthrough curves for the layer and lens cases.

chemical properties. Therefore, this method was used to tag each spatial location as either vitric tuff or zeolitic tuff. Note, however, that the use of a threshold is still an improvement over the method used in previous studies in which entire layers were assigned either zeolitic or vitric properties.

In reality, the percent of zeolitic alteration is a continuous property which varies from 0-100%. In this section, we examine various sources of field data to determine whether the hydrologic (e.g. permeability and characteristic curve parameters for relative permeability) and chemical properties (e.g. distribution coefficient K_d) of the tuffs can be correlated to zeolitic abundance. Such correlations are expected because the physical and chemical properties of geologic medium can often be related back to fundamental measurable properties such as grain or pore size (Smith et al, 1996). Specifically, the process of zeolitic alteration acts to reduce the pore sizes of the vitric tuffs. If such correlations could be developed, the need for using a threshold cutoff would be eliminated.

The correlations presented are a combination of empirical relationships obtained from field data and theoretical relationships. Several regression relationships have been developed by various researchers within the Yucca Mountain Project. Theoretical relationships with physical bases also exist and could be used to correlate the various properties. The following subsections describe relationships that could be used to generate realizations of multiply correlated properties (permeability, characteristic curve parameters, and K_d). The methodology for generating such realizations will be discussed in section 12.8. The Monte Carlo method is then used to stochastically determine how correlated fields of permeability, relative permeability and K_d can affect ^{237}Np transport.

12.6.1 Correlation between Permeability and Zeolitic Abundance

Flint (1996) developed a relationship between K_{sat} and the percent of clinoptilolite in the Calico Hills unit (Figure 12-6). The data set is limited because data points exist at low and high percentages of zeolitic abundance, but not at intermediate percentages. The regression relationship clearly shows that there is not a 1:1 relationship between K_{sat} and the percent zeolite. However, zeolitic alteration does clearly lower the permeability of the tuff. Others have also shown that zeolitic alteration causes a large reduction in the hydraulic conductivity (Loeven, 1993). Although the correlation coefficient of the regression is low, it captures a trend that is physically correct.

12.6.2 Correlation between Porosity and Permeability

Numerous permeability and porosity measurements exist from the Calicò Hills unit. Data from Altman et al. (1996) were used to determine the relationship between porosity and K_{sat} (Figure 12-7). Each data point was tagged as being zeolitic or vitric. However, the zeolitic abundance of each sample was not recorded and no threshold cutoff was reported.

The relationship between porosity and K_{sat} was obtained from a large number of measurements and is well correlated. The zeolitic samples all fall in the low permeability, low porosity range, whereas the vitric and devitrified tuffs vary in porosity and permeability over a

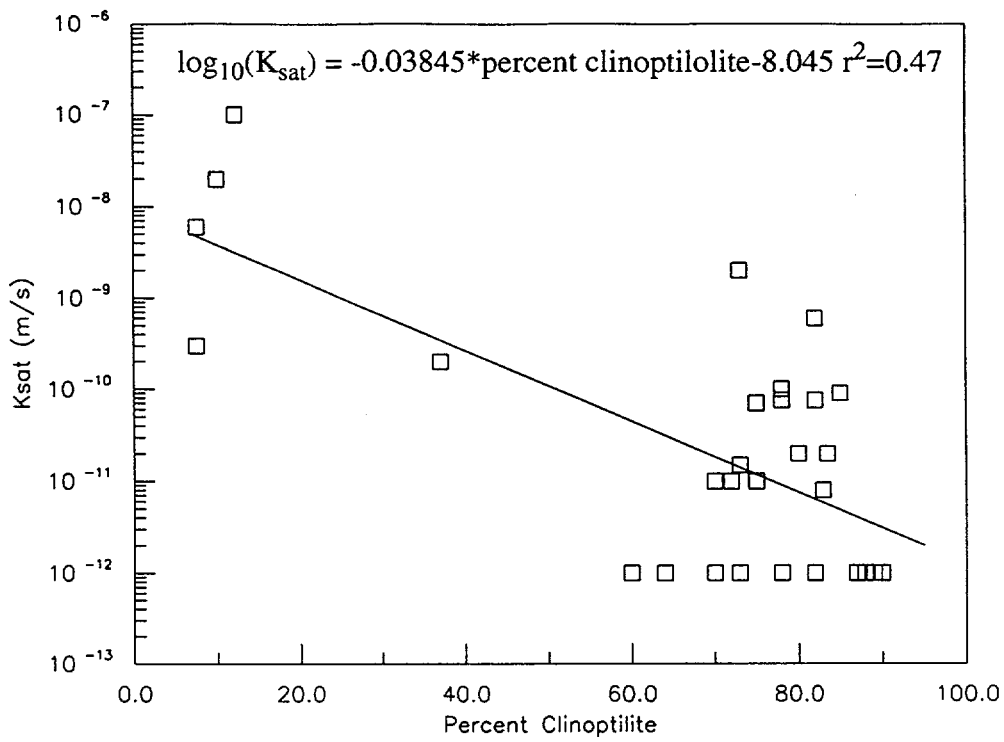

Figure 12-6. Data relating% clinoptilolite to $K_{sat,}$ (from Flint, 1996).

much wider range. There is however some overlap in the porosity and permeability ranges of the vitric and zeolitic tuffs.

A large number of porosity measurements are available from Yucca Mountain lithologies. If a method were available to relate porosity measurements to zeolitic abundance, the porosity data could be used to generate a variogram which would provide information about the spatial structure of the zeolites. Zeolitic alteration causes a large reduction in K_{sat} but a very small reduction in porosity (Loeven, 1993). Rautman and Engstrom (1996) has used a technique that uses porosity information as an indicator for zeolitic abundance. In this study, we do not use the porosity data but instead opt to use the direct measurement of zeolitic abundance contained in the mineralogic model. In the future, we hope to use both the mineralogical data and the porosity data.

12.6.3 *Correlation Between Permeability and Reactivity*

A theoretical correlation between physical and geochemical heterogeneity for idealized porous media is given by Smith et al. (1996). The derivation assumes that the permeability,

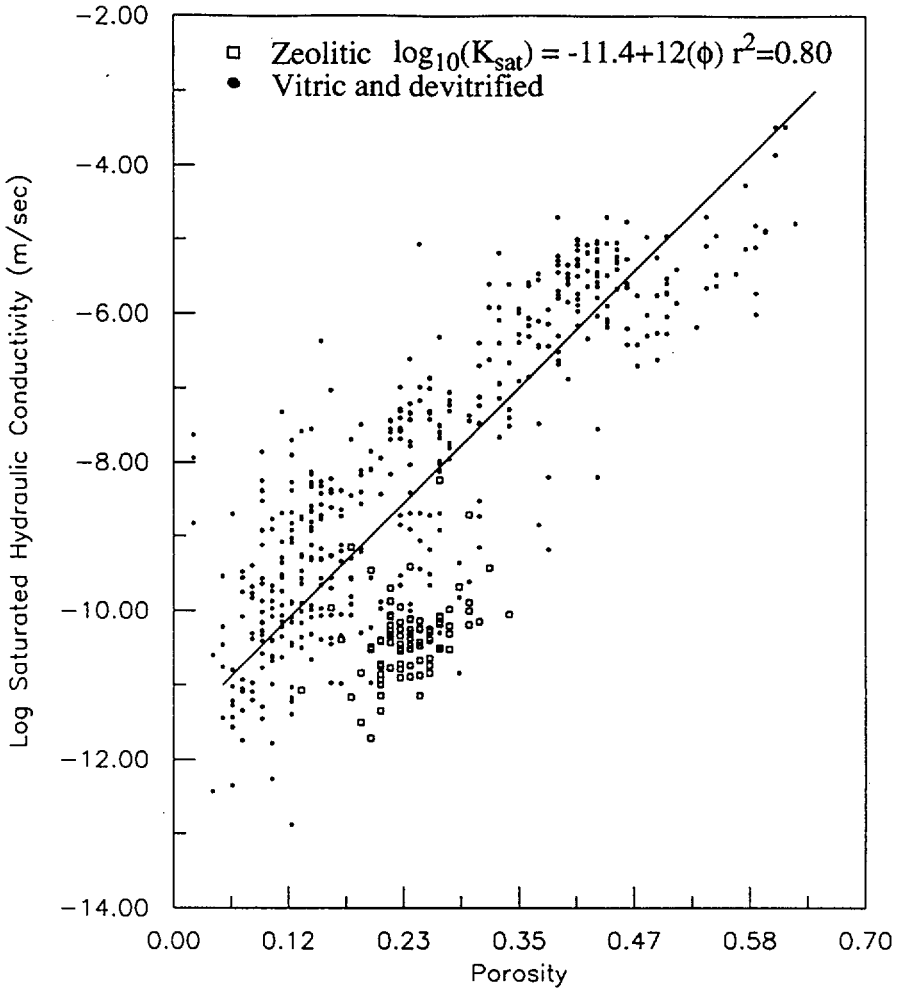

Figure 12-7. Data from Altman et al. (1996) relating porosity to K_{sat}.

porosity, and grain surface area are related through the concept of a hydraulic radius (Smith et al., 1996). The relationship is given by:

$$K_{d,m} = \frac{K_{d,a}}{\rho} \cdot \frac{\theta}{1-\theta} \cdot \sqrt{\frac{\theta}{2\tau k}} \qquad \text{(Eq. 12-1)}$$

where $K_{d,m}$ is the distribution coefficient based on the mass of rock, $K_{d,a}$ is the distribution coefficient based on surface area, ρ is grain density, τ is tortuosity, k is permeability, and θ is porosity. Equation 12-1 shows that $K_{d,m}$ is inversely proportional to the square root of k for an ideal monomineralic porous media. Whether this correlation is applicable to ^{237}Np migration through zeolitic tuff needs to be determined by examining sorption data for experiments performed by

Triay et al (1996a, b, c, d). A qualitative examination of the sorption data indicate that equation 12-1 produces the correct trends. Specifically, Triay et al. (1996a, b, c, d) found that the K_d for ^{237}Np is a linear function of surface area.

12.6.4 Correlation Between Permeability and Relative Permeability

The van Genuchten function is used for predicting capillary pressure (van Genuchten, 1980). Qualitatively, α is inversely related to the air entry pressure, and n is inversely related to the width of the pore-size distribution. Therefore, a theoretical correlation between permeability and relative permeability may be possible. Although no theoretical correlation has been found, an empirical relationship exists between α and permeability. Altman et al. (1996) performed a linear regression between the hydraulic conductivity (K_{sat}) and α using core data from the Calico Hills unit.

$$\log(\alpha) = -1.62 + 0.41\log(K_{sat}) \quad r^2=0.81 \qquad \text{(Eq. 12-2)}$$

where α is in units of 1/Pa and K_{sat} is in units of m/s (Figure 12-8). Since the range of n is only from 1.21 to 1.73, Altman et al (1996) suggest that a constant mean value of 1.60 can be used. A constant residual saturation of 0.0453 is assumed for the Calico Hills tuffs. This parameter is obtained via fits to data rather than direct measurement, and thus is very poorly constrained. For this reason, we hold the value constant in the simulation.

12.6.5 Summary of Field Data

The empirical nature of these regression relationships poses a problem. The linear regressions are not, by and large, based on physical relationships. Therefore, it is possible to find linear relationships (especially with poor correlation coefficients) between properties even if a true correlation between these properties does not exist. Therefore, the flow and transport simulations which use correlated random fields based on these regression relationships may include"false" correlations leading to unrealistic results. An eventual goal of the current research is to use or develop relationships between variables that are based on a theoretical foundation. Another goal is

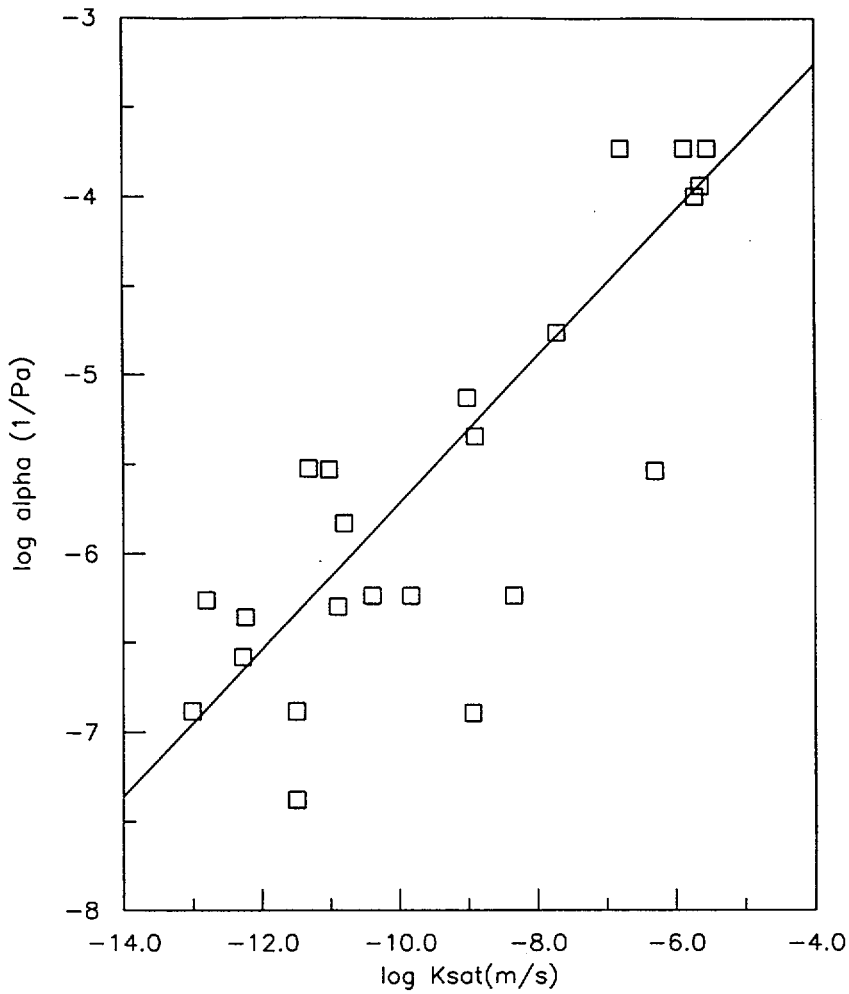

Figure 12-8. Data from Altman et al. (1996) relating α to K_{sat}.

to factor in the error component of these regressions into any correlated random fields that are generated. Section 12.7 discusses methods to generate such realizations.

12.7 Generating Realistic Zeolite Distributions

Before the above correlations can be used in numerical simulations, realistic distributions of zeolites must be constructed. The geostatistical package RC^2 was used in conjunction with STRATAMODEL to perform several geostatistical operations. First, the stratigraphic information and the well data were ported to RC^2, which was used to generate horizontal and vertical variograms of zeolitic abundance. The variograms provide a measure of spatial correlation by

characterizing how sample data are related with distance and direction. These variograms are necessary to perform kriging and sequential Gaussian simulation (discussed in section 12.4). Kitanidis (1996) states that variogram analysis cannot be performed using a set procedure; instead, creating a variogram is more of an "art". A variogram should be constructed from knowledge of the underlying processes generating the data and by customization of the available tools. The main goal of a variogram analysis is to construct a variogram that best estimates the autocorrelation structure of the underlying stochastic process. For simplicity, in this preliminary study, the horizontal variogram was chosen to be isotropic. Specifically, the spatial correlation of zeolites in the east-west direction was chosen to be the same as the spatial correlation in the north-south direction. Rautman has shown that there are some significant differences between the east-west and north-south zeolite distributions (C. Rautman, pers. comm., 1997). In the future, directional horizontal variograms will be used in the analysis.

Given the number of lags, and the lag distances, RC^2 calculates the experimental horizontal variogram along each stratigraphic layer. RC^2 is then used to fit a theoretical model to the experimental variogram. Figure 12-9a shows the horizontal variogram chosen for the analyses shown in this chapter. A vertical variogram was chosen using a similar procedure and is shown in Figure 12-9b. These variograms were generated with RC^2 using the MINPET data from the Calico Hills and Prow Pass units. The horizontal variogram predicts a correlation length of 2000 m in the horizontal, whereas, the vertical variogram predicts a correlation length of 16 m. The spherical variogram model was used for the analyses. The reason for the small correlation length in the vertical direction is because properties were distributed within each layer (each layer is about 50 m in thickness). These results qualitatively agree with the results of Rautman (C. Rautman, pers. comm., 1997). Rautman of SNL has done a significant amount of work in developing variograms for zeolitic abundance at Yucca Mountain. In the future, we plan to collaborate more closely with Rautman to refine the variograms used in this analysis. Meanwhile, these present variograms are sufficient for these preliminary analyses.

(a) horizontal variogram (b) vertical variogram

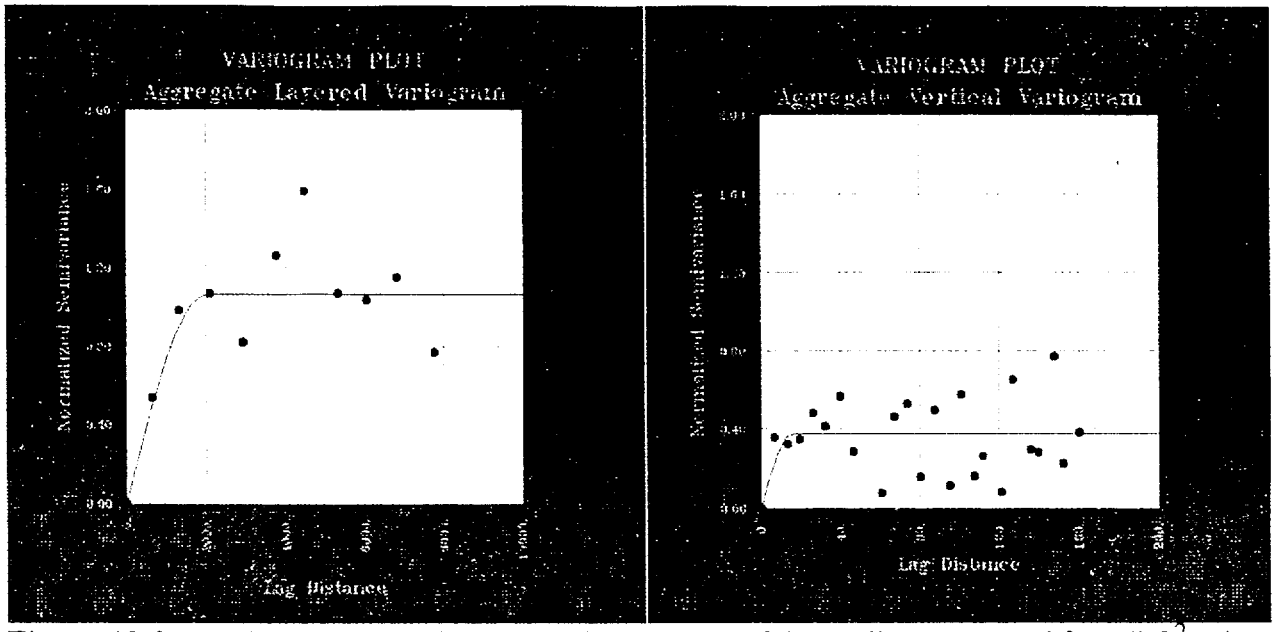

Figure 12-9.v Variograms depicting the spatial structure of the zeolites generated from RC^2 using data from the Calico Hills and Prow Pass units.

The horizontal and vertical variograms can be used to perform ordinary kriging of zeolitic abundance (Kitanidis, 1996). Ordinary kriging provides a weighted linear estimate of zeolitic abundance at unsampled areas. Ordinary kriging also provides a map of the uncertainty in the data which is known as the kriging variance. Figure 12-10 shows the kriging estimate of the percent zeolitic abundance for both a north-south and an east-west cross section. The estimate clearly shows the distinct zeolitic horizons that exist in the Calico Hill units. In general, kriging acts to smooth the data and therefore may not resemble the zeolitic distribution actually present in the field. Later, we use sequential Gaussian simulation to generate equally likely realizations of zeolitic abundance. These conditional simulations will result in more realistic distributions of zeolites.

Figure 12-11 shows the kriging variance for the cross sections shown in figure 12-10. At locations near the wells, the standard deviation of zeolitic abundance approaches zero. Locations far from well data approach the variance (900) of zeolitic abundance (standard deviation = 30%). The kriging variance assumes that the data at all of the wells are accurate. Therefore, nearby wells

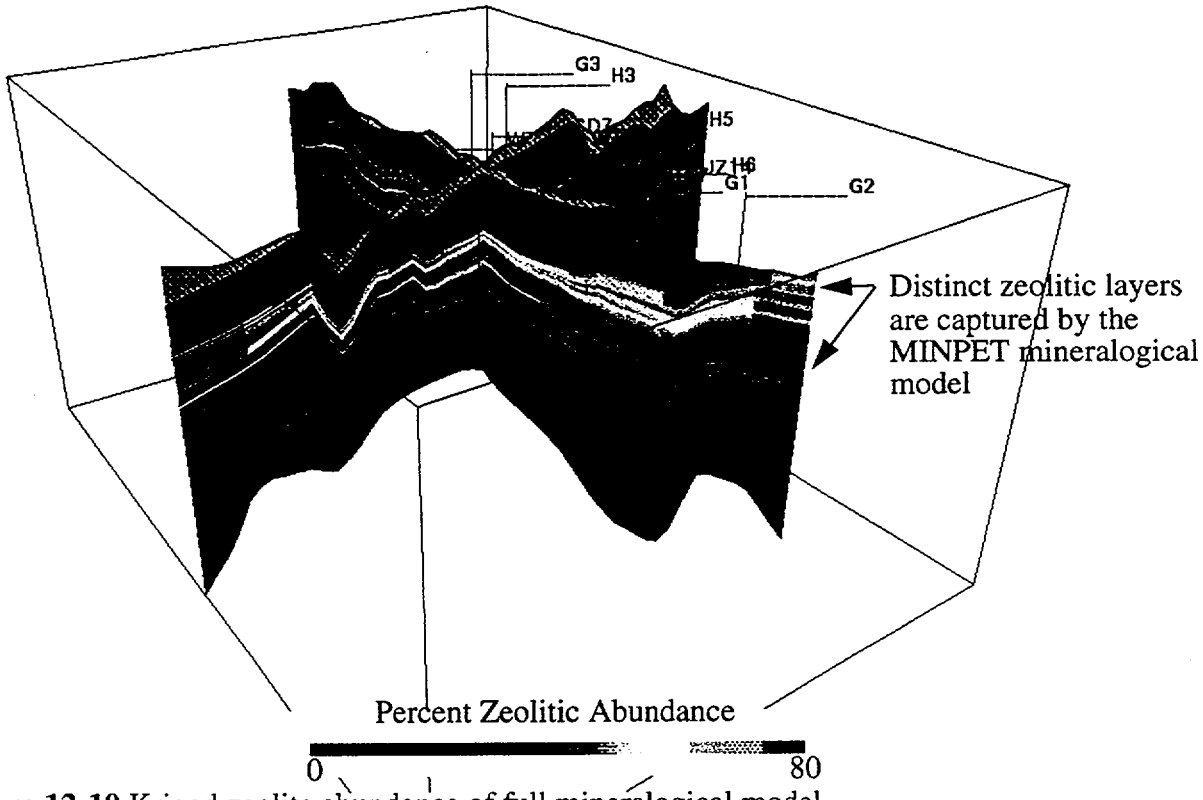

Figure 12-10. Kriged zeolite abundance of full mineralogical model.

with conflicting data will still result in a low kriging variance, whereas, in reality, the uncertainty at such a location is large. Even with these limitations, the kriging variance still provides a quantitative measure of the uncertainty of zeolitic abundance.

Sequential Gaussian simulations produce conditional simulations given an initial random number seed. Changing the seed for each simulation yields a different realization, resulting in equally probable maps of zeolitic abundance. Each conditional simulation can capture heterogeneity at much finer scales than is possible with the smooth kriging map. The ensemble mean of numerous conditional simulations should theoretically approach the kriged map of zeolitic abundance. However, flow and transport through a given conditional simulation may result in significantly different results than flow and transport through the kriged map. This is because the conditional simulations do not smooth out the heterogeneities in zeolitic abundance. In order to capture these smaller-scale heterogeneities, the mineralogical model domain was refined. For flow and transport simulations, the model domain was chosen to be much smaller than the domain of

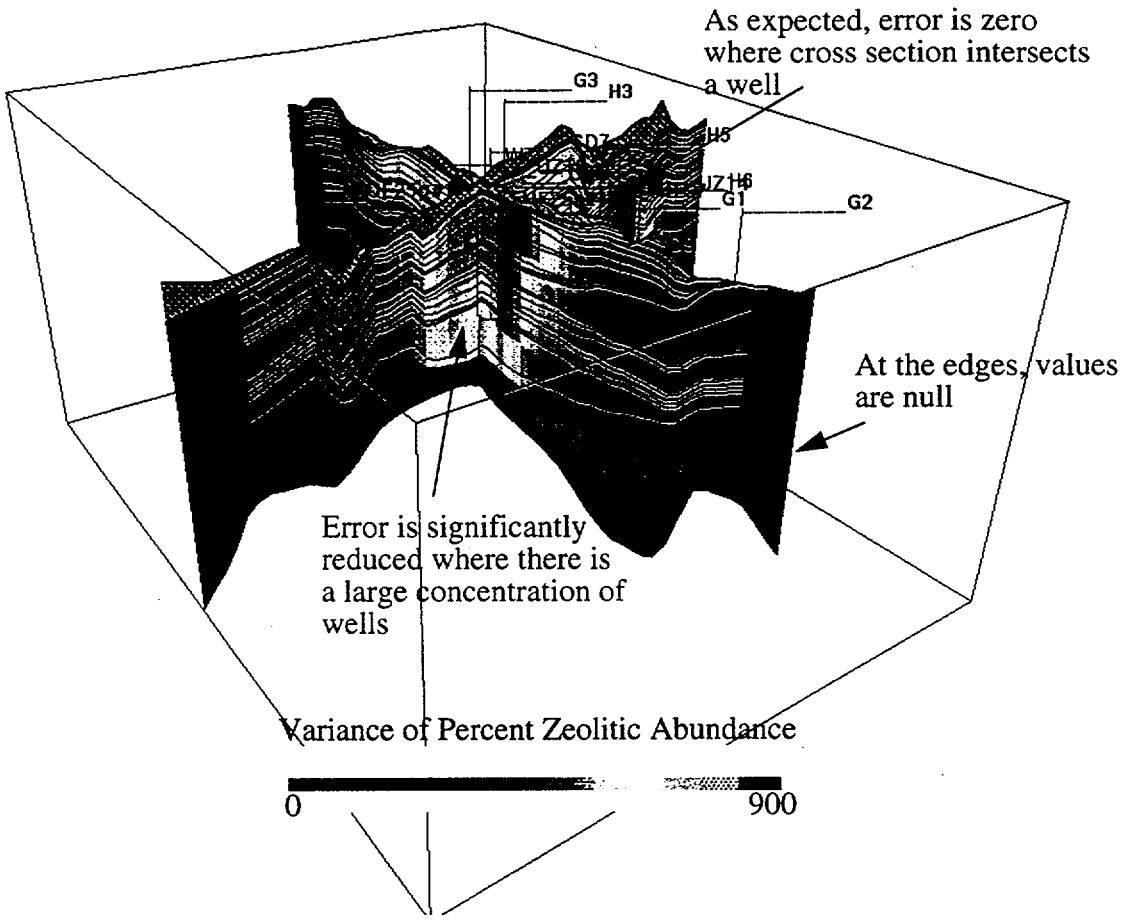

Figure 12-11. Variance of Kriged zeolite abundance in full mineralogical model.

the full mineralogical model. Specifically, only zeolites between the repository and the water table are of interest for radionuclide migration. In addition, we constrain the geostatistically simulated domain to be between the Ghost Dance and Solitario Canyon faults. With this smaller subset of the STRATAMODEL mineralogical model, a finer grid spacing (40 meters) can be chosen in the x and y directions, rather than the 243.84 m spacing of the full model, without greater computational expense. Because the horizontal variogram indicated that zeolitic abundance has a correlation length of about 2000 m, the 40 m spacing in the x and y directions should be adequate to capture the small scale heterogeneities in zeolitic abundance. The vertical direction already contained sufficient refinement and therefore was not refined. Figure 12-12 shows the refined subsection of the full mineralogical model. Figure 12-13 compares the kriged map to several conditional simulations. The kriged map clearly smooths out many of the small-scale heterogeneities that are

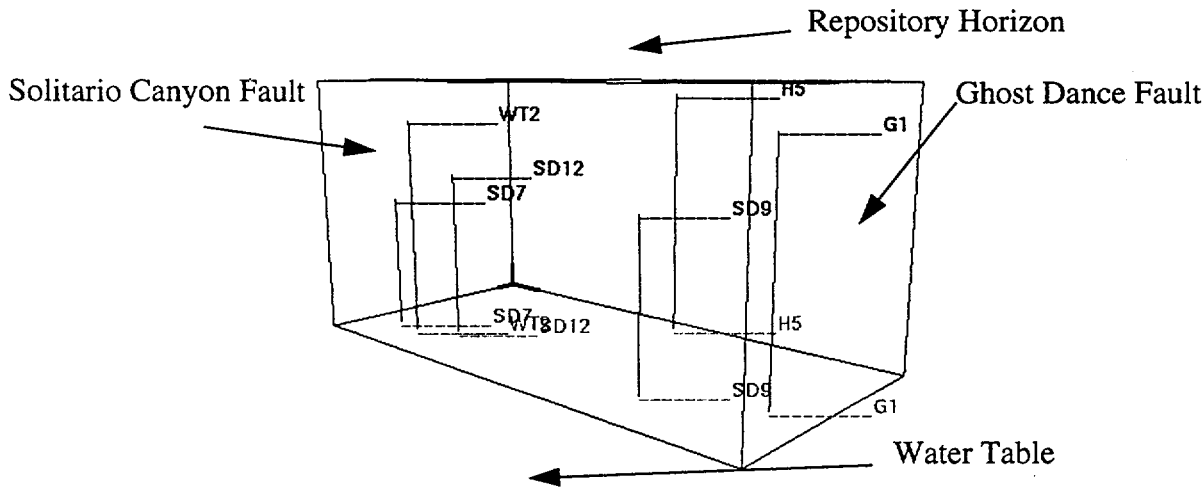

Figure 12-12. Three-dimensional block for high resolution study (4000mx2000mx300m). present in the conditional simulations. The conditional simulations also differ substantially at locations that are not close to well

After each conditional simulation of zeolitic abundance is generated, the results must be mapped onto the computational mesh. Conditional simulation 1 shown in Figure 12-13 was mapped onto the refined Antler Ridge cross section computational mesh (Section 8.8) and the result is shown in Figure 12-14. The mapping algorithm is discussed in Section 3.3. Note that the conditional simulation is mapped between the Solitario Canyon and Ghost Dance faults. All zeolites outside this region simply contain the 10% zeolite cutoff since transport of ^{237}Np occurs primarily in the zeolites between the Solitario Canyon and Ghost Dance faults at this cross section.

12.8 Generating Correlated Properties from Maps of Zeolitic Abundance

Section 12.6 showed that relationships exist between zeolitic abundance and hydraulic conductivity (empirical); porosity and hydraulic conductivity (empirical); permeability and the distribution coefficient (theoretical); and α and hydraulic conductivity (empirical). As experimentalists gather more data, knowledge of these relationships may improve. With these correlations, the relevant properties can be distributed using a random field generator. The ultimate

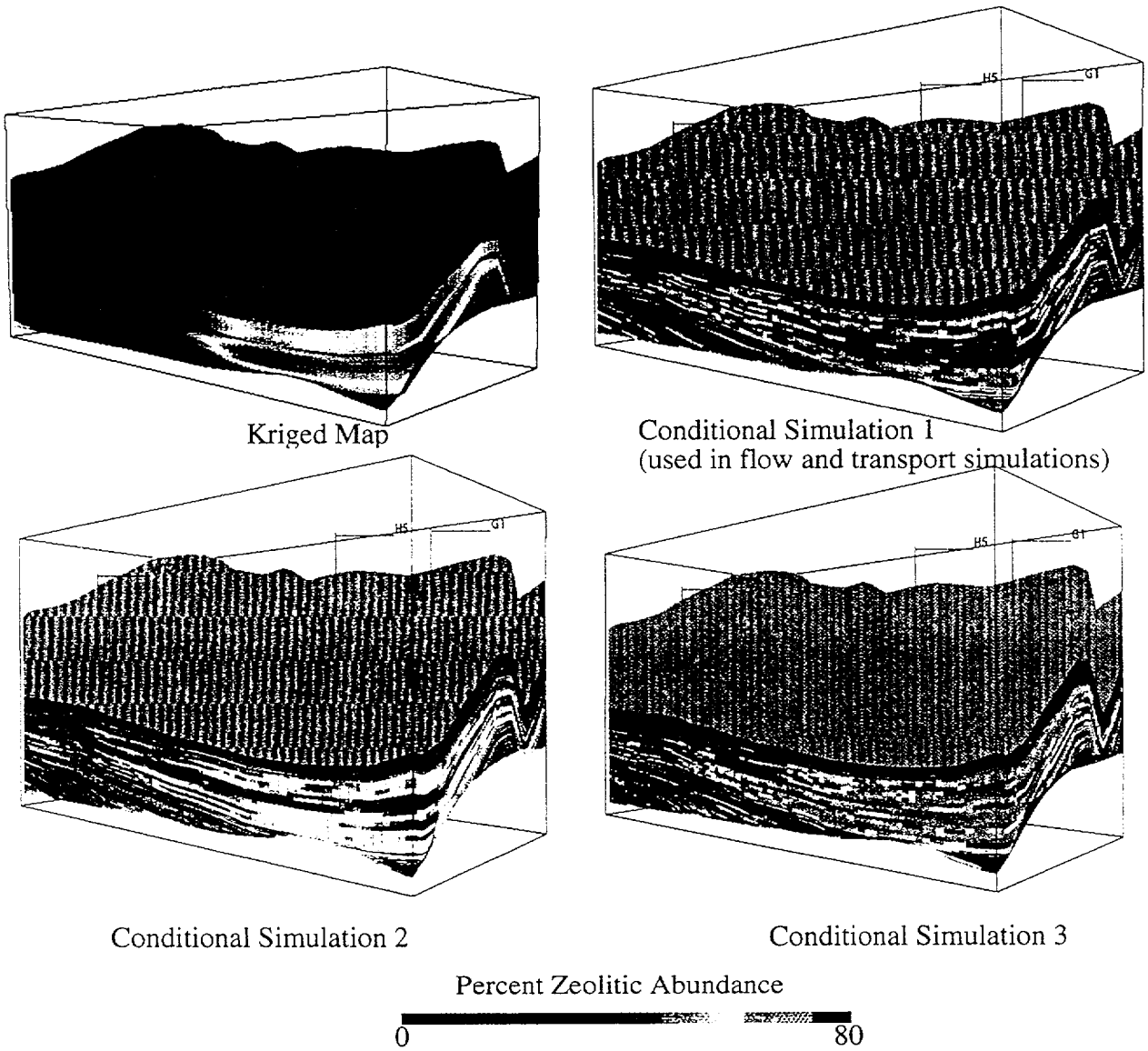

Figure 12-13. Comparison of the kriged map and three conditional simulations.

goal of the simulation process is to generate from a map of zeolitic abundance realizations of multiple properties (permeability, relative permeability, porosity, and K_d) which honor the univariate statistics of each property, the covariances between properties and the spatial statistics of each property as well as the spatial cross-covariances between properties.

One possible method for distributing properties is to use cosimulation (Deutsch and Journel, 1992). However, cosimulation requires the statistical moments of each property, the variogram of each property, and the cross-variogram between all pairs of properties. For many of

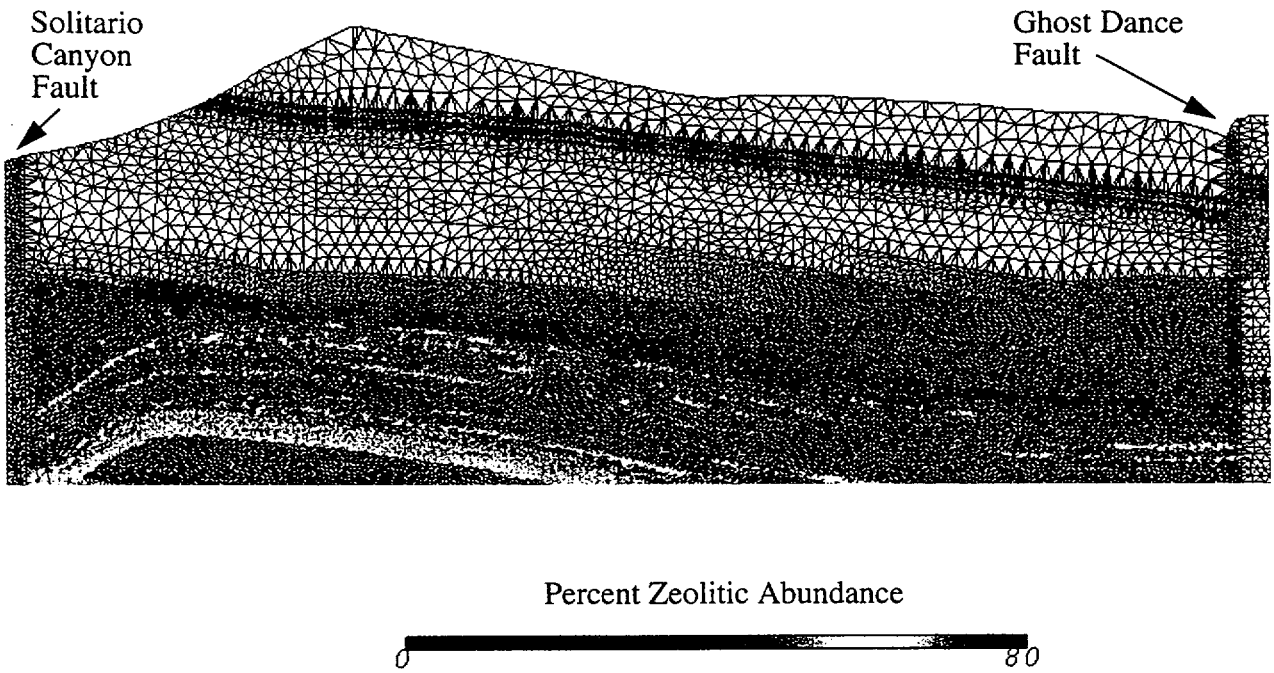

Figure 12-14. Conditional simulation of percent zeolitic abundance mapped onto the refined computational mesh between the Solitario Canyon and Ghost Dance faults.

the relevant properties, available data are not sufficient to construct a variogram or a cross variogram. Previous attempts to generate realizations of multiple properties within the Yucca Mountain Project generated a realization of a primary property such as porosity. A simple regression relationship between the primary property (e.g. porosity) and the secondary property was then used to generate secondary properties (e.g. permeability) at each spatial location. This approach may not produce satisfactory results when the regression relationship contains a large error component (r^2). Ignoring the error term implies an unrealistic 1:1 correlation between the primary and secondary properties. The previous section showed that many of the regression relationships contain large error components. Therefore, Altman et al. (1996) suggest that for Yucca Mountain data, linear coregionalization (Journel and Huijbregts (1978) and Luster (1985)) is a possible compromise between cosimulation and regression techniques.

Linear coregionalization lies somewhere between true cosimulation, where the information contained on the primary variable informs and constrains the simulation of the secondary variable, and regression techniques (Altman et al. (1996)). Coregionalization honors the univariate statistics

of each property, the covariances between properties and the spatial cross-covariances between properties. A constraint of the linear coregionalization model is the requirement that variograms and cross-variograms of all simulated properties have the same model type and structure. Since zeolitic alteration of the vitric tuff is the physical process affecting k, α and K_d in the Calico Hills units, this constraint is not a problem. For example, we can infer all parameters in a variogram model for percent zeolitic abundance from the 3D mineralogical model (3817 measurements are available). Secondary properties such as K_{sat}, ϕ, K_d, and α can then be obtained from the regression relationships which also honor the structure of the zeolitic distribution. Specifically, the univariate statistics, the covariances between properties and the spatial cross-covariances between the primary property and all secondary properties will be honored. The linear coregionalization method is described by Journel and Huijbregts (1978) and Luster (1985). Altman et al. (1996) summarizes the method for two correlated properties, although there is no theoretical limit on the number of correlated properties that can be generated.

12.9 Flow and Transport Simulations with Geostatistics

In this preliminary investigation, linear coregionalization was not used. Instead, we simply use the zeolitic abundance at each spatial location and correlate it to K_{sat}, α, and K_d. As stated above, this assumes a 1:1 correlation between properties. As work continues, linear coregionalization will be used to distribute correlated properties to avoid this problem. In addition, other parameters such as fracture spacing may be correlated to zeolitic abundance if appropriate.

Figure 12-15 shows the permeability distribution derived from the conditional simulation of zeolitic abundance shown in Figure 12-14. All layers above the Calico Hills unit are assigned the property values of parameter set 6541. The Calico Hills and Prow Pass units are given permeabilities which correspond to zeolitic abundance using the correlation shown in Figure 12-6. The relationship between α and K_{sat} was used to assign values for α in the Calico Hills and Prow Pass units (Figure 12-8). No relationship currently exists which relates zeolitic abundance to K_d.

Although experiments by Triay et al (1996a, b, c, d) clearly have shown that K_d increases with zeolitic abundance. As zeolitic abundance increases, the surface area available for sorption increases resulting in a higher K_d. We used a simple linear relationship to relate K_d to zeolitic abundance. At 0% zeolite, we assume that no sorption of ^{237}Np will occur. We then choose different slopes to relate the zeolitic abundance to K_d. By running simulations at several different slopes we bracket the variability in K_d.

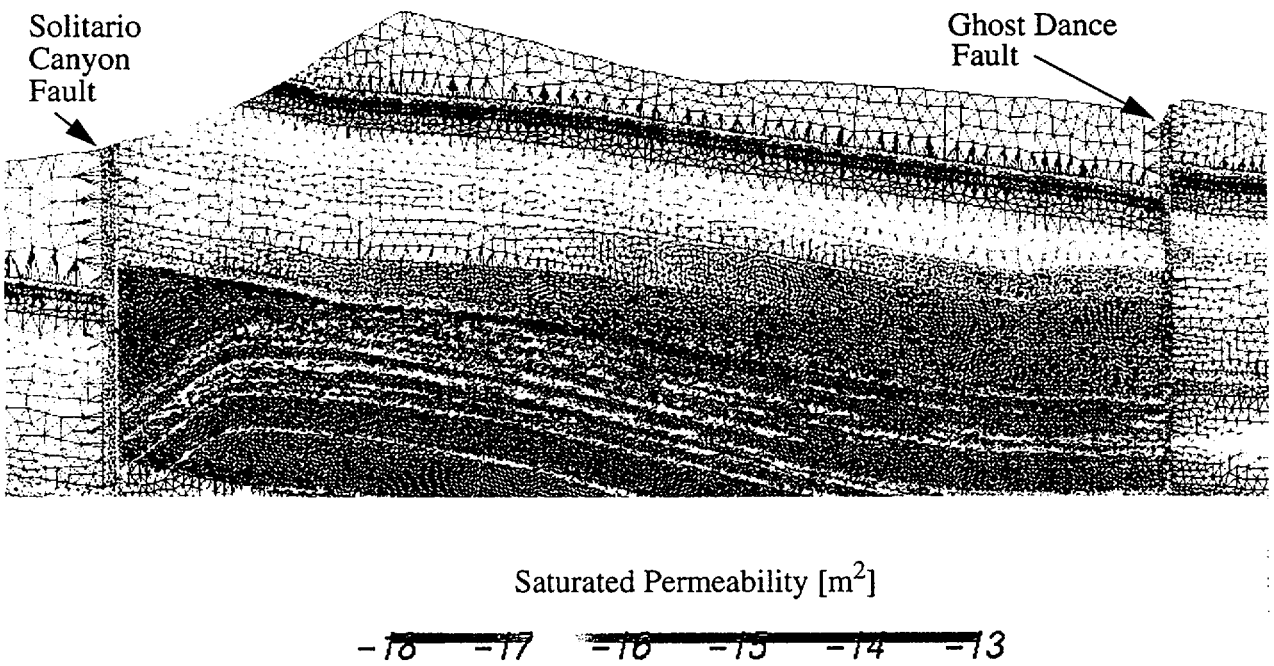

Figure 12-15. Permeability distribution for a conditional simulation. Percent zeolitic abundance-permeability correlation is used between the Solitario Canyon and Ghost Dance faults for all layers below the repository. The rest of the computational domain is assigned default permeability values.

Figure 12-16 shows the matrix and fracture saturations for the conditional simulation. In general the saturation profiles look similar to the saturation profiles which resulted from using a 10% threshold cutoff.

Figure 12-17 compares the 10% zeolite cutoff and the conditional simulation for a conservative tracer. Again, the breakthrough curves look similar. This result is not surprising since the saturation profiles for the two cases are similar. The differences in the simulations only appear

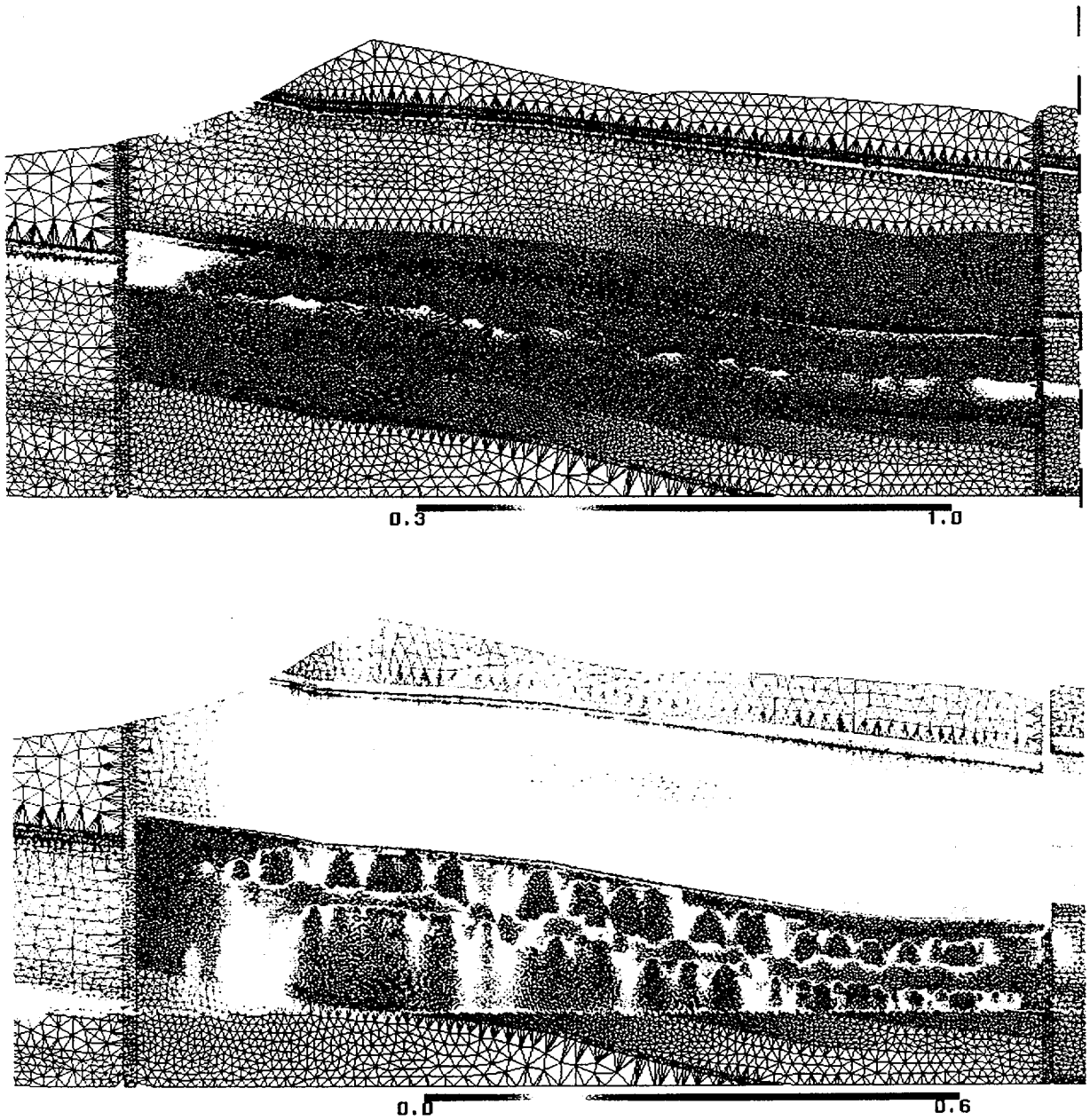

Figure 12-16. Saturation profile of the conditional simulation. (a) matrix saturation, (b) fracture saturation.

as the retardation of ^{237}Np is included. The correlation between permeability, α and K_d then play an important role.

Recall that Section 8.8 showed that for most property sets, even a zeolitic K_d of 20 did not strongly retard radionuclides for the 10% zeolitic threshold case. However, for the conditional simulation, K_d has a large effect on the travel time. Even for the case in which K_d varies linearly

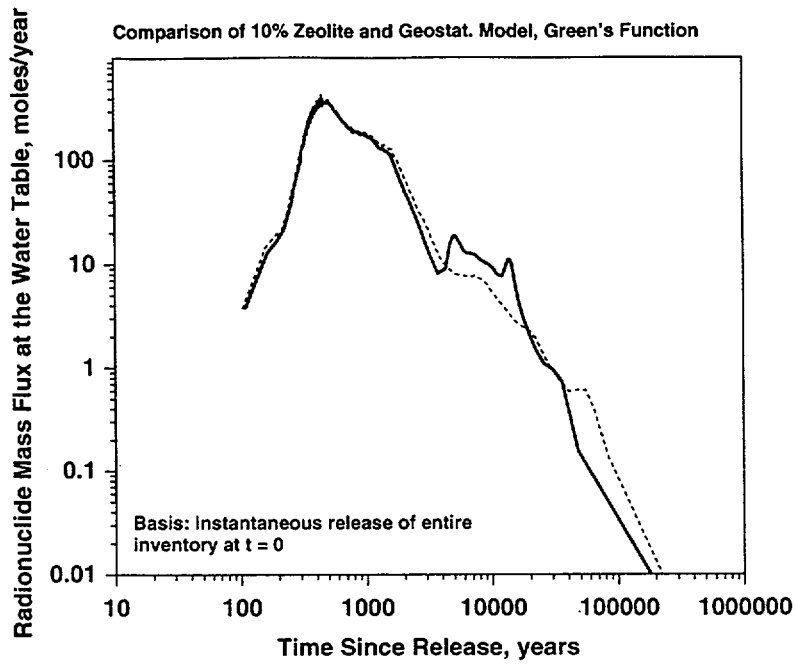

Figure 12-17. Comparison of the 10% zeolite cutoff runs of Chapter 8 and a conditional simulation for a conservative tracer.

with zeolitic abundance from 0 to 5 g/cc, the retardation is much larger than the retardation predicted by the K_d of 20, 10% cutoff case (Figure 12-18). Figure12-19 shows that for the 1/3 infiltration rate case (discussed in previous chapters), the conditional simulation again results in much larger retardation.

The reason for larger retardation of ^{237}Np for the conditional simulation is due to small, but significant, K_d at locations with zeolite abundance less than 10%. The increased sorption is not caused by high K_ds of 5 g/cc at high zeolite percentages. Very little flow travels through these highly zeolitized locations since they are very low in permeability. We can prove this by returning to the 10% threshold case. If we assign a small K_d (just 10% of the maximum K_d) to all locations with zeolite abundance between 0 and 10%, we prove that even small but significant amounts of sorption on rock with low zeolite abundance can strongly affect the travel times of ^{237}Np (Figure 12-20). Figure 12-20 shows that modifying the 10% threshold case to include some sorption for locations with zeolites abundances less than 10% closely matches the conditional simulation.

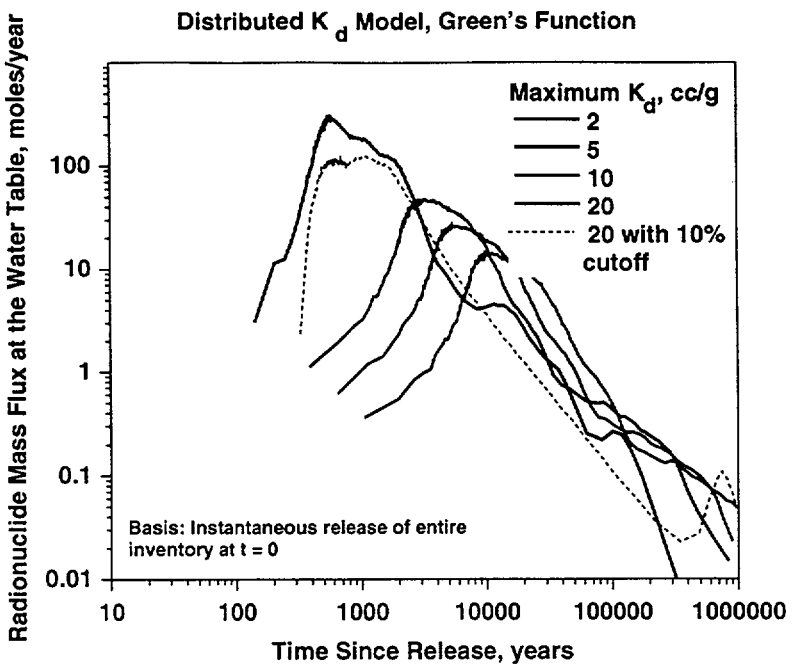

Figure 12-18. Conditional simulation with different K_ds compared to the 10% cutoff case with a K_d of 20.

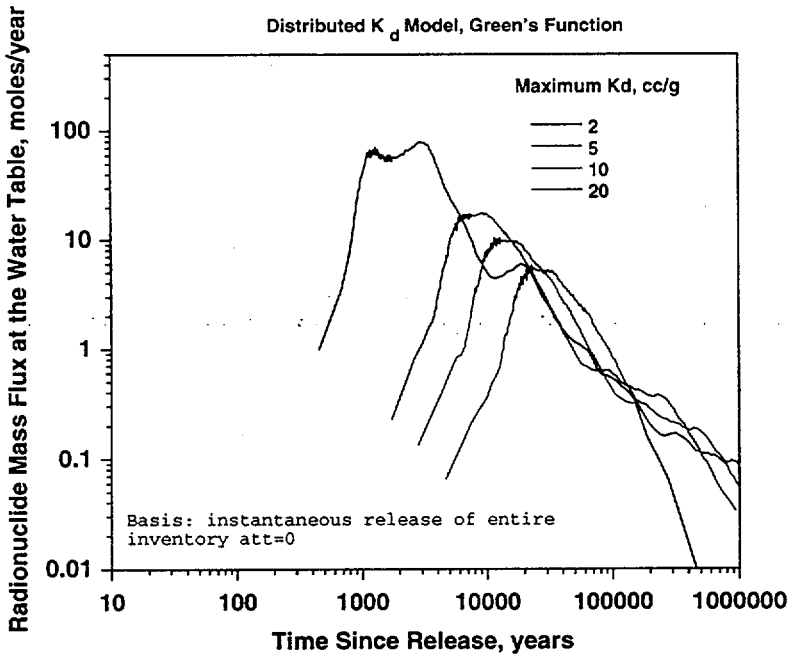

Figure 12-19. Conditional simulation using different K_ds with 1/3 the infiltration rate in Figure 12-18.

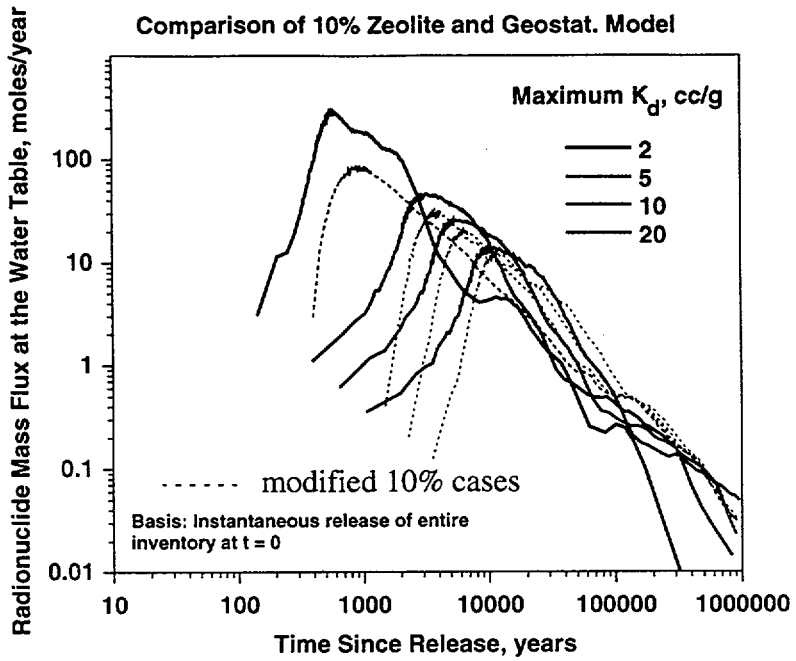

Figure 12-20. Modification of the 10% zeolite case to better match the conditional simulation. The dotted lines show the results when all rocks with zeolitic abundance less than 10% are assigned a K_d of $0.1*K_d$.

Therefore a key conclusion to this study is to recommend that experimentalists determine whether rocks with low but non-zero zeolitic abundance exhibit measurable sorption of radionuclides like ^{237}Np and Uranium. Rocks with high zeolitic abundance may not be as effective in retarding these radionuclides since these rocks generally have low permeability, and contaminants would primarily enter these regions through molecular diffusion. In addition, any fractures in these highly zeolitized rocks will provide a mechanism for fluid and radionuclides to bypass these regions. However, small but significant sorption of rocks with low zeolite content may have a very large impact on the travel times for ^{237}Np through the unsaturated zone. ^{237}Np transports through the matrix of these rocks and even a small K_d of 1 cc/g can have a large impact. For the purposes of abstracting these results, we set nonzero K_d's in the vitric tuffs (Figure 12-20).

In order to draw more substantial conclusions, many more conditional simulations need to be performed. In addition we plan to refine the correlations and variograms and implement linear coregionalization models. In this study, the general framework has been developed to integrate

geostatistical information into the site-scale flow and transport calculations. These powerful tools provide a means for determining the uncertainties associated with radionuclide transport through the unsaturated zone at scales not normally studied in site-scale models. In addition, we can use these more rigorous simulations to check the validity of simplifying assumptions used for other flow and transport simulations.

12.10 Conclusions

Small scale variability of chemical and hydrologic properties can play an important role on the prediction of flow and transport in the unsaturated zone. The variation in chemical and hydrologic properties is strongly dependent on the mineral distribution. Due to the correlation between mineral distribution and hydrologic and chemical properties, the distribution of minerals such as zeolites can strongly influence the flow patterns of percolating fluids and the sorption of many radionuclides. In this chapter, the zeolitic threshold method used in previous chapters is replaced with more rigorous geostatistical modeling. With this more sophisticated modeling approach, we examine whether using a threshold cutoff for zeolitic abundance is an appropriate upscaling method for characterizing small scale heterogeneity.

The methodology for integrating geostatistical techniques into the mineralogical model is first developed. These geostatistical techniques are used to develop variograms, kriging maps, and conditional simulations of zeolitic abundance. The kriging maps are used to estimate the uncertainty in the mineralogical model. The conditional simulations result in equally probable maps of zeolitic abundance. Eventually, simulating flow and transport for many conditional simulations, we will be able to estimate the uncertainty in ^{237}Np travel times using monte carlo techniques.

Using the algorithms discussed in Chapters 2 and 3, a conditional simulation of zeolitic abundance was mapped on top of the geologic model. We investigate the relationship between

percent alteration, permeability changes due to alteration, sorption due to alteration, and their overall effect on radionuclide transport.

A key conclusion to the study is that the retardation due to sorption predicted by a conditional simulation is much larger than the retardation predicted by the zeolite threshold method. The reason for larger retardation of ^{237}Np for the conditional simulation is a small but significant K_d at locations with zeolite abundance less than 10%. At these locations, the K_d is low (less the 1 cc/g) but permeability is large enough for the flow to be matrix dominated. By contrast, the increased retardation is not due to high K_d values which occur at high zeolite abundance. since very little flow travels through these low permeability regions. Modifying the 10% threshold case to include some sorption at locations with zeolite abundances less than 10% closely matches the more rigorous conditional simulation. For the purposes of abstracting these results, setting nonzero K_d's in the vitric tuffs may be an effective way to mimic the more rigorous conditional simulations.

We therefore recommend that experimentalists determine whether rocks with low but non-zero zeolitic abundance exhibit measurable sorption of radionuclides like ^{237}Np and Uranium. Rocks with high zeolitic abundance may not be as effective in retarding these radionuclides since these rocks also in general have low permeability and contaminants can only enter these regions through molecular diffusion. In addition, any fractures in these highly zeolitized rocks will provide a mechanism for fluid and radionuclides to bypass these regions. However, small but significant sorption of rocks with low zeolite content may have a very large impact on the travel times for ^{237}Np and other radionuclides through the unsaturated zone. The planned transport test at Busted Butte should provide results for testing this hypothesis.

In order to draw more substantial conclusions, many more conditional simulations will need to be performed. In addition we plan to refine the correlations and variograms and implement linear coregionalization models. In this study, the general framework has been developed to integrate geostatistical information into the site scale flow and transport calculations. These powerful tools provide a means for determining the uncertainties associated with radionuclide

transport through the unsaturated zone at small scales not normally studied in site scale models. In addition, we can use these more rigorous simulations to check the validity of the simplifying assumptions incorporated into other flow and transport simulations.

Chapter 13 - Conclusions

The site-scale unsaturated-zone transport model for Yucca Mountain integrates information from the field, the laboratory, and other Project modeling efforts into an assessment of the geologic barrier from the potential repository to the water table. The integration begins with the Project's geologic and mineralogic models describing the structural features and the zeolite distribution in the unsaturated zone. Our software integration system brings these two different models together into one structural and geochemical representation of the study system. The automatic grid generation capabilities play a large role in integrating these data sets as well as generating reliable finite-element grids on which accurate flow and transport calculations can be performed. These grids capture nearly exactly the structural controls at Yucca Mountain represented in the Integrated Site Model of geology. Surfaces which are output from that model feed directly into the GEOMESH grid generation package. Thus, the dipping, faulted beds of spatially varying thickness and extent are captured with as high a resolution as the geologic model puts out. Figures throughout this document and particularly in Chapter 3 show that even the most complex features such as layer pinchouts and fault offsets are captured with high resolution. These grids follow state-of-the-art quality control procedures to insure that grid related errors are minimized in the simulation of flow and transport.

Most of the transport simulations presented in this study are performed with the FEHM particle tracking module. The technique is used for unsaturated transport simulations because the limitations of standard finite-element of finite-difference methods (small time steps and spatial resolution) are mostly eliminated with this cell-based approach. Accurate simulation of dual-permeability systems in which there is a vast disparity in the travel times depending on whether the transport is in the fractures or the matrix are achieved efficiently with this method.

The FEHM particle tracking module is first used in this study to perform a screening analysis of the multiple property sets recently developed by LBNL to represent the unsaturated zone hydrologic material properties. Sensitivities for the various parameter sets to transport time from the potential repository to the water table were evaluated. From the initial group of 10 different parameter sets, 5 were screened as requiring further attention in the two- and three-dimensional models of radionuclide transport. This screening exercise also served as a code validation check by comparing the results of FEHM and TOUGH2, two of the Project's simulation models for unsaturated zone analyses. This comparison provided valuable insight into the grid resolution necessary to capture flow transition from predominantly fracture flow to mostly matrix flow at the TSw/CHn interface. It also highlighted some issues associated with different approaches for weighting material properties across interfaces. Based on this evaluation, we recommend that in mountain-scale flow and transport simulations, the absolute permeability be harmonically weighted, and/or the grid be more finely discretized near interfaces of contrasting flow and transport properties.

In an assessment of flow and transport between the ground and the potential repository, we apply the FEHM particle tracking method to our study of environmental isotopes in the hydrologic system. Like the property assessment study, this study serves to evaluate the multiple different parameter sets generated recently by LBNL to describe the material properties. Whereas the property sets study focussed on the pathway between the potential repository and the water table, this analysis focuses on the pathway to the potential repository and the ESF, where sampling for $^{36}Cl/Cl$ ratios has led to a substantial database. The flow and transport simulations are performed in one-, two-, and three-dimensions and serve to describe a complex system where travel times through the PTn depend of infiltration flux, PTn thickness, and the parameters representing the PTn properties. All of these can vary in space thus leading to a system where responses such as rapid transport in fractures may occur in one portion of the site but not in another. The general conclusions from this study are that transient responses at the potential repository are more likely to occur in the southern portion of the site, but the infiltration may be low enough that they never

occur. Moving north, the PTn thickens and the capacity to imbibe even large pulses of short duration increase. In the simulations, the proportion of flow that stays in the fractures of the PTn is sensitive to the model of fracture-matrix coupling. Whereas two different representations of that process may lead to similar predictions of matrix saturation, the amount of flow that is sustained in the PTn fractures may vary between representations. The difference tends to be most prominent in the South. Finally, the results of this study serve to address alternative conceptual models. One model suggests that very young water is moving ubiquitously through the system at the ESF level, having bypassed most of the PTn matrix in the fractures. The present model parameters would support such a hypothesis in the southern portion of the ESF. The data, however, indicate more fast paths to the ESF in the North with virtually no such indication at any of the southern stations. This result also serves to indicate that the estimated infiltration rate leads to faster travel to the ESF than the data indicate, even through the PTn matrix in the North. A scaled version of the current infiltration map leads to simulation of travel times that match the apparent ages based on assumptions about higher $^{36}Cl/Cl$ ratios in infiltrating water 10,000 years ago.

Until now, we have used geochemical databases to constrain and evaluate the validity of our flow and transport models in order to provide a strong scientific basis for the abstractions of these products used by Performance Assessment. We have also focussed on the water chemistry databases for pore waters and perched waters, in order to identify and discuss alternate models for flow and transport in Yucca Mountain.

Alternative conceptual flow and transport models for Yucca Mountain are being entertained based on hydrologic and hydrochemical databases. Explanations for the water chemistry variations in perched and pore waters at depth in the vicinity of the potential repository site are needed so as to further evaluate the hydrologic system. We have integrated the chemical and hydrologic databases to evaluate different model conceptualizations of the hydrologic behavior of the mountain at low and high infiltration rates. The premise for this exercise is that chemical data, when combined with hydrologic data, provide the most relevant information for

"validating" radionuclide transport models, as the movement of naturally occurring solutes is closely related to the potential migration of radionuclides. Two end-member hypotheses pertaining to the origin of perched water at Yucca Mountain are explored: a "fast pathway" fracture flow hypothesis, and a transient-mixing hypothesis.

The overall consequence of the "fast pathway" fracture flow hypothesis is that it predicts poor performance for the unsaturated zone, as the Calico Hills transport barrier is essentially bypassed by fracture flow. Since this model is based on non-calibrated fracture properties, we propose an alternative to this model in the transient-mixing hypothesis, based on the integration of all elements of the hydrologic and chemical databases at Yucca Mountain. Its main strength is that it explains simultaneously seemingly contradictory evidence represented by:

- The inversion in apparent ages between pore waters and perched water in the unsaturated zone,
- The low chloride content of perched waters relative to the overlying TSw and underlying CHn pore waters.
- The apparent dissequilibrium in pore water and perched water contents.

All of the data above are consistent with a model of transient flow, and furthermore, the stable isotope data and apparent ^{14}C and $^{36}Cl/Cl$ ages can be interpreted as resulting from a mixture of late Pleistocene/early Holocene water with modern waters. The existence of these mixed ancient/modern perched water bodies therefore implies that an additional retardation mechanism exists above the Calico Hills formation. The ubiquitous young ^{14}C ages in the Calico Hills formation pore waters beneath the perched water bodies and in other areas, also imply that a lateral component of flow occurs in the vitric Calico Hills and that this formation is not bypassed.

The implication of this conceptual model for Performance Assessment is an improved performance of the Calico Hills Transport barrier beneath the repository by 1) the additional barrier component which regulates the downward flow of water to the saturated zone, and 2) increased water residence times in the unsaturated zone due to the presence of long term perched water

bodies at depth, and lateral diversion above the basal vitrophyre and/or the underlying Calico Hills vitric units.

For radionuclide transport predictions, a variety of two- and three-dimensional simulations are presented. Multiple parameter sets from the LBNL site-scale flow model and variations on the USGS infiltration map are used in the simulation of radionuclides from the potential repository to the water table. For most of these parameter sets, radionuclides tend to bypass the zeolites of the Calico Hills via fracture transport when base-case infiltration conditions are simulated. When the infiltration rate is scaled by 1/3, significant fracture flow in the zeolites is still simulated with most parameter sets. A modification increasing CHn zeolite matrix permeabilities by a factor of 5 leads to substantially greater matrix flow and, hence, retardation of sorbing radionuclides. This process leads to dramatic improvement in the performance of the unsaturated zone. These studies demonstrate the overriding importance of proper characterization of the zeolitic units for performance assessment. Presently, there is significant uncertainty in the characteristics of these units due to data limitations. Enhanced characterization efforts, including the planned field test at Busted Butte, would reduce the uncertainty in these calculations and lead to a better understanding of the true nature of the hydrologic and transport behavior of the CHn.

Long-time transient simulations show that the flux of radionuclide at the water table under transient conditions is closely approximated by a quasi-steady state model. This finding supports a key abstraction being proposed for TSPA-VA simulations.

Comparing two-dimensional and three-dimensional model simulations, we found that greater spreading in the travel time distribution curve is simulated in three dimensions due to the additional flow paths sampling a greater range of property variability that occur in three dimensions. This variability leads to cumulative breakthrough curves at the water table spanning the range from 10 years to 10,000 years. Part of this spreading is caused by a propensity for radionuclides released from the northern end of the repository to experience rapid transport to the water table compared to radionuclides released in the southern portion of the potential repository.

In general, this type of variability has a greater influence on unsaturated zone performance than diffusion or dispersion mechanisms. The diffusion coefficient influences the breakthrough curves simulated with the three-dimensional model, especially for the portion of the inventory with the shortest travel times. Diffusion into the rock matrix and sorption onto zeolites retard the transport of ^{237}Np traveling in fractures. The dispersion coefficient is shown to have very little impact on the unsaturated zone transport.

We then predict the radionuclide mass flux response at the water table to the large variety of near field environment (NFE) release scenarios. This is accomplished efficiently by decoupling the far-field and near-field models and using numerical convolution to link the models. For nonsorbing radionuclides like ^{99}Tc, there is no retardation in any material between the potential repository and the water table. For all of the different property sets developed by LBNL, fracture flow through the zeolitic Calico Hills and underlying units results in bypassing of most of the unsaturated zone matrix material for the USGS infiltration estimates. Therefore, near-field release rates control the maximum concentration flux at the water table. As with nonsorbing radionuclides, those that do sorb to zeolites like ^{237}Np still show early arrivals at the water table after release begins for these parameter sets due to the simulated fracture bypass of the zeolites. However, relatively small changes from the LBNL parameters in the Calico Hills and underlying units lead to vastly improved performance with respect to sorbing radionuclides. Reduction in uncertainty of the actual hydrologic properties of the Calico Hills (both fracture and matrix) would clarify whether these predictions of poor far-field barrier performance is indeed warranted or whether they are a by-product of a calibration procedure that was not well constrained by data indicating the degree of fracture flow in the units below the basal vitrophyre. Finally, in the absence of sorption onto the mobile colloids, Plutonium migration is limited due to large sorption coefficients. Assuming reversible sorption, when partitioning onto colloids approaches 99% or more, Plutonium mobility becomes potentially important to performance.

With regard to repository heat effects, we investigated the coupled effects of chemical interactions and heat on neptunium transport from the potential repository to the water table. The simulations indicate that in the absence of irreversible changes in the hydrologic and transport properties, the heat pulse does not significantly affect the migration of neptunium, as the time scale of heat pulse propagation is shorter than the time scales associated with neptunium release and migration. Water chemistry, particularly pH, calcium, and sodium concentration significantly affect the retardation of neptunium by the zeolitic rocks between the repository and the water table.

A final topic studied in detail is the potential influence of small scale variability of chemical and hydrologic properties on radionuclide migration. Due to the correlation between mineral distribution and hydrologic and chemical properties, the distribution of minerals such as zeolites can strongly influence the flow patterns of percolating fluids and the sorption of many radionuclides. Large-scale models typically do not capture these processes in detail. In this study we used geostatistical techniques to develop variograms, kriging maps, and conditional simulations of zeolitic abundance. This conditional simulation was mapped onto the geologic model. We then investigate the relationship between percent alteration, permeability changes due to alteration, sorption due to alteration, and their overall effect on radionuclide transport. A key conclusion to the study is that the retardation due to sorption predicted by a conditional simulation is much larger than the retardation predicted by the zeolite threshold method. The reason for larger retardation of ^{237}Np for the conditional simulation is a small but significant K_d at locations with zeolite abundance less than 10%. At these locations, the K_d is low (less the 1 cc/g) but permeability is large enough for the flow to be matrix dominated. This effect had a large beneficial impact on performance, especially because of the tendency in other simulations for zeolites to be bypassed. For the purposes of abstracting these results, setting nonzero K_d's in the vitric tuffs may be an effective way to mimic the more rigorous conditional simulations.

Chapter 14 - References

This chapter lists documents published, in press, in review and/or submitted for publication. Personnal communications are by definition non-Q and are not listed here. They are listed only in the body of the text, where appropriate.

Akindunni, F. F., R. W. Gillham, B. Conant, and T. Franz, Modeling of contaminant movement near pumping wells: saturated-unsaturated flow with particle tracking, *Groundwater*, 33 (2), 264-274, 1995.

Allison, G. B., W. J. Stone, and M. W. Hughes, Recharge in karst and dune elements of a semi-arid landscape as indicated by natural isotopes and chloride, *J. Hydrol.*, 76, 1-26, 1985.

Altman, S.J., B.W. Arnold, C.K. Ho, S.A. McKenna, R.W. Barnard, G.E. Barr, and R.E. Eaton, Flow calculations for Yucca Mountain ground water travel time (GWTT-95). Technical Report SAND96-0819, Sandia National Laboratories, 1996.

Andrews, R. W., et al., Total System Performance Assessment - 1995: An Evaluation of the Potential Yucca Mountain Repository, TRW Document number B00000000-01717-2200-00136, Rev. 01, November, 1995.

Bandurraga, T.M., S. Finsterle, and G.S. Bodvarsson. Saturation and capillary pressure analysis, in Development and calibration of the three-dimensional site-scale unsaturated zone mode of Yucca Mountain, NV (eds. G.S. Bodvarsson and T.M. Bandurraga), Technical Report LBNL-39315, Lawrence Berkeley National Laboratory, 1996.

Behie, A., D. Collins, P. A. Forsyth, and P. H. Sammon, Fully coupled multiblock wells in oil simulation, *SPE J.*, 535-542, 1985.

Benson, L. V., J. H. Robinson, R. K. Blankennagel, and A. E. Ogard, Chemical composition of groundwater and the locations of permeable zones in the Yucca Mountain area, Nevada, U.S. Geological Survey Open-File Report 83-854, 1983.

Benson, L.V. and P.W. McKinney, Chemical composition of ground water in the Yucca Mountain area, Nevada, 1971-1984, U.S. Geological Survey Open-File Report 85-484, 1985.

Benson, L.V. and H. Klieforth, Stable isotopes in precipitation and ground water in the Yucca Mountain region, Southern Nevada: paleoclimatic implications, *Geophysical Monograph* 55, 41-59, 1989.

Bertetti, F. P., R. T. Pabalan, D. R. Turner, and M. G. Almendarez, Neptunium (V) Sorption behavior on clinoptilolite, quartz, and montmorillonite, *Mat. Res. Soc. Symp., Proc.*, 412, 631-638, 1996.

Birdsell, K. H., K. Campbell, K. G. Eggert, and B. J. Travis, Three-dimensional simulations of radionuclide transport at Yucca Mountain, *Rad. Waste Manag. and Environ. Restor.*, 19, 165-192, 1994.

Bish, D. L., Thermal behavior of natural zeolites, in natural zeolites '93, (eds. D. W. Ming and F. A. Mumpton), *Int. Comm. Natural Zeolites*, 259-269, 1995.

Blinov, A., The dependence of cosmogenic isotope production rate on solar activity and geomagnetic field variations, Secular Solar and Geomagnetic Variations in the Last 10,000 years, (eds. F.R. Stephenson and A.W. Wolfendale), 329-340, 1988.

Bodvarsson, G. S., and T. M. Bandurraga (eds)., Development and calibration of the three-dimensional site-scale unsaturated zone mode of Yucca Mountain, NV, Technical Report LBNL-39315, Lawrence Berkeley National Laboratory, 1996.

Bodvarsson G.S., T.M. Barndurraga, and Y.S. Wu. The site-scale unsaturated zone model of Yucca Mountain, Nevada, for the Viability Assessment. Technical Report LBNL-40378, Lawrence Berkeley National Laboratory, 1997.

Bowers, T.S. and R.G. Burns, Activity diagrams for clinoptilolite: Susceptibility of this zeolite to further diagenetic reactions, *American Mineralogist*, 75, 601-619, 1990.

Brownell, D. H., S. K. Garg, and J. W. Pritchett, Computer simulation of geothermal reservoirs, proc. 45th Calif. Regional Mtg. Soc. Petrol. Engng., Ventura, CA, 1975.

Broxton, D. E., S. J. Chipera, F. M. Byers, and C. A. Rautman, Geologic evaluation of six nonwelded tuff sites in the vicinity of Yucca Mountain, Nevada for a surface-based test facility for the Yucca Mountain Project, Technical Report LA-12542-MS, Los Alamos National Laboratory, 1993.

Buesch, D.C., Spengler, R.W., Moyer, T.C., and J.K. Geslin, Revised stratigraphic nomenclature and macroscopic identification of lithostratigraphic units of the Paintbrush Group exposed at Yucca Mountain, Nevada, U.S. Geological Survey Open-File Report 94-496, 1996.

Buscheck, T. A., and J. J. Nitao, Repository-Heat-Driven Hydrothermal Flow at Yucca Mountain, Part I: Modeling and Analysis, *Nuclear Technology*, 104(3) 418-448, 1993.

Buscheck, T. A., J. J. Nitao, and L. D. Ramspott, Localized dryout: an approach for managing the thermal-hydrological effects of decay heat at Yucca Mountain, *Mat. Res. Soc. Symp., Proc.*, 412, 715-722, 1996.

Cederberg, G. A., R. L. Street, and J. O. Leckie, A groundwater mass transport and equilibrium chemistry model for multicomponent systems, *Water Resour. Res.*, 21(8), 1095-1104, 1985.

Chiang, C. Y., M. F. Wheeler, and P. D. Bedient, A modified method of characteristics technique and mixed finite elements method for simulation of groundwater solute transport, *Water Resour. Res.*, 25 (7), 1541-1549, 1989.

Chipera, S.J., K. Carter-Krogh, D.T. Vaniman, D.L. Bish, and J.W. Carey, Preliminary three-dimensional mineralogical model of Yucca Mountain, Nevada, Los Alamos National Laboratory YMP Milestone SP321AM4, 1997a.

Chipera, S.J., D.T. Vaniman, D.L. Bish, and J.W. Carey, Mineralogic variation in drill holes USW NRG-6, NRG-7/7a, SD-7, SD-9, SD-12, and UZ#14: New data from 1996-1997 analyses, Los Alamos National Laboratory YMP Milestone SP321BM4, 1997b.

Clayton, R. W., W. P. Zelinski and C. A. Rautman, (CRWMS), ISM2.0: A 3-D geological framework and integrated site model of Yucca Mountain: Version ISM1.0, Doc ID B00000000-01717-5700-00004 Rev 0, MOL.19970122.0053, Civilian Radioactive Waste Management System Management and Operating Contractor, February 1997.

Conca, J., Diffusion barrier transport properties of unsaturated Paintbrush Tuff rubble backfill, proc. High Level Radioactive Waste Management,1, 394-401, 1990.

Conca, J. and J. Wright, Transport property testing of engineered barrier materials for the Yucca Mountain Project, NESTT Interim Report, Los Alamos National Laboratory, May, 1996.

Conca, J. L. and I. R. Triay, Validity of batch sorption data to describe selenium transport through unsaturated tuff, Technical Report LA-12957-MS, Los Alamos National Laboratory, 1996.

Cordes, C., and W. Kinzelbach, Continuous groundwater velocity fields and path lines in linear, bilinear, and trilinear finite elements, *Water Resour. Res.*, 28 (11), 2903-2911, 1992.

Czarnecki, J.B., O'Brien, G.M., Nelson, P.H., Sass, J.H., Nelson, P.H., Bullard, J.W., and Flint, A.L., Is there perched water under Yucca Mountain in borehole USW G-2?, *Trans. American Geophysical Union, EOS*, 75(44), 249-250, 1994.

Czarnecki, J. B., Preliminary Site Saturated-Zone 3D Ground-Water Flow Model, USGS YMP Milestone Number 3GWM611M,1996a.

Czarnecki, J. B., C. C. Faunt, C. W. Gable, and G. A. Zyvoloski, On the development of a three-dimensional, finite-element, ground-water flow model of the saturated zone, Yucca Mountain, Nevada: proc. of the ModelCare 96 Symposium, Golden, CO, Sept. 24-26, 1996b.

Dash, Z.V., B.A. Robinson, and G.A. Zyvoloski, V & V plan and procedures for the FEHM application, Los Alamos YMP document FEHM VVP, ECD-22, 1996a.

Dash, Z.V., B.A. Robinson, and G.A. Zyvoloski, V & V report for the FEHM application, Los Alamos YMP document FEHM VVR, ECD-22, 1996b.

Desbarats, A. J., Macrodispersion in sand-shale sequences, *Water Resour. Res.*, 26, 1, 153-164, 1990.

Desbarats, A. J., Reply: Comment on "Macrodispersion in sand-shale sequences" , *Water Resour. Res.*, 27(1), 141-143, 1991.

Deutsch, C.V. and A.G. Journel, GSLIB: Geostatistical Software Library and User's Guide, New York: Oxford University Press, pp 340, 1992.

Efurd, D. W., W. Runde, J. C. Banar, F. R. Roensch, D. L. Clark, P. D. Palmer, and C. D. Tait, Measured solubilities and speciation of neptunium and plutonium in J-13 groundwater, Los Alamos National Laboratory YMP Milestone 3411, 1996.

Engesgaard, P. and K. L. Kipp, A geochemical model for redox-controlled movement of mineral fronts in ground-water flow systems: a case of nitrate removal by oxidation of pyrite, *Water Resour. Res.*, 28, 3308-3327, 1992.

Engstrom, D.A., and Rautman, C.A., Geology of the USW SD-9 Drill Hole, Yucca Mountain, Nevada, Technical Report SAND96-2030, Sandia Natl. Laboratories, 1996.

Fabriol, R., J. P. Sauty, and G. Ouzounian, Coupling geochemistry with a particle tracking transport model, *J. Contam. Hydrol.*, 13, 117-129, 1993.

Fabryka-Martin, J. T., S. J. Wightman, W. J. Murphy, M. P. Wickham, M. W. Caffee, G. J. Nimz, J. R. Southon, and P. Sharma, Distribution of chlorine-36 in the unsaturated zone at Yucca Mountain: An indicator of fast transport paths, proc. FOCUS '93: Site Characterization and Model Validation, Las Vegas, NV, American Nuclear Society, La Grange Park, Ill., 58-68, 1993.

Fabryka-Martin, J. T., P. R. Dixon, S. Levy, B. Liu, H. J. Turin, and A. V. Wolfsberg, Summary report of chlorine-36 studies: systematic sampling for chlorine-36 in the Exploratory Studies Facility, Los Alamos National Laboratory YMP Letter Milestone number 3783 AD, 1996a.

Fabryka-Martin, J. T., A. V. Wolfsberg, P. R. Dixon, S. Levy, B. Liu, and H. J. Turin, Summary report of chlorine-36 studies: sampling, analysis and simulation for chlorine-36 in the Exploratory Studies Facility, Los Alamos National Laboratory YMP Milestone number 3783 M, 1996b.

Fabryka-Martin, J.T., H.R. Turin, D. Brenner, P.R. Dixon, B. Liu, J. Musgrave, and A.V. Wolfsberg. Summary report of chlorine-36 studies, Los Alamos National Laboratory YMP Milestone Report 3782M, 1996c.

Flint, A.L. and L.E. Flint, Spatial distribution of potential near surface moisture flux at Yucca Mountain, Proceeding of the Fifth Intl. Conf. on High Level Radioactive Waste Management, Las Vegas, NV, May 22-26, 1994, American Nuclear Societally Grange Park, IL, pp2352-2358, 1994

Flint, A.L, J. Hevesi, and L.E. Flint, Conceptual and numerical model of infiltration for the Yucca Mountain Area, Nevada, USGS WRIR MOL 19970409.0087, GS960908312211.003DOE Milestone, 3GUI623M., U.S. Geological Survey, (*in preparation*), 1996.

Flint, L.E., Matrix properties of hydrogeologic units at Yucca Mountain Nevada, U.S. Geological Survey Open File Report, MOL 19970324.0046, GS950308312231.002, (*in preparation*), 1996.

Forester, R.M., Late glacial to modern climate near Yucca Mountain, Nevada, *Proceedings Fifth International High-Level Radioactive Waste Management Conference*, American Nuclear Society, Las Vegas, NV, 2750-2754, 1994.

Forester, R.M. and A.J. Smith, Late glacial climate estimates for southern Nevada: the ostracode fossil record, *Proceedings Fifth International High-Level Radioactive Waste Management Conference*, American Nuclear Society, Las Vegas, NV, 2553-2561, 1994.

Freeze, R. A., and J. A. Cherry, *Groundwater*, Prentice-Hall, Inc., Englewood Cliffs, NJ, 1979.

Gable, C.W, T. A. Cherry, H.E. Trease, and G. A. Zyvoloski, GEOMESH grid generation, Technical Report, LA-UR-95-4143, Los Alamos National Laboratory, 1995.

Gable, C.W, H.E. Trease, and T. A. Cherry, Automated grid generation from odels of complex geologic structure and stratigraphy, Santa Barbara: National Center for Geographic Information and Analysis, proceedings paper, Technical Report, LA-UR-96-1083, Los Alamos National Laboratory, 1996.

Gable, C. W., H. Trease and T. Cherry, Geological applications of automatic grid generation tools for finite elements applied to porous flow modeling, *Numerical Grid Generation in Computational Fluid Dynamics and Related Fields*, ed. B. K. Soni, J. F. Thompson, H. Hausser and P. R. Eiseman, Engineering Research Center, Mississippi State Univ. Press, 1996.

Gauthier, J.H. and M.L. Wilson, Infiltration and percolation rates, *Total-system performance assessment for Yucca Mountain - SNL second iteration (TSPA-1993)*, Technical Report SAND93-2675, 8.1-8.17, Sandia National Laboratories, 1994.

Gelhar, L. W., Stochastic Subsurface Hydrology, Prentice-Hall, Inc., Englewood Cliffs, N.J., 1993.

Glasstone S. (ed.) *The Effects of Nuclear Weapons*, Revised edition, U.S. Atomic Energy Commission, Washington, D.C., 730 p., 1962.

Goode, D. J., Particle velocity interpolation in block-centered finite difference groundwater flow models, *Water Resour. Res.*, 26 (5), 925-940, 1990.

Goode, D. J., and, A. M. Shapiro, Comment on "Macrodispersion in Sand-Shale sequences" , *Water Resour. Res.*, 27(1), 135-139, 1991.

Greenland Ice-Core Project Members (GRIP), Climate instability during the last interglacial period recorded in the GRIP ice core, *Nature*, 364, 203-207, 1993.

Hevesi, J.A., A. L. Flint and J.D Istok, Precipitation estimation in mountainous terrain using multivariate geostatistics, Part II: Isohyetal maps, *J. Applied Meteorology*, 31, 661-676, 1991.

Hevesi, J.A. and A. L. Flint, Geostatistical model for estimating precipitation and recharge in the Yucca Mountain region, Nevada-California, U.S. Geological Survey Water Resources Investigations Report 96-4123, 1996.

Ho, C. K., S. J. Altman, and B. W. Arnold, Alternative conceptual models and codes for unsaturated flow in fractured tuff: Preliminary assessments for GWTT-95, Technical Report SAND95-1546, Sandia National Laboratories, 1995.

Ho, C. K., Models of fracture-matrix interactions during multiphase heat and mass flow in unsaturated fractured porous media, Sixth Symposium on Multiphase Transport in Porous Media, 1997 ASME International Mechanical Engineering Congress and Exposition, Dallas, TX, November 16-21, 1997.

Hudson, D.B., and a.l. Flint, Estimation of shallow infiltration and presence of potential fast pathways for shallow infiltration in the yucca Mountain area, Nevada, U.S. Geological Survet Water Resources Report, (*in review*), 1996.

Imbrie, J., and J.Z. Imbrie, Modeling the climatic response to orbital variations, *Science*, 207, 943-953, 1980.

Imbrie, J., J. Hay, D.G. Martinson, A. McIntyre, A.C. Mix, J.J. Morley, N.G. Pisias, W.L. Press, and N.J. Shackleton, The orbital theory of pleistocene climate: Support from a revised chronology of the marine ^{18}O record, *Milankovich and Climate, Part 1*, A. Berger, J. Imbrie, J. Hay, S. Gupka, B. Saltzman (Eds.), Reidel, Boston, MA, 269-305, 1984.

Imbrie, J., A theoretical framework for the pleistocene ice ages, *J. Geol. Soc. London*, 142, 417-432, 1985.

Johnson, J. A., V. Ravi, and J. K. Rumery, Estimation of solute concentrations using the pathline counting method, *Groundwater*, 32 (5), 719-726, 1994.

Journel, A.G. and Ch.J. Huijbregts, Mining Geostatistics, Academic Press, New York, pp. 600, 1978.

Kinzelbach, W., The random walk method in pollutant transport simulation, in E. Custodio et al. (eds.), *Groundwater Flow and Quality Modeling*, D. Reidel Publishing Company, 227-245, 1988.

Kinzelbach, W., W. Schafer, and J. Herzer, Numerical modeling of natural and enhanced denitrification processes in aquifers, *Water Resour. Res.*, 27, 1123-1135, 1991.

Kitanidis, P., Introduction to Geostatistics with Applications in Hydrogeology, 1996.

Kwicklis, E.M. and J.P. Rousseau, Implications for waste isolation, *Hydrogeology of the unsaturated zone, North Ramp area of the Exploratory Studies Facility, Yucca Mountain, Nevada*, J.P. Rousseau, E.M. Kwicklis and D.C. Gillies (Eds.), U.S. Geological Survey Water Resources Investigations Report, (*in review*), 1996.

Lasaga, A. C., Chemical kinetics of water-rock interactions, *J. Geophys. Res.*, 89, 4009-4025, 1984.

Latinopoulos, P., and K. Katsifarakis, A boundary element and particle tracking model for advective transport in zoned aquifers, *J. Hydrol.*, 124, 159-176, 1991.

Lecain, G.D. and G. Patterson, Technical analysis/interpretation, air permeability and hydrochemistry data through January 31, 1997, YMP level 4 milestone SPH35EM4, U.S Geological Survey, 1996.

Levy, S. S., Studies of altered vitrophyre for the prediction of nuclear waste repository-induced thermal alteration at Yucca Mountain, Nevada, *Mater. Res. Soc., Symp. Proc.*, 26, 959-966, 1984.

Levy, S. S., and J. R. O'Neil, Moderate-temperature zeolitic alteration in a cooling pyroclastic deposit, *Chem. Geol.*, 76, 321-326, 1989.

Levy, S. S., D.S. Sweetkind J.T. Fabryka-Martin, P.R. Dixon, J.L. Roach, L.E. Wolfsberg, D. Elmore, and P. Sharma. Investigations of structural controls and mineralogic associations of chlorine-36 fast pathways in the ESF. Los Alamos National Laboratory YMP milestone SP2301M4,1997.

Lichtner, P. C., Continuum formulation of multicomponent-multiphase reactive transport, *Rev. in Mineralogy*, 34(1), 1-81, 1996.

Lichtner and Seth, Multiphase-multicomponent nonisothermal reactive transport in partially saturated porous media, Proceedings of the International Conference on Deep Geological Disposal of Radioactive Waste, Winnipeg, Canada, p. 3-133 -142, 1996.

Liu, B., J. Fabryka-Martin, A. Wolfsberg, and B. Robinson, Significance of apparent discrepancies in water ages derived from atmospheric radionuclides at Yucca Mountain, Nevada, proc. 1995 American Institute of Hydrology Annual Meeting, May 14-18, Denver, CO, 1995.

Loeven, C. A Summary and Discussion of Hydrologic Data from the Calico Hills Nonwelded Hydrogeologic Unit at Yucca Mountain, Nevada, Technical Report LA-12376-MS, Los Alamos National Laboratory, 1993.

Lu, N., A semianalytical method of path line computation for transient finite-difference groundwater flow models, *Water Resour. Res.*, 30 (8), 2449-2459, 1994.

Luster, G. R., 1985, Raw Materials for Portland Cement: Applications of conditional simulation of coregionalization, Ph.D. dissertation. Stanford, CA: Stanford University, Department of Applied Earth Sciences, pg. 531.

Maloszewski, P., and A. Zuber, Tracer experiments in fractured rocks – Matrix diffusion and the validity of models, *Water Resour. Res.*, 29 (8), 2723-2735, 1993.

Maloszewski, P., and A. Zuber, Influence of matrix diffusion and exchange reactions on radiocarbon ages in fissured carbonate aquifers," *Water Resours. Res.*, 27 (8), 1937-1945, 1991.

Mangold, D. C., and C. F. Tsang, A summary of subsurface hydrological and hydrochemical models, *Rev. Geophys.*, 29, 51-79, 1991.

Marshall, B.D., Z.E. Peterman and J.S. Stuckless, Strontium isotopic evidence for a higher water table at Yucca Mountain, *Proceedings Fourth International Conference of High Level Radioactive Waste Management, Las Vegas, NV*, American Nuclear Society, La Grange Park, IL, 1984-1952, 1993.

Mazaud, A., C. Laj, E. Bard., M. Arnold, and E. Tric, Geomagnetic Control of ^{14}C Production over the Last 80 ky: Implications for the Radiocarbon Time-scale, *Geophys. Res. Letters.,* 18, 1885-1888, 1991.

Meijer, A., A Strategy for the Derivation and use of sorption coefficients in performance assessment calculations for the Yucca Mountain site, proc. DOE/Yucca Mountain Site Characterization Project Radionuclide Adsorption Workshop at Los Alamos National Laboratory, 9-40, Technical Report LA-12325-C, Los Alamos National Laboratory, 1992.

Meijer, A., Conceptual model of ground water chemistry, YMP Milestone 3098, 1996.

Mercer, J. W., and C. R. Faust, Simulation of water- and vapor-dominated hydrothermal reservoirs, proc. 50th Annual Fall Mtg. Soc. Petrol. Engng., Dallas, Texas, 1975.

Montazer, P., and Wilson,W.E., Conceptual hydrologic model of flow in the unsaturated zone, Yucca Mountain, Nevada, U.S. Geological Survey Water Resources Investigations Report 84-4355, 1984.

Moyer, T.C. and J.K. Geslin, Lithostratigraphy of the Calico Hills formation and Prow Pass Tuff (Crater Flat group) at Yucca Mountain, Nevada, U.S. Geological Survey Open-File Report 94-460, 1995.

Narasimhan, T. N., A. F. White, and T. Tokunaga, Groundwater contamination from an inactive uranium mill tailings pile 2. application of a dynamic mixing model, *Water Resour. Res.*, 22, 1820-1834, 1986.

Neretnicks, I., Diffusion in the rock matrix: An important factor in radionuclide migration? *J. Geophys. Res.*, 85 (B8), 4379-4397, 1980.

Neuman, S. P., Adaptive Eulerian-Lagrangian finite element method for advection-dispersion, *Int. J. Numer. Meth. Engng.*, 20, 321-337, 1984.

Neuman, S., Universal scaling of hydraulic conductivities and dispersivities in geologic media, *Water Resour. Res.*, 26 (8), 1749, 1990.

Nitao, J.J., Reference manual for the NUFT flow and transport code, Version 1.0, Technical Report UCRL-ID-113520, Lawrence Livermore National Laboratory, 1995.

Nitsche, H., R. C. Gatti, E. M. Standifer, S. C. Lee, A. Muller, T. Prussin, R. S. Deinhammer, H. Maurer, K. Becraft, S. Leung, S. A. Carpenter. Measured solubilities and speciations of neptunium, plutonium, and americium in a typical groundwater (J-13) from the Yucca Mountain region, Technical Report LA-12562-MS, Los Alamos National Laboratory, 1993.

O'Brien, G., draft in preparation, Data summary sheet, water-level and related data collected during aquifer tests conducted in borehole USW G-2, April 8 to December 17, 1996, U.S. Geological Survey, 1996.

Ogard, A.E. and J.F. Kerrisk, Groundwater chemistry along flow paths between a proposed repository site and the accessible environment,Technical Report LA-10188-MS, Los Alamos National Laboratory, 1984.

Ortiz, T. S., R. L. William, F. B. Nimick, B. C. Whittet, and D. L. Smith, A three-dimensional model of reference thermal/mechanical and hydrological stratigraphy at Yucca Mountain, Southern Nevada, Technical Report SAND 84-1076, Sandia National Laboratories, 1985.

Pabalan, R. T., Thermodynamics of ion exchange between clinoptilolite and aqueous solutions of Na^+/K^+ and Na^+/Ca^{2+}, *Geochim. et Cosmochim. Acta*, 58, 4573-4590, 1994.

Paces, J.B., E.M. Taylor and C. Bush, Late quaternary history and uranium isotopic compositions of ground water discharge deposits, Crater Flat, Nevada, *Proceedings Fourth International Conference of High Level Radioactive Waste Management, Las Vegas, NV*, American Nuclear Society, La Grange Park, IL, 1573-1580, 1993.

Paces, J. B., L. A. Leymark, B. D. Marshall, J. F. Whelan, and Z. E. Peterman, Ages and origins of subsurface secondary minerals in the exploratory studies facility (ESF), U. S. Geological Survey Open-File Report 3GQH450M, 1996.

Phillips, F.M., Environmental tracers for water movement in desert soils of the American southwest, *Soil Sci. Soc. Am. J.*, 58, 15-24, 1994.

Plummer, L. N., and E. Busenberg, The solubilities of calcite, aragonite, and valerite in CO_2-H_2O Solutions Between 0 and 90°C, and an evaluation of the aqueous model for the system $CaCO_3$-H_2O, *Geochim. et Cosmochim. Acta*, 46, 1101, 1982.

Plummer, M. A., F. M. Phillips, J. Fabryka-Martin, H. J. Turin, P. E. Wigand, and P. Sharma, Chlorine-36 in fossil rat urine: an archive of cosmogenic nuclide deposition during the past 40,000 years, *(submitted)*, 1996.

Pollack, D. W., Semianalytical computation of path lines for finite-difference models, *Groundwater*, 26 (6), 743-750, 1988.

Pruess, K., TOUGH user's guide, NUREG/CR-4645, Nuclear Regulatory Commission, 1987.

Pruess, K., TOUGH2 - A general-purpose numerical simulator for multiphase fluid and heat flow, Technical Report LBL-29400, Lawrence Berkeley National Laboratory, 1991.

Pruess, K., J. S. Y. Wang, and Y. W. Tsang, On thermohydrologic conditions near high-level nuclear wastes emplaced in partially saturated fractured tuff. 2. Effective continuum approximation, *Water Resour. Res.*, 26 (6), 1249-1261, 1990.

Rautman, C.A. and D.A. Engstrom, Geology of the USW SD-7 drill hole, Yucca Mountain, Nevada, Technical Report SAND96-1474, Sandia National Laboratories, 1996.

Reimus, P.W., The use of synthetic colloids in tracer transport experiments in saturated rock fractures, Ph.D. Dissertation, University of New Mexico, Albuquerque, New Mexico, 1995.

Reimus, P. W. and H. J. Turin, Draft report of results of hydraulic and tracer tests at the C-holes complex, Los Alamos NAtional Laboratory YMP Milestone SP23APMD, 1997.

ResMod: A Geostatistical Modeling Program, User's Manual, Reservoir Characterization Research & Consulting, Inc., 1994.

Robinson, B.A., Fracture network modeling of a hot dry rock geothermal reservoir, proc. Thirteenth Workshop on Geothermal Reservoir Engineering, Stanford University, Stanford, CA, 211-218, 1988.

Robinson, B. A., A strategy for validating a conceptual model for radionuclide migration in the saturated zone beneath Yucca Mountain," *Rad. Waste Manag. Environ. Restor.*, 19, 73-96, 1994.

Robinson, B.A., C.W. Gable, and G.A. Zyvoloski, Summary of recent retardation sensitivity analysis activity, Los Alamos National Laboratory YMP Milestone 3416, 1994.

Robinson, B.A., A.V. Wolfsberg, G.A. Zyvoloski, and C.W. Gable, An unsaturated zone flow and transport model of Yucca Mountain, Los Alamos National Laboratory YMP Milestone 3468, 1995.

Robinson, B.A., A.V. Wolfsberg, H.S. Viswanathan, C.W. Gable, G.A. Zyvoloski, and H.J Turin,. Modeling of flow, radionuclide migration, and environmental isotope distributions at Yucca Mountain, Los Alamos National Laboratory YMP Milestone 3672, 1996.

Robinson, B.A. and S. E. Henderson, A cell-based particle tracking technique for solute transport in porous media, *Water Resour. Res.*, (*submitted*), 1997.

Ross, B., S. Amter, N. Lu, Numerical studies of rock-gas flow in Yucca Mountain, Technical Report SAND 91-7034, Sandia National Laboratories, 1992.

Rousseau, J.P., Kwicklis, E.M., and D.G. Gillies, Hydrogeology of the unsaturated zone, north ramp area of the exploratory studies facility, Yucca Mountain, Nevada, U.S. Geological Survey Water Resources Investigation Report 96-####, (*in review*), 1996.

Saad, Y., and M. H. Schultz, GMRES: A generalized minimum residual algorithm for solving non-symmetric linear systems, *SIAM J. Sci. and Stat. Comput.*, 7 (3), 856-869, 1986.

Scanlon, B. R., Evaluation of moisture flux from chloride data in desert soils, *J. Hydrol.*, 128, 137-156, 1991.

Schafer-Perini, A. L., and J. L. Wilson, Efficient and accurate front tracking for two-dimensional groundwater flow models, *Water Resour. Res.*, 27 (7), 1471-1485, 1991.

Scheibe, T. D., and C. R. Cole, Non-gaussian particle tracking: Application to scaling of transport processes in heterogeneous porous media, *Water Resour. Res.*, 30 (7), 2027-2039, 1994.

Scott, R.B., and J. Bonk., Preliminary geologic map of Yucca Mountain, Nye County, Nevada, with geologic sections, U.S. Geological Survey Open-File Report 84-494, 9 pages + map, 1984.

Smith, R.W., A.L. Schafer, A.F.B. Tompson, Theoretical relationships between reactivity and permeability for monominerallic porous media, in *Proceedings, XIX Symposium of the Scientific Basis for Nuclear Waste Management*, edited by W.M. Murphy and D.F. Knecht, *Mater. Res. Symp. Proc.*, 412, (*in press*), 1996.

Spaulding W.G., Vegetation and climates of the last 45,000 years in the vicinity of the Nevada Test Site, south-central Nevada, U.S. Geological Survey Professional Paper 1329, Alexandria, VA, 1985.

Starr, R. C., R. W. Gillham, and E. A. Sudicky, Experimental investigation of solute transport in stratified porous media 2. The reactive case, *Water Resour. Res.*, 2 (7), 1043-1050, 1985.

Steefel, C.I. and A.C. Lasaga, A coupled model for transport of multiple chemical species and kinetic precipitation/dissolution reactions with application to reactive flow in single phase hydrothermal systems, *Amer. J. Sci.*, 294, 529-592, 1994.

Steefel, C. I., and S. B. Yabusaki, OS3D/GIMRT, Software for multicomponent-multidimensional reactive transport, user manual and programmer's guide, Technical Report PNL-11166, Pacific Northwest National Laboratory, 1996.

Stratigraphic Geocellular Modeling Reference Guide, Landmark Graphics Corporation, 540 pp., 1995.

Striffler, P., G. M. O'Brien, T. Oliver, and P. Berger, Perched water characteristics and occurrences, Yucca Mountain, Nevada, Memo to Technical Project Officer, 1996.

Sweetkind, D.S., J. Fabryka-Martin, A. Flint, C. Potter, and S. Levy, 1997, Evaluation of the structural significance of bomb-pulse 36Cl at sample locations in the Exploratory Studies Facility, Yucca Mountain, Nevada, *U.S.Geological Survey memorandum transmitting Level 4 milestone SPG33M4* to R. Craig, Yucca Mountain Project Branch, 29 August, 1997.

Tait, C. D., S. A. Ekberg, D. L. Clark, P. D. Palmer, I. R. Triay, and C. R. Cotter, Sorption as a function of groundwater chemistry to elucidate sorption mechanisms, Los Alamos National Laboratory YMP Milestone 3219, 1996.

Tang, D. H., E. O. Frind, and E. A. Sudicky, Contaminant transport in fractured porous media: Analytical solution for a single fracture, *Water Resour. Res.*, 17 (3), 555-564, 1981.

Tebes-Stevens, C., A. J. Valocchi, J. M. VanBriesen, and B. E. Rittmann, Multicomponent transport with coupled geochemical and microbiological reactions: model description and example simulations, (*submitted*), 1996.

Thomas, K.W., Summary of sorption measurements performed with Yucca Mountain, Nevada, tuff samples and water from Well J-13, Technical Report LA-10960-MS, Los Alamos National Laboratory, 1987.

Tompson, A. F. B., and L. W. Gelhar, Numerical simulation of solute transport in three-dimensional, randomly heterogeneous porous media, *Water Resour. Res.*, 26 (10), 2541-2562, 1990.

Tompson, A.F.B., A.L. Schafer, R.W. Smith, Impacts of physical and chemical heterogeneity on cocontaminant transport in a sandy porous medium, *Wat. Resour. Res.*, 32 (4), 801-818, 1996.

Trease, H., D. George, C. W. Gable, J. Fowler, A. Kuprat and A. Khamyaseh, The X3D grid generation system, *Numerical Grid Generation in Computational Fluid Dynamics and Related Fields*, ed. B. K. Soni, J. F. Thompson, H. Hausser and P. R. Eiseman, Engineering Research Center, Mississippi State Univ. Press, 1996.

Triay, I. R., A. Meijer, J. L. Conca, K. S. Kung, R. S. Rundberg, and E. A. Streitelmeier, Summary and synthesis report on radionuclide retardation for the Yucca Mountain Site Characterization Project, Los Alamos National Laboratory YMP Milestone 3784, 1996a.

Triay, I.R., C.R. Cotter, S.M. Kraus, M.H. Huddleston, S.J Chipera, D.L. Bish, Radionuclide sorption in Yucca Mountain tuffs with J-13 well water: neptunium, Uranium, and Plutonium, Los Alamos National Laboratory Yucca Mountain Site Characterization Project Milestone 3338, Technical Report LA-12956-MS, 1996b.

Triay, I.R., C.R. Cotter, M.H. Huddleston, D. E. Leonard, S. C. Weaver, S. J. Chipera, D.L. Bish, A. Meijer, and J. A. Canepa, Batch sorption results for neptunium transport through Yucca Mountain tuffs, Technical Report LA-12961-MS, Los Alamos National Laboratory , 1996c.

Triay, I. R., A. C. Furlano, S. C. Weaver, S. J. Chipera, and D. L. Bish, Comparison of neptunium sorption results using batch and column techniques, Technical Report LA-12958-MS, Los Alamos National Laboratory, 1996d.

Triay, I.R., "et.al.," Summary report geochemistry/transport laboratory tests, Los Alamos National Laboratory YMP Milestone SP23QM3, 1997.

Valet, J.-P., and L. Meynadier, Geomagnetic field intensity and reversals during the past four million years, *Nature*, 366, 234-238, 1993.

van Genuchten, M. T., A closed form equation for predicting hydraulic conductivity of unsaturated soils, *Soil Sci. Soc. Am. J.*, 44, 892-898, 1980.

Vaniman, D.T., D. Bish and S. Chipera, Dehydration and rehydration of a tuff vitrophyre, *J. Geophys. Res.*, 98 (22),309-22,320, 1993.

Vaniman D. T., and D. L. Bish, The importance of zeolites in the potential high-level radioactive waste repository at Yucca Mountain, Nevada, in Natural Zeolites '93, D. W. Ming and F. A. Mumpton (eds.), *Int. Comm. Natural Zeolites*, 533-546, 1995.

Vaniman D. T., and S. Chipera, Paleotransport of lanthanides and strontium recorded in calcite compositions from tuffs at Yucca Mountain, Nevada, USA, *Geochim. Cosmochim. Acta* 60, 4417-4433, 1996.

Viani, B. E., and C. J. Bruton, "Modeling Ion Exchange in Clinoptilolite Using the EQ3/6 Geochemical Modeling Code," Report No. UCRL-JC-109952, presented at 7th International Symposium Rock Water Interaction, Park City, Utah, July 13-18, 1993.

Viswanathan, H. S., Modification of the Finite Element Heat and Mass Transfer Code (FEHMN) to Model Multicomponent Reactive Transport, M.S. Thesis, University of Illinois, Champaign-Urbana, Illinois, September, 1995, Technical Report LA-13167-T, Los Alamos National Laboratory, 1996.

Viswanathan, H., B. Robinson, A.J. Valocchi, and I. Triay, A reactive transport model of neptunium migration from the potential repository at Yucca Mountain, J. Hydrol., (*submitted*), 1997.

Walter, A. L., E. O. Frind, D. W. Blowes, C. J. Ptacek, and J. W. Molson, Modeling of multicomponent reactive transport in groundwater 1. Model development and evaluation, *Water. Resour. Res.*, 30, 3137-3148, 1994.

Wanner, H. and I. Forest, *Chemical Thermodynamics of Uranium, Volume 1*, Elsevier Science Publishing Company, NY, 1992.

Whitfield, M.S., W. Thordarson and D.P. Hammermeister, Drilling and geohydrologic data for test hole USW UZ-1, Yucca Mountain, Nye County, Nevada, U.S. Geological Survey Open-File Report 90-354, 1990.

Wilson, M. L., et al., Total-System Performance Assessment for Yucca Mountain - SNL Second Iteration, Technical Report SAND93-2675, Sandia National Laboratories, 1994.

Winograd, I. J., Radioactive waste disposal in thick unsaturated zone, *Science*, 212 (4502), 1457-1464, 1981.

Winograd, I.J., T.B. Coplen, J.M. Landwehr, A.C. Riggs, K.R. Ludwig, B.J. Szabo, P.T. Kolesar and K.M. Revesz, Continuous 500,000 year climate record from vein calcite in Devils Hole, Nevada, *Science*, 258, 255-260, 1992.

Wittwer, C., G. Chen, G. S. Bodvarsson, M. Chornack, A. Flint, L. Flint, E. Kwicklis, and R. Spengler, Preliminary development of the LBL/USGS three-dimensional site-scale model of Yucca Mountain, Nevada, Technical Report LBL-37356/UC-814, Lawrence Berkeley National Laboratory, 1995.

Wolery, T. J., EQ3NR, A computer program for geochemical aqueous speciation-solubility calculations: theoretical manual, user's guide, and related documentation (Version 7.0), Technical Report UCRL-MA-110662-PT-IV, Lawrence Livermore National Laboratory, 1992.

Wolfsberg, A. V., and D. L. Freyberg, Efficient simulation of single species and multispecies transport in groundwater with local adaptive grid refinement, *Water Resour. Res.*, 30 (11), 2979-2991, 1994.

Wylie, C. R., Advanced engineering mathematics, Fourth Edition, McGraw-Hill Book Company, N.Y., 1975.

Yamashita, R., and H. Kimura, Particle-tracking technique for nuclide decay chain transport in fractured porous media, *J. Nucl. Sci. Tech.*, 27 (11), 1041-1049, 1990.

Yang, I. C., Flow and Transport Through Unsaturated Rock - Data From Two Test Holes, Yucca Mountain, Nevada, proc. Third International Conference on High-Level Radioactive Waste Management, Las Vegas, NV, 732-737, 1992.

Yang, I. C., G. W. Rattray, and P. Yu, Interpretations of chemical and isotopic data from boreholes in the unsaturated zone at Yucca Mountain, Nevada, U. S. Geological Survey Water Resources Investigations Report WRIR 96-4058, 1996.

Yang, I. C., P. Yu, G.W. Rattray, and D.C. Thorstenson, Hydrochemical investigations and geochemical modeling in characterizing the unsaturated zone at Yucca Mountain, Nevada, (*in preparation*), 1997.

Yeh, G. T., A Lagrangian-Eulerian method with zoomable hidden fine-mesh approach to solving advective-dispersion equations, *Water Resour. Res.*, 26 (6), 1133-1144, 1990.

Yeh, G. T., and V. S. Tripathi, A critical evaluation of recent developments in hydrogeochemical transport models of reactive multichemical components, *Water Resour. Res.*, 25, 93-108, 1989.

Zelinski, W.P., and R.W. Clayton, A 3D geologic framework and integrated site model if Yucca Mountain, version ISIM 1.0: Civilian Radioactive Waste Management System Management and Operating Contractor Document B00000000-01717-5700-00002, TRW Environmental Safety Systems Inc., Las Vegas, Nev., 1996.

Zheng, C., Extension of the method of characteristics for simulation of solute transport in three dimensions, *Groundwater*, 31 (3), 456-465, 1993.

Zheng, C., Analysis of particle tracking errors associated with spatial discretization, *Groundwater*, 32 (5), 821-828, 1994.

Zimmerman, R. W., G. Chen, T. Hadgu, and G. S. Bodvarsson, A numerical dual-porosity model with semianalytical treatment of fracture/matrix flow, *Water Resour. Res.*, 29 (7), 2127-2137, 1993.

Zyvoloski, G. A., Finite element methods for geothermal reservoir simulation, *Int. J. Numer. Anal. Meth. Geomech.*, 7, 75-86, 1983.

Zyvoloski, G. A., Incomplete factorization methods for finite elements, *Int. J. Numer. Meth. Engng.*, 23, 1101-1109, 1986.

Zyvoloski, G. A., Z. V. Dash, and S. Kelkar, FEHMN 1.0: Finite element heat and mass transfer code, Technical Report LA-12062-MS, Rev. 1, Los Alamos National Laboratory, 1992.

Zyvoloski, G. A., B. A. Robinson, Z. V. Dash, and L. L. Trease, Users manual for the FEHMN application, Technical Report LA-UR-94-3788, Rev. 1, Los Alamos National Laboratory, 1995a.

Zyvoloski, G. A., B. A. Robinson, Z. V. Dash, and L. L. Trease, Models and methods summary for the FEHMN application, Technical Report LA-UR-94-3787, Rev. 1, Los Alamos National Laboratory, 1995b.

Zyvoloski, G. A., J. B. Czarnecki, B. A. Robinson, C. W. Gable, and C. Faunt, Saturated zone radionuclide transport model, Los Alamos National Laboratory YMP Milestone 3624, 1996.

Zyvoloski, G.A., B A. Robinson, K.H. Birdsell, C W. Gable, J. B. Czarnecki, K M. Bower, and C. Faunt, Model analysis of radionuclide transport in the saturated zone beneath Yucca Mountain, Los Alamos National Laboratory YMP Milestone SP25CM3A, 1997.

Chapter 15 - Appendix

Table 15-1. Correlation of Geologic Formations, Hydrological Units and the Model Layers of Both LANL and LBL.

Buesch et al. 1996	Flint 1996	Clayton & Zelinski 1997	LANL	Matrix Properties		LBL
			7/97	Non-Zeolitic	Zeolitic	7/97
Tiva Canyon Tuff (Tpc)		"bedrock"				
crystal-rich member (Tpcr)	CCR					
vitric zone (Tpcrv)						
nonlithophysal zone (Tpcrn)						
subvitro transition subzone (Tpcrn4)						TCw1
pumice-poor subzone (Tpcrn3)	CUC					and
mixed pumice subzone (Tpcrn2)						TCw2
crystal transition subzone (Tpcrn1)			22	CW		
lithophysal zone (Tpcr1)						
crystal-poor member (Tpcp)						
upper lithophysal zone (Tpcpul)	CUL					
middle nonlithophysal zone (Tpcpmn)	CW					
lower lithophysal zone (Tpcpll)						
lower nonlithophysal zone (Tpcpln)						
hackly subzone (Tpcplnh)						
columnar subzone (Tpc-plnc)						
argillic pumice interval (Tpcplnc)	CMW					
vitric zone (Tpcpv)		44	21	CMW		
densely welded subzone (Tpcpv3v)						TCw13
moderately welded sub-zone (Tpcpv2)	CNW	42				
non-to part welded sub-zone(Tpcpv1)			20	BT4		Ptn21

Table 15-1. Correlation of Geologic Formations, Hydrological Units and the Model Layers of Both LANL and LBL.

Buesch et al. 1996	Flint 1996	Clayton & Zelinski 1997	LANL	Matrix Properties		LBL
			7/97	Non-Zeolitic	Zeolitic	7/97
Pre-Tiva Canyon Tuff bed. tuff (Tpbt4)	BT4	41				
Yucca Mountain Tuff (Tpy)	TPY	40	19	TPY		Ptn22
Pre-Yucca Mtn Tuff bedded tuff (Tpbt3)	BT3	39	18	BT3		Ptn23
Pah Canyon Tuff (Tpp)	TPP	38				Ptn24
Pre-Pah Canyon Tuff bedded tuff (Tpbt2)	BT2	37	17	BT2		
Topopah Spring Tuff (Tpt)		36				
crystal-rich member (Tptr)						Ptn25
vitric zone (Tptrv)						
nonwelded subzone (Tptrv3)						
monderately welded subzone (Tptrv2)						Tsw31
densely welded subzone (Tptrv1)	TC	34	16	TC		Tsw31
nonlithophysal zone (Tptrn)		33				
dense subzone (Tptrn3)						Tsw32
vapor-pha corroded subzone (Tptrn2)	TR		15	TR		
lithophysal zone (Tptrl)	TUL					
crystal-poor member (Tptp)						Tsw33
upper lithophysal zone (Tptpul)		32	14	TUL		
mid nonlithophysal zone (Tptpmn)	TMN	31	13	TMN		Tsw34
lower lithophysal zone (Tptpll)	TLL	30	12	TLL		Tsw35
lower nonlithophysal zone (Tptpln)	TM2	29				Tsw36
	TM1		11	TM1		
vitric zone (Tptpv)	PV3	28	10	PV3		
densely welded subzone (Tptpv3)						Tsw37
moderately welded subzone (Tptpv2)	PV2	26	nz z			

Table 15-1. Correlation of Geologic Formations, Hydrological Units and the Model Layers of Both LANL and LBL.

Buesch et al. 1996	Flint 1996	Clayton & Zelinski 1997	LANL 7/97		Matrix Properties Non-Zeolitic	Matrix Properties Zeolitic	LBL 7/97
nonwelded subzone (Tptpv1)			9	39	BT1	BT1a	Ch1
Pre-Topopah Spring Tuff bedded tuff	BT1a & BT1	25					
Calico Hills Fm (Tac)		24					
Unit 4 Pumiceous pyroclastif flow	CHV						
Unit 3 Lithic-rich pyroclastic flow	CHZ		8	38	CHV	CHZ	Ch2,3
Unit 2 Pumiceous pyroclastic flow							
Unit 1 Lithic-rich pyroclastic flow							
Bedded Tuff (Tacbt)	BT	23					
Basal Sandstone (Tacbs)			7	37	BT1	PP4	
Prow Pass Tuff (Tcp)		22					Ch4
Unit 4 Pyroxene rich	PP4						
Unit 3 Welded pyroclastic flow	PP3	21	6	36	PP3	PP1	pp3v
	PP2						
Unit 2 Lithic-rich pyroclastic flow	PP1	18					pp1,2z
Unit 1 Pumiceous pyroclastic flow			5	35	PP2	PP1	
Pre-Prow Pass bedded tuff (Tcpbt)		17					
Bullfrog Tuff (Tcb) Unwelded		16	4	34	BF3	BF2	bf3
middle, variably welded	BF3	15	3	33	BF3	BF2	
lower, nonwelded/altered	BF2	12	2	32	BF3	BF2	
bedded tuff		11					
Tram Tuff (Tct)		10	1	31	BF3	BF2	bf2
bedded tuff							
BASEMENT		1					

Table 15-2. Property Set 6412a

Property Set 6412a

Based on Bodvarsson et al. (1997) Table 6.4.1-2

	LBL Properties							FEHM parameters							
	$\log K_m$	$\log K_f$	$\log(\alpha_m)$	$\log(\alpha_f)$	m_m	m_f	K_f	α_m 1/m	n_m	α_f 1/m	n_f	k_f	K_m	ϕ_f	
tcw1	17.27	11.22	5.94	3.4	0.231	0.667	6.03E-12	0.011	1.30	3.90	3.00	2.58E-08	5.37E-18	2.33E-04	tcw1
tcw2	17.27	11.22	5.89	3.4	0.236	0.667	6.03E-12	0.013	1.31	3.90	3.00	2.02E-08	5.37E-18	2.99E-04	tcw2
tcw3	16.3	11.62	6.14	4.04	0.437	0.667	2.40E-12	0.007	1.78	0.89	3.00	3.40E-08	5.01E-17	7.05E-05	tcw3
ptn1	13.8	12.54	4.44	2.96	0.230	0.667	2.88E-13	0.356	1.30	10.75	3.00	5.96E-09	1.58E-14	4.84E-05	ptn1
ptn2	14.48	12.35	5.09	2.73	0.050	0.667	4.47E-13	0.080	1.05	18.26	3.00	9.25E-09	3.31E-15	4.83E-05	ptn2
ptn3	13.27	11.52	4.36	2.46	0.289	0.667	3.02E-12	0.428	1.41	33.99	3.00	2.32E-08	5.37E-14	1.30E-04	ptn3
ptn4	13.06	12.93	4.41	3.04	0.353	0.667	1.17E-13	0.381	1.55	8.94	3.00	1.69E-09	8.71E-14	6.94E-05	ptn4
ptn5	12.49	12.49	3.80	3.8	0.288	0.288	3.24E-13	1.554	1.40	1.55	1.40	3.89E-09	3.24E-13	8.32E-05	ptn5
tsw1	16.12	10.49	4.53	4.18	0.220	0.667	3.24E-11	0.289	1.28	0.65	3.00	3.63E-07	7.59E-17	8.92E-05	tsw1
tsw2	15.2	12.07	4.65	4.03	0.273	0.657	8.51E-13	0.219	1.38	0.91	2.92	6.60E-09	6.31E-16	1.29E-04	tsw2
tsw3	16.81	12.03	5.18	3.82	0.247	0.666	9.33E-13	0.065	1.33	1.48	2.99	8.89E-09	1.55E-17	1.05E-04	tsw3
tsw4	16.97	12.37	5.97	4.08	0.322	0.667	4.27E-13	0.011	1.47	0.82	3.00	3.44E-09	1.07E-17	1.24E-04	tsw4
tsw5	16.84	12.06	5.49	3.99	0.230	0.667	8.71E-13	0.032	1.30	1.00	3.00	2.65E-09	1.45E-17	3.29E-04	tsw5
tsw6	16.02	11.92	6.12	3.79	0.414	0.667	1.20E-12	0.007	1.71	1.59	3.00	3.01E-09	9.55E-17	3.99E-04	tsw6
tsw7	17.05	11.92	6.22	3.92	0.372	0.667	1.20E-12	0.006	1.59	1.18	3.00	2.44E-09	8.91E-18	4.92E-04	tsw7
ch1z	16.97	13.59	6.53	2.94	0.359	0.667	2.57E-14	0.003	1.56	11.26	3.00	2.34E-09	1.07E-17	1.10E-05	ch1z
ch3z	17.05	13.61	5.58	2.98	0.221	0.667	2.45E-14	0.026	1.28	10.27	3.00	2.23E-09	8.91E-18	1.10E-05	ch3z
ch4z	16.76	13.71	6.12	2.94	0.477	0.667	1.95E-14	0.007	1.91	11.26	3.00	1.77E-09	1.74E-17	1.10E-05	ch4z
pp3v	14.72	12.15	4.74	2.85	0.313	0.667	7.08E-13	0.178	1.46	13.85	3.00	9.92E-09	1.91E-15	7.14E-05	pp3v
pp2z	16.56	12.79	5.75	3.85	0.317	0.667	1.62E-13	0.017	1.46	1.38	3.00	1.47E-08	2.75E-17	1.10E-05	pp2z
ch1v	11.8	12.76	4.01	2.93	0.195	0.667	1.74E-13	0.958	1.24	11.52	3.00	2.43E-09	1.58E-12	7.14E-05	ch1v
ch2v	12.82	12.54	4.17	2.93	0.227	0.667	2.88E-13	0.663	1.29	11.52	3.00	4.04E-09	1.51E-13	7.14E-05	ch2v
ch4v	12.82	12.54	4.17	2.93	0.227	0.667	2.88E-13	0.663	1.29	11.52	3.00	4.04E-09	1.51E-13	7.14E-05	ch4v

$\log K_m$	Log permeanility of matrix material
$\log K_f$	Log permeanility of matrix material
$\log(\alpha_m)$	Log vanGenuchten alpha paramter of matrix material
$\log(\alpha_f)$	Log vanGenuchten alpha paramter of fracture material
m_m	vanGenuchten m paramter for matrix material
m_f	vanGenuchten m paramter for fracture material
K_f	Bulk pemeability of fracture material
α_m	vanGenuchten alpha paramter for matrix material (1/meters)
α_f	vanGenuchten alpha paramter for fracture material (1/meters)
n_m	vanGenuchten n paramter for matrix material ($1/1-m_m$)
n_f	vanGenuchten n paramter for fracture material ($1/1-m_f$)
k_f	Intrinsic fracure permeability
K_m	Matrix permeability
ϕ_f	Fracture volume fraction

Table 15-3. Property Set 6412b

Property Set 6412b

Based on Bodvarsson et al. (1997) Table 6.4-1-2

	LBL Properties							FEHM parameters							
	$\log K_m$	$\log K_f$	$\log(\alpha_m)$	$\log(\alpha_f)$	m_m	m_f	K_f	α_m 1/m	n_m	α_f 1/m	n_f	k_f	K_m	ϕ_f	
tcw1	17.27	11.22	5.93	3.53	0.232	0.492	6.026E-12	0.012	1.30	2.89	1.97	2.58E-08	5.37E-18	2.33E-04	tcw1
tcw2	17.27	11.22	5.88	3.53	0.236	0.492	6.026E-12	0.013	1.31	2.89	1.97	2.02E-08	5.37E-18	2.99E-04	tcw2
tcw3	16.31	11.62	6.19	4.04	0.427	0.492	2.399E-12	0.006	1.75	0.89	1.97	3.40E-08	4.90E-17	7.05E-05	tcw3
ptn1	13.51	12.52	4.42	2.96	0.231	0.492	3.02E-13	0.373	1.30	10.75	1.97	6.24E-09	3.09E-14	4.84E-05	ptn1
ptn2	14.52	12.36	5.06	2.74	0.488	0.492	4.365E-13	0.085	1.95	17.84	1.97	9.04E-09	3.02E-15	4.83E-05	ptn2
ptn3	13.08	11.54	4.34	2.47	0.287	0.492	2.884E-12	0.448	1.40	33.22	1.97	2.22E-08	8.32E-14	1.30E-04	ptn3
ptn4	12.94	12.93	4.37	3.03	0.349	0.492	1.175E-13	0.418	1.54	9.15	1.97	1.69E-09	1.15E-13	6.94E-05	ptn4
ptn5	12.61	12.61	3.71	3.71	0.279	0.279	2.455E-13	1.912	1.39	1.91	1.39	2.95E-09	2.45E-13	8.32E-05	ptn5
tsw1	16.31	11.78	5	4.4	0.237	0.481	1.66E-12	0.098	1.31	0.39	1.93	1.86E-08	4.90E-17	8.92E-05	tsw1
tsw2	15.56	11.74	4.64	4.03	0.273	0.488	1.82E-12	0.225	1.38	0.91	1.95	1.41E-08	2.75E-16	1.29E-04	tsw2
tsw3	16.94	12.05	5.17	3.75	0.247	0.492	8.913E-13	0.066	1.33	1.74	1.97	8.49E-09	1.15E-17	1.05E-04	tsw3
tsw4	17.39	12.35	5.99	4.01	0.322	0.492	4.467E-13	0.010	1.47	0.96	1.97	3.60E-09	4.07E-18	1.24E-04	tsw4
tsw5	16.81	11.86	5.48	3.96	0.229	0.492	1.38E-12	0.032	1.30	1.07	1.97	4.20E-09	1.55E-17	3.29E-04	tsw5
tsw6	16.05	11.92	6.13	3.88	0.414	0.492	1.202E-12	0.007	1.71	1.29	1.97	3.01E-09	8.91E-17	3.99E-04	tsw6
tsw7	16.89	11.92	5.81	3.93	0.387	0.492	1.202E-12	0.015	1.63	1.15	1.97	2.44E-09	1.29E-17	4.92E-04	tsw7
ch1z	16.86	13.62	6.08	2.95	0.366	0.492	2.399E-14	0.008	1.58	11.00	1.97	2.18E-09	1.38E-17	1.10E-05	ch1z
ch3z	17.04	13.93	5.71	2.91	0.22	0.492	1.175E-14	0.019	1.28	12.06	1.97	1.07E-09	9.12E-18	1.10E-05	ch3z
ch4z	16.81	13.81	6.11	2.94	0.477	0.492	1.549E-14	0.008	1.91	11.26	1.97	1.41E-09	1.55E-17	1.10E-05	ch4z
pp3v	14.55	12.16	4.76	2.85	0.311	0.492	6.918E-13	0.170	1.45	13.85	1.97	9.69E-09	2.82E-15	7.14E-05	pp3v
pp2z	16.24	13.19	5.78	3.43	0.316	0.492	6.457E-14	0.016	1.46	3.64	1.97	5.87E-09	5.75E-17	1.10E-05	pp2z
ch1v	11.88	12.76	4.18	2.93	0.19	0.492	1.738E-13	0.648	1.23	11.52	1.97	2.43E-09	1.32E-12	7.14E-05	ch1v
ch2v	12.59	12.54	4.13	2.93	0.224	0.492	2.884E-13	0.727	1.29	11.52	1.97	4.04E-09	2.57E-13	7.14E-05	ch2v
ch4v	12.59	12.54	4.13	2.93	0.224	0.492	2.884E-13	0.727	1.29	11.52	1.97	4.04E-09	2.57E-13	7.14E-05	ch4v

$\log K_m$	Log permeanility of matrix material
$\log K_f$	Log permeanility of matrix material
$\log(\alpha_m)$	Log vanGenuchten alpha paramter of matrix material
$\log(\alpha_f)$	Log vanGenuchten alpha paramter of fracture material
m_m	vanGenuchten m paramter for matrix material
m_f	vanGenuchten m paramter for fracture material
K_f	Bulk pemeability of fracture material
α_m	vanGenuchten alpha paramter for matrix material (1/meters)
α_f	vanGenuchten alpha paramter for fracture material (1/meters)
n_m	vanGenuchten n paramter for matrix material ($1/1-m_m$)
n_f	vanGenuchten n paramter for fracture material ($1/1-m_f$)
k_f	Intrinsic fracure permeability
K_m	Matrix permeability
ϕ_f	Fracture volume fraction

Table 15-4. Property Set 6412c

Property Set 6412c

Based on Bodvarsson et al. (1997) Table 6.4.1-2

	LBL Properties							FEHM parameters							
	$\log K_m$	$\log K_f$	$\log(\alpha_m)$	$\log(\alpha_f)$	m_m	m_f	K_f	α_m 1/m	n_m	α_f 1/m	n_f	k_f	K_m	ϕ_f	
tcw1	17.27	11.22	5.94	3.4	0.231	0.667	6.03E-12	0.011	1.30	3.90	3.00	2.58E-08	5.37E-18	2.33E-04	tcw1
tcw2	17.27	11.22	5.89	3.4	0.236	0.667	6.03E-12	0.013	1.31	3.90	3.00	2.02E-08	5.37E-18	2.99E-04	tcw2
tcw3	16.3	11.62	6.14	4.04	0.437	0.667	2.40E-12	0.007	1.78	0.89	3.00	3.40E-08	5.01E-17	7.05E-05	tcw3
ptn1	13.8	12.54	4.44	2.96	0.230	0.667	2.88E-13	0.356	1.30	10.75	3.00	5.96E-09	1.58E-14	4.84E-05	ptn1
ptn2	14.48	12.35	5.09	2.73	0.050	0.667	4.47E-13	0.080	1.05	18.26	3.00	9.25E-09	3.31E-15	4.83E-05	ptn2
ptn3	13.27	11.52	4.36	2.46	0.289	0.667	3.02E-12	0.428	1.41	33.99	3.00	2.32E-08	5.37E-14	1.30E-04	ptn3
ptn4	13.06	12.93	4.41	3.04	0.353	0.667	1.17E-13	0.381	1.55	8.94	3.00	1.69E-09	8.71E-14	6.94E-05	ptn4
ptn5	12.49	12.49	3.80	3.8	0.288	0.288	3.24E-13	1.554	1.40	1.55	1.40	3.89E-09	3.24E-13	8.32E-05	ptn5
tsw1	16.12	10.49	4.53	4.18	0.220	0.667	3.24E-11	0.289	1.28	0.65	3.00	3.63E-07	7.59E-17	8.92E-05	tsw1
tsw2	15.2	12.07	4.65	4.03	0.273	0.657	8.51E-13	0.219	1.38	0.91	2.92	6.60E-09	6.31E-16	1.29E-04	tsw2
tsw3	16.81	12.03	5.18	3.82	0.247	0.666	9.33E-13	0.065	1.33	1.48	2.99	8.89E-09	1.55E-17	1.05E-04	tsw3
tsw4	16.97	12.37	5.97	4.08	0.322	0.667	4.27E-13	0.011	1.47	0.82	3.00	3.44E-09	1.07E-17	1.24E-04	tsw4
tsw5	16.84	12.06	5.49	3.99	0.230	0.667	8.71E-13	0.032	1.30	1.00	3.00	2.65E-09	1.45E-17	3.29E-04	tsw5
tsw6	16.02	11.92	6.12	3.79	0.414	0.667	1.20E-12	0.007	1.71	1.59	3.00	3.01E-09	9.55E-17	3.99E-04	tsw6
tsw7	17.05	11.92	6.22	3.92	0.372	0.667	1.20E-12	0.006	1.59	1.18	3.00	2.44E-09	8.91E-18	4.92E-04	tsw7
ch1z	16.97	13.59	6.53	2.94	0.359	0.667	2.57E-14	0.003	1.56	11.26	3.00	2.34E-09	1.07E-17	1.10E-05	ch1z
ch3z	17.05	13.61	5.58	2.98	0.221	0.667	2.45E-14	0.026	1.28	10.27	3.00	2.23E-09	8.91E-18	1.10E-05	ch3z
ch4z	16.76	13.71	6.12	2.94	0.477	0.667	1.95E-14	0.007	1.91	11.26	3.00	1.77E-09	1.74E-17	1.10E-05	ch4z
pp3v	14.72	12.15	4.74	2.85	0.313	0.667	7.08E-13	0.178	1.46	13.85	3.00	9.92E-09	1.91E-15	7.14E-05	pp3v
pp2z	16.56	12.79	5.75	3.85	0.317	0.667	1.62E-13	0.017	1.46	1.38	3.00	1.47E-08	2.75E-17	1.10E-05	pp2z
ch1v	11.8	12.76	3.92	2.93	0.350	0.667	1.74E-13	1.179	1.54	11.52	3.00	2.43E-09	1.58E-12	7.14E-05	ch1v
ch2v	12.82	12.54	4.13	2.93	0.450	0.667	2.88E-13	0.727	1.82	11.52	3.00	4.04E-09	1.51E-13	7.14E-05	ch2v
ch4v	12.82	12.54	3.25	2.93	0.390	0.667	2.88E-13	5.513	1.64	11.52	3.00	4.04E-09	1.51E-13	7.14E-05	ch4v

$\log K_m$	Log permeanility of matrix material
$\log K_f$	Log permeanility of matrix material
$\log(\alpha_m)$	Log vanGenuchten alpha paramter of matrix material
$\log(\alpha_f)$	Log vanGenuchten alpha paramter of fracture material
m_m	vanGenuchten m paramter for matrix material
m_f	vanGenuchten m paramter for fracture material
K_f	Bulk pemeability of fracture material
α_m	vanGenuchten alpha paramter for matrix material (1/meters)
α_f	vanGenuchten alpha paramter for fracture material (1/meters)
n_m	vanGenuchten n paramter for matrix material ($1/1-m_m$)
n_f	vanGenuchten n paramter for fracture material ($1/1-m_f$)
k_f	Intrinsic fracure permeability
K_m	Matrix permeability
ϕ_f	Fracture volume fraction

Table 15-5. Property Set 6522

Property Set 6522

Based on Bodvarsson et al. (1997) Table 6.5.2-2

	LBL Properties							FEHM parameters							
	K_m	K_f	α_m	α_f	m_m	m_f	K_f	α_m 1/m	n_m	α_f 1/m	n_f	k_f	K_m	ϕ_f	
tcw1	5.40E-18	6.00E-12	1.15E-06	2.37E-04	0.232	0.492	6.00E-12	0.011	1.30	2.32	1.97	2.57E-08	5.40E-18	2.33E-04	tcw1
tcw2	5.40E-18	6.00E-12	1.29E-06	2.37E-04	0.231	0.492	6.00E-12	0.013	1.30	2.32	1.97	2.01E-08	5.40E-18	2.99E-04	tcw2
tcw3	5.00E-17	2.40E-12	7.30E-07	9.12E-05	0.426	0.492	2.40E-12	0.007	1.74	0.89	1.97	3.40E-08	5.00E-17	7.05E-05	tcw3
ptn1	1.60E-14	2.88E-13	3.65E-05	1.10E-03	0.228	0.492	2.88E-13	0.358	1.30	10.78	1.97	5.95E-09	1.60E-14	4.84E-05	ptn1
ptn2	3.30E-15	4.57E-13	7.56E-06	1.85E-03	0.492	0.492	4.57E-13	0.074	1.97	18.14	1.97	9.46E-09	3.30E-15	4.83E-05	ptn2
ptn3	5.40E-14	3.02E-12	3.66E-05	3.45E-03	0.279	0.492	3.02E-12	0.359	1.39	33.82	1.97	2.32E-08	5.40E-14	1.30E-04	ptn3
ptn4	8.80E-14	1.17E-13	4.30E-05	9.13E-04	0.326	0.492	1.17E-13	0.422	1.48	8.95	1.97	1.69E-09	8.80E-14	6.94E-05	ptn4
ptn5	1.27E-13	1.27E-13	1.96E-04	1.96E-04	0.272	0.272	1.27E-13	1.922	1.37	1.92	1.37	1.53E-09	1.27E-13	8.32E-05	ptn5
tsw1	6.87E-16	2.08E-12	1.33E-05	1.49E-04	0.23	0.491	2.08E-12	0.130	1.30	1.46	1.96	2.33E-08	6.87E-16	8.92E-05	tsw1
tsw2	3.63E-16	2.25E-12	2.31E-05	9.13E-05	0.278	0.487	2.25E-12	0.226	1.39	0.90	1.95	1.74E-08	3.63E-16	1.29E-04	tsw2
tsw3	2.11E-17	8.91E-13	6.44E-06	1.63E-04	0.248	0.492	8.91E-13	0.063	1.33	1.60	1.97	8.49E-09	2.11E-17	1.05E-04	tsw3
tsw4	6.75E-18	4.27E-13	1.14E-06	9.73E-05	0.323	0.492	4.27E-13	0.011	1.48	0.95	1.97	3.44E-09	6.75E-18	1.24E-04	tsw4
tsw5	7.96E-18	9.12E-13	3.16E-06	1.26E-04	0.232	0.492	9.12E-13	0.031	1.30	1.24	1.97	2.77E-09	7.96E-18	3.29E-04	tsw5
tsw6	9.62E-17	1.20E-12	6.92E-07	1.32E-04	0.414	0.492	1.20E-12	0.007	1.71	1.29	1.97	3.01E-09	9.62E-17	3.99E-04	tsw6
tsw7	6.69E-18	1.20E-12	1.34E-06	1.19E-04	0.372	0.492	1.20E-12	0.013	1.59	1.17	1.97	2.44E-09	6.69E-18	4.92E-04	tsw7
ch1z	6.00E-17	2.51E-14	6.90E-07	1.14E-03	0.359	0.492	2.51E-14	0.007	1.56	11.18	1.97	2.28E-09	6.00E-17	1.10E-05	ch1z
ch3z	1.87E-18	2.51E-14	2.49E-06	1.14E-03	0.221	0.492	2.51E-14	0.024	1.28	11.18	1.97	2.28E-09	1.87E-18	1.10E-05	ch3z
ch4z	1.33E-17	2.51E-14	7.83E-07	1.14E-03	0.476	0.492	2.51E-14	0.008	1.91	11.18	1.97	2.28E-09	1.33E-17	1.10E-05	ch4z
pp3v	1.24E-15	7.08E-13	1.81E-05	1.42E-03	0.31	0.492	7.08E-13	0.177	1.45	13.92	1.97	9.92E-09	1.24E-15	7.14E-05	pp3v
pp2z	9.40E-18	2.51E-14	1.71E-06	1.14E-03	0.312	0.492	2.51E-14	0.017	1.45	11.18	1.97	2.28E-09	9.40E-18	1.10E-05	pp2z
ch1v	1.60E-12	1.74E-13	9.80E-05	1.18E-03	0.187	0.492	1.74E-13	0.961	1.23	11.57	1.97	2.44E-09	1.60E-12	7.14E-05	ch1v
ch2v	5.50E-14	2.88E-13	8.65E-05	1.18E-03	0.222	0.492	2.88E-13	0.848	1.29	11.57	1.97	4.03E-09	5.50E-14	7.14E-05	ch2v
ch4v	5.50E-14	2.88E-13	8.65E-05	1.18E-03	0.222	0.492	2.88E-13	0.848	1.29	11.57	1.97	4.03E-09	5.50E-14	7.14E-05	ch4v

K_m	Permeanility of matrix material
K_f	Permeanility of matrix material
α_m	vanGenuchten alpha paramter of matrix material (1/Pa)
α_f	vanGenuchten alpha paramter of fracture material (1/Pa)
m_m	vanGenuchten m paramter for matrix material
m_f	vanGenuchten m paramter for fracture material
K_f	Bulk pemeability of fracture material

α_m	vanGenuchten alpha paramter for matrix material (1/meters)
α_f	vanGenuchten alpha paramter for fracture material (1/meters)
n_m	vanGenuchten n paramter for matrix material ($1/1-m_m$)
n_f	vanGenuchten n paramter for fracture material ($1/1-m_f$)
k_f	Intrinsic fracure permeability
K_m	Matrix permeability
ϕ_f	Fracture volume fraction

Table 15-6. Property Set 6531b

Property Set 6531b

Based on Bodvarsson et al. (1997) Table 6.5.3-1

	LBL Properties							FEHM parameters							
	K_m	K_f	α_m	α_f	m_m	m_f	K_f	α_m 1/m	n_m	α_f 1/m	n_f	k_f	K_m	ϕ_f	
tcw1	5.40E-18	4.85E-12	1.17E-06	1.08E-04	0.399	0.643	4.85E-12	0.011	1.66	1.06	2.80	2.08E-08	5.40E-18	2.33E-04	tcw1
tcw2	5.40E-18	6.28E-12	1.38E-06	1.55E-04	0.408	0.674	6.28E-12	0.014	1.69	1.52	3.07	2.10E-08	1.00E+00	2.99E-04	tcw2
tcw3	5.00E-17	2.40E-12	8.00E-07	9.12E-05	0.471	0.681	2.40E-12	0.008	1.89	0.89	3.13	3.40E-08	1.00E+00	7.05E-05	tcw3
ptn1	3.20E-13	3.97E-13	1.79E-04	1.10E-03	0.207	0.667	3.97E-13	1.755	1.26	10.78	3.00	8.20E-09	1.00E+00	4.84E-05	ptn1
ptn2	3.30E-15	4.57E-13	2.90E-05	1.85E-03	0.348	0.667	4.57E-13	0.284	1.53	18.14	3.00	9.46E-09	1.00E+00	4.83E-05	ptn2
ptn3	2.82E-13	3.02E-12	4.57E-04	3.45E-03	0.217	0.667	3.02E-12	4.480	1.28	33.82	3.00	2.32E-08	1.00E+00	1.30E-04	ptn3
ptn4	8.75E-14	1.17E-13	4.00E-04	9.13E-04	0.321	0.667	1.17E-13	3.922	1.47	8.95	3.00	1.69E-09	1.00E+00	6.94E-05	ptn4
ptn5	3.20E-13	2.19E-13	5.79E-04	1.11E-03	0.27	0.667	2.19E-13	5.676	1.37	10.88	3.00	2.63E-09	1.00E+00	8.32E-05	ptn5
tsw1	3.39E-15	1.20E-12	8.85E-06	3.96E-05	0.288	0.667	1.20E-12	0.087	1.40	0.39	3.00	1.35E-08	1.00E+00	8.92E-05	tsw1
tsw2	2.99E-15	7.08E-13	3.78E-05	3.88E-05	0.328	0.667	7.08E-13	0.371	1.49	0.38	3.00	5.49E-09	1.00E+00	1.29E-04	tsw2
tsw3	8.42E-17	8.91E-13	6.57E-06	1.43E-05	0.247	0.683	8.91E-13	0.064	1.33	0.14	3.15	8.49E-09	1.00E+00	1.05E-04	tsw3
tsw4	8.03E-18	6.07E-13	1.09E-06	1.22E-05	0.327	0.703	6.07E-13	0.011	1.49	0.12	3.37	4.90E-09	1.00E+00	1.24E-04	tsw4
tsw5	2.81E-17	1.29E-12	3.20E-06	1.51E-05	0.235	0.677	1.29E-12	0.031	1.31	0.15	3.10	3.92E-09	1.00E+00	3.29E-04	tsw5
tsw6	7.54E-18	1.25E-12	1.24E-06	1.79E-05	0.416	0.687	1.25E-12	0.012	1.71	0.18	3.19	3.13E-09	1.00E+00	3.99E-04	tsw6
tsw7	7.23E-18	1.20E-12	1.74E-06	3.31E-05	0.384	0.657	1.20E-12	0.017	1.62	0.32	2.92	2.44E-09	1.00E+00	4.92E-04	tsw7
ch1z	8.77E-18	2.51E-14	1.72E-06	1.44E-04	0.369	0.667	2.51E-14	0.017	1.58	1.41	3.00	2.28E-09	1.00E+00	1.10E-05	ch1z
ch3z	8.94E-18	2.51E-14	5.00E-06	3.67E-05	0.227	0.676	2.51E-14	0.049	1.29	0.36	3.09	2.28E-09	1.00E+00	1.10E-05	ch3z
ch4z	7.65E-18	2.51E-14	1.26E-06	8.07E-05	0.474	0.667	2.51E-14	0.012	1.90	0.79	3.00	2.28E-09	1.00E+00	1.10E-05	ch4z
pp3v	5.90E-15	7.08E-13	1.82E-05	1.42E-04	0.313	0.667	7.08E-13	0.178	1.46	1.39	3.00	9.92E-09	1.00E+00	7.14E-05	pp3v
pp2z	2.63E-17	2.51E-14	1.45E-06	1.14E-04	0.315	0.667	2.51E-14	0.014	1.46	1.12	3.00	2.28E-09	1.00E+00	1.10E-05	pp2z
ch1v	1.60E-12	1.74E-12	7.08E-05	1.18E-03	0.191	0.667	1.74E-12	0.694	1.24	11.57	3.00	2.44E-08	1.00E+00	7.14E-05	ch1v
ch2v	2.02E-13	2.88E-13	7.44E-05	1.18E-03	0.227	0.667	2.88E-13	0.729	1.29	11.57	3.00	4.03E-09	1.00E+00	7.14E-05	ch2v
ch4v	2.02E-13	2.88E-13	7.44E-05	1.18E-03	0.227	0.667	2.88E-13	0.729	1.29	11.57	3.00	4.03E-09	1.00E+00	7.14E-05	ch4v

K_m	Permeanility of matrix material
K_f	Permeanility of matrix material
α_m	vanGenuchten alpha paramter of matrix material (1/Pa)
α_f	vanGenuchten alpha paramter of fracture material (1/Pa)
m_m	vanGenuchten m paramter for matrix material
m_f	vanGenuchten m paramter for fracture material
K_f	Bulk pemeability of fracture material

α_m	vanGenuchten alpha paramter for matrix material (1/meters)
α_f	vanGenuchten alpha paramter for fracture material (1/meters)
n_m	vanGenuchten n paramter for matrix material ($1/1-m_m$)
n_f	vanGenuchten n paramter for fracture material ($1/1-m_f$)
k_f	Intrinsic fracure permeability
K_m	Matrix permeability
ϕ_f	Fracture volume fraction

Table 15-7. Property Set 6541

Property Set 6541

Based on Bodvarsson et al. (1997) Table 6.5.4-1

	LBL Properties							FEHM parameters							
	K_m	K_f	α_m	α_f	m_m	m_f	K_f	α_m 1/m	n_m	α_f 1/m	n_f	k_f	K_m	ϕ_f	
tcw1	5.40E-18	4.85E-12	1.17E-06	1.08E-04	0.399	0.643	4.85E-12	0.011	1.66	1.06	2.80	2.08E-08	5.40E-18	2.33E-04	tcw1
tcw2	5.40E-18	6.28E-12	1.38E-06	1.55E-04	0.408	0.674	6.28E-12	0.014	1.69	1.52	3.07	2.10E-08	1.00E+00	2.99E-04	tcw2
tcw3	5.00E-17	2.40E-12	8.00E-07	9.12E-05	0.471	0.681	2.40E-12	0.008	1.89	0.89	3.13	3.40E-08	1.00E+00	7.05E-05	tcw3
ptn1	3.20E-13	3.97E-13	1.79E-04	1.10E-03	0.207	0.667	3.97E-13	1.755	1.26	10.78	3.00	8.20E-09	1.00E+00	4.84E-05	ptn1
ptn2	3.30E-15	4.57E-13	2.90E-05	1.85E-03	0.348	0.667	4.57E-13	0.284	1.53	18.14	3.00	9.46E-09	1.00E+00	4.83E-05	ptn2
ptn3	2.82E-13	3.02E-12	4.57E-04	3.45E-03	0.217	0.667	3.02E-12	4.480	1.28	33.82	3.00	2.32E-08	1.00E+00	1.30E-04	ptn3
ptn4	8.75E-14	1.17E-13	4.00E-04	9.13E-04	0.321	0.667	1.17E-13	3.922	1.47	8.95	3.00	1.69E-09	1.00E+00	6.94E-05	ptn4
ptn5	3.20E-13	2.19E-13	5.79E-04	1.11E-03	0.27	0.667	2.19E-13	5.676	1.37	10.88	3.00	2.63E-09	1.00E+00	8.32E-05	ptn5
tsw1	3.39E-15	1.20E-12	8.85E-06	3.96E-05	0.288	0.667	1.20E-12	0.087	1.40	0.39	3.00	1.35E-08	1.00E+00	8.92E-05	tsw1
tsw2	2.99E-15	7.08E-13	3.78E-05	3.88E-05	0.328	0.667	7.08E-13	0.371	1.49	0.38	3.00	5.49E-09	1.00E+00	1.29E-04	tsw2
tsw3	8.42E-17	8.91E-13	6.57E-06	1.43E-05	0.247	0.683	8.91E-13	0.064	1.33	0.14	3.15	8.49E-09	1.00E+00	1.05E-04	tsw3
tsw4	8.03E-18	6.07E-13	1.09E-06	1.22E-05	0.327	0.703	6.07E-13	0.011	1.49	0.12	3.37	4.90E-09	1.00E+00	1.24E-04	tsw4
tsw5	2.81E-17	1.29E-12	3.20E-06	1.51E-05	0.235	0.677	1.29E-12	0.031	1.31	0.15	3.10	3.92E-09	1.00E+00	3.29E-04	tsw5
tsw6	7.54E-18	1.25E-12	1.24E-06	1.79E-05	0.416	0.687	1.25E-12	0.012	1.71	0.18	3.19	3.13E-09	1.00E+00	3.99E-04	tsw6
tsw7	7.23E-18	1.20E-12	1.74E-06	3.31E-05	0.384	0.657	1.20E-12	0.017	1.62	0.32	2.92	2.44E-09	1.00E+00	4.92E-04	tsw7
ch1z	8.77E-18	2.51E-14	1.72E-06	1.44E-04	0.369	0.667	2.51E-14	0.017	1.58	1.41	3.00	2.28E-09	1.00E+00	1.10E-05	ch1z
ch3z	8.94E-18	2.51E-14	5.00E-06	3.67E-05	0.227	0.676	2.51E-14	0.049	1.29	0.36	3.09	2.28E-09	1.00E+00	1.10E-05	ch3z
ch4z	7.65E-18	2.51E-14	1.26E-06	8.07E-05	0.474	0.667	2.51E-14	0.012	1.90	0.79	3.00	2.28E-09	1.00E+00	1.10E-05	ch4z
pp3v	5.90E-15	7.08E-13	1.82E-05	1.42E-04	0.313	0.667	7.08E-13	0.178	1.46	1.39	3.00	9.92E-09	1.00E+00	7.14E-05	pp3v
pp2z	2.63E-17	2.51E-14	1.45E-06	1.14E-04	0.315	0.667	2.51E-14	0.014	1.46	1.12	3.00	2.28E-09	1.00E+00	1.10E-05	pp2z
ch1v	1.60E-12	1.74E-12	7.08E-05	1.18E-03	0.191	0.667	1.74E-12	0.694	1.24	11.57	3.00	2.44E-08	1.00E+00	7.14E-05	ch1v
ch2v	2.02E-13	2.88E-13	7.44E-05	1.18E-03	0.227	0.667	2.88E-13	0.729	1.29	11.57	3.00	4.03E-09	1.00E+00	7.14E-05	ch2v
ch4v	2.02E-13	2.88E-13	7.44E-05	1.18E-03	0.227	0.667	2.88E-13	0.729	1.29	11.57	3.00	4.03E-09	1.00E+00	7.14E-05	ch4v

K_m	Permeanility of matrix material
K_f	Permeanility of matrix material
α_m	vanGenuchten alpha paramter of matrix material (1/Pa)
α_f	vanGenuchten alpha paramter of fracture material (1/Pa)
m_m	vanGenuchten m paramter for matrix material
m_f	vanGenuchten m paramter for fracture material
K_f	Bulk pemeability of fracture material
α_m	vanGenuchten alpha paramter for matrix material (1/meters)
α_f	vanGenuchten alpha paramter for fracture material (1/meters)
n_m	vanGenuchten n paramter for matrix material (1/1-m_m)
n_f	vanGenuchten n paramter for fracture material (1/1-m_f)
k_f	Intrinsic fracure permeability
K_m	Matrix permeability
ϕ_f	Fracture volume fraction

TRW Environmental
Safety Systems Inc.

1180 Town Center Drive
Las Vegas, NV 89134
702.295.5400

WBS: 1.2.3.4.1.5.1
QA: N

Contract #: DE-AC01-91RW00134
LV.SPO.PP.TAG.08/97-090

August 29, 1997

Stephan J. Brocoum, Assistant Manager
for Licensing
U.S. Department of Energy (DOE)
Yucca Mountain Site Characterization Office
P.O. Box 30307
North Las Vegas, NV 89036-0307

Attention: Technical Publications Management

Dear Dr. Brocoum:

Subject: Completion of Level 3 Fiscal Year (FY) 1997 M&O Milestone SP25CM3A, "Saturated Zone Radionuclide Transport Model," Work Breakdown Structure (WBS)1.2.3.4.1.5.1

Three copies of the above-referenced deliverable are being submitted for deliverable acceptance review in accordance with YAP-5.1Q. This action completes delivery of Milestone SP25CM3A. A second YAR form is also included for the related deliverable SP341RM3. This YAR may be approved when acceptance of SP25CM3A is completed.

If you have any questions regarding this deliverable, please contact Roger Henning at (702) 295-5743, or me at (702) 295-5604.

Sincerely,

Larry R. Hayes

Larry R. Hayes, Manager
Site Evaluation Program Operations
Management and Operating Contractor

LRH/clt

Enclosures:
(1) Deliverable Acceptance Review Forms
(2) Participant Planning Sheet
(3) Milestone SP25CM3A

Distribution
cc wo/encls:
W. E. Barnes, DOE/YMSCO, Las Vegas, Nevada
S. J. Brocoum, DOE/YMSCO, Las Vegas, Nevada
P. R. Burke, M&O, Las Vegas, Nevada
L. D. Foust, M&O, Las Vegas, Nevada
S. Klapproth, M&O, Las Vegas, Nevada
C. L. Lugo, M&O, Las Vegas, Nevada
R. G. Vawter, M&O, Las Vegas, Nevada
R. J. Henning, M&O, Las Vegas, Nevada
R. L. Patterson, DOE/YMSCO, Las Vegas, Nevada

cc w/encl:
M. D. Voegele, M&O, Las Vegas, Nevada
LV RPC = ~~175~~ pages (previously processed)
165 [illegible] 9/1/97